PON RICERCA E INNOVAZIONE 2014 - 2020

UNIONE EUROPEA

Ministero dell'Università e della Ricerca

Doctoral Thesis

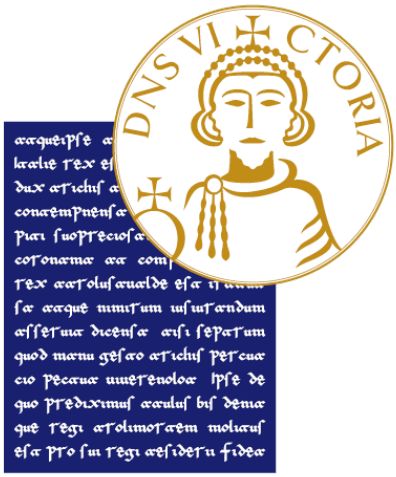

Title: From Sensing to Insight: Modeling and Characterization of Measurement Systems for Precision Agriculture

Submitted by
Fatemeh Khalesi

In fulfillment of the requirements for the degree of Doctor of Philosophy

PhD. course in Information Technology for Engineering

Coordinator: **Prof. Massimiliano Di Penta**
Advisor: **Prof. Pasquale Daponte**

Department of Engineering
University of Sannio, Benevento, Italy

(Summer 2025)

Advisor:
Pasquale Daponte, Full Professor
Department of Engineering
University of Sannio
Benevento, Italy

Co-advisor:
Francesco Picariello, Assistant Professor
Luca De Vito, Associate Professor
Department of Engineering
University of Sannio
Benevento, Italy

Examiners:
Francesco Lamonaca, Associate Professor
Department of Computer Science, Modelling, Electronics and Systems Engineering (DIMES)
University of Calabria
Rende (CS), Italy

João Valente, Assistant Professor
Tenured Scientist in UAVs, Robotics, and Artificial Intelligence
Centre for Automation and Robotics (CAR)
Spanish National Research Council (CSIC)
Madrid, Spain

«وَ مَنْ يَتَّقِ اللَّهَ يَجْعَلْ لَهُ مَخْرَجاً وَ يَرْزُقْهُ
مِنْ حَيْثُ لا يَحْتَسِبُ وَ مَنْ يَتَوَكَّلْ عَلَى اللَّهِ فَهُوَ حَسْبُهُ
إِنَّ اللَّهَ بالِغُ أَمْرِهِ قَدْ جَعَلَ اللَّهُ لِكُلِّ شَيْءٍ قَدْرا»

PE: و هر که از خدا پروا کند، خدا برای او راه بیرون شدن [از مشکلات و تنگناها را] قرار می دهد و او را از جایی که گمان نمی برد روزی می دهد، و هر که بر خدا توکل کند خدا او را کفایت خواهد کرد که خدا امرش را نافذ و روان می‌سازد و بر هر چیز قدر و اندازه‌ای مقرّر داشته است.

EN: And whoever fears Allah, He will make for him a way out [from difficulties and hardships] and provide for him from where he does not expect. And whoever relies on Allah, He will suffice him. Certainly Allah fulfills His purpose, and He has determined for everything a measure.

IT: A chi teme Allah, Egli apre una via d'uscita, e gli concede provvidenze da dove non ne attendeva. Allah basta a chi confida in Lui. In verità Allah realizza i Suoi intenti. Allah ha stabilito una misura per ogni cosa.

Acknowledgements

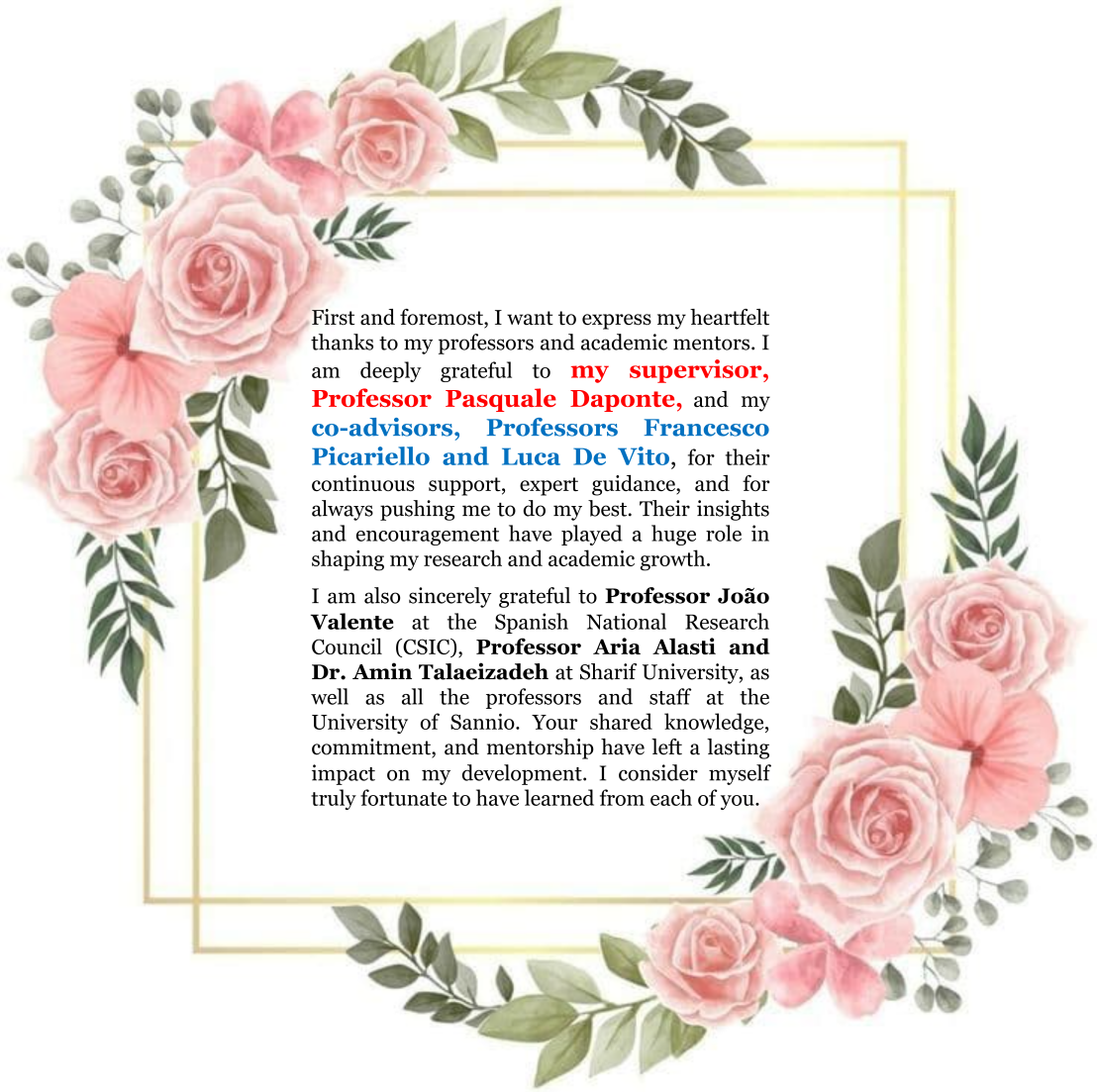

First and foremost, I want to express my heartfelt thanks to my professors and academic mentors. I am deeply grateful to **my supervisor, Professor Pasquale Daponte,** and my **co-advisors, Professors Francesco Picariello and Luca De Vito**, for their continuous support, expert guidance, and for always pushing me to do my best. Their insights and encouragement have played a huge role in shaping my research and academic growth.

I am also sincerely grateful to **Professor João Valente** at the Spanish National Research Council (CSIC), **Professor Aria Alasti and Dr. Amin Talaeizadeh** at Sharif University, as well as all the professors and staff at the University of Sannio. Your shared knowledge, commitment, and mentorship have left a lasting impact on my development. I consider myself truly fortunate to have learned from each of you.

Acknowledgements

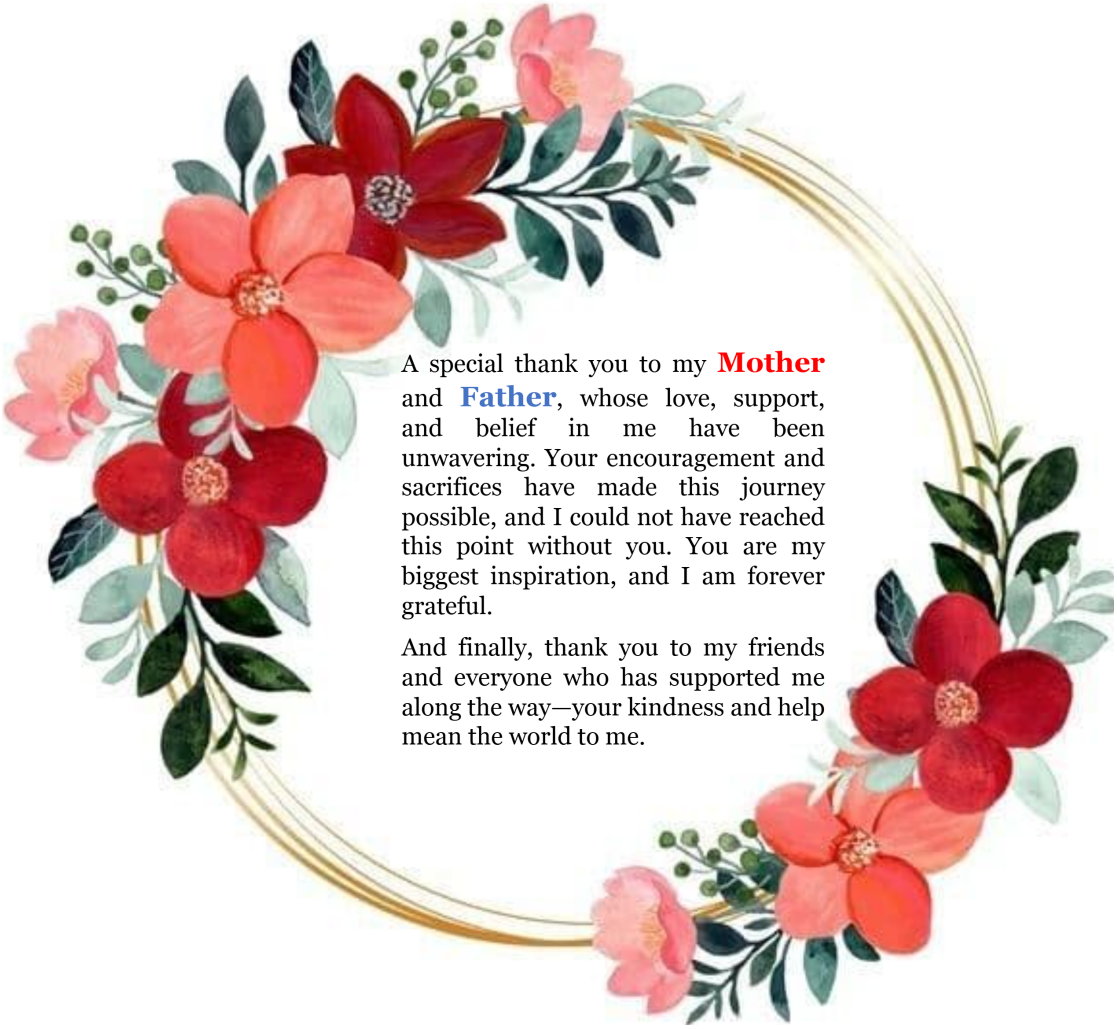

A special thank you to my **Mother** and **Father**, whose love, support, and belief in me have been unwavering. Your encouragement and sacrifices have made this journey possible, and I could not have reached this point without you. You are my biggest inspiration, and I am forever grateful.

And finally, thank you to my friends and everyone who has supported me along the way—your kindness and help mean the world to me.

Abstract

Agriculture faces growing challenges from climate change and population pressures, making the efficient use of resources essential for ensuring global food security. Precision Agriculture (PA), known as precision farming, emerges as a critical response to these challenges. This advanced agricultural approach utilizes digital technologies to monitor and optimize farming processes, aiming to improve both the quantity and quality of crop production while enhancing resource use efficiency and promoting plant health through data-driven decision-making.

At the core of PA are cutting-edge technologies such as advanced sensors, Unmanned Aerial Vehicle (UAV)s, satellite monitoring systems, and positioning technologies like Global Navigation Satellite System (GNSS). These tools generate high-resolution, site-specific data on key factors such as soil health, crop growth, moisture levels, and environmental conditions. Sensors deployed on ground-based platforms, UAVs, or satellite systems offer real-time, large-scale field monitoring, facilitated by advanced image processing techniques, Machine Learning (ML), Artificial Intelligence (AI), and other methodologies. These technologies and methodolgies enable the early detection of crop stress, diseases, and nutrient deficiencies. By integrating these approaches, PA supports the targeted application of water, fertilizers, and pesticides, optimizing resource utilization while enhancing crop yield and promoting sustainable agricultural practices.

Measurement forms the foundation of PA, transforming traditional farming into a highly data-intensive, efficient, and sustainable practice. However, the effectiveness of these measurements depends on their accuracy and reliability, which can be affected by measurement uncertainty. Measurement uncertainty refers to the degree of doubt or variability associated with a measured value, encompassing potential errors, biases, or inaccuracies introduced during data collection, processing, or interpretation. In PA, uncertainty can arise from various sources, including equipment limitations, environmental variability, or challenges in integrating diverse data sources. As measurement technology continues to advance through sensor innovation, data analytics, and automation, addressing and managing uncertainty remains critical to driving the future of agriculture. This thesis aims to enhance the reliability of measurement systems in PA across three key technologies: UAV imagery for NDVI measurement, ML for plant disease detection, and IoT-based tree health monitoring. It includes developing an uncertainty quantification and radiometric compensation framework for NDVI measurements, using

an ML-based identification model for plant disease and assessing its robustness under image variability caused by various uncertainty sources, and designing an IoT-based system for continuous environmental and tree monitoring. Together, these contributions support more accurate, stable, and data-driven decision-making in agricultural practices.

Contents

List of Tables

List of Figures

List of Abbreviations and Symbols

Abbreviations

PA Precision Agriculture

ML Machine Learning

AI Artificial Intelligence

RS Remote Sensing

IoT Internet of Things

UAV Unmanned Aerial Vehicle

RGB Red-Green-Blue

LiDAR Light Detection and Ranging

VI Vegetation Index

VIs Vegetation Indices

NDVI Normalized Difference Vegetation Index

NDMI Normalized Difference Moisture Index

CWSI Crop Water Stress Index

EVI Enhanced Vegetation Index

SAVI Soil Adjusted Vegetation Index

PRI Photochemical Reflectance Index

NDWI Normalized Difference Water Index

GNDVI Green Normalized Difference Vegetation Index

OSAVI Optimized Soil-Adjusted Vegetation Index

RVI Radiometric Vegetation Index

TVI Triangular Vegetation Index

LAI Leaf Area Index

VIM International Vocabulary of Metrology

GNSS Global Navigation Satellite System

NMIs National Metrology Institutes

NIST National Institute of Standards and Technology

NPL National Physical Laboratory

SNR Signal-to-Noise Ratio

ESC Electronic Speed Control

INS Inertial Navigation System

IMU Inertial Measurement Unit

GPS Global Positioning System

EM ElectroMagnetic

PMM Physics-based Modeling Method

ELM Empirical Line Method

HSI Hyperspectral Imaging

R Red

NIR Near-InFrared

UV Ultraviolet

VIS Visible

SWIR Short-Wave Infrared

GUM The Guide to the Expression of Uncertainty in Measurement

PRM Path Radiance Method

ACCP Accelerated Canopy Chemistry Program

RMSE Root Mean Square Error

rRMSE Relative Root Mean Square Error

OD Optical Density

DNs Digital Numbers

DN Digital Number

SSI Solar Spectral Irradiance

SIM Spectral Irradiance Monitor

AU Astronomical Unit

VNIR visible/near-infrared

MCS Monte Carlo Simulation

DL Dry Leaf

FL Fresh Leaf

MED Median

Min Minimum

Max Maximum

SD Standard Deviation

IQR Interquartile Range

Q1 First Quartile

Q3 Third Quartile

LS Leaf State

ATMC Atmosphere Conditions

VTOL Vertical Take-Off and Landing

H0 Null Hypothesis

H1 Alternative Hypothesis

ADDL Atmosphere Dry-clear and Dry Leaf

ADFL Atmosphere Dry-clear and Fresh Leaf

AHDL Atmosphere Humid-hazy and Dry Leaf

AHFL Atmosphere Humid-hazy and Fresh Leaf

AMDL Atmosphere Mixed for Dry Leaf

AMFL Atmosphere Mixed for Fresh Leaf

DOS Dark Object Subtraction

MODTRAN MODerate resolution atmospheric TRANsmission

CMOS Complementary Metal-Oxide-Semiconductor

CNN Convolutional Neural Network

TSEB-PT Two-Source Energy Balance model - Priestley-Taylor equation

LST Land Surface Temperature

SZA Solar Zenith Angle

TOD Time Of Day

FA Flight Altitude

LoRa Long Range

LoRaWAN Long Range Wide Area Network

LPWAN Low-Power Wide Area Network

SPI Serial Peripheral Interface

MCU Microcontroller Unit

ADC nalog-to-Digital Converter

USB Universal Serial Bus

PAR Photosynthetically Active Radiation

ePAR Extended Photosynthetically Active Radiation

SO2 Sulfur Dioxide

NO2 Nitrogen Dioxide

O3 Ozone

CO2 Carbon Dioxide

CO Carbon Monoxide

VOC Volatile Organic Compound

N2O Nitrous Oxide

CH4 Methane

I2C Inter-Integrated Circuit

SDI Serial Digital Interface

IMU Inertial Measurement Unit

PM Particulate Matter

IAQ Indoor Air Quality

ROI Regions Of Interest

ANOVA ANalysis Of Variance

DCNN Deep Convolutional Neural Network

LDA Linear Discriminant Analysis

SVM Support Vector Machine

RF Random Forest

MLP MultiLayer Perceptron

3DCNN 3-Dimensional Convolutional Neural Network

AR Augmented Reality

VRT Variable Rate Technology

GHG Greenhouse Gas

GIS Geographic Information Systems

NIST National Institute of Standards and Technology

PF Permaflect

CHM Canopy Height Model

DTM Digital Terrain Model

DSM Digital Surface Model

MEMS Microelectromechanical Systems

AGB Above Ground Biomass

LRM Linear Regression Method

UAS Unmanned Aerial System

IDM Inverse Distance Weighted

NDRE Normalized Difference Red Edge Index

KNN K Nearest Neighbors

OOS Object Oriented Segmentation

MLP Multi Layer Perceptron

BRDF Bidirectional Reflectance Distribution Function

AMSP Agisoft Metashape Single Panel Compensation

P4DSP Pix4D Fields Single Panel Compensation

AMMP Agisoft Metashape Multiple Panel Compensation

MSSP MicaSense Single Panel Compensation

NRMSE Normalized Root Mean Square Error

MSMP MicaSense Multiple Panel compensation

ELMMP Empirical Line Method Multiple Panel compensation

Chapter 1

Introduction and Motivation

As the global population continues to rise, projected to reach approximately 9.7 billion by 2050, the demand for food and fiber is escalating at an unprecedented rate. Traditional agricultural practices are increasingly insufficient to meet this demand sustainably, prompting a need for innovative solutions that enhance productivity while conserving resources. Modern agricultural production relies heavily on monitoring crop status by observing and measuring various factors, including soil conditions, plant health, the impact of fertilizers and pesticides, irrigation efficiency, and crop yield. Managing these elements presents significant challenges for crop producers, necessitating rapid advancements in monitoring agricultural growth and health assessment to ensure efficient resource use and effective crop yield management [14].

PA has emerged as a cutting-edge approach adopted worldwide, characterized as an advanced innovation and optimized field-level management strategy aimed at enhancing resource productivity in agricultural fields. Implementing PA technologies enables farmers to better understand local soil types, enhance soil quality, make informed crop choices, and manage critical agricultural tasks such as irrigation scheduling, planting and harvesting times, and pest and disease control [15, 16]. These technologies also assist in nutrient application and yield prediction. By minimizing wasteful actions and providing timely management information, PA optimizes the use of water, chemicals, and energy, thereby reducing the sector's vulnerability to climate change, including droughts, extreme weather events, and climate-related pests and diseases [15, 17].

The technologies underpinning PA are continually evolving, integrating Remote Sensing (RS), Internet of Things (IoT), big data analysis, AI, and ML to optimize and synthesize information for informed management decisions. PA applies these technologies to provide, process, and analyze multisource data with high spatial and temporal resolution [2, 18, 19, 20]. Remote sensors used in PA can operate at various distances from the crops being observed, ranging from close-proximity ground-based systems to more distant spaceborne sensors, such as satellites, each with its advantages and disadvantages. While ground-based RSs provide critical data on crop health, soil moisture, and nutrient

levels—facilitating optimized irrigation, pest management practices, and more—they are often hindered by high initial setup costs and infrastructure requirements, which can be prohibitively expensive for small-scale farmers [18]. Additionally, ongoing maintenance and calibration demand substantial resources and specialized expertise, limiting their accessibility. The complexity of data management may also require advanced analytical skills or reliance on external assistance, making it less feasible for some producers. Furthermore, ground-based sensors typically have restricted coverage areas, rendering them less effective for large-scale agriculture compared to aerial or satellite remote sensing technologies. Environmental factors, such as soil composition and weather conditions, can further affect their accuracy, potentially compromising data reliability.

In contrast, satellite RS is well-suited for large-scale studies but often falls short of meeting the spatial resolution requirements necessary for many PA applications [19]. As an alternative, UAVs have emerged as invaluable aerial platforms widely used in PA to acquire detailed environmental data. Operating near crops without causing disturbance, UAVs can capture high-resolution imagery that is less affected by cloud cover and atmospheric conditions compared to satellite-based observations. Equipped with advanced sensors—including RGB, multispectral, hyperspectral, and thermal cameras, as well as LiDAR—UAVs enable comprehensive assessments of vegetation health and soil characteristics, providing critical insights for PA. These sensors facilitate critical measurements for tasks such as irrigation management, pesticide application, fertilizer optimization, and yield prediction. By detecting and analyzing the electromagnetic energy reflected, emitted, or backscattered from soil, crops, and vegetation across specific spectral bands and frequencies, numerous Vegetation Indices (VIs) have been proposed in the literature to assess plant health and soil conditions. These indices include the NDVI, measures plant greenness and biomass by comparing Near-InFrared (NIR) and Red (R) light reflectance, Normalized Difference Moisture Index (NDMI), assesses vegetation water content using NIR and Short-Wave Infrared (SWIR) reflectance, Crop Water Stress Index (CWSI), estimates plant water stress by analyzing canopy temperature relative to air temperature, Enhanced Vegetation Index (EVI), improves sensitivity over high biomass areas and reduces atmospheric influences, compared to NDVI, Soil Adjusted Vegetation Index (SAVI), similar to NDVI but adjusts for soil brightness in areas with sparse vegetation, Photochemical Reflectance Index (PRI), reflects changes in photosynthetic efficiency and light-use efficiency of plants, Normalized Difference Water Index (NDWI), detects water content in vegetation and soil by using NIR and green wavelengths), Green Normalized Difference Vegetation Index (GNDVI) (a variant of NDVI using green instead of R light, more sensitive to chlorophyll content), Triangular Vegetation Index (TVI) (estimates chlorophyll content and biomass based on a triangular area defined by R, green, and NIR reflectance, Leaf Area Index (LAI), represents the

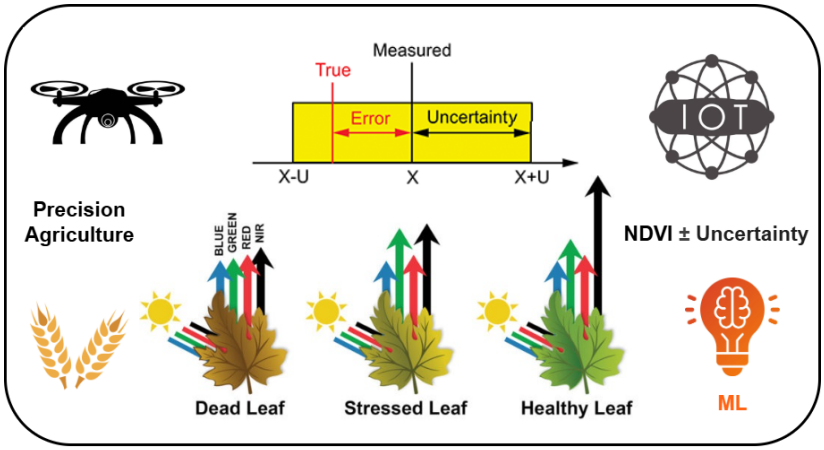

FIGURE 1.1: An integrated overview of this thesis within the context of PA is visually presented in this figure. It highlights the fundamental components of the research, including the use of UAVs for capturing multispectral images from the field, the application of NDVI for evaluating the crop health, and using the methodologies for assessing the effect of uncertainty sources on the NDVI measurement, using ML, and the integration of IoT technologies in PA.

total leaf area per unit ground area - indicating canopy density and productivity, among others. [21, 2, 22, 23, 24, 25].

This thesis explores the complexities of PA and its associated technologies, focusing on the critical issue of measurement using sensors deployed in ground-based IoT systems and UAVs. IoT systems, which integrate networks of sensors, actuators, and data communication technologies, are fundamental to real-time monitoring and control in PA, and their contribution to accurately measuring and considering the effects of uncertainty sources in their measurement and data reliability warrants further analysis [26]. For UAV platforms, a workflow is developed to quantify the effect of uncertainty sources on NDVI measurements by creating a radiometric compensation method, offering valuable insights to enhance the reliability and effectiveness of PA practices. By addressing these challenges, the thesis aims to contribute to sustainable agricultural solutions in the face of global challenges. Fig. 1.1 provides an integrated overview of the concepts explored in this thesis within the context of PA. It includes the use of multispectral images captured by UAVs for NDVI measurement, along with the evaluation of uncertainty sources affecting this VI. It also covers the use of ML models for identifying wheat diseases, as well as the application of IoT technologies for monitoring the health status of trees.

1.1 Role of Measurement in PA

Measurement is important in many areas of science, technology, industry, and everyday life. It is used to describe and compare things accurately, whether they are physical, chemical, biological, or abstract. Scientists use measurement to test ideas, collect data, and confirm results, especially in fields like physics, climate science, and engineering, where accuracy matters a lot. In industries such as healthcare, environmental monitoring, and manufacturing, measurement helps ensure quality, safety, and that rules are followed. It's also useful in economics and business for making good decisions, analyzing finances, and understanding markets. By using common standards, measurement helps people around the world work together and make progress [27, 28].

Measurement traditionally aims to provide precise, objective data on physical quantities, independent of interpretation. However, due to the complexities of real-world interactions, measurements often yield approximate values rather than exact ones. These values are estimates of the true quantity, determined under ideal conditions by flawless systems. Measurement uncertainty reflects the degree of incomplete knowledge regarding the true value of the measurand. It arises from two main sources: (1) the conditions of the measurement process, including external influences on the system, and (2) the accuracy of the measuring system, encompassing both precision and trueness. According to the International Vocabulary of Metrology (VIM), measurement uncertainty is a non-negative parameter that quantifies the dispersion of values that could reasonably be attributed to the measurand [29]. It reflects the degree of doubt about the measurement result, based on the available information, and accounts for factors such as limitations in the measurement process, instruments, and environmental conditions.

In PA, measurement is essential for data-driven decision-making to optimize agricultural practices. PA focuses on managing crop production inputs (e.g., water, nutrients, pesticides) site-specifically to maximize yield, minimize waste, and reduce environmental impact. Here are some examples of how measurement contributes to PA.

The **measurement of soil and crop health** is a central component of PA. Soil sampling and analysis, which includes the measurement of parameters such as pH, nutrient levels, moisture content, and organic matter, allows for the evaluation of soil fertility and health. This data forms the basis for site-specific recommendations regarding fertilizers and soil amendments, thus optimizing crop growth and minimizing unnecessary resource application. Moreover, crop health can be assessed using remote sensing technologies, such as multispectral and hyperspectral sensors, which enable the measurement of indicators like chlorophyll content, nutrient deficiencies, and plant stress. These technologies allow for the early detection of crop issues, facilitating timely interventions and reducing input waste [30].

In **precision irrigation**, accurate measurement of soil moisture using sensors is essential for maintaining optimal water application strategies. The sensors provide real-time data on the volumetric water content of soil, enabling precise control of irrigation timing and quantity. This minimizes both over-irrigation and under-irrigation, thereby conserving water resources while maintaining adequate moisture levels to support plant growth. Over-irrigation not only results in water waste but also promotes surface runoff and deep percolation, which can lead to the leaching of essential nutrients such as nitrogen and potassium from the root zone. This nutrient loss not only reduces fertilizer use efficiency but also poses environmental risks through contamination of groundwater and nearby water bodies. To enhance decision-making, precision irrigation systems often integrate meteorological data, such as precipitation, evapotranspiration rates, temperature, and relative humidity, from localized weather stations. These data inputs allow for dynamic adjustment of irrigation schedules in response to current and forecasted climatic conditions, improving water-use efficiency and optimizing crop yield outcomes [31, 32].

Yield monitoring and forecasting play an important role in maximizing crop output and resource efficiency. Through yield mapping, which combines GPS data and yield monitors integrated into harvesting equipment, farmers can assess the variation in crop performance across fields. This spatial variability enables the identification of low- and high-productivity zones, facilitating targeted interventions such as selective fertilization and pest management. Moreover, predictive models that incorporate historical yield data along with real-time measurements offer valuable insights for forecasting future yields. These models help farmers anticipate crop performance, optimize inputs, and reduce waste [33].

In **pest and disease management**, measurement technologies enable the early detection and localized treatment of pest populations and disease outbreaks. For example, pest populations can be monitored using traps, and remote sensing technologies can detect changes in the environment indicative of pest infestations. Similarly, sensors that measure parameters such as leaf temperature or moisture content provide early indicators of disease-prone conditions. These measurements allow for the targeted application of pest control agents and disease treatments, reducing pesticide use and mitigating environmental impacts [34].

Precision fertilization relies heavily on accurate measurements of soil and plant nutrient levels. Tools such as handheld devices and UAVs measure plant nutrient uptake, particularly nitrogen, ensuring that fertilizers are applied only where necessary. This targeted approach reduces excess fertilizer use, preventing nutrient runoff and environmental contamination. Furthermore, Variable Rate Technology (VRT) combines field measurements with applicator systems to adjust fertilizer application rates in real-time. This system ensures that each part of the field receives the appropriate amount

of fertilizer, promoting both efficient resource use and sustainable agricultural practices [35, 36].

Environmental sustainability in PA is further supported by the measurement of greenhouse gas emissions emissions—such as CO2, Methane (CH4), and Nitrous Oxide (N2O)—as well as nutrient and contaminant fluxes across soil, water, and air systems. These measurements capture key processes including soil–atmosphere carbon exchange, plant uptake, nutrient mineralization and leaching, and runoff of phosphorus, base cations, and heavy metals [37]. By combining real-time data from in-situ sensors, remote sensing, and environmental models, precision agriculture enables targeted agronomic interventions that reduce emissions, prevent nutrient loss, and protect surrounding ecosystems, thus supporting a transition toward more sustainable and resource-efficient farming systems [37].

Economic optimization in PA is driven by measurement-based decision-making tools. By quantifying input costs (e.g., water, fertilizer, and seed) and relating them to yield outcomes, farmers can assess the cost-effectiveness of different agricultural practices. This enables more efficient use of resources and increases profitability. For instance, data on input efficiency and crop performance can be used to optimize the allocation of resources, ensuring that inputs are applied where they are most needed to maximize yield while minimizing costs [36].

1.2 Open Issues

From a methodological perspective, significant ambiguity persists regarding the efficacy of measurement in accurately representing the true value of measured quantities in PA, as measurements are conducted under uncontrolled environmental conditions. Assessing the uncertainties associated with various influencing factors remains a critical and unresolved issue [4, 38]. These include atmospheric and lighting conditions, flight parameters such as altitude and image overlap, environmental variables like temperature and humidity, sensor tilt, camera limitations (such as image resolution), object radiation emissivity, and other factors. To enhance the accuracy and reliability of measurements, it is crucial to thoroughly understand and effectively mitigate these uncertainties. Achieving this will require advanced methodologies and technologies to quantify and correct these influencing factors, thereby improving the precision and validity of agricultural measurements.

IoT technologies hold significant potential for PA, their implementation faces several challenges. The limitations of each sensor in measurement such as limited accuracy, sensitivity to environmental conditions, and noise interference. Synchronization of devices for accurate and energy-efficient operation is complicated by their low computational

power. Power efficiency is critical, as many devices rely on batteries or solar energy. The large volumes of data generated by IoT devices, combined with limited bandwidth, necessitate edge computing for local processing. As deployments scale, issues such as interoperability, network congestion, and firmware updates emerge. Additionally, high initial costs, lack of standardization, and environmental durability requirements pose barriers to widespread adoption [39, 40, 41].

1.3 General Challenges

PA encounters several measurement-related challenges that are critical to its successful implementation and overall effectiveness. Below are some of these key challenges:

1. **Accuracy, Reliability, and Precision of Measurement:** Accuracy refers to how close a measured or estimated value is to the true value. Reliability refers to the ability of a measurement system to produce consistent and repeatable results under consistent conditions over time, and precision is the degree to which repeated measurements under the same conditions yield the same result [42]. In PA, ensuring reliable and consistent data is challenging due to environmental variability, sensor limitations, and the complex nature of agricultural systems. Factors like soil, moisture, and crop differences can affect sensor readings, while low-cost sensors may suffer from performance degradation and calibration issues. These challenges can result in inaccurate assessments and suboptimal management decisions, ultimately reducing the effectiveness of PA.

2. **Traceability of Measurement:** Metrological traceability is the property of a measurement result whereby the result can be related to a reference through a documented, unbroken chain of calibrations, each contributing to the measurement uncertainty. This means that every step in the chain must be recorded and verifiable (documented), there must be a continuous link to a recognized standard—typically national or international (unbroken chain), each link in the chain must involve a calibration process, and every calibration contributes to the total uncertainty associated with the final measurement [43]. Traceability is a challenge in PA due to the complexity and diversity of data sources, lack of standardization, and the difficulty of maintaining consistent calibration across sensors and devices. Data from GNSS, sensors, UAV, and machinery often come with varying accuracy and undocumented uncertainties, making it hard to establish a clear, traceable link to recognized standards. Sensor drift, human error, and incompatible systems further complicate reliable measurement. Additionally, the cost and effort required to

maintain traceable calibration processes can be prohibitive, especially for smaller farms.

3. **Calibration and Compensation:** In VIM 2.39 [44], calibration is defined as a two-step process conducted under specified conditions. The first step involves establishing a relationship between the quantity values, along with their associated measurement uncertainties, provided by measurement standards and the corresponding indications, which also have associated uncertainties. In the second step, this established relationship is then used to derive a measurement result from an indication. On the other hand, in metrology, compensation refers to the application of a correction to a measurement result or system to mitigate the influence of known systematic effects or environmental factors that are not part of the measurand but can affect its accurate determination. This concept, as outlined in the VIM [45], is intrinsically linked to a correction, which is a compensation for an estimated systematic effect, and to influence quantities, such as temperature or pressure, which affect the measurement without being the object of measurement themselves.

   For example, the compensation model described in [46] corrects uneven seed spacing that occurs when multi-row planters follow curved paths. As the planter turns, positioning errors can cause inconsistent seed placement, leading to uneven growth and reduced yields. The compensation model uses GNSS and Inertial Measurement Unit (IMU) sensors to adjust the real-time position and speed of each seeding unit, predicting the next optimal seeding position to maintain uniform spacing despite changes in direction, thereby improving crop growth and yield.

   Therefore, in PA, correction methods are generally applied as compensation to mitigate the effects of uncertainty sources during operation, without altering the fundamental calibration of the measuring instruments.

4. **Mastering Documentation:** Proper documentation is vital for measurement traceability in PA. This includes detailed records of calibrations, methods used, standards referenced, and quantified uncertainties. However, the extensive data generated by modern PA technologies can make thorough documentation challenging. Effective data management systems are required to ensure that all relevant information is captured, stored, and easily retrievable. This level of documentation is essential for verifying the traceability of measurements and ensuring their reliability [47, 48].

5. **Ensuring Competence:** The competence of personnel involved in data collection and analysis is essential for maintaining measurement traceability in PA. Farmers

and agricultural technicians must receive adequate training to properly operate measurement instruments and consider the significance of calibration and documentation. Achieving this level of competence across the agricultural sector, which encompasses a wide range of diverse and dispersed stakeholders, presents a substantial challenge [49]. To address this, targeted training programs and certification processes are necessary to develop and sustain this expertise effectively.

6. **Standardizing:** Standardizing measurement protocols and ensuring the calibration of sensors and instruments across different environments and systems are essential for data comparability and accuracy. Without standardized measurements, it becomes difficult to compare data over time or across different locations, potentially leading to incorrect conclusions and suboptimal farming decisions [50]. Promoters of PA are pushing for standardization to solve the problem of systems not working well together. By creating common rules, they aim to make it easier for farmers to use data and digital tools, no matter what brand of equipment they have. This helps farmers adopt new technologies without needing to replace everything they already use [51].

7. **Integration of Data:** PA relies on integrating data from multiple sources, including sensors, satellite imagery, UAVs, and farm machinery. For example, weather stations installed on the farm track temperature, humidity, and rainfall patterns; satellite data helps monitor VIs like NDVI for crop vigor assessment; UAVs can be equipped with thermal cameras to identify irrigation issues; and harvesters collect yield data in real-time as they operate in the field. Ensuring compatibility, synchronization, and reliability of these data streams—each potentially using different formats and time intervals—poses challenges in measurement and data management [52].

8. **Data Interpretation and Decision Support:** Collecting data is only the first step; interpreting the data and converting it into actionable insights requires advanced analytics and decision support systems. For example, when soil moisture levels are excessively high, soil sensors may reach their maximum measurable value, making it difficult to determine whether flooding has occurred. In such cases, aerial imagery captured by UAVs can provide a more accurate assessment. Additionally, plant moisture content and the extent of foliage development can be monitored through both ground-based observations and aerial imagery. A more precise evaluation and interpretation are achieved by integrating data from both sources. Integrating complex datasets into user-friendly interfaces for farmers and agronomists is crucial for effective decision-making [53].

Overcoming these challenges requires integrating diverse data sources, maintaining instrument calibration, accurately quantifying uncertainties, thoroughly documenting, ensuring personnel competence, and implementing robust quality management systems. Addressing these issues will enhance the effectiveness of PA, leading to better resource management, higher crop yields, and sustainable farming practices.

1.3.1 Open Challenges Discussed in This Thesis

The research presented in this thesis is structured around three technological domains: multispectral imaging using UAV-mounted sensors, IoT-based systems, and the application of ML techniques in agricultural contexts. Specifically, the work focuses on measurement systems involving sensors deployed on both UAV and ground-based platforms. It incorporates metrological principles to evaluate measurement accuracy and investigates uncertainty by analyzing results and, in some cases, identifying and addressing sources of uncertainty. It is important to note that the factors contributing to uncertainty vary across different platforms. Fig. 1.2 illustrates the open challenges addressed in this thesis.

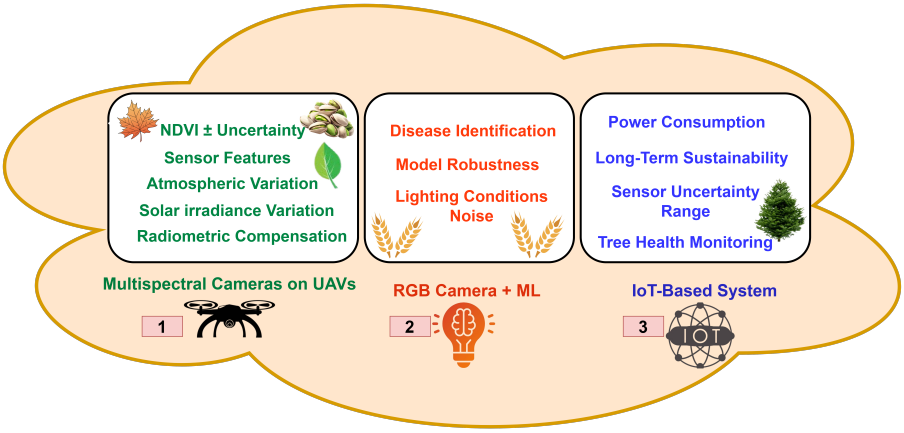

FIGURE 1.2: The open challenges in PA that are addressed in this research.

1. **Open Challenges in the Use of Multispectral Cameras on UAVs:**

   - **Sensor Features and Accuracy:** Characterizing sensor features involves complex procedures that may not consistently yield reliable results across different UAV platforms and operating conditions [54, 4]. The characterization

process aims to quantify the spectral performance of a camera, focusing on the accuracy of the acquired radiation values per wavelength and the camera's SNR. However, when dealing with different sensors, this task is not straightforward, as each sample is measured according to a local reference system, which is heavily influenced by the specific characteristics and design of the sensor [54].

- **Atmospheric and Radiometric Variability:** Variations in lighting and atmospheric conditions, such as changes in humidity and temperature, can significantly affect the multispectral data. These factors can reduce the precision of VIs like NDVI, which are highly sensitive to light scattering and absorption. While radiometric compensation models can mitigate these effects, their effectiveness can be compromised by fluctuating environmental conditions [55].

Research Objective: This thesis aims to develop a comprehensive workflow to quantify the impact of various uncertainty sources on multispectral imagery by proposing an effective radiometric compensation model to improve the accuracy of NDVI measurements. This approach will address key challenges, including sensor specification and the effects of atmospheric variability, Fig. 1.2(1).

2. **Open Challenges in AI:**

   - **Data Interpretation and Decision Support:** AI algorithms rely heavily on large datasets. However, agricultural datasets can be sparse, unbalanced, or noisy, making it difficult to train robust models. Moreover, AI models often struggle with interpreting complex, heterogeneous data, which can lead to incorrect predictions or missed insights [56].
   - **Model Robustness:** Another challenge lies in the generalization of AI models that are robust concerning environmental noise. A model that performs well in one region or crop type may not transfer effectively to others due to variations in environmental conditions, soil types, and farming practices [56].

   Research Objective: This thesis aims to explore the application of ML algorithms for identifying plant diseases using sufficiently small datasets, in contrast to the large datasets typically used in AI, and to conduct sensitivity assessments to evaluate model robustness against uncertainties (Fig. 1.2(2)).

3. **Open Challenges in IoT-Based Systems:**

- **Sensor Network Deployment:** While IoT-based systems hold great promise for continuous monitoring, the deployment of a dense network of sensors in agricultural fields faces challenges related to power consumption, wireless communication, and network reliability, especially in remote or expansive environments [57, 58, 59].
- **Measurement Accuracy and Sensor Uncertainty:** Accurate and reliable sensor measurements are crucial for informed decision-making in PA. However, each type of sensor (e.g., temperature, humidity, soil moisture) exhibits inherent uncertainties due to factors like sensor drift, environmental interference, and manufacturing variability. Quantifying these uncertainties is essential to ensure the validity of sensor data and improve the overall robustness of IoT-based monitoring systems [26]. According to the manufacturer, the sensor functions within a defined measurement range and provides a specified accuracy, which indicates the potential deviation from the true value. Understanding both the sensor's operating range and its uncertainty is essential for accurately interpreting the measured data.
- **Data Management and Integration:** Managing and integrating data from various IoT devices (e.g., soil moisture sensors, weather stations, irrigation controllers) is often cumbersome. Ensuring the interoperability of devices from different manufacturers and handling the large volume of real-time data is a key challenge in IoT-based PA systems [57, 58].
- **Long-Term Sustainability:** The sustainability of IoT systems in agriculture, especially in terms of energy consumption and maintenance of sensors over long periods, remains an open challenge. Efficient power management and renewable energy solutions are necessary for the continuous operation of these systems [57, 58].

Research Objective: This thesis aims to design and implement an IoT-based system for continuous tree health monitoring, addressing challenges related to specifying sensor uncertainty range, energy efficiency, network deployment, and real-time data integration, Fig. 1.2(3).

1.4 Aims of the Thesis

The primary objectives of this thesis are to quantify the effects of various sources of uncertainty on NDVI measurements and propose a radiometric compensation model for multispectral imagery. This model is then applied to NDVI evaluation to assess its effectiveness in mitigating light and atmospheric variations. Furthermore, the thesis

explores the use of ML algorithms for identifying the plant disease, conducts a sensitivity assessment of the model in the presence of uncertainty sources, and develops an IoT-based system for continuous monitoring of plant health within PA applications. An integrated view of all measurement topics addressed in this thesis is described in three main chapters as follows:

1. **Develop and Evaluate a Comprehensive Workflow for NDVI Measurements by Considering the Effect of Uncertainty Sources Using Multispectral Images Captured by UAVs:** This chapter introduces a systematic and comprehensive workflow for modeling and evaluating the effect of uncertainties in NDVI measurement derived from multispectral cameras mounted on UAVs. The workflow begins with the modeling of the camera sensor's nominal wavelength, which is identified as a primary source of uncertainty. Initial uncertainty quantification and sensitivity analysis are performed following GUM, law of uncertainty propagation, Type A and B guidelines. The result shows that the estimated uncertainty values range from 0.03 to 0.09 for both dry and fresh vegetation. To more closely reflect real conditions, the model is extended to include the camera's Optical Density (OD) within its nominal wavelength and limited spectral bandwidth. The results indicate that variation in the camera's nominal wavelength contributes significantly to the overall uncertainty, with values reaching up to 0.1. This degree of uncertainty introduces considerable overlap in NDVI values for dry and fresh leaves, making accurate differentiation between vegetation states based solely on NDVI measurements unreliable.

   The workflow is further expanded to incorporate additional contributing factors in NDVI measurement, including leaf reflectance, solar irradiance, atmospheric conditions, and the camera's Signal-to-Noise Ratio (SNR). Monte Carlo Simulation (MCS) is employed to assess the individual and combined impacts of the variation of factors as uncertainty sources, on NDVI accuracy. The results indicate no overlap between the NDVI values of dry and fresh leaves, suggesting that a threshold can be established to distinguish between the two leaf states under varying atmospheric conditions. However, this threshold is sensitive to changes in environmental factors and must be adjusted accordingly. Then, the proposed workflow is finalized with the integration of a radiometric compensation step. A key contribution of this study is the development of a radiometric compensation method by using the DJI white paper [1]. This method emulated reflectance panels constructed from Permaflect sheets with reflectance values ranging from 5% to 94% (this approach enables the development of an effective radiometric compensation method across diverse lighting and surface scenarios), and validating the model useing a real reference panel under field conditions. The proposed method is applied

to the multispectral images captured by UAV from healthy pistachio canopies, and the resulting NDVI values are validated against ground-truth data and compared to results obtained via the conventional Agisoft Metashape compensation method. Findings demonstrate that the proposed radiometric compensation approach significantly reduces the influence of atmospheric variability, thereby enhancing the precision and consistency of NDVI assessments.

The paper is organized as follows: Section 2 reviews related work, presenting recent studies and techniques for radiometric compensation. Section 3 introduces the proposed radiometric compensation method. Section 4 describes the experimental setup, including the study area and data collection process, focusing on pistachio crops near their harvesting time. Section 5 presents the segmentation and data analysis of the NDVI measurements, detailing the methodology used for evaluating pistachio leaf area and processing NDVI measurement by DJI Mavic 3. Section 6 validates the development of the radiometric compensation method by comparing the reflectance values of in-field reference targets captured by the UAV. The proposed method is then applied to UAV imagery to compute NDVI values, which are compared with those obtained using the conventional radiometric compensation approach in Agisoft Metashape. Additionally, the results are compared against ground truth data collected in the field. Finally, Section 7 summarizes the findings and offers recommendations.

Looking ahead, future research should aim to incorporate additional sources of uncertainty, such as UAV flight parameters (e.g., altitude and image overlap), environmental variables (e.g., temperature and humidity), and sensor orientation. Furthermore, it is recommended to evaluate the compensation method on both healthy and stressed vegetation, across multiple crop species, to assess its broader applicability. Extending validation across a wider range of atmospheric conditions will also be essential for improving the robustness and generalizability of the approach. Finally, applying the workflow to additional VIs could further expand its relevance in PA.

2. **Develop a Workflow for Detecting Yellow Rust Disease for Winter Wheat Using RGB Images Captured by UAVs:** This chapter focuses on creating a workflow for detecting yellow rust disease for winter wheat through the analysis of RGB images captured by UAVs. This includes employing image processing tools to extract critical features, utilizing one-way ANalysis Of Variance (ANOVA) to prioritize these features, and applying ML algorithms for disease classification. Additionally, the aim is to perform a sensitivity analysis of the ML model to assess

its robustness against uncertainties such as blurring, lighting conditions, and noise, thereby improving the precision of disease detection in vegetation.

The findings demonstrate that the LDA algorithm achieved the highest classification accuracy (85.0 %) among the tested ML models for six yellow rust classes, making it the preferred approach. While its accuracy is lower than that of UAV-based hyperspectral imaging for binary classification (up to 96 % [60]), the use of an RGB camera offers a more cost-effective solution. The sensitivity analysis of the LDA model shows it is resistant to speckle noise but sensitive to contrast noise. Future work will focus on applying a radiometric compensation method to address lighting variations. Additionally, segmentation can be automated using ML or DL techniques to enhance efficiency and reduce manual effort.

3. **Design and Implement an IoT-Based System for Monitoring Health Tree:** This chapter presents an IoT-based system for monitoring the health state of trees, incorporating a range of sensors and electronic components to enable real-time data acquisition and analysis. The proposed system establishes an efficient communication infrastructure between sensor-integrated nodes and a central gateway using LoRa technology. In addition, a comprehensive examination of the selected sensors is provided, including the sensors' operational principles, functionalities, and integration within the overall IoT framework. Furthermore, the sensors' performance and energy consumption are experimentally evaluated under controlled conditions at the LESIM laboratory.

   Future activities could focus on improving field deployment by enhancing energy efficiency through smart power management and integrating renewable energy. The use of UAVs, satellite imagery, and ML algorithms will enable large-scale tree health monitoring and early detection of stress or disease.

Chapter 2

Use of UAV for PA: Evaluating Uncertainty of NDVI Measurement

The UAV sensors, such as RGB, multispectral, hyperspectral, and thermal cameras, are commonly utilized for measuring vegetation and soil quantities in the case of vegetation health and soil texture monitoring, like irrigation, pesticide, fertilizer management, and yield estimation. These sensors, as measurement instruments, are sensitive to the objects' reflected, emitted, or backscattered electromagnetic energy in specific frequencies and spectral bands [61]. In the literature, several VIs based on the reflected electromagnetic energy were proposed [62]. These indices, such as NDVI, NDMI, and CWSI, aim to provide measurement information related to the health state of the vegetation. These indices are extracted from computer vision and image processing algorithms that manipulate color and hyperspectral data, combining information from RGB, NIR, Far Infrared, and other cameras to enhance relevant features while mitigating environmental disturbances [63, 64]. The utilization of VIs allows researchers to effectively detect, quantify, and identify anomalies in crops [65], vegetation phenology, and plant attributes associated with nitrogen levels [66], chlorophyll content [67], and plant phenotyping [65]. This capability facilitates the monitoring of crop health parameters, soil nutrient content, water availability, temperature distribution, indirect photosynthetic activity, and responding to various stressors [18, 55, 68, 69].

The NDVI is a widely recognized and extensively employed vegetation metric derived from the NIR to R reflectance [70, 71]. This index has long held a prominent position as the standard methodology in RS for the comprehensive assessment of plant health, LAI, biomass quantification, plant productivity, and fractional vegetation cover in the agricultural industry [69, 72, 73].

The quality of UAV imagery data is subject to various influencing factors, including

sensor characteristics, camera noise, topographic variations, lighting geometry, and meteorological conditions [74, 75]. Consequently, the pixel values in the captured images at different wavelengths do not accurately reflect the surface reflectance, due to their susceptibility to these influence factors [74, 75]. To facilitate quantitative analysis in RS applications, radiometric compensation of multispectral images is essential [76, 75, 77]. This process involves converting pixel values into units of scene reflectance to account for atmospheric and solar conditions, ensuring accuracy in quantitative RS. Radiometric compensation for images acquired by UAV platforms is inherently challenging due to variations in imaging conditions for each capture. Therefore, an established and systematic procedure is imperative to conduct comprehensive radiometric compensation and generate multispectral images with reflectance [78, 79, 80].

From a methodological perspective, there remains ambiguity regarding the efficacy of measurement indices, such as NDVI, in accurately representing the actual value of the measured quantity in PA. Evaluating the uncertainties tied to these measurement indices remains a persistent challenge. A range of factors contribute to these uncertainties, including atmospheric and lighting conditions, flight parameters such as altitude and image overlap, environmental variables like temperature and humidity, sensor tilt, limitations of the camera sensor (such as image resolution), object emissivity, and additional influencing elements. All these factors can substantially affect the accuracy of the measurement results. A comprehensive understanding and effective mitigation of these sources of uncertainty are imperative for enhancing the accuracy and reliability of measurements in the context of PA [2, 4]. Currently, there are no models available in the literature that can assess the uncertainty of NDVI measurements. This absence stems from the complexity of controlling various factors, such as atmospheric conditions and camera settings, in experiments.

The structure of this section is as follows: Subsection 2.1 reviews relevant literature, providing an overview of prior research on UAV and NDVI measurement, including the sources of uncertainty and methods used for evaluation in the field. Subsection 2.2 discusses UAV-based measurement systems for PA, emphasizing the critical role of UAVs in obtaining accurate data in agricultural monitoring. Subsection 2.3 examines compensation methods for environmental effects, focusing on strategies used to account for factors such as lighting, atmospheric conditions, and other environmental variables that can affect the multispectral imaging. Subsection 2.4 describes the figures of merit used in PA, outlining key metrics for assessing the quality, precision, and reliability of NDVI measurements in agricultural applications. Subsection 2.5 addresses measurement uncertainty assessment, providing foundational concepts and frameworks that guide the methodologies presented in subsequent subsections.

Subsection 2.6 presents the first methodology, which involves a preliminary evaluation

of NDVI uncertainty using law of uncertainty propagation (Type A and B) evaluation according to the GUM. A detailed analysis of the measurement uncertainty associated with NDVI is presented. Initially, a model that considers the wavelength variability of the multispectral camera as an uncertainty source is proposed [2]. Then, this model is refined in Subsection 2.7 to incorporate the bandwidth limitations of the camera sensor and variability in OD within its nominal wavelengths, specifically in the R and NIR bands. Such variability introduces uncertainty into NDVI measurements. The refined uncertainty model is applied to datasets of dry and fresh Douglas fir leaves.

Subsequently, in Subsection 2.8, a workflow is presented to assess NDVI uncertainty by focusing on the impact of atmospheric conditions on solar irradiation and vegetation reflection as captured by a multispectral UAV camera. This analysis explores the effects of atmospheric conditions in three scenarios: dry-clear, humid-hazy, and a combination of both. Additionally, it considers variations in solar irradiance and the SNR of the camera. However, the NDVI measurement process is a complex procedure that involves several non-linear operations. MCS are used for assessing a sensitivity analysis to evaluate the influence of these uncertainty sources individually and in combination. The results highlight that the primary contributors to NDVI uncertainty are atmospheric conditions, camera wavelength tolerance, and the variability of NDVI values under different leaf conditions (dry and fresh).

Moreover, in Subsection 2.9, the workflow is concluded by incorporating a radiometric compensation step aimed at mitigating the effects of atmospheric conditions on NDVI measurements. The results demonstrate that the radiometric compensation performs effectively. During the evaluation of the radiometric compensation method, the effect of various sources of uncertainty by using MCS is considered. Following this, in Subsection 2.9.3.1, the proposed radiometric compensation method is validated by in-field reference panel reflection then it is applied to uncalibrated images captured in a pistachio field and compared with ground truth data and compared to results obtained via the conventional Agisoft Metashape compensation method. This process serves to validate the model and demonstrate that the proposed radiometric compensation approach significantly reduces the influence of atmospheric variability, thereby enhancing the precision and consistency of NDVI assessments.

Finally, the last Subsection 2.12 summarizes the key topics addressed in the study, while the future work part outlines potential directions for further research in this field.

The content of this chapter has been disseminated through the following venues: (i) the IEEE Workshop on Metrology for Agriculture and Forestry (MetroAgriFor) in 2022 [2] and 2023 [3]; (ii) the journal Sensors (MDPI, 2024) [4]; (iii) the IEEE I2MTC 2025; and (iv) the journal Measurement (Elsevier, 2025).

2.1 Related Works

The paper [81] asserts NDVI will undeniably persist as a predominant vegetation metric. However, the efficacy of NDVI depends on the quality of multispectral data and the accurate interpretation of NDVI values, it is noteworthy that no two RS images are identical. The primary challenges associated with NDVI encompass its susceptibility to atmospheric effects, ease of saturation, and variations in sensor quality. This paper critically examines and explains these significant challenges to guide NDVI users, particularly end-users lacking in-depth RS expertise, toward a cautious utilization of NDVI data. The study conducted by [82] claims to enhance hyperspectral imaging from unmanned aerial systems under diverse weather conditions. The research focuses on addressing two key challenges: compensating for data captured by the miniaturized hyperspectral sensor to ensure accurate radiometric and spectral measurements, and mitigating the impact of tilting the sensor angle relative to the solar rays on downwelling irradiance data. A method is developed to effectively alleviate tilting effects and accurately correct the downwelling irradiance data. Furthermore, the study addresses striped illumination artifacts in mapping the surface reflectance factor to the hyperspectral radiance images. This is achieved through comprehensive spectral and radiometric compensation, along with irradiance correction. The research conducted by [83] is centered on the development and testing of a comprehensive image pre-processing workflow. This workflow is designed for the radiometric and geometric correction of UAV-hyperspectral data obtained from a spectrally complex environment. The detailed procedures encompass sensor compensation, radiometric correction, automatic band alignment, mosaicking, and georeferencing. The devised workflow facilitates the efficient acquisition of hypercubes from a challenging environment with limited ground control points. Unlike conventional methods that rely on photogrammetric reconstruction for mosaicking, the proposed workflow progressively generates a mosaicked output by combining different orthogonally projected hypercubes. Techniques from diverse disciplines to present a simplified workflow effective in challenging spectrally complex environments are integrated, resulting in a radiometrically and geometrically accurate mosaicked output at very high resolution. The paper [84] presents an integrated radiometric compensation methodology tailored for high-resolution UAV-based multispectral RS utilizing miniaturized large-array commodity Complementary Metal-Oxide-Semiconductor (CMOS) cameras. The methodology encompasses both indoor and outdoor radiometric compensation techniques. The outdoor compensation procedure addresses the correction of atmospheric path radiance and reflectance. This correction is achieved through the application of an empirical line method derived from the dark target method. The proposed integrated radiometric compensation method provides a valuable benchmark for the precise radiometric compensation of large-array

CMOS multispectral cameras. In the investigation conducted by the paper [85], a thorough examination of hyperspectral atmospheric correction techniques is undertaken, with a particular focus on mitigating challenges associated with spectral smoothing. The study identifies and reviews three primary approaches commonly employed in atmospheric correction: scene-based empirical approaches, radiative transfer modeling approaches, and hybrid approaches. In scene-based empirical approaches, methods were developed to eliminate atmospheric effects in hyperspectral imaging for deriving relative surface reflectance spectra. The atmosphere removal algorithm in radiative transfer modeling uses theoretical techniques to simulate atmospheric influences, extracting land surface reflectance. It models the absorptive and scattering impacts of atmospheric gases and aerosols. Hybrid approaches combine radiative modeling and empirical methods to improve surface reflectance derivation from hyperspectral imaging data. The study [85] underscores the existing need for enhancements in current atmospheric correction algorithms. Specifically, it advocates for integrating a module to model the absorption effects of atmospheric nitrogen dioxide in the visible spectrum. This proposed augmentation elevates the accuracy and efficacy of atmospheric correction methods. In [86], the authors compare two deep learning methods, DeepLabV3+ and a customized Convolutional Neural Network (CNN), in the application of NDVI for vegetation detection. The evaluation focuses on their detection performance when training and testing datasets originate from different geographical sites with different image resolutions. Additionally, the study proposes an object-based vegetation detection approach that incorporates NDVI, computer vision, and ML techniques. Upon comparing the deep learning and NDVI-ML approaches, the authors observe that the NDVI-ML method yields significantly better results than the two deep learning methods. Although this may seem surprising given the general expectation that deep learning methods outperform conventional techniques, a closer examination of the results and images indicates that these findings are reasonable from two perspectives. Firstly, the optimal performance of deep learning methods necessitates a substantial amount of training data. Without sufficient data, the performance will not be good. Secondly, for satisfactory performance, it is advantageous for the training and testing images to closely resemble each other to be suitable for use in deep learning methods. In the paper [73], thermal, multispectral, and RGB images obtained from UAVs are used to calculate various parameters related to plant growth and water consumption. Specifically, the study claims to assess actual canopy Transpiration (Tr), soil Evaporation (E), and EvapoTranspiration (ET) of potato plants grown under different irrigation treatments on sandy soil. The traditional method of estimating Tr and E using the Two-Source Energy Balance model - Priestley-Taylor equation (TSEB-PT) with satellite-derived Land Surface Temperature (LST) has limitations in accuracy, especially at high spatial–temporal resolutions. The paper in [73] proposes an energy flux

modeling framework based on TSEB-PT, leveraging high-resolution thermal and multispectral data collected by UAVs. The research, conducted during drought conditions in 2018 and 2019, recorded diurnal variations of LST in agricultural fields. The results showed that a 1 m spatial resolution produced the highest correlation for estimating Tr compared to other resolutions. This paper's model shows how well it can accurately predict irrigation needs and differentiate between drought and heat stress impacts on crop productivity. In the paper [87], the influence of operation parameters such as Solar Zenith Angle (SZA), Time Of Day (TOD), Flight Altitude (FA), and the growth level of paddy rice on UAV-acquired NDVI values was comprehensively evaluated. Results indicated significant impacts of these parameters on UAV-NDVIs, with SZA/TOD exerting the largest influence, followed by growth level and FA. Notably, smaller SZAs yielded higher SNRs, reflecting more realistic growth status values. These findings are crucial for optimizing flight campaigns aimed at collecting NDVI values over paddy rice fields, providing valuable insights for PA applications. The study [88] investigates the impact of time of day and sky conditions on various VIs derived from both active and passive optical sensors, as well as from imagery captured by a UAV. Conducted in a wheat crop in south-west Germany with varying nitrogen application treatments, measurements were taken at different solar times and under sunny versus overcast conditions. Results reveal significant differences in most VIs between paired time measurements, with the smallest variations observed between 14:00 and 16:00 h. The most stable indices over time and sky conditions were the NIR/R edge ratio, water index, and REIP index, while simple ratios like NIR/R and NIR/Green were more variable. Passive hyperspectral sensors and the active Crop Circle ACS num 470 sensor demonstrated the most stable measurements throughout the day and under different sky conditions. Notably, the handheld passive spectrometer showed slightly higher dependency on time and sky conditions compared to the vehicle-based sensor. The study suggests that with careful selection of optimized indices, both ground-based and UAV-based sensors can provide reliable measurements across varying environmental conditions, offering valuable insights for on-farm applications in PA. The study in [89] evaluates four radiometric compensation methods for UAV imagery to enhance accuracy in agricultural monitoring, particularly for tracking crop growth and estimating plant traits such as Above Ground Biomass (AGB) and LAI. The methods examined include: (A) camera-only compensation, which adjusts images based on camera properties and known reflectance targets; (B) camera with sun irradiance adjustment, which normalizes images using data from a sun irradiance sensor to account for lighting variations during the flight; (C) camera with sun irradiance and sun angle adjustment, which further refines compensation by considering the direction of sunlight and the sensor-camera angle; and (D) an irradiance sensor-based method that uses an external sensor to measure sunlight and adjust images accordingly, eliminating the need

for a reference target. UAV flights were conducted over a winter wheat field at different altitudes (30 m, 60 m, and 90 m) and times of day under both clear and cloudy skies. The study analyzed how lighting conditions, flight altitude, and time of day under both clear and cloudy skies influenced reflectance and the VIs. Results indicated that method D provided the most consistent reflectance, particularly in the morning and under stable illumination. In contrast, methods B and C exhibited errors due to incorrect sun sensor angles, which impacted reflectance calculations but had minimal effect on VIs. Under cloudy skies, method D was effective unless direct sunlight was obstructed. Flight altitude significantly influenced reflectance and VIs, affecting LAI estimates but having little impact on AGB calculations. Additionally, the study highlighted that sunlight can vary considerably during longer UAV flights, especially around sunrise and sunset, underscoring the need for careful radiometric compensation to ensure accurate data collection. The paper [55] focuses on radiometric compensation of multispectral UAV imagery under varying imaging conditions using the Linear Regression Method (LRM). LRM estimates surface reflectance by modeling the linear relationship between DN values and reflectance using reference targets. It involves measuring DN values, deriving compensation equations, and applying them to all bands for compensation. Radiometric compensation was performed using a Mini MCA 6 camera mounted on a UAV, with images captured at different flight altitudes, flight times, and weather conditions. The methodology involved testing and selecting optimal reference targets. The results confirmed that using dark, moderate, and white reference targets improved compensation accuracy. Atmospheric effects increased with altitude, but reflectance variations were minimal at altitudes below 100 m. This study also tested mosaic images to assess the impact of image stitching on radiometric compensation accuracy. Results showed that mosaicking introduced minor errors but did not significantly affect reflectance values, supporting the use of mosaic images for radiometric compensation efficiency. The LRM performed well under different weather conditions, but cloud cover influenced reflectance measurements, with lower values recorded on cloudy days. The findings emphasize the importance of proper radiometric compensation to ensure accurate NDVI and VIs in UAV-based remote sensing applications [55]. The study [90] evaluated five radiometric compensation methods for multispectral Unmanned Aerial System (UAS) imagery using a Parrot Sequoia camera. Data were collected with a fixed-wing UAS, processed in Pix4D, and accuracy was assessed using RMSE and validation targets. The methods are as follows: (A) One-Point compensation involved capturing images of a target with known reflectance at different viewing angles during the flight, allowing Pix4D to calibrate the data based on reflectance differences in each camera band; (B) One-Point compensation Plus Sunshine Sensor expanded on method A by incorporating sunshine sensor data collected during the flight, the default approach in Pix4D for calibrating

multispectral images from the Parrot Sequoia R camera; (C) Pre-compensation using the Simplified Empirical Line followed the approach of Wang and Myint (2015), where a grey reference panel was placed in the study area, and relationships between its reflectance and raw DN values were established to calibrate raw images before processing in Pix4D; (D) One-Point compensation Plus Sunshine Sensor Plus Post-compensation initially applied Method B, followed by an additional compensation using the empirical compensation targets from Method C, mapping and correcting reflectance differences across the study area via Inverse Distance Weighted (IDM) interpolation, which estimates values based on nearby points, giving more weight to closer ones for smoother compensation; (E) Post-compensation Using the Simplified Empirical Line performed radiometric compensation after image processing, using reflectance-DN relationships from Method C to correct processed rasters by subtracting mapped reflectance differences. These methods were tested to assess their effectiveness in improving radiometric accuracy in UAV imagery. Radiometric errors were analyzed to determine their impact on VIs like NDVI and Normalized Difference Red Edge Index (NDRE). Results showed no single method was consistently best. The combined manufacturer and empirical approach (Method D) had the highest accuracy, followed by the post-processing empirical method (Method E) [90]. The paper [91] investigates radiometric compensation for occluded crops using high-resolution UAV imagery, addressing the issue of shadow-induced distortions that impact crop characterization. A brightness tuning and thresholding approach was applied to restore radiometric properties in occluded areas, allowing for improved classification of crops like maize and soil. Various classification algorithms, including K Nearest Neighbors (KNN), Maximum Likelihood, Multi Layer Perceptron (MLP), and Object Oriented Segmentation (OOS), were used to assess the impact of radiometric compensation on land feature classification. KNN, which classifies pixels based on their similarity to neighboring labeled pixels, predicted a 40.56 % increase in maize coverage and a 12.37 % increase in soil area after radiometric compensation. The Maximum Likelihood classifier, which assigns pixels based on probability distributions, estimated an 18.03 % increase in maize coverage and a 1.46 % increase in soil area. MLP, a neural network-based approach that captures complex patterns in data, showed a 22.42 % increase in maize and a 10.05 % increase in soil coverage. Unlike pixel-based methods, OOS groups pixels into objects based on spectral, spatial, and textural properties. The OOS classifier predicted the highest increases, with maize coverage expanding by 30.64 % and soil area by 14.29 %. These results indicate that radiometric compensation enhances the classification of occluded land features, improving the accuracy of land cover assessments [91]. The paper [92] tested five compensation methods for the MicaSense RedEdge MX Dual Camera System: Agisoft Metashape Single Panel Compensation (AMSP), Pix4D Fields Single Panel Compensation (P4DSP), Agisoft

Metashape Multiple Panel Compensation (AMMP), MicaSense Single Panel Compensation (MSSP), MicaSense Multiple Panel compensation (MSMP), and Empirical Line Method Multiple Panel compensation (ELMMP). AMSP and P4DSP use raw TIF images with a single reference target for compensation and follow the default workflows in Agisoft Metashape and Pix4D Fields, respectively. The AMMP method applies an empirical line compensation to the orthophoto generated by AMSP. MSSP, MSMP, and ELMMP involve a pre-processing step in Python to correct raw images before using Agisoft Metashape. The methods were evaluated using RMSE, bias, and Relative Root Mean Square Error (rRMSE), and the results indicate that more complex methods like ELMMP improved calibration accuracy, especially in clear-sky conditions. However, in overcast conditions, the accuracy of simpler methods like Pix4D Fields and Agisoft Metashape was still quite reasonable, making them viable for faster and less complex workflows. For highly accurate calibration, especially in variable weather conditions, the ELMMP method provided the best performance, but the choice of method depends on the specific requirements of the project (accuracy vs. speed) [92]. The study [93] aimed to improve the quality of UAV multispectral images captured with the DJI Mavic 3 Multispectral (M3M) camera, with the help of the white paper [1]. UAV imaging is cheaper and provides high-resolution images, but when stitching multiple images together to cover large areas, issues like visible seam lines and varying light conditions arise. To solve these problems, the study applied different compensation methods to make the images more accurate, including irradiance compensation, which adjusts pixel values based on variations in lighting due to sunlight angles and terrain, ensuring consistent illumination across the image. Vignette compensation addresses the darker edges caused by lens design by applying a model that normalizes brightness, particularly at the image corners, for a more uniform appearance. Lastly, Bidirectional Reflectance Distribution Function (BRDF) compensation compensates for surface reflectance variations by modeling how light interacts with surfaces at different angles, ensuring consistent reflectance across the mosaic. Together, these techniques enhance the final image's accuracy and smoothness, making it more reliable for further analysis and reducing visual distortions. And results indicated that applying both BRDF and vignette filters produced accurate outcomes, even with lower image overlap, and the method improved the accuracy of reflectance-based indices like NDVI [93]. In the literature, several indices are proposed; however, their uncertainties are not often assessed. The important contributions of the current study, particularly from a metrological perspective, involve evaluating the impact of uncertainty sources on NDVI measurements. In addition, various studies have proposed different methods for radiometric compensation by assessing model performance, often through metrics such as RMSE, examining the accuracy of ML and DL models, or checking the effect of radiometric compensation on the resulting VIs. From a

metrological point of view, it remains an open challenge to find an efficient radiometric compensation method, assess its impact on a VI, and test it against ground truth VI measurements. However, the novelty of the present study lies in the development of a radiometric compensation method, which is guided by the white paper [1] using a hybrid approach. This approach includes: (i) the emulation of reference panels composed of Permaflect sheets that cover a range of reflectance values (5 %, 10 %, 18 %, 50 %, 80 %, and 94 %) - these panels facilitate effective radiometric compensation under various lighting and surface conditions, and (ii) adding the reflection of a real reference panel which is used in real scenarios. Moreover, in this study, the impact of some uncertainty sources is considered during the evaluation of the radiometric compensation method, which is neglected in the literature. The proposed method is then applied to multispectral UAV images, with the evaluated NDVI values validated against ground-truth NDVI measurements and compared to conventional approaches used in Agisoft Metashape—aspects often overlooked in previous research.

2.2 UAV-based Measurement Systems for PA

UAVs are classified into various types based on their design, wings, size, weight, degree of autonomy, and power source [94]. During their flight missions, they must (i) control their altitude, (ii) avoid obstacles, (iii) land automatically based on battery state, (iv) stabilize during image acquisition, (v) estimate their position, and (vi) avoid objects along their mission path. To perform these tasks, UAVs require a basic architecture and two types of sensors: navigation sensors and mission sensors [95]. The basic UAV architecture generally includes (i) a frame and propellers, (ii) brushless motors, (iii) Electronic Speed Control (ESC) modules, (iv) a control board, (v) an Inertial Navigation System (INS), and (vi) transmitter and receiver modules [95]. Navigation sensors are crucial for UAV flight control [96], comprising (i) an IMU, (ii) Global Positioning System (GPS) or Differential GPS sensor, (iii) Light Detection and Ranging (LiDAR), (iv) ultrasonic sensors, (v) barometers, and (vi) accelerometers, gyroscopes, and magnetometers. Mission sensors and actuators are typically located in the payload. In PA, UAV payloads include RGB, multispectral, hyperspectral, and thermal cameras, as well as LiDAR systems. Standard aerial images captured by RGB cameras cover the visible part of the ElectroMagnetic (EM) spectrum. Utilizing other parts of the EM spectrum, such as the infrared band, provides more detailed information about an object's surface and interior. Cameras that capture spectral data from specific parts of the EM spectrum are called multispectral or hyperspectral cameras. Airborne multispectral imaging systems typically use 3 to 10 single-wavelength bands, each with a filter lens for a specific band, allowing data analysis from composite images or individual bands [97].

Multispectral cameras are used to quantify the state of monitored vegetation in terms of (i) chlorophyll content, (ii) leaf water content, and (iii) ground cover, such as LAI, and so on. However, the reflectance from different vegetation species is highly correlated due to their similar biochemical and biophysical properties, which are influenced by environmental factors. Spectral variations can also occur within a species due to differences in age, micro-climate, soil and water background, precipitation, topography, and stress factors. Hyperspectral sensors collect data in numerous small and continuous wavelength bands, typically hundreds of narrow bands between 5 nm and 10 nm [98], allowing for the estimation of vegetation biophysical and biochemical parameters (e.g., pigment concentration, nitrogen) and the detection of subtle changes, such as stress signs, with high sensitivity and accuracy. Hyperspectral imagery has proven effective in accurately discriminating vegetation species [99]. However, compared to multispectral imagery, hyperspectral imagery is more expensive and time-consuming to acquire, even for small areas [97]. Thermal cameras measure surface temperature, which plays a crucial role in plant physiological processes. In recent years, thermal sensors have gained popularity due to technological advancements and cost reductions. They enable rapid monitoring of plant growth and stress. There are two types of thermal cameras: cooled and uncooled. Thermal cameras used for satellite applications operate at very high temperatures (196°C) and require robust cooling systems. The more efficient the cooling system, the more accurate the measurements [61]. However, cooled sensors are large, heavy, expensive, and consume more energy, making them unsuitable for UAVs. Uncooled thermal cameras, with less sensitive detectors (± 0.1°C), are ideal for UAVs [61]. Thermal images from UAVs provide valuable information for agronomic applications with greater temporal and geographical resolution than satellite images [100].

2.2.1 Basic Principles of Thermography

When the light impinges on a black body, the light is completely absorbed without any reflection or transmission. The absorbed energy is transferred to the kinetic energy of the charged particles of the black body, and naturally, the body's internal energy increases. There is a direct relationship between the surface temperature of a black body and the intensity of the light it emits. This relationship is described by the Stefan-Boltzmann Law. The black body is an ideal model; however, in real applications, objects do not completely absorb the light but reflect or transmit some part of it. The term that shows how close a real object can be to an ideal black body is called emissivity e. The object having emissivity equal to one means it completely absorbs the light and is considered an ideal black body, while, when the emissivity is zero, it means the object does not absorb any light and the light is completely reflected, so-called "White Body". Measuring the real object emissivity is a kind of uncertainty source. To measure the power emitted by

an object in the real world, the object's emissivity is multiplied by the Stefan-Boltzmann Law formula [101].

$$P = e \cdot \sigma \cdot A \cdot T^4 \tag{2.1}$$

Where A is the object's surface area, T is its temperature, and σ is the Stefan-Boltzmann's constant ($5.67 \cdot 10^{-8} W \cdot m^{-2} \cdot K^{-4}$). The power emitted by an object is captured by the thermal camera and shown in thermal images.

2.2.2 Basic Fundamentals of Spectral Imaging

Light propagates energy radially from a source, and a light beam can be described as a stream of particles known as photons. The energy of an individual photon, which is a quantum of energy, is quantified by Planck's equation, indicating a direct proportionality to its frequency [102]. When light encounters an object, three primary interactions can occur: reflection and scattering, absorption, or transmission of the photons. Additionally, the object may emit light. The distinction between reflected and emitted light lies in their origins; emitted light consists of photons generated by an intrinsic light source, while reflected light comprises photons originating from an external source.Moreover, it is essential to clarify two key concepts: radiance and irradiance. Irradiance refers to the total light incident on a point from all possible directions, while radiance denotes the light incoming to a point from a specific direction. Radiance is simply irradiance normalized by the solid angle (in steradians) corresponding to the observation direction of light propagation. In the context of RS, the electromagnetic spectrum serves as a crucial domain, especially for data acquired through UAV platforms utilizing multispectral or hyperspectral imaging techniques. The interaction of solar radiation with atmospheric gases and aerosols modifies the solar irradiation spectrum before it reaches the Earth's surface. This alteration impacts the radiance reflected from the Earth's surface, a phenomenon particularly relevant when analyzing vegetation through UAVs multispectral cameras. Fig. 2.1 visually illustrates this scenario, highlighting the complex interactions between solar irradiation, atmospheric components, and the resultant reflected radiance captured by a UAV multispectral camera. Understanding and mitigating atmospheric effects on acquired data is essential for precise and reliable vegetation analysis in RS applications [103]. Moreover, the effects of atmospheric conditions are amplified when the multispectral sensor is deployed on a satellite, as light must pass through atmospheric layers twice. In contrast, for UAVs, which typically fly at low altitudes around 100 meters, the effect of the atmosphere below the UAV is negligible compared to the total atmospheric effect. Therefore, only the single path from the sun to the ground is considered. Spectral radiance, denoted in $\mathrm{W\,sr^{-1}\,m^{-2}\,\mu m^{-1}}$, measures the energy flux detected by a sensor in a specific wavelength. For practical storage and analysis, these radiance

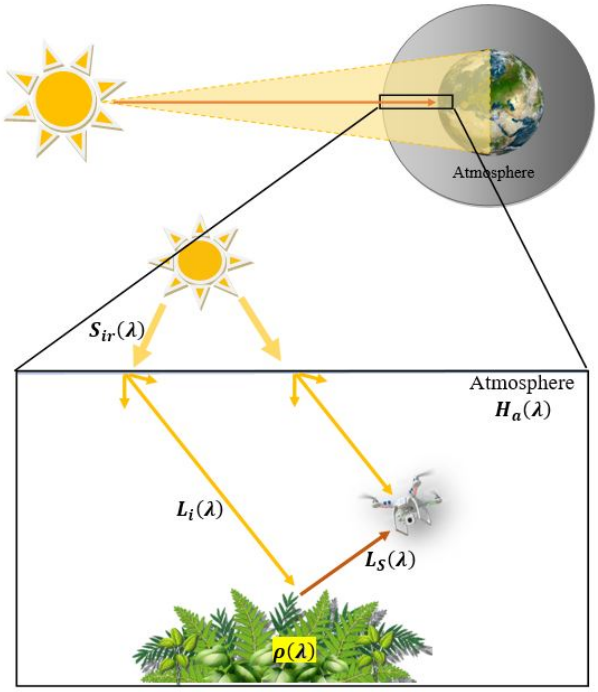

FIGURE 2.1: The diagram illustrates the interactions between solar radiation ($S_{ir}(\lambda)$), the Earth's atmosphere, and the Earth's surface. Initially, solar radiation penetrates the atmosphere and undergoes scattering and absorption by atmospheric particles and gases, with $H_a(\lambda)$ representing the atmospheric effect response. The multispectral camera mounted on the UAV captures the reflected radiance ($L_s(\lambda)$), which contains valuable information about surface properties, such as vegetation features [4].

values are transformed into Digital Numbers (DNs), or pixel values. The bit-depth for DN representation varies by sensor type, including 6-bit or 7-bit for Multispectral Scanner (MSS) sensors, 8-bit for DJI P4-multispectral camera, Thematic Mapper (TM), and Enhanced Thematic Mapper Plus (ETM+) sensors, and 12-bit for Landsat 8 sensors [81]. A spectral sensor measures the spectral radiance $L_s(\lambda)$ which can be expressed by the following equation [104]:

$$L_s(\lambda) = \rho(\lambda) \cdot L_i(\lambda) \tag{2.2}$$

Here, $L_s(\lambda)$ represents the product of the scene radiance $L_i(\lambda)$ and the material reflectance spectrum $\rho(\lambda)$, both as functions of wavelength λ. The reflectance spectrum $\rho(\lambda)$ can be used to identify materials in a scene, as it is independent of the illumination conditions. By comparing the reflectance spectra from the scene to a library of

known spectra, material identification becomes possible [104]. With more detail $L_i(\lambda)$ is evaluated from the solar radiance, $S_{ir}(\lambda)$, multiplied by the atmospheric effect response, $H_a(\lambda)$:

$$L_i(\lambda) = S_{ir}(\lambda) \cdot H_a(\lambda) \tag{2.3}$$

From a metrological perspective, estimating $\rho(\lambda)$ necessitates measuring $L_i(\lambda)$. Typically, a radiometer is mounted on a UAV platform to record solar irradiance for this purpose. In the context of multispectral cameras, the incident light sensor captures the irradiance for each band. Consequently, by measuring $L_i(\lambda)$ and $L_s(\lambda)$ using Equation (2.2), $\rho(\lambda)$ can be determined.

2.2.3 Sampling Operations for Spectral Imaging

Spectral image data collection involves four primary sampling operations: spatial, spectral, radiometric, and temporal. The combined data from these operations is represented in a three-dimensional hyperspectral data cube, as shown in Fig. 2.2. In this cube, the x and y axes correspond to spatial information, while the z axis represents spectral data [104]. Spectral information is obtained by decomposing the radiance received in each spatial pixel into several wavebands. These wavebands can vary in resolution and may be overlapping, contiguous, or separate, depending on the sensor design. The analog radiance measured in each spectral channel is then converted to digital data at a specified radiometric resolution, referred to as the radiometric sample. Temporal sampling involves collecting multiple spectral images of the same scene at different times [104].

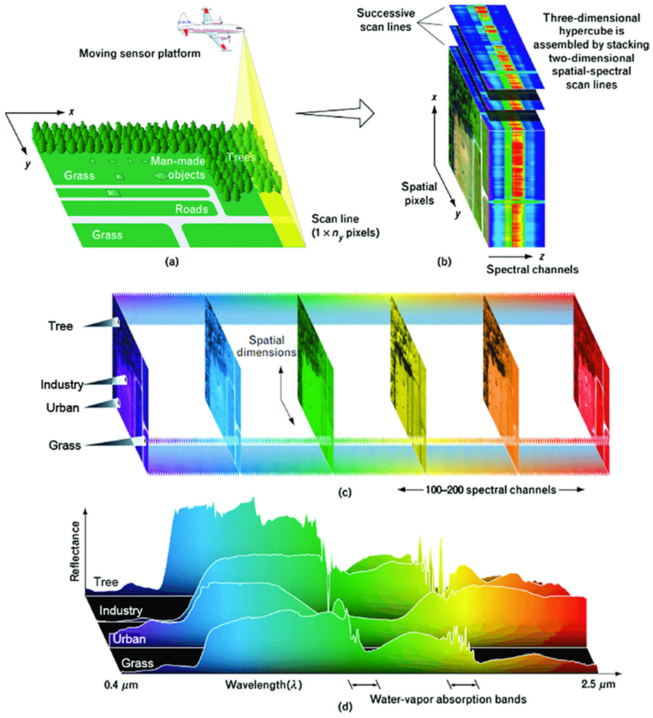

FIGURE 2.2: Structure of a hyperspectral data cube. The cube consists of two spatial dimensions (x, y) representing the scene, and one spectral dimension λ representing the range of wavelengths captured. Each pixel in the spatial plane contains a spectrum of intensity values across numerous narrow, contiguous wavelength bands, providing detailed spectral information for material identification and analysis.

2.3 Compensation Methods for Environmental Effects

Several sources of uncertainty affect spectral measurements, including atmospheric absorption and scattering, reflection from nearby objects, other environmental effects, and object emissivity, as illustrated in Fig. 2.3. The atmosphere's wavelength-dependent absorption and scattering of light significantly impact sensor imaging by: (i) modulating solar illumination before it reaches the ground, (ii) scattering some solar radiation into the sensor's field of view without reaching the ground, and (iii) acting as a secondary source of diffuse colored illumination, particularly in the blue region of the visible spectrum, which illuminates objects in shadow under direct sunlight. Additionally, clouds and ground cover can cast shadows on the target, altering surface illumination. Moreover, nearby objects may also reflect or scatter sunlight onto the target, adding various

FIGURE 2.3: Uncertainty sources affecting UAV spectral imaging.

colored illuminations to the primary direct solar illumination [104]. To estimate and compensate for atmospheric effects in multispectral or hyperspectral imaging, four methods are proposed in the literature: (i) the Path Radiance Method (PRM), (ii) the Empirical Line Method (ELM), (iii) methods based on UAV or ground radiometric sensor measurements, and (iv) methods utilizing LiDAR for shadow compensation. The PRM involves developing a mathematical model that describes the relationship between ground reflectance and radiance under specific atmospheric conditions, enabling the correction of sensor data for atmospheric disturbances. The ELM, on the other hand, compensates for atmospheric effects by observing reference objects with known reflectance properties placed in the surveyed environment, thereby adjusting the sensor images based on these known standards. For varying light conditions, radiometric sensors mounted on UAVs, on the ground, or both to measure solar irradiance, allowing for corrections that account for changing illumination during the data acquisition process [105]. This approach ensures that the spectral data remains consistent despite fluctuations in lighting. Additionally, for shadow correction, geometric information from 3D terrestrial LiDAR data can be employed to compensate for illumination inconsistencies and neighborhood effects in close-range HSI [106]. By incorporating the 3D structure of the terrain, LiDAR data helps to accurately model and correct for shadows, thereby enhancing the accuracy of the hyperspectral measurements. In PA, addressing uncertainties is crucial for accurate multispectral and hyperspectral data interpretation. Variations in atmospheric conditions, crop and soil reflectance, and sensor angles require site-specific calibration

and careful planning of UAV flight paths. Advanced algorithms help correct these factors, improving the reliability of spectral data for assessing crop health, detecting stress, and optimizing resource use.

2.4 Figures of Merit in PA

Several VIs based on reflected electromagnetic energy, such as NDVI, NDMI, and CWSI, have been proposed to assess vegetation health and soil condition [62]. The NDVI is a widely utilized index for assessing vegetation health, based on the distinct optical properties of chlorophyll in green vegetation. Chlorophyll absorbs radiation primarily in the R and blue wavelengths while reflecting significantly in the green and NIR regions. Monitoring NIR reflectance is a reliable method for evaluating the health and vigor of vegetation, and NDVI is calculated using the following equation [99, 107].

$$NDVI = \frac{NIR - R}{NIR + R} \tag{2.4}$$

Here, NIR and R are the percentages of the object's reflection in the NIR and R spectra bands, denoted as $\rho(NIR)$ and $\rho(R)$, respectively. These values are calculated as the ratios of $L_s(\lambda)$ to $L_i(\lambda)$ based on Equation (2.2). NDVI values range from -1 to 1. Negative values indicate the presence of water, values close to 1 indicate dense green vegetation, and values around zero indicate a lack of green vegetation. Plant water stress is a critical component of abiotic stress. Early detection of heat stress symptoms, before the onset of irreversible damage, enables the implementation of optimal irrigation schedules. This proactive approach not only alleviates water stress but also mitigates the effects of heat stress. The NDMI offers valuable insights into moisture levels within vegetation. Spectral reflectance in the SWIR range is regulated by water availability within the leaf structure, while NIR reflectance is primarily influenced by the internal leaf structure and dry matter, independent of water content. By integrating NIR and SWIR reflectance measurements, the accuracy of vegetation water content retrieval is significantly enhanced. The NDMI is calculated as follows [107]:

$$NDMI = \frac{NIR - SWIR}{NIR + SWIR} \tag{2.5}$$

Like NDVI, NDMI values range from -1 to 1. Negative values indicate bare soil, values near zero suggest high water stress or moderate to low canopy cover, and positive values indicate full canopy cover and no water stress. The CWSI assesses water deficits by

analyzing the temperature of vegetation. [108]:

$$CWSI = \frac{T_{canopy} - T_{wet}}{T_{dry} - T_{wet}} \tag{2.6}$$

where T_{canopy} is the average canopy temperature, and T_{wet} and T_{dry} are the temperatures of reference surfaces that are completely wet and dry, respectively. Evaluating T_{canopy} requires separating pure canopy pixels from the background (including the sky, soil, and artificial objects), as discussed in [98]. CWSI values range from -1 to 1, with -1 to 0 indicating excess water and 1 indicating no water availability. The degree of water stress when CWSI is between 0 and 1 depends on the type of plant or soil. Generally, as crop stress or soil water deficit increases, the CWSI value increases [109]. Two main issues have limited the widespread use of CWSI: changing atmospheric conditions and distinguishing pixel temperatures between background soil and pure canopy temperature. Although UAV platforms are less affected by these issues compared to satellites, as they experience fewer atmospheric condition changes and provide higher spatial resolution.

2.5 Measurement Uncertainty Assessment

GUM provides a framework for assessing this uncertainty, offering two methods (Type A and B) for evaluation [110].

2.5.1 Mathematical Model for Evaluating Standard Uncertainty of NDVI

In this part, the application of the law of propagation of uncertainty based on the GUM to assessing the uncertainty of the NDVI is employed. The uncertainty is derived from an assumed probability density function, based on the degree of belief regarding the occurrence of an event. This method, also known as subjective probability, relies on scientific judgment and considers all available information about the possible variability of the inputs. Consider a measurement model Y that is indirectly computed from N other quantities. Theoretically, the uncertainty of Y is evaluated concerning these N terms. The calculation of uncertainty varies depending on whether the input quantities are independent or dependent. For uncorrelated input quantities, the combined standard uncertainty $u_c(y)$ is computed as follows:

$$u_c^2(y) = \sum_{i=1}^{N} \left(\frac{\partial f}{\partial x_i} \right)^2 \cdot u^2(x_i) \tag{2.7}$$

For correlated input quantities, the combined standard uncertainty $u_{cr}(y)$ is given by:

$$u_{cr}^2(y) = u_c^2(y) + 2\sum_{i=1}^{N-1}\sum_{j=i+1}^{N}\left(\frac{\partial f}{\partial x_i}\right)\cdot\left(\frac{\partial f}{\partial x_j}\right)\cdot u(x_i, x_j) \tag{2.8}$$

The uncertainty model for the NDVI varies based on whether the input reflections in the R and NIR bands are correlated or uncorrelated. This relationship is influenced by factors such as camera technology and bandwidth overlap. For cases where the input quantities are uncorrelated, the uncertainty of NDVI is determined as follows [110]:

$$\begin{aligned} u_c^2(\text{NDVI}) = &\left[\frac{2\cdot R}{(R+NIR)^2}\right]^2 \cdot u^2(NIR) \\ &+ \left[\frac{-2\cdot NIR}{(R+NIR)^2}\right]^2 \cdot u^2(R) \end{aligned} \tag{2.9}$$

For correlated input quantities, the uncertainty of the NDVI is expressed by [110]:

$$u_{cr}^2(\text{NDVI}) = u_c^2(\text{NDVI}) + 2\cdot\left[\frac{2\cdot R}{(R+NIR)^2}\right]\cdot\left[\frac{-2\cdot NIR}{(R+NIR)^2}\right]\cdot u(R, NIR) \tag{2.10}$$

These formulas allow us to quantify the uncertainty in NDVI measurements, thereby improving the reliability and accuracy of vegetation health assessments in PA.

2.6 Preliminary Evaluation of NDVI Uncertainty Using the Law of Propagation of Uncertainty According to the GUM

This section presents a preliminary assessment of the measurement uncertainty related to NDVI by modeling vegetation reflection, the camera sensor's nominal wavelength, while considering wavelength variation as an uncertainty source. This evaluation is conducted based on the uncertainty assessment as outlined in the GUM [2].

2.6.1 Vegetation Reflection

When the light incident on a part of a plant, it can be reflected, scattered, absorbed, or transmitted [2]. Various plant species can be distinguished based on their ability to absorb specific wavelengths of light, and the resulting images of their reflected solar energy are referred to as their spectral signatures. These signatures have been extensively

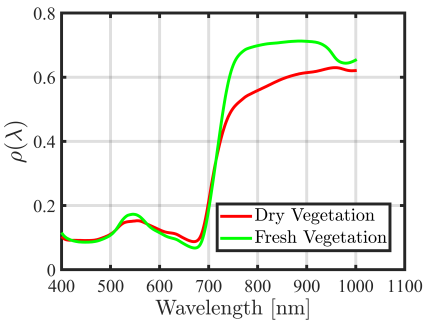

(A) Wavelength 400 - 980 nm.

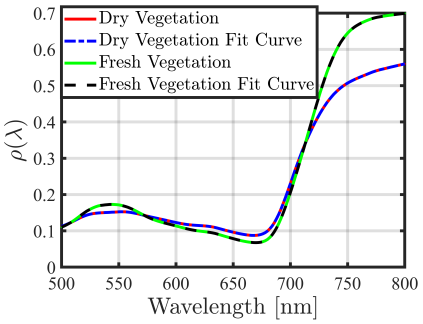

(B) R and its fitted curve

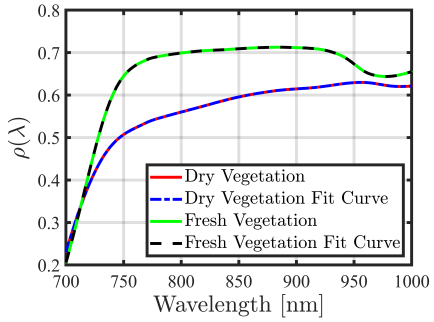

(C) NIR and its fitted curve

FIGURE 2.4: The spectral reflectance of fresh and dry Douglas fir leaf samples, randomly selected from the seedling canopy study site, is depicted within the wavelength range of (a) 400 nm to 980 nm, (b) the R band, and (c) the NIR band [2] © 2022 IEEE.

documented through comprehensive laboratory measurements [2, 111]. To quantify these spectral signatures, the property of spectral reflectance is considered and used. The plant's spectral reflectance, $\rho(\lambda)$, is evaluated from Equation (2.2) as follows [2]:

$$\rho(\lambda) = \frac{L_S(\lambda)}{L_i(\lambda)} \tag{2.11}$$

where $L_s(\lambda)$ is the reflected energy by the plant, and $L_i(\lambda)$ is the incident energy, across different wavelengths [104]. The graphical representation of a plant's spectral reflectance as a function of wavelength is known as the spectral reflectance curve [112, 2]. Fig. 2.4 displays the spectral reflectance curves of fresh and dry leaf samples of Douglas fir, captured in the visible and NIR wavelength bands. These samples were randomly selected from the seedling canopy study site of Douglas fir during the Accelerated Canopy Chemistry Program (ACCP) data collection [113]. The dataset comprises samples ranging

from 400 to 2498 nm at 2 nm intervals, with a resolution of 10 nm. In the experimental part of this research, we focused on the reflectance of dry and fresh vegetation from 400 to 980 nm, as shown in Fig. 2.4a. The purpose of using these data is to evaluate a mathematical model for NDVI estimation. To achieve this, the part of the data related to the reflectance in the R and NIR bands is selected, and the best-fitting curves with a Root Mean Square Error (RMSE) of less than 0.001 by using MATLAB tools is evaluated. These curves, along with their corresponding data, are presented in Fig. 2.4b and Fig. 2.4c, [2].

2.6.2 Camera Sensor

Suppose the experimental data are captured using a UAV multispectral camera, such as the DJI P4-multispectral camera [114]. This camera features six 1/2.9 CMOS sensors, including an RGB sensor for visible light images and five monochrome sensors for multispectral image acquisition, with filters at R: 650 nm ± 16 nm and NIR: 840 nm ± 26 nm. For this example, it is hypothesized that the bandwidth of the multispectral camera for both R and NIR is comparable to the bandwidth of a hyperspectral camera, approximately 10 nm. DJI P4-multispectral camera has non-overlapping filter bands in R and NIR, where these two bands are used for NDVI measurements [2].

2.6.3 Experimental Part and Results

In this part, the DJI P4-multispectral camera, which has non-overlapping filter bands, is utilized to evaluate the primary uncertainty in the NDVI model. Due to the uncorrelated nature of the input in the NDVI evaluation, Equation (2.9) is applied [2]. To assess the uncertainties in the reflectance measurements in the R and NIR bands, denoted as $u(NIR)$ and $u(R)$, it is assumed that these uncertainties follow a uniform distribution. In this scenario, $u(NIR)$ and $u(R)$ are equivalent to their standard deviations within each band, evaluated from the derivation of the mathematical model of their fitting curves (Figs. 2.4b and 2.4c). These standard deviations are then multiplied by their respective tolerance wavelengths (based on the camera specifications) and divided by $\sqrt{3}$. Subsequently, to evaluate the combined uncertainty of the NDVI measurements, $u_c(NDVI)$, Equation (2.9) is used [2]. The quantities of reflectance values in the R and NIR bands are selected in three ways: (i) from the dataset within the R and NIR bandwidths, (ii) as random numbers between $(0, 1)$, and (iii) as sequential numbers between $(0, 1)$. Assuming that the NDVI measurements follow a Gaussian distribution, we use a coverage factor $k = 3$, corresponding to a 99.7% confidence level, to ensure the highest level of confidence. The resulting NDVI values and their expanded uncertainties are presented in Fig. 2.5 and Table 2.1 for these three data models [2].

TABLE 2.1: Plural maxima and plural minima values of NDVI measurements and their expanded uncertainty for data selected from dry and fresh vegetation data set, random, and in order numbers between $(0, 1)$ with three levels of wavelength tolerance [2]

Data	$\delta\lambda$	Min(NDVI)	Max(NDVI)	Min(Uncertainty NDVI)	Max(Uncertainty NDVI)
DataSet Dry Leaf	1/2	0.418	0.75	0.024	0.036
DataSet Dry Leaf	1	0.418	0.75	0.049	0.071
DataSet Dry Leaf	2	0.42	0.75	0.073	0.11
DataSet Fresh Leaf	1/2	0.546	0.827	0.025	0.035
DataSet Fresh Leaf	1	0.546	0.827	0.050	0.070
DataSet Fresh Leaf	2	0.546	0.827	0.074	0.10
Random (0 1)	1/2	-0.93	0.93	0.006	0.22
Random (0 1)	1	-0.93	0.93	0.01	0.45
Random (0 1)	2	-0.93	0.93	0.02	0.67
Inorder (0 1)	1/2	-0.80	0.82	0.007	0.084
Inorder (0 1)	1	-0.80	0.82	0.01	0.17
Inorder (0 1)	2	-0.80	0.82	0.02	0.25

Table 2.1 also displays the plural maxima and plural minima NDVI values and their expanded uncertainties for the experimental dataset, including dry and fresh vegetation, and random and sequential numbers. Additionally, various tolerance values have been considered by scaling the tolerance wavelength $\delta\lambda$ of the DJI P4-multispectral camera by factors of $\frac{1}{2}$ to 2. The results obtained from these considerations are also reported in Table 2.1, [2]. According to the results, for example, when the NDVI value is 0.6823 for $\rho(R) = 0.101$ and $\rho(NIR) = 0.5716$, the uncertainty value is computed as 0.067. For the NDVI measurement and its uncertainty, in the first case, the relationship between R and NIR reflectance is inversely proportional. This means that a decrease in R reflectance and an increase in NIR reflectance result in higher NDVI values and corresponding uncertainty values. Additionally, the results indicate that smaller variations in NIR reflectance combined with larger variations in R reflectance lead to higher NDVI and uncertainty values [2].

2.7 Extension of the Preliminary Evaluation of NDVI Uncertainty Through Modeling the Camera's Optical Density

A preliminary model for evaluating the uncertainty of NDVI measurements was proposed in Section 2.6 and paper [2]. While this model considers vegetation reflectance within a specific wavelength, it does not account for the camera's incident OD. In practical scenarios, cameras capture the OD of the reflected light within the fixed range of the

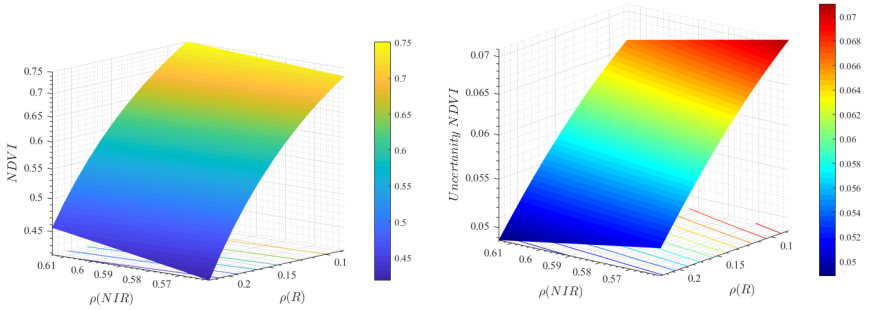

(A) Data Set

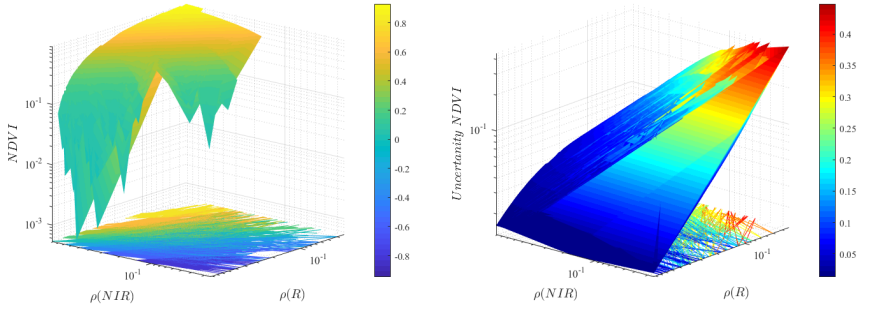

(B) Random number between $(0, 1)$

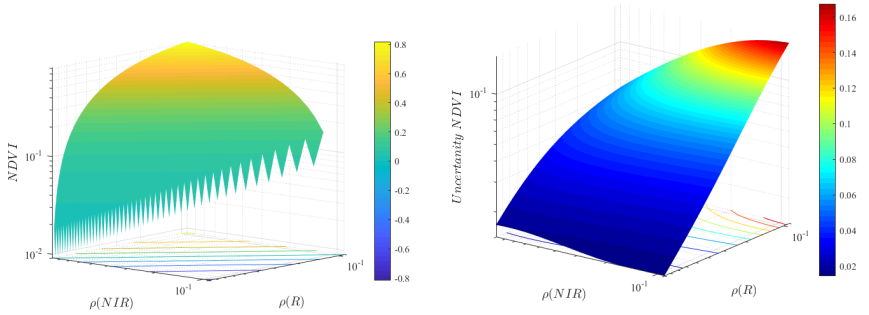

(C) Inorder number between $(0, 1)$

FIGURE 2.5: The values of NDVI measurement and their expanded uncertainty for three ways of data selection [2] © 2022 IEEE.

camera bandwidth for a specific wavelength [3]. This section proposes an uncertainty model for NDVI measurements that considers the limited bandwidth of the sensors embedded in a multi-spectral camera and the variability in OD within their nominal wavelengths, specifically in the R and NIR bands, during the process of spectral data.

This variability is an uncertainty source in the NDVI measurements [3].

2.7.1 Modeling of Vegetation Reflectance and Camera Sensors for NDVI Assessment

This section outlines the approach to modeling vegetation reflectance and camera sensor performance, incorporating vegetation properties and sensor specifications for more accurate NDVI measurements, as shown in Fig. 2.6, [3].

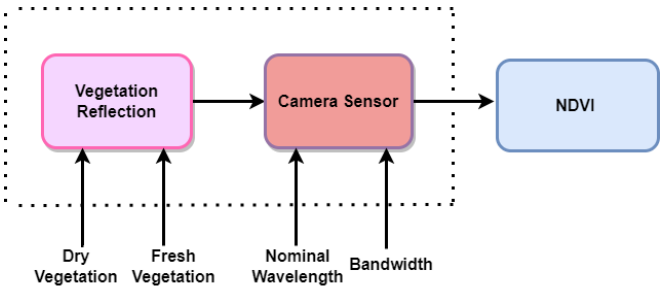

FIGURE 2.6: Modeling Vegetation Reflectance and Camera Sensor Performance for NDVI Assessment [3] © 2023 IEEE.

1. **Vegetation Reflectance Characteristics:** The model considers the spectral reflectance properties of vegetation in both dry and fresh states. These characteristics, which influence the reflectance measurements in the R and NIR spectral bands as modeled in subsection 2.6.1, are used for NDVI calculation.

2. **Camera Sensor Attributes:** The model incorporates the camera sensor's nominal wavelength and filter bandwidth, as variations in these parameters can impact the accuracy of reflectance measurements and, consequently, the NDVI values. Additionally, the model includes the sensor's capability to capture OD within a specified wavelength range.

2.7.2 Modeling Camera Sensor

According to the details in subsection 2.2.3, hyperspectral camera sensors capture spectral images as three-dimensional data cubes, illustrated in Fig. 2.7a [115, 2]. In this data cube, the (x, y) coordinates represent the spatial dimensions, while the third dimension, λ, records spectral information as OD, expressed in units of (watts $\cdot$ steradian^{-1} $\cdot$ m^{-2} $\cdot$ nm^{-1}) [116, 3]. OD quantifies the amount of light or radiance blocked by a filter. Practically, camera sensors measure OD within a specific bandwidth around their nominal

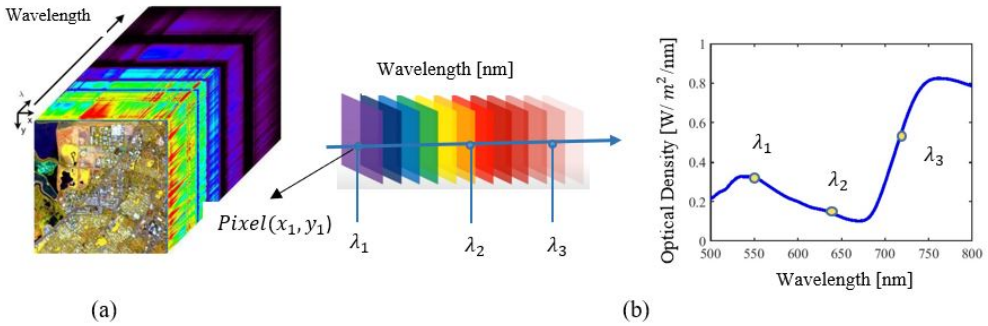

FIGURE 2.7: (a) Data cube of a hyperspectral image, (b) OD spectrum affecting a single pixel, $Pixel(x_1, y_1)$, in the image [3] © 2023 IEEE.

wavelength and provide data corresponding to this bandwidth. It is important to note that camera sensors do not measure radiance at a precise wavelength directly but instead measure within a bandwidth close to the desired wavelength and report the data as OD for that bandwidth. Fig. 2.7b shows the ODs corresponding to various wavelengths within a single pixel of the image, denoted as Pixel(x_1, y_1) [3]. For the modeling camera sensor, we consider the DJI P4-multispectral camera, as described in subsection 2.6.2 [114]. In this study, it is assumed that the bandwidth range of the multispectral camera for each nominal wavelength is 10 nm, which is comparable to the bandwidth of a hyperspectral camera (approximately 10 nm) [3].

2.7.3 Uncertainty assessment for NVDI

In this part, the uncertainty of NDVI is assessed using the type B approach based on the definition of GUM when the input quantities are not correlated, as mentioned in the subsection 2.7. In order to evaluate Equation (2.9), the uncertainty of $u(NIR)$ and $u(R)$ will be computed as follows [3]:

$$u(W) = \frac{\partial E_W(\lambda)}{\partial \lambda_W} \cdot \frac{\Delta \lambda_W}{\sqrt{3}} \tag{2.12}$$

Where $\Delta\lambda_W$ represents the tolerance in camera wavelengths and $E_W(\lambda)$ denotes the area under the fitted curve of the vegetation spectral reflectance, $\rho(\lambda)$, which is evaluated based on information captured by the camera at its nominal wavelength. Furthermore,

$E_W(\lambda)$ is calculated as follows [3]:

$$E_W(\lambda) = \int_{\lambda-\Delta\lambda}^{\lambda+\Delta\lambda} \rho(\lambda^*)\, d\lambda^* \tag{2.13}$$

In practical scenarios, the camera measures OD. In this model, we hypothesize that an ideal compensation method for atmospheric effects has been employed to estimate $\rho(\lambda)$ values based on the solar radiance and measured OD [3].

2.7.4 Experimental Assessment

To quantify the uncertainty of NDVI using the proposed approach, a mathematical model is required to evaluate the impact of measurement uncertainty in vegetation reflectance for the R and NIR bands. For this purpose, a specific portion of the sample data corresponding to reflectance in the R and NIR bands, as shown in Fig. 2.4, is selected. Using MATLAB tools, best-fitting curves with a RMSE of less than 0.001 are generated [3]. Due to the non-overlapping filter bands of the DJI P4-multispectral camera, as mentioned in subsection 2.6.2, the model for assessing NDVI uncertainty is considered uncorrelated and is evaluated based on Equation (2.9), [3]. According to details in Subsection 2.7.2, the camera sensor operates based on OD for each wavelength with a fixed camera bandwidth. Therefore, in the model to evaluate OD, the reflected area under the fitted curve based on the camera's nominal wavelength in the R and NIR bands is calculated according to Equation (2.13), considering a fixed bandwidth of 10 nm, [3]. To assess the uncertainties $u(NIR)$ and $u(R)$, Equation (2.12) is used. The uncertainties of $u(NIR)$ and $u(R)$ are determined as the derivative of the reflected area in each band,

TABLE 2.2: Dataset fresh leaves [3] © 2023 IEEE.

Data	NDVI	Uncertainty NDVI
Sample 1 Fresh Leaf	0.829	0.049
Sample 2 Fresh Leaf	0.814	0.055
Sample 3 Fresh Leaf	0.815	0.063
Sample 4 Fresh Leaf	0.838	0.037
Sample 5 Fresh Leaf	0.821	0.056
Sample 6 Fresh Leaf	0.805	0.078
Sample 7 Fresh Leaf	0.799	0.087
Sample 8 Fresh Leaf	0.818	0.056
Sample 9 Fresh Leaf	0.767	0.095
Sample 10 Fresh Leaf	0.805	0.078

TABLE 2.3: Dataset dry leaves [3] © 2023 IEEE.

Data	NDVI	Uncertainty NDVI
Sample 1 Dry Leaf	0.741	0.081
Sample 2 Dry Leaf	0.742	0.070
Sample 3 Dry Leaf	0.728	0.077
Sample 4 Dry Leaf	0.771	0.057
Sample 5 Dry Leaf	0.739	0.071
Sample 6 Dry Leaf	0.697	0.098
Sample 7 Dry Leaf	0.718	0.087
Sample 8 Dry Leaf	0.742	0.063
Sample 9 Dry Leaf	0.674	0.093
Sample 10 Dry Leaf	0.697	0.098

multiplied by their tolerance wavelengths (based on camera specifications), and divided by $\sqrt{3}$ (assuming a rectangular probability distribution for the nominal wavelength). Subsequently, the uncertainty of NDVI measurements, denoted as $u_c(NDVI)$, is evaluated, Equation (2.9), [3]. To test the model, the reflectance quantities of 10 sample leaves in the R and NIR wavelengths from the dataset were selected. Assuming that the NDVI measurement follows a Gaussian distribution, a coverage factor of $k = 3$ was used to ensure a confidence level of 99.7%. The results of the NDVI measurements and the corresponding expanded uncertainties for the experimental dataset, for both dry and fresh vegetation, are presented in Tables 2.2 and 2.3, [3]. The findings indicate that the nominal wavelength of the camera sensor is a significant source of uncertainty, with values ranging from approximately 0.03 to 0.1 for both dry and fresh vegetation. For instance, when the NDVI of a fresh leaf is determined to be 0.814, accounting for its uncertainty of 0.055, the true estimate of the NDVI value for the fresh leaf can fall within the range of $(0.759, 0.869)$, which overlaps with the corresponding range for the dry leaf. Consequently, distinguishing between dry and fresh leaves based solely on the given NDVI values is not precise. To address this issue, it is important to use a multispectral camera with higher accuracy in terms of its nominal wavelength than the DJI P4-multispectral camera [3]. Another assessment, using the same camera parameters, was conducted with vegetation reflectance measurements obtained from the upper surface of a green leaf sourced from a quaking aspen (Populus tremuloides) tree, as available in [117]. The resultant NDVI was determined to be 0.766, with an associated uncertainty of 0.069 [3]. It is important to emphasize that one of the main limitations of this model is understanding how much uncertainty due to sensor bandwidth alone contributes to the overall uncertainty. However, the results of this study provide a lower bound for

assessing the uncertainty of NDVI measurement, thereby aiding in sensor selection [3].

2.8 A Workflow for Evaluating NDVI by Modeling Solar Irradiance, Atmospheric Conditions, Leaf Reflectance, and Camera Features While Considering the Effects of Uncertainty Sources

This section presents a workflow for evaluating the uncertainty in NDVI measurements by analyzing key factors influencing its accuracy. The study focuses on the impact of atmospheric conditions on solar irradiation and vegetation reflectance, as captured by a multispectral UAV camera operating in the R and NIR bands. Additionally, it accounts for variability in the camera's nominal wavelengths within these bands. The analysis is structured across three atmospheric scenarios: dry-clear, humid-hazy, and a mixed condition combining both. These scenarios are pivotal in assessing how atmospheric states affect NDVI measurement accuracy. Variations in solar irradiance and the camera's SNR are also incorporated as significant factors influencing data quality. A detailed sensitivity analysis is conducted using MCS, enabling the independent and combined examination of each uncertainty source. This statistical approach quantifies the impact of these factors on overall NDVI uncertainty. Results indicate that the primary contributors to NDVI uncertainty are atmospheric conditions, particularly humidity and haze, camera wavelength tolerance, and intrinsic variability in NDVI under different leaf conditions (dry vs. fresh). These findings underscore the importance of accounting for both environmental and instrumental factors in accurate NDVI assessments, crucial for applications in RS and PA [4].

2.8.1 Proposed Workflow

As illustrated in Fig. 2.8, the workflow begins with modeling solar irradiation and its interaction with the Earth's atmosphere. The atmospheric transmission is considered in two distinct scenarios: dry-clear and humid-hazy. These conditions significantly affect the amount of solar radiation reaching the Earth's surface, impacting the accuracy of NDVI measurements. It is important to note that in this workflow, the effect of atmospheric transmission is considered only in the single path between the sun and the ground, as the impact on the reflected light is deemed negligible. The workflow also includes analyzing vegetation reflection, which varies in the health state of the plant (dry and fresh). The camera sensor's performance is a crucial factor in this analysis. For this study, the variation in the nominal wavelength is assumed to have a specified

and constant bandwidth of 20 nm. The next step involves evaluating the incident OD captured by the camera and converting it to digital format through 8-bit quantization. During this digitization stage, the SNR of the camera is applied to ensure the reliability of the captured data. The digital data obtained is then used to compute the NDVI values.

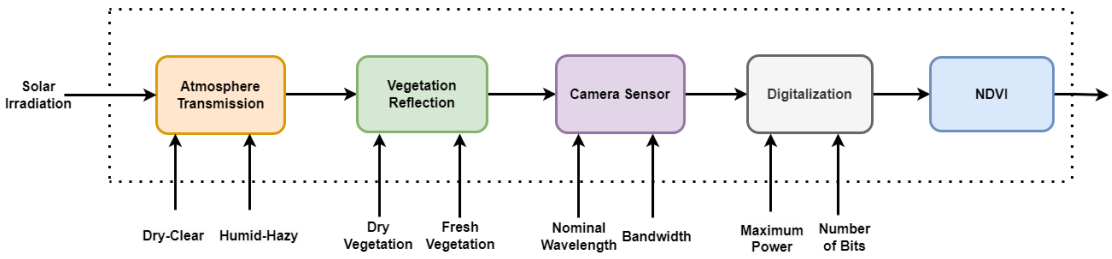

FIGURE 2.8: The proposed workflow for NDVI evaluation presented in this study includes modeling solar irradiation, assessing atmospheric transmission under different conditions (such as dry-clear and humid-hazy scenarios), analyzing vegetation reflection for both dry and fresh leaf states, and evaluating the performance of the camera sensor along with the digitization process [4].

2.8.1.1 Solar Irradiation

To model the Solar Spectral Irradiance (SSI), a publicly available dataset sourced from measurements by the Spectral Irradiance Monitor (SIM) instrument is utilized [118]. The dataset comprises averaged measurements over a 24-hour period, covering a spectral range from 200 nm to 2400 nm, with a spectral resolution ranging from 2 nm (for wavelengths below 0.28 µm) to 45 nm (for wavelengths above 0.4 µm). These measurements were acquired at a mean solar distance of 1 Astronomical Unit (AU) and zero relative line-of-sight velocity relative to the Sun. The absolute uncertainty of the SIM instrument in measuring SSI is approximately 0.2 %. The dataset includes Julian day, minimum wavelength, maximum wavelength, instrument mode, data version number, irradiance value, irradiance uncertainty, and data quality. Fig. 2.9a illustrates the measured SSI averaged over a 24 h period. To meet the modeling objectives, spectral bands around the R and NIR wavelengths of SSI are selected. The best-fitting curves for these spectral bands were determined using a linear interpolation function, implemented through MATLAB software tools. The resulting curves for the R and NIR bands are depicted in Figs. 2.9b and 2.9c [118].

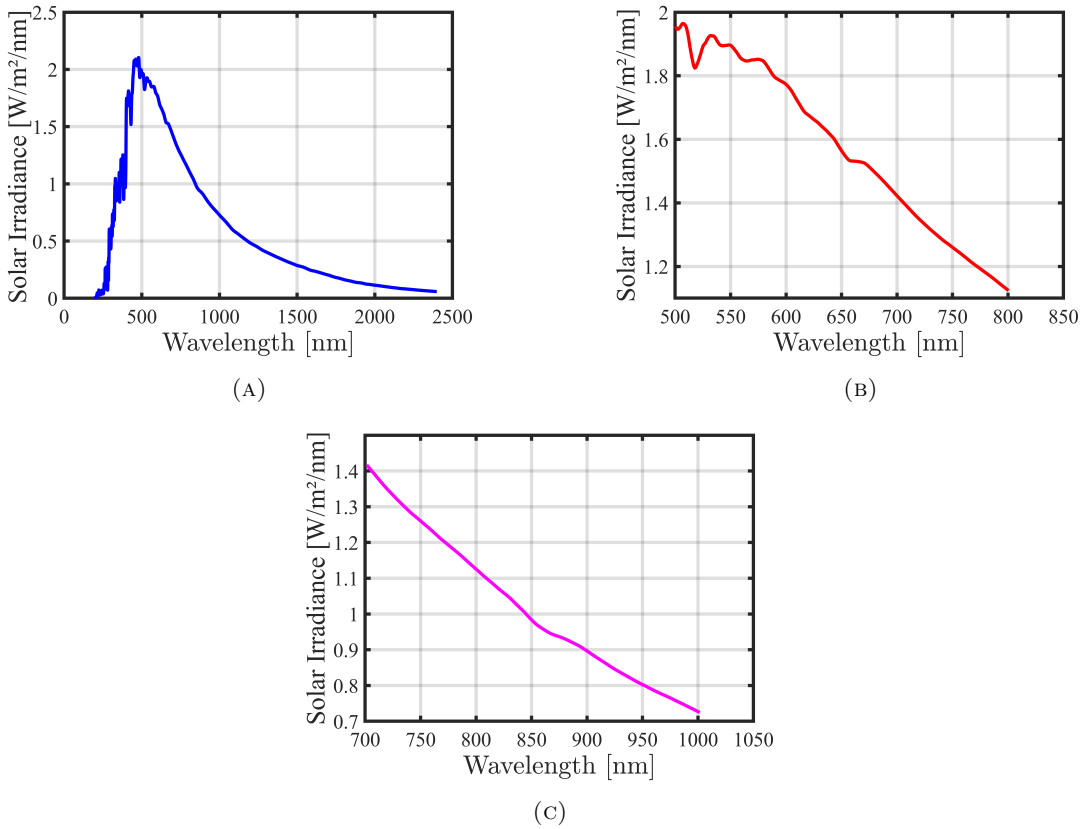

FIGURE 2.9: SSI measured by SIM at 1AU (24-Hour average) Z to Z. (a) SSI over the 200 nm to 2400 nm, (b) SSI around the R band, (c) SSI around the NIR band [4].

2.8.1.2 Atmosphere Transmission

To accurately model the behavior of solar radiation at the ground surface, it is essential to consider the atmospheric influence on solar irradiance and estimate its impact for inclusion in the modeling process. In the wavelength range below 2500 nm, incident solar radiation undergoes several influences, including: (i) absorption by well-mixed gases such as ozone (O_3), oxygen (O_2), methane (CH_4), and carbon dioxide (CO_2); (ii) absorption by water vapor; (iii) scattering by molecules; and (iv) scattering and absorption by aerosols and hydrometeors [68]. Gas absorption can significantly alter the received solar flux, with prominent effects at different wavelengths. In contrast, aerosol absorption, considered a smoothly varying continuous function, typically results

in limited absorption loss, varying from maritime aerosols to urban aerosols rich in carbon. Maritime aerosols exhibit minimum absorption, while maximum absorption is prevalent in urban aerosols containing significant carbon content [68]. Scattering, whether from molecules or aerosols, modifies the incident solar flux. Molecular scattering effects are significant in the visible/near-infrared (VNIR) range, diminishing at longer wavelengths. Aerosol scattering has a noticeable impact on the VNIR/SWIR range, particularly due to larger aerosol particle sizes [68]. Fig. 2.10a, created from the graph mentioned in [68], illustrates atmospheric transmittance for several significant gaseous,

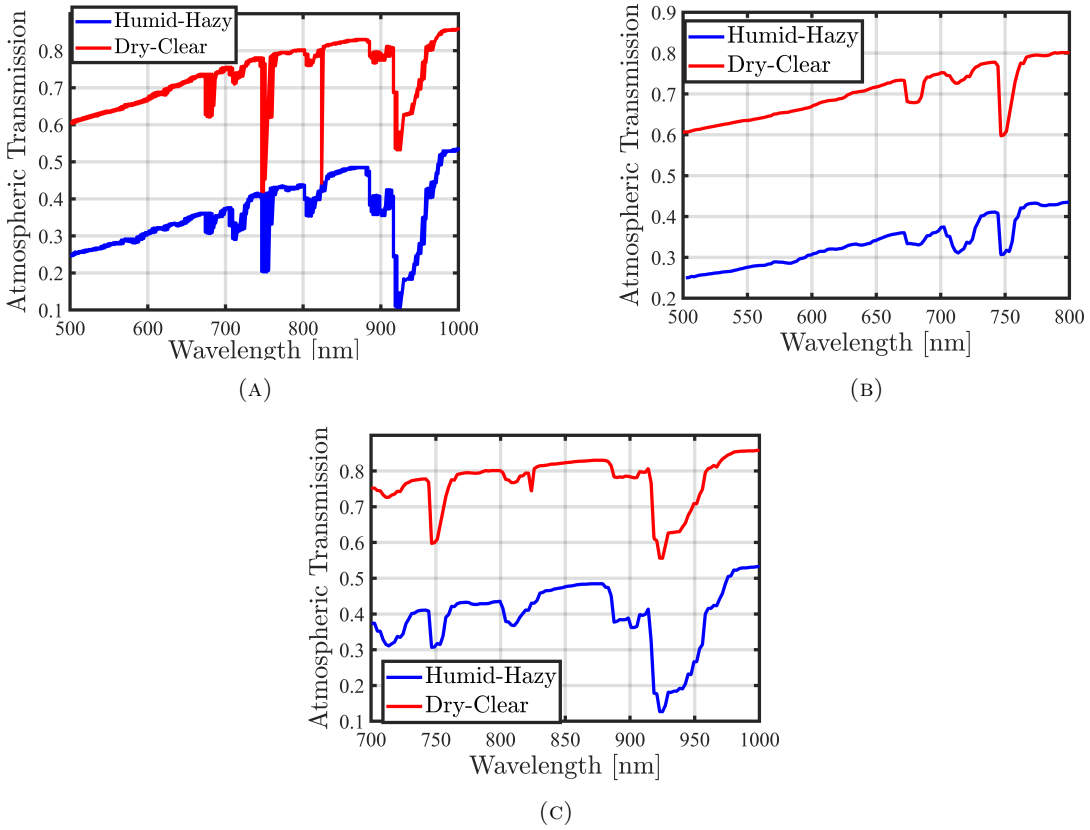

FIGURE 2.10: (a) The atmospheric transmission in the spectral range of 500 nm to 1000 nm is plotted for two conditions: dry-clear (red) and humid-hazy (blue). This plot illustrates the contributions to the overall transmission from mixed gases, aerosols, and water vapor, with data estimated from the referenced paper. Accordingly, (b) depicts the spectral wavelength around the R band, while (c) shows the spectral wavelength around the NIR band [4].

water vapor, and aerosol absorption features observed in the spectral region 400 nm to 2500 nm under two atmospheric conditions: dry-clear and humid-hazy. For modeling atmospheric transmission, the spectral range 500 nm to 1000 nm is selected and shown in Fig. 2.10a. In this spectral range, ozone exhibits weak absorption in the interval 500 nm to 700 nm, while a strong and narrow oxygen absorption line is present at 760 nm. Water vapor absorption in the VNIR spectrum is characterized by numerous bands of varying strengths and spectral widths. Two very weak absorption bands are present at 600 nm and 660 nm, while slightly stronger absorption and more significant bands are located at 730 nm, 820 nm, and 910 nm. Additionally, a distinct and robust water vapor absorption is observed at 940 nm. To achieve the modeling goals, spectral bands around the R and NIR wavelengths of atmospheric transmission are chosen. Utilizing the linear interpolation function with MATLAB software tools, the fitting curves for these selected spectral bands are determined. The resulting curves for R and NIR can be observed in Figs 2.10b and 2.10c [68].

2.8.1.3 Modeling Transmission of Solar Irradiance Through the Atmosphere Conditions

The mathematical models derived from Sections 2.8.1.1 and 2.8.1.2 provide critical representations of solar irradiance and atmospheric transmission, respectively. By integrating these models, the study achieves a comprehensive understanding of the effects of atmospheric conditions on solar irradiance transmission under varying scenarios, including dry-clear and humid-hazy conditions. To account for these effects, the models for solar irradiance and atmospheric transmission are multiplied for both the R and NIR bands under dry-clear and humid-hazy conditions [119]. The models are sampled at specific wavelengths with a resolution of 1 nm. The resulting data points from these curves are then multiplied element-wise. The outcomes of these calculations are illustrated in Fig. 2.11, providing insights into the behavior of solar radiation as it propagates through Earth's atmospheric layers.

2.8.1.4 Vegetation Reflection Affected by Solar Irradiance Passed Through Atmospheric Conditions

To assess the reflection of vegetation in the context of solar irradiance passing through the atmosphere under both dry-clear and humid-hazy conditions, the mathematical curves obtained from Subsection 2.8.1.3 (which represent solar irradiance modified by atmospheric conditions) are multiplied with the vegetation reflectance curve derived from Subsection 2.6.1. This multiplication provides an estimate of how solar irradiance and atmospheric conditions impact vegetation reflection [119, 4]. The curves are sampled at

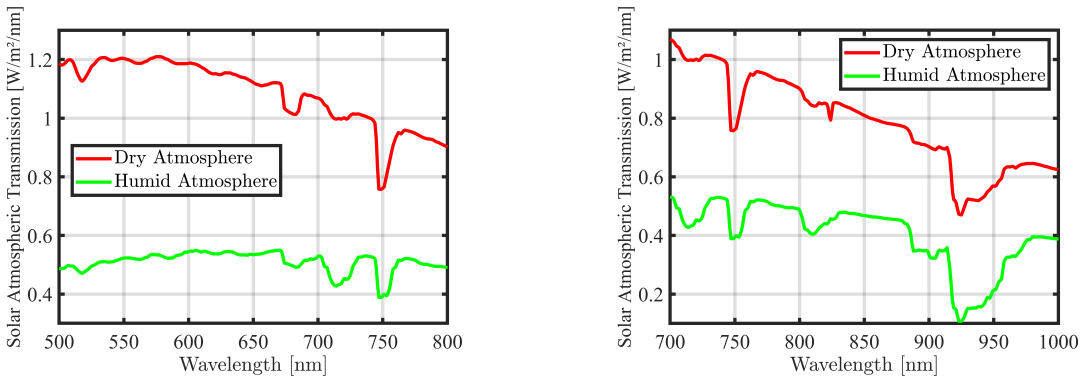

FIGURE 2.11: Solar irradiation is influenced by two atmospheric conditions: dry-clear (indicated in red) and humid-hazy (indicated in green). This impact is illustrated in (a) for the R band and (b) for the NIR band [4].

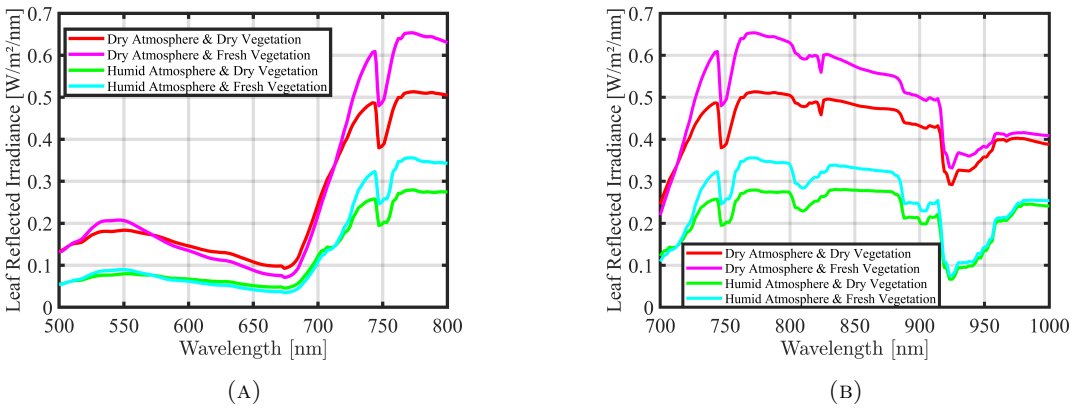

FIGURE 2.12: The spectral reflected irradiance of dry and fresh vegetation is influenced by two atmospheric conditions—dry-clear and humid-hazy—across both (a) the R band and (b) the NIR band [4].

specific wavelengths with a resolution of 1 nm, and the corresponding data points from the two curves are multiplied element-wise. The results of this estimation are presented in Figure 2.12, which illustrates the reflection of both dry and fresh leaves under dry-clear and humid-hazy atmospheric conditions for the R and NIR bands separately [4].

2.8.1.5 Digitalization

In this study, the DJI P4-multispectral camera, as described in Subsection 2.6.2, is utilized to capture and convert energy from real scenes into DNs for each pixel. The camera operates with an 8-bit depth, providing a numerical range from 0 to 255. Accurate modeling of the digitalization function necessitates knowledge of the maximum energy levels in the real scenario [4]. To evaluate the maximum energy for the R and NIR bands, a hypothetical empty scene on the Earth's surface is considered. In this scenario, solar irradiance, after passing through atmospheric conditions, is fully reflected by the bare ground surface with no vegetation present [4]. For the R band, the maximum energy is determined by analyzing the reflected irradiance within the wavelength range of 614 nm to 686 nm, considering a sensor bandwidth of 20 nm. The energy under the curve is calculated by multiplying the solar irradiance, as detailed in Subsection 2.8.1.1, with the atmospheric conditions (dry-clear or humid-hazy, evaluated separately) discussed in Subsection 2.8.1.2. This results in a maximum energy density of 22.962 $\mathrm{W\,m^{-2}}$ for the R band [4]. A similar procedure is followed to ascertain the maximum energy for the NIR band, considering a wavelength range from 794 nm to 886 nm with a bandwidth of 20 nm. The maximum energy density for the NIR band is computed to be 16.908 $\mathrm{W\,m^{-2}}$ [4].

2.8.2 Sensitivity Assessment

Sensitivity analysis examines how changes in independent variables impact a specific dependent variable under a set of defined assumptions. This study aims to understand how variations in atmospheric conditions and instrumental parameters, by adjusting design or operational settings, affect multispectral imaging in the measurement of NDVI [4]. To achieve this, MCS are utilized to assess the uncertainties introduced by atmospheric conditions and camera sensor characteristics. This approach helps to quantify the individual contributions of these factors to the overall uncertainty in NDVI measurements [4].

2.8.2.1 Monte Carlo Simulation

The methodology for assessing uncertainty in this research follows the principles established in the GUM [120], specifically utilizing the MCS approach [4]. The process MCS method involves several key steps: (1) establishing a model equation for the measurand based on the influence of individual parameters; (2) identifying the significant sources of uncertainty; (3) determining the probability density functions corresponding to each identified uncertainty source; (4) selecting the number of Monte Carlo trials; and (5) calculating the results by applying the model equation to the measurand [121, 4]. MCS employs random sampling to estimate the potential outcomes of uncertain events or systems. By generating multiple scenarios with randomly assigned parameter values,

MCS simulates the probability distribution of various outcomes. This method is particularly valuable for assessing risk and making informed decisions in the presence of unpredictable factors [122, 4]. For multispectral images, as outlined in the workflow depicted in Fig. 2.8, MCS is employed to estimate uncertainty and determine the distribution of pixel values. MCS conducting through 100 observations, as shown in Fig. 2.13. These simulations account for random variations in each influencing factor, including solar irradiance, atmospheric conditions, and camera sensor characteristics separately, as well as their combinations.

2.8.3 Results

The evaluation of NDVI measurement uncertainty involves analyzing the impact of parameter variations at each stage of the workflow, as illustrated in Fig. 2.8. This analysis is divided into six components: (i) NDVI uncertainty relative to nominal wavelength, (ii) NDVI uncertainty relative to the standard deviation of solar irradiance, (iii) NDVI uncertainty relative to camera SNR, (iv) NDVI uncertainty related to leaf state, (v) NDVI uncertainty considering all sources of uncertainty, and (vi) comparison with an alternative camera sensor. These assessments are performed on solar irradiance (discussed in subsection 2.8.1.1) under different atmospheric conditions (outlined in subsection 2.8.1.2), utilizing datasets of both dry and fresh leaves (described in subsection 2.6.1), and employing a specific camera sensor (referenced in subsection 2.6.2). Detailed analyses and results for each component are presented in the subsequent subsections [4].

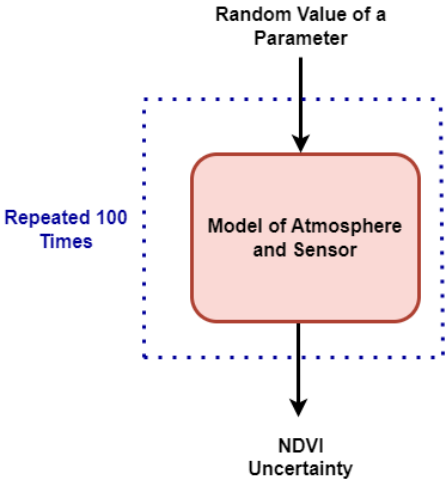

FIGURE 2.13: Sensitivity analysis of the proposed workflow using MCS [4].

2.8.3.1 NDVI Uncertainty vs Nominal Wavelength

In the experiment, one dried and one fresh leaf are selected. For MCS, a loop with 100 trials is employed, wherein the nominal wavelength is randomly changed based on the nominal wavelength tolerance of the camera. This random value is selected from a uniform distribution function. Then the energy of the multiplied curves, encompassing

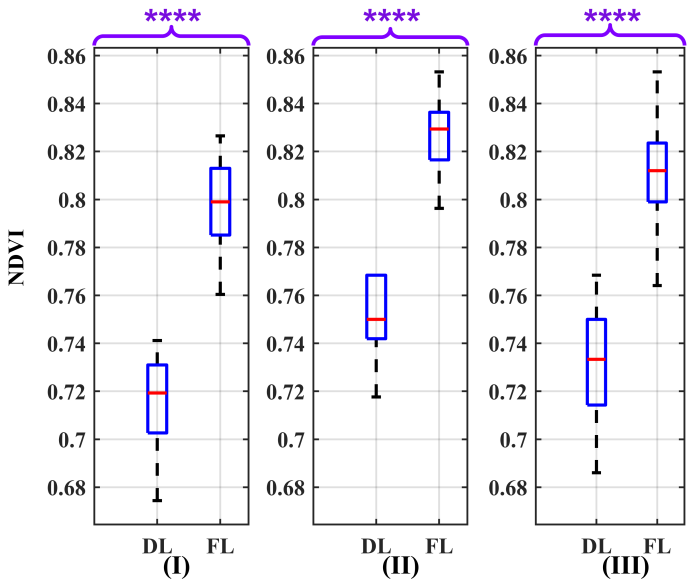

FIGURE 2.14: Box plots illustrating the effect of nominal wavelength as a source of uncertainty on NDVI values for atmosphere conditions: (I) Dry-clear, (II) Humid-hazy, and (III) Mixed, considering both DL and FL [4].

TABLE 2.4: Statistical parameters MED, first and third Quartiles (Q1, Q3), IQR and distance of first quartiles of fresh leaf and third quartiles of dry leaf when the effect of nominal wavelength as an uncertainty source on NDVI values for different LS, and ATMC is evaluated [4].

LS	ATMC	MED	Q1	Q3	IQR	$Q1_F - Q3_D$
Fresh	Humid-Hazy	0.829	0.817	0.836	0.019	0.049
	Dry-Clear	0.799	0.785	0.813	0.028	0.054
	Mixed	0.812	0.799	0.824	0.025	0.049
Dry	Humid-Hazy	0.750	0.742	0.768	0.026	0.049
	Dry-Clear	0.719	0.703	0.731	0.028	0.054
	Mixed	0.733	0.714	0.750	0.036	0.049

(i) solar irradiance without considering its standard deviation, (ii) atmospheric transmission, and (iii) leaf reflection in both the R and NIR spectra, as mentioned in subsection 2.8.1.4, is assessed [4]. After evaluating the energy, a quantization function for 8-bits, considering the maximum energy evaluated separately in R and NIR as mentioned in subsection 2.8.1.5, is applied. Subsequently, an unsigned integer value is computed for each wavelength in R and NIR. Then NDVI value is calculated using these two integers, based on Equation (2.4). Out of the 100 trials, 100 NDVI values are used to evaluate the effect of the uncertainty source on NDVI values [4]. To precisely investigate the degree of this effect, it is imperative to determine the distribution of NDVI values. The chi-square test is applied to the NDVI values, revealing that NDVI does not follow a Gaussian distribution. Moreover, the NDVI values in dry and fresh leaves are independent. As NDVI values are independent and do not conform to a Gaussian distribution, the Wilcoxon Rank Sum Test, also recognized as the Mann-Whitney U test, is employed. This non-parametric test, which does not assume known distributions and avoids dealing with parameters, is utilized to assess the extent of overlap in NDVI values, determining whether NDVI values for distinct leaves are likely to originate from the same population [4]. In this test, the Null Hypothesis (H0) is that the two input data are samples from the same distribution with identical medians, while the Alternative Hypothesis (H1) assumes they are not. Rejecting the H0 implies evidence of a shift in one distribution relative to the other and provides evidence that the medians of the two populations differ. Moreover, the p-value indicates the probability of observing the data if the H1 is true [4]. The outcome of this test is depicted in Fig. 2.14 for each separate air condition. The resultant p-values are significantly below 0.0001 ($p \leq 0.0001$), so to report them, 4 asterisks are used to denote the level of significance. This level of significance implies strong evidence to reject the H0 in favor of the H1. Therefore, there is a difference between dry and fresh leaves under different conditions. With a more reliable and trustworthy multispectral camera and data about leaf chemical composition and species, it is possible to distinguish leaves' status [4]. Table 2.4 presents the conclusive outcomes of the conducted evaluation, incorporating the MED NDVI along with its associated First Quartile (Q1), Third Quartile (Q3), and Interquartile (IQR) for Leaf State (LS) in both dry and fresh leaves under various Atmosphere Conditions (ATMC). These conditions include humid-hazy, dry-clear, and a mix of air conditions. The variability of the NDVI with respect to fresh leaves, assessed through the IQR, is determined to be 0.028, while for dry leaves, it is measured at 0.036. Despite considering nominal wavelength as a potential source of uncertainty, these values exhibit low magnitudes, indicative of the stability of NDVI values. Also, the table includes the distance between Q1 of the fresh leaf ($Q1_F$) and Q3 of the dry leaf ($Q3_D$) in the same air condition, providing information about the ability to distinguish between the two leaf conditions [4].

In the context of distinguishing between dry and fresh leaves, the MED of fresh leaves consistently surpasses that of dry leaves. Consequently, the assessment of the distance of the leaf condition involves quantifying between $Q1_F$ and $Q3_D$. A greater distance indicates a higher ability to distinguish the leaf under different conditions based on NDVI values and setting a threshold [4]. By setting a threshold of NDVI value around 0.775, it is possible to distinguish between dry and fresh leaves under various air conditions. However, in a dry-clear atmosphere, the threshold can be below 0.775, while in a humid-hazy atmosphere, it can be above 0.775. Therefore, the choice of the threshold depends on the atmospheric conditions [4]. Moreover, the distance, $Q1_F - Q3_D$, in different air conditions shows the highest value in dry-clear atmospheric conditions, which is 0.054, than in humid-hazy and mixed air conditions, which are 0.049. Therefore, the ability to differentiate between leaf states in a dry atmosphere is more feasible [4].

2.8.3.2 NDVI Uncertainty vs Solar Irradiance Standard Deviation

For this test, the same procedure as mentioned in subsection 2.8.3.1 is repeated. However, the difference lies in the initial step where data regarding the uncertainty of the solar irradiance instrument for each wavelength within the dataset mentioned in [118] is added, along with white Gaussian noise, to the solar irradiance curve. Furthermore, the nominal wavelength is fixed to match the camera's nominal wavelength in R and NIR spectra [4]. The outcome of the Wilcoxon Rank Sum Test on the NDVI values is presented in the box plot shown in Fig. 2.15. The obtained p-value is markedly below 0.0001 ($p \leq 0.0001$), which signifies robust evidence for rejecting the H0 in favor of the H1. Furthermore, the absence of any overlap between the boxes in Fig. 2.15 indicates the feasibility of distinguishing between dry and fresh leaves under various conditions [4]. The conclusive outcomes of the conducted assessment are presented in Table 2.5. The IQR values indicate the NDVI variability for fresh and dry leaves as 0.039 and 0.047, respectively. Despite accounting for the standard deviation of solar irradiance as a potential source of uncertainty, these variation values exhibit low magnitudes, signifying the stability of NDVI values [4]. Moreover, the table incorporates the $Q1_F$ to $Q3_D$ distance in the same air condition, providing insights into the capability to differentiate between the two leaf conditions. By establishing a threshold for the NDVI value within the range of 0.777 to 0.787, it becomes feasible to discern between dry and fresh leaves under various air conditions [4]. In a dry-clear atmosphere, the threshold can shift slightly downward, and in a humid-hazy atmosphere, it can shift slightly upward. Furthermore, the $Q1_F - Q3_D$ distance across different air conditions reveals a higher magnitude in dry-clear atmospheric conditions (0.076) compared to humid-hazy (0.068) and mixed air conditions (0.029). As a result, the practicality of distinguishing between leaf states in a dry atmosphere is enhanced [4].

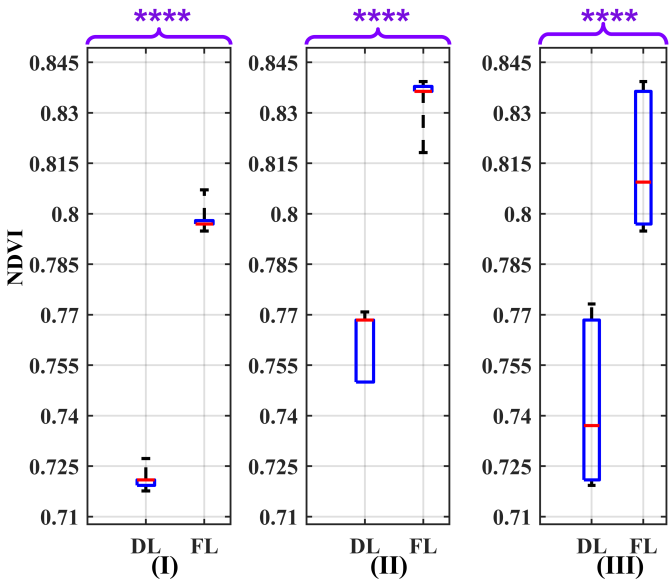

FIGURE 2.15: Box plots illustrating the effect of the variability in solar irradiance measurement as a source of uncertainty on NDVI values for atmosphere conditions: (I) Dry-clear, (II) Humid-hazy, and (III) Mixed, considering both DL and FL [4].

TABLE 2.5: Statistical parameters MED, first and third Quartiles (Q1, Q3), IQR and distance of first quartiles of fresh leaf and third quartiles of dry leaf when the effect of solar irradiance standard deviation as an uncertainty source on NDVI values for different LS, and ATMC is evaluated [4].

LS	ATMC	MED	Q1	Q3	IQR	$Q1_F - Q3_D$
Fresh	Humid-Hazy	0.836	0.836	0.838	0.002	0.068
	Dry-Clear	0.797	0.797	0.798	0.001	0.076
	Mixed	0.809	0.797	0.836	0.039	0.029
Dry	Humid-Hazy	0.768	0.750	0.768	0.018	0.068
	Dry-Clear	0.721	0.719	0.721	0.002	0.076
	Mixed	0.737	0.721	0.768	0.047	0.029

2.8.3.3 NDVI Uncertainty vs Camera SNR

The signal in a pixel is quantified by the total number of detected photoelectrons, and a higher quantum efficiency or larger pixel size yields an increased signal due to a higher count of photoelectrons [123]. The SNR measures the relationship between the useful

signal and unwanted background noise within a pixel [4]. In various embedded vision applications (crop detection), particularly those involving edge-based processing with AI or ML algorithms analyzing processed images for intelligent decision-making, a high SNR is essential to deliver detailed and accurate image outputs [124]. The SNR varies depending on the device, and based on literature reviews, an SNR range from 40 dB to 60 dB has been measured for multispectral cameras [125, 124]. This range is estimated to be suitable for maintaining a balance between signal strength and noise levels [4]. In this test, the same procedure as mentioned in subsection 2.8.3.1 is repeated, using a fixed camera's nominal wavelength in R and NIR. During the quantization function step, the SNR value, along with an additive white Gaussian noise, is incorporated into the quantization function, as mentioned in subsection 2.8.1.5, for the conversion of analog data to digital. The SNR value is initialized at 40 dB and incremented by 10 dB in each iteration of Monte Carlo analysis until reaching 60 dB [4]. The results of the Wilcoxon Rank Sum Test on the NDVI values, are depicted in the box plots shown in Fig.2.16 for SNR values of 40 dB, 50 dB, and 60 dB, respectively. These box plots indicate the absence of any overlap between the boxes [4]. The computed p-value, significantly below 0.0001, provides robust evidence for rejecting the H0 in favor of the H1. This outcome thereby enables the differentiation of leaf state under varying air conditions [4]. Table 2.6 presents the definitive outcomes of the conducted assessment for SNR values of 40 dB, 50 dB, and 60 dB. The IQR for NDVI variability in fresh leaves is 0.039, and for dry leaves, it is 0.047. The analysis indicates that different SNR values do not significantly influence the degree of NDVI variation. Considering camera SNR as a potential source of uncertainty, the variation of NDVI values displays low magnitudes, indicative of the stability of NDVI values [4]. By establishing a threshold of NDVI value between 0.770 and 0.790, it becomes feasible to distinguish between dry and fresh leaves under various air conditions. In dry conditions, the threshold can shift slightly down; in humid-hazy conditions, it can shift slightly up [4]. In addition, the distance, $Q1_F - Q3_D$, in different air conditions reveals a higher magnitude in dry-clear atmospheric conditions (0.076) compared to humid-hazy (0.068) and mixed air conditions (0.029). Importantly, varying SNR values do not impact the magnitude of this distance. Also, the practicality of distinguishing between leaf states in a dry atmosphere remains high [4].

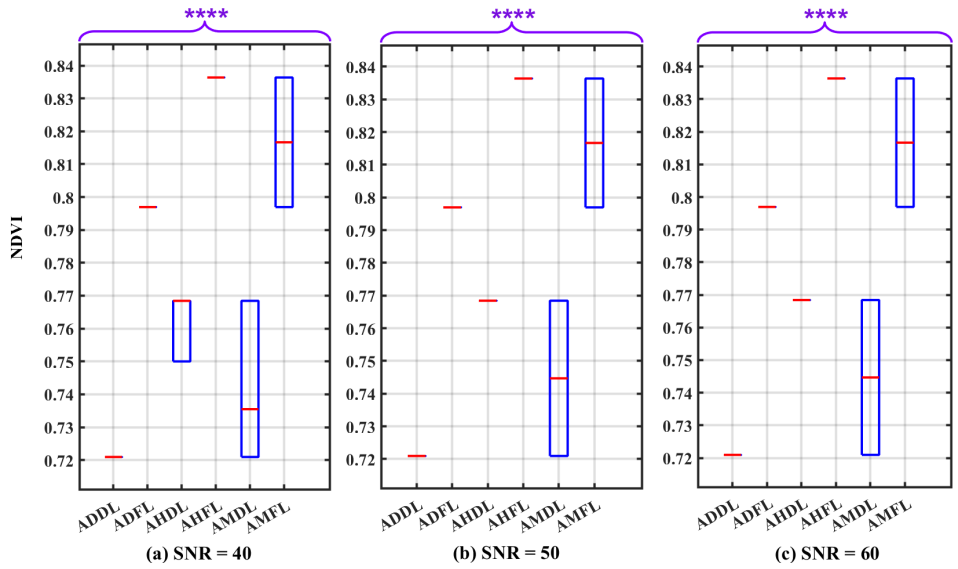

FIGURE 2.16: Box plots illustrating the influence of the camera sensor under three different SNR conditions: (a) SNR = 40 dB, (b) SNR = 50 dB, and (c) SNR = 60 dB, serving as uncertainty factors on NDVI values. The plot considers various atmospheric conditions and leaf states, including: ADDL, ADFL, AHDL, AHFL, AMDL, and AMFL [4].

TABLE 2.6: Statistical parameters MED, first and third Quartiles (Q1, Q3), IQR and distance of first quartiles of fresh leaf and third quartiles of dry leaf when the effect of camera SNR at 40 dB, 50 dB, and 60 dB as an uncertainty source on NDVI values for different LS, and ATMC is evaluated [4].

LS	ATMC	SNR[dB]	MED	Q1	Q3	IQR	$Q1_F - Q3_D$
Fresh	Humid-Hazy	40	0.836	0.836	0.836	0.000	0.068
		50	0.836	0.836	0.836	0.000	0.068
		60	0.836	0.836	0.836	0.000	0.068
	Dry-Clear	40	0.797	0.797	0.797	0.000	0.076
		50	0.797	0.797	0.797	0.000	0.076
		60	0.797	0.797	0.797	0.000	0.076
	Mixed	40	0.817	0.797	0.836	0.039	0.029
		50	0.817	0.797	0.836	0.039	0.029
		60	0.817	0.797	0.836	0.039	0.029
Dry	Humid-Hazy	40	0.768	0.750	0.768	0.018	0.068
		50	0.768	0.768	0.768	0.000	0.068
		60	0.768	0.768	0.768	0.000	0.068
	Dry-Clear	40	0.721	0.721	0.721	0.000	0.076
		50	0.721	0.721	0.721	0.000	0.076
		60	0.721	0.721	0.721	0.000	0.076
	Mixed	40	0.735	0.721	0.768	0.047	0.029
		50	0.745	0.721	0.768	0.047	0.029
		60	0.745	0.721	0.768	0.047	0.029

2.8.3.4 NDVI Uncertainty vs Leave State

In this sensitivity analysis, the uncertainty due to the binary model of the leaf state (fresh or dry) is assessed. Therefore, for the Monte Carlo analysis, a set of 49 leaf samples is selected for each leaf state. The sample size must meet a minimum requirement of 30, as certain statistical tests, such as the T-square test, are not applicable for sample sizes below this number. Consequently, 49 leaf samples are chosen, as this quantity is readily available within the dataset [113, 4]. By maintaining a fixed nominal wavelength equivalent to the camera's nominal wavelength in the R and NIR spectra, the identical procedure outlined in subsection 2.8.3.1 is utilized [4]. The result of the Wilcoxon Rank Sum Test is employed to elucidate the impact of this uncertainty source on NDVI values in detail, as depicted in the box plots presented in Fig. 2.17. The derived p-value, notably below 0.0001, provides robust evidence for rejecting the H0 in favor of the H1. Moreover, the absence of any overlap between the boxes, in Fig. 2.17, emphasizes the feasibility of

discriminating between dry and fresh leaves under varying air conditions [4]. Table 2.7 summarizes the conclusive results of the conducted assessment. The IQR values for the NDVI variability in fresh leaves and dry leaves are 0.032 and 0.046, respectively. These values, considering the distribution of measured leave values in dry and fresh states with respect to the NDVI measurement as a potential source of uncertainty, demonstrate low magnitudes, suggesting the low variability of the NDVI values [4]. In the context of distinguishing between dry and fresh leaves, setting a threshold around 0.790 for the NDVI value makes it possible to differentiate between them under various air conditions. However, in a dry atmosphere, this threshold can move a bit downward, and in a humid atmosphere, it can move a bit upward. Therefore, selecting the threshold also depends on atmospheric conditions. Moreover, the $Q1_F - Q3_D$ distance in different air conditions reveals a higher magnitude in dry-clear atmospheric conditions (0.057) compared to humid-hazy (0.042) and mixed air conditions (0.040). Hence, the feasibility of differentiating between leaf states in a dry atmosphere is increased [4].

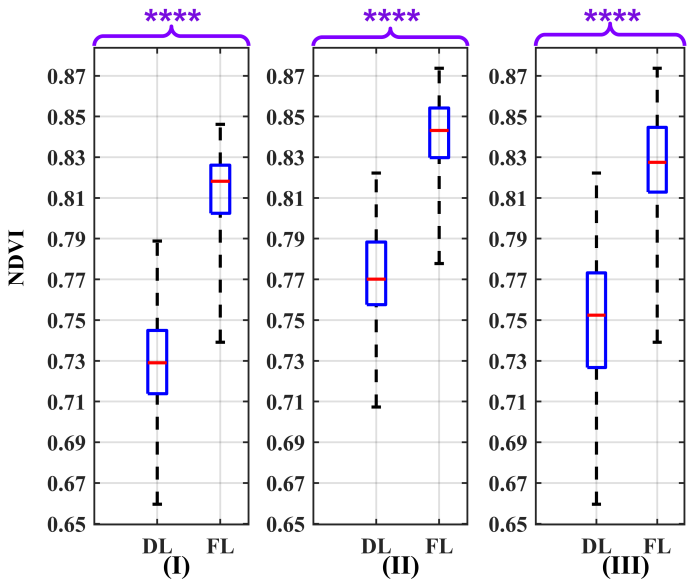

FIGURE 2.17: Box plots illustrating the effect of the variability of NDVI values as a source of uncertainty on NDVI values for atmosphere conditions: (I) Dry-clear, (II) Humid-hazy, and (III) Mixed, considering both DL and FL [4].

TABLE 2.7: Statistical parameters MED, first and third Quartiles (Q1, Q3), IQR and distance of first quartiles of fresh leaf and third quartiles of dry leaf when the effect of the variability of NDVI values as an uncertainty source on NDVI values for different LS, and ATMC is evaluated [4].

No./ LS	ATMC	MED	Q1	Q3	IQR	$Q1_F - Q3_D$
49/Fresh Leaf	Humid-Hazy	0.843	0.830	0.854	0.024	0.042
	Dry-Clear	0.818	0.802	0.826	0.024	0.057
	Mixed	0.827	0.813	0.845	0.032	0.040
49/Dry Leaf	Humid-Hazy	0.770	0.758	0.788	0.030	0.042
	Dry-Clear	0.729	0.714	0.745	0.031	0.057
	Mixed	0.752	0.727	0.773	0.046	0.040

2.8.3.5 NDVI Uncertainty vs All Uncertainty Sources

In this section, all the uncertainty sources, including variations in solar irradiance standard deviation, camera SNR, camera nominal wavelength, and the variability of the measurand within each considered leaf state, are applied to the dataset for the assessment of NDVI uncertainty. In the Monte Carlo analysis, a dataset of 49 leaf samples is selected. Solar irradiance standard uncertainty, modeled by a Gaussian distribution function, and SIM instrument's uncertainty, are applied to the solar irradiance curve before its utilization in energy evaluation. Variations in nominal wavelength, introduced through a Uniform distribution function, are applied [4]. The SNR value is initialized and incremented in the same procedure as mentioned in subsection 2.8.3.3. Following this, the resulting energy is calculated using the same procedure as that used in subsection 2.8.3.1. The Wilcoxon Rank Sum Test results to elucidate the extent of the effect of these uncertainty sources on NDVI values in detail are portrayed in the box plots presented in Fig. 2.18 for SNR values of 40 dB, 50 dB, and 60 dB, respectively. These box plots indicate the absence of overlap between the boxes. The computed p-value, significantly below 0.0001, provides robust evidence for rejecting the H0 in favor of the H1. This outcome thereby enables the differentiation of leaf state under varying air conditions [4]. Table 2.8 summarizes the conclusive results of the evaluation with SNR values of 40 dB, 50 dB, and 60 dB. The IQR for the NDVI variability in fresh leaves is 0.043, and for dry leaves, it is 0.053. Different SNR values have a minor impact on the variability. These NDVI variability values show low magnitudes and suggest the stability of NDVI values [4]. Additionally, setting a threshold for the NDVI value just around 0.790 makes it challenging but possible to distinguish between dry and fresh leaves under various air conditions. In a dry-clear atmosphere, the threshold can shift down a bit, while in a humid-hazy atmosphere, it can shift up a bit. Furthermore, the

distance, $Q1_F - Q3_D$, in various air conditions, reveals a higher magnitude in dry-clear atmospheric conditions (0.047) than in humid-hazy and mixed air conditions, which are 0.040 and different SNR values have a negligible effect on this distance. Therefore, the feasibility of differentiating between leaf states in a dry atmosphere is higher [4].

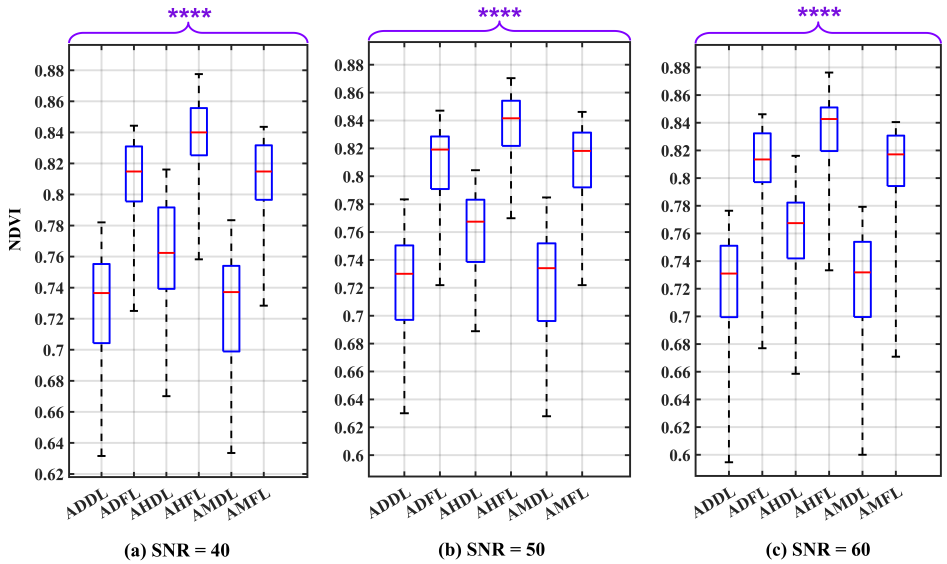

FIGURE 2.18: Box plots illustrating the effect of all uncertainty sources under three different SNR conditions: (a) SNR = 40 dB, (b) SNR = 50 dB, and (c) SNR = 60 dB, serving as uncertainty factors on NDVI values. The plot considers various atmospheric conditions and leaf states, including: ADDL, ADFL, AHDL, AHFL, AMDL, and AMFL [4].

TABLE 2.8: Statistical parameters MED, first and third Quartiles (Q1, Q3), IQR and distance of first quartiles of fresh leaf and third quartiles of dry leaf when the effect of the combination of all uncertainty sources on NDVI values for different LS, and ATMC is evaluated [4].

No./ LS	ATMC	SNR [dB]	MED	Q1	Q3	IQR	$Q1_F - Q3_D$
49/Fresh	Humid-Hazy	40	0.840	0.825	0.856	0.031	0.035
		50	0.842	0.822	0.854	0.032	0.039
		60	0.843	0.820	0.851	0.031	0.040
	Dry-Clear	40	0.815	0.796	0.831	0.035	0.036
		50	0.819	0.791	0.829	0.038	0.041
		60	0.813	0.797	0.832	0.035	0.047
	Mixed	40	0.829	0.808	0.843	0.035	0.038
		50	0.825	0.800	0.843	0.043	0.030
		60	0.828	0.810	0.842	0.032	0.040
49/Dry	Humid-Hazy	40	0.762	0.739	0.792	0.053	0.035
		50	0.767	0.739	0.783	0.044	0.039
		60	0.767	0.742	0.782	0.040	0.040
	Dry-Clear	40	0.737	0.704	0.755	0.051	0.036
		50	0.730	0.697	0.750	0.053	0.041
		60	0.731	0.699	0.751	0.052	0.047
	Mixed	40	0.743	0.724	0.768	0.044	0.038
		50	0.748	0.720	0.771	0.051	0.030
		60	0.748	0.718	0.770	0.052	0.040

2.8.4 Comparison with Another Camera Sensor

The proposed workflow has been evaluated considering another multispectral sensor available in the market, the AQ600 multispectral camera [126], composed of five spectral channels of 3.2 M pixels each, along with one 12.3 M pixel RGB channel. It features a sapphire optical window, a large aperture, low distortion, broad-spectrum transmission, and an all-glass lens. The AQ600 offers advantages such as fast imaging speed, high resolution, and accurate image quality, making it more suitable for Vertical Take-Off and Landing (VTOL) and fixed-wing UAVs [4]. The filters used in the camera have specific wavelength ranges, R: 660 nm $\pm$ 22 nm, and NIR: 840 nm $\pm$ 30 nm. Its resolution is 12 bit for the multispectral camera, and 8 bit for the RGB channels [4]. In the valuation, the integration of all uncertainty sources, following the procedure outlined in subsection 2.8.3.5 with 12 bit quantization, is applied. Subsequently, the Wilcoxon Rank Sum Test is conducted to thoroughly examine the NDVI values, with detailed portrayal in the box plots presented in Fig. 2.19 for SNR values of 40 dB, 50 dB, and 60 dB, respectively.

The computed p-value, significantly below 0.0001, provides robust evidence for rejecting the H0 in favor of the H1. This outcome facilitates the differentiation of leaf state under varying air conditions [4] Table 2.9 presents the comprehensive findings of the evaluation across SNR values of 40 dB, 50 dB, and 60 dB. The IQR for NDVI variability in fresh leaves is 0.038, and for dry leaves, it is 0.059. Minor fluctuations in NDVI variability are observed with varying SNR values, indicating the stability of NDVI measurements [4]. Moreover, the difference between $Q1_F$ and $Q3_D$ within the same atmospheric condition is slightly higher in dry-clear atmospheric conditions (0.050) compared to humid-hazy and mixed air conditions, which measure 0.047 and 0.048. Different SNR values have a negligible impact on this difference. Establishing a threshold for the NDVI value around 0.790 enables the distinction between dry and fresh leaves under diverse air conditions. In dry-clear atmospheres, the threshold may shift downward slightly, while in humid-hazy atmospheres, it may shift upward marginally [4]. In comparing the DJI P4-multispectral and AQ600, despite differences in their quantization level, number of bits, and filter bands in R and NIR, it is feasible to differentiate between leaf states and the NDVI values exhibit changes on the order of a few thousandths, indicating that the cameras' features contribute less to the overall uncertainty compared to other sources [4].

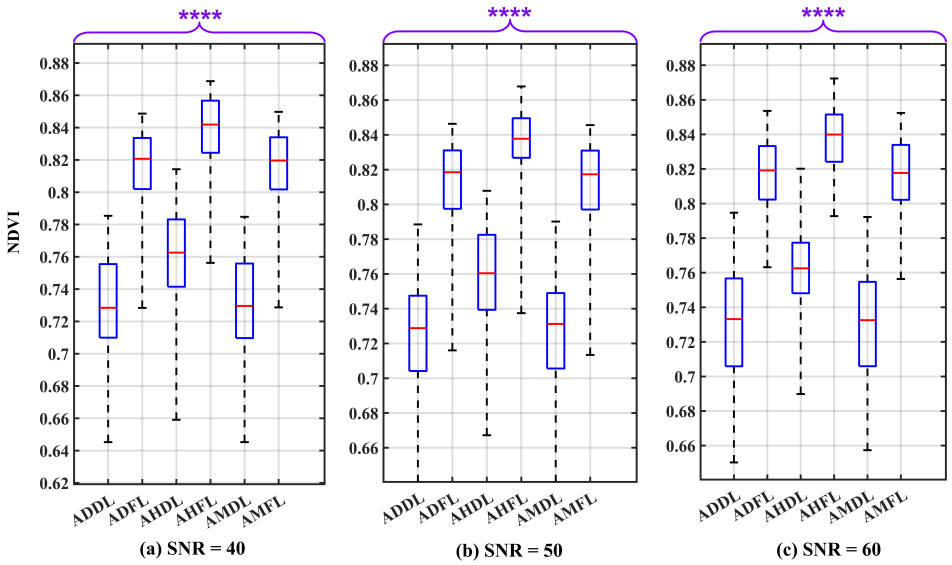

FIGURE 2.19: Box plots illustrating the effect of all uncertainty sources by using the AQ600 camera features under three different SNR conditions: (a) SNR = 40 dB, (b) SNR = 50 dB, and (c) SNR = 60 dB, serving as uncertainty factors on NDVI values. The plot considers various atmospheric conditions and leaf states, including: ADDL, ADFL, AHDL, AHFL, AMDL, and AMFL [4].

TABLE 2.9: Statistical parameters MED, first and third Quartiles (Q1, Q3), IQR, and distance of first quartiles of fresh leaf and third quartiles of dry leaf when the effect of the combination of all uncertainty sources by using the AQ600 camera's features on NDVI values for different LS, and ATMC is evaluated [4].

No./ LS	ATMC	SNR[dB]	MED	Q1	Q3	IQR	$Q1_F - Q3_D$
49/Fresh	Humid-Hazy	40	0.842	0.824	0.857	0.033	0.041
		50	0.838	0.827	0.850	0.023	0.044
		60	0.840	0.824	0.852	0.028	0.047
	Dry-Clear	40	0.821	0.802	0.834	0.032	0.047
		50	0.819	0.797	0.831	0.034	0.050
		60	0.819	0.802	0.833	0.031	0.045
	Mixed	40	0.829	0.809	0.847	0.038	0.037
		50	0.827	0.806	0.843	0.037	0.034
		60	0.831	0.814	0.841	0.027	0.048
49/Dry	Humid-Hazy	40	0.763	0.741	0.783	0.042	0.041
		50	0.760	0.739	0.783	0.044	0.044
		60	0.763	0.748	0.777	0.029	0.047
	Dry-Clear	40	0.728	0.710	0.755	0.045	0.047
		50	0.729	0.704	0.747	0.043	0.050
		60	0.733	0.706	0.757	0.051	0.045
	Mixed	40	0.752	0.722	0.772	0.05	0.037
		50	0.745	0.713	0.772	0.059	0.034
		60	0.751	0.725	0.766	0.041	0.048

2.8.5 Discussion

Looking at the boxplot reported in Figs. 2.14-2.19, it is possible to observe that, when only one of the considered uncertainty sources is considered, the median values referring to the same leaf state and in the same atmospheric conditions are distributed around similar values. On the contrary, the median values referring to the same leaf state show a significant change when the atmospheric conditions change. This demonstrates that the atmospheric conditions introduce a bias in the NDVI measurements [4]. In PA applications, it is often important to classify the state of the crop. In this research, for each considered uncertainty source, after having determined the distribution of the NDVI values, its effect on a possible classification has been evaluated. This helps anticipate the accuracy of a classifier working on the measurements affected by uncertainty, according to the proposed workflow [4]. The classification must consider the bias introduced by

the atmospheric conditions, provided that they are stable throughout the survey. Therefore, the threshold for the classification should be defined depending on the atmospheric conditions [4]. The bias introduced by the atmospheric effects could be corrected either by identifying the model of the atmospheric transmission or using a radiometric compensation [127]. This correction is needed when the analysis is carried out on data acquired in different weather and light conditions, such as in the case of multi-temporal comparison [128], or when parts of the field are occluded by clouds or shadows [129, 91]. The atmospheric correction allows for minimizing the bias and therefore the median values of the samples, even when they are obtained in different environmental conditions. This will allow a classifier threshold to be set independently on the atmospheric conditions [4]. Several methods can be used to compensate for atmospheric effects. The DOS method identifies regions within an image with minimal reflectance, typically shadowed areas [91] or water bodies, and subtracts their radiance values to diminish cloud and atmospheric contributions. Advanced radiative transfer models, exemplified by MODerate resolution atmospheric TRANsmission (MODTRAN) [130], facilitate precise correction by simulating the complex interactions of electromagnetic radiation with atmospheric components. Additionally, reference targets strategically positioned in the scene, such as Lambertian sheets [131], and empirical line compensation methodologies establish correlations between sensor readings and ground-truth reflectance values, enabling accurate adjustment of sensor data [132, 133]. Spectral matching techniques further refine calibration efforts by ensuring consistency across different sensors [133, 4]. Even though using radiometric compensation may mitigate the variation of solar irradiance, it has some limitations. Firstly, some radiometric compensation methods are not cost-effective for UAV applications, such as the physical-based methods [55] which require the use of several sensors to estimate the atmospheric conditions. Secondly, the empirical linear methods assume a linear behavior of the multispectral camera sensors, which is not always valid [132], and usually, the compensation is performed once during a flight mission with reference targets, thus they are not able to follow possible changes of the atmospheric conditions [132, 4].

2.9 Extending the Workflow with a Radiometric Compensation Step to Mitigate the Effect of Atmospheric Conditions on NDVI Measurement

Radiometry, a key aspect of analyzing optical sensor data, involves the measurement of electromagnetic radiation across various wavelengths. In PA, UAVs and other platforms, whether at high or low altitudes, capture the solar radiation reflected from the Earth's

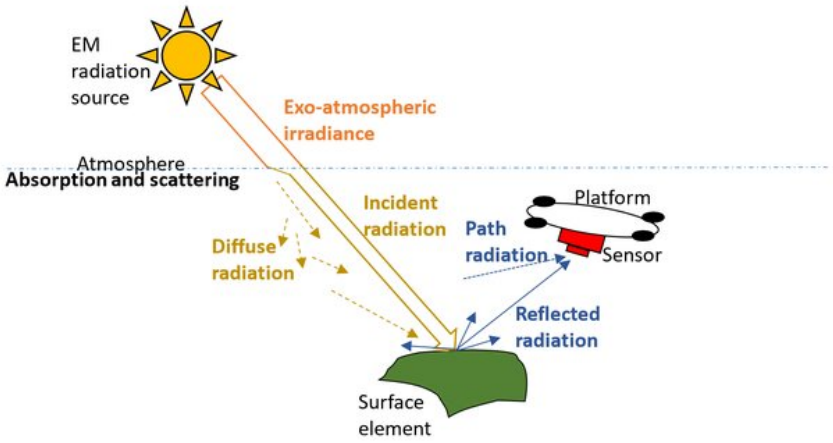

FIGURE 2.20: Basic radiance diagram for an optical sensor on a low-altitude platform [9].

surface. However, this radiation is modified along its path by processes such as absorption, scattering, and reflection before it reaches the sensor. Fig. 2.20 provides a visual representation of how incident solar radiation interacts with atmospheric and surface elements before being recorded by the optical sensor [9]. As a result, the recorded DN values do not directly reflect the surface's true radiance due to factors including sensor characteristics, camera settings, vignetting, solar angle, and atmospheric conditions like fog or aerosols. To approximately correct these variations, radiometric compensation is essential. Radiometric compensation refers to the process of correcting or adjusting images or measurements to account for variations in lighting, sensor characteristics, or environmental factors, ensuring that the observed radiometric values accurately represent the true properties of the scene or object being imaged. This process is crucial in scenarios where consistent radiometric information is needed across different images or over time, such as in Augmented Reality (AR), computer vision, or remote sensing. Radiometric compensation is conducted before any further image processing to maintain data integrity. One key aspect of radiometric compensation is **illumination compensation**, which addresses variability in lighting conditions that can cause differences in the perceived brightness and color of images. This compensation often relies on reflectance models that adjust radiance values based on the lighting conditions at the time of image capture. Another critical component is the correction of **sensor characteristics**, such as sensor non-uniformity, which can lead to inconsistencies in the captured image due to pixel-to-pixel variations. Additionally, **vignetting correction** is performed to counteract the reduction in image brightness towards the edges caused by optical system

limitations. **Temporal compensation** is also essential, especially in applications like remote sensing, where the radiometric properties of the scene may change over time due to factors like weather, solar angle, or sensor aging. This type of compensation ensures that the radiometric properties remain consistent across a sequence of images, maintaining image quality over time. Lastly, **geometric compensation** accounts for variations in viewing geometry, ensuring accurate radiometric values regardless of the angle or perspective from which the image is captured. To perform radiometric correction, the following fundamental steps are required.

1. **Sensor Correction**:
   - Determination of Sensor Response: The sensor's response to incident radiance is characterized, often under controlled laboratory conditions. This characterization involves quantifying the sensor's spectral sensitivity across different wavelengths, which is fundamental for accurate radiometric measurements.
   - Non-Uniformity Correction: Correction procedures include correcting for pixel-to-pixel variations in sensor array responses, which may arise due to manufacturing inconsistencies or aging of the sensor components.

2. **Dark Signal Correction**: Every sensor inherently records a baseline signal, known as the dark current or bias, even in the absence of incident radiation. This baseline must be subtracted from the raw data to isolate the true radiometric signal corresponding to the observed scene.

3. **Gain and Offset Correction**: The relationship between the recorded DN values and the incident radiance is typically modeled as a linear function characterized by a gain (slope) and an offset (intercept). Radiometric correction involves determining these parameters to convert the DNs into radiance units accurately.

4. **Atmospheric Correction**: The atmosphere introduces various distortions to the radiative signal due to scattering, absorption, and emission processes. Accurate radiometric correction requires correcting these atmospheric effects, which may be achieved using atmospheric radiative transfer models or empirical ground-based measurements.

5. **Conversion to Physical Quantities**: The corrected DNs are converted into radiometric units such as radiance ($\mathrm{W \cdot m^{-2} \cdot sr^{-1} \cdot nm^{-1}}$) or reflectance (dimensionless ratio of reflected to incident radiation). This conversion enables the interpretation of the data in physically meaningful terms.

6. **Validation**: The accuracy of the corrected radiometric data is validated through comparison with ground-truth measurements or by using well-characterized reference targets. This step is crucial for ensuring that the data meets the required standards for scientific analysis.

2.9.1 Reflectance Target, Lambertian Surface

To obtain a ground truth measurement for compensating the camera of a UAV, a reference target is commonly used. A reflectance target is a surface or object with known reflectance properties. These targets are designed to have stable and uniform reflectance across different wavelengths, making them ideal for compensating and validating the radiometric response of imaging systems. Reflectance targets can be Lambertian or nearly Lambertian, meaning they reflect light diffusely and uniformly in all directions. A Lambertian surface is a theoretical concept. This ideal surface is named after Johann Heinrich Lambert, who first described the concept in the 18th century. The Lambertian surface model is a crucial concept in radiometry and remote sensing, serving as a baseline for accurate radiometric compensation, understanding, and interpreting the behavior of real-world surfaces in the context of light reflection and measurement. The characteristics of a Lambertian surface are as follows:

1. **Uniform Reflection**: A Lambertian surface reflects incoming radiation equally in all directions. This means that the intensity of the reflected radiation is consistent regardless of the angle from which it is observed, Fig. 2.21 [10].

2. **Diffuse Reflection**: Unlike specular surfaces that reflect light in a specific direction (like a mirror), Lambertian surfaces exhibit diffuse reflection. The reflected light is scattered uniformly over a hemisphere, Fig. 2.21 [10].

3. **Lambert's Cosine Law**: The radiance (R) of a Lambertian surface is proportional to the incident irradiance (L) and is given by Lambert's cosine law:

$$R = \frac{L \cdot \cos(\theta)}{\pi}$$

   where θ is the angle of incidence, and π normalizes the reflection over the hemisphere.

4. **Idealization**: True Lambertian surfaces do not exist in nature, but many real-world surfaces approximate this idealized model. Examples include matte paints and certain rough, non-metallic surfaces.

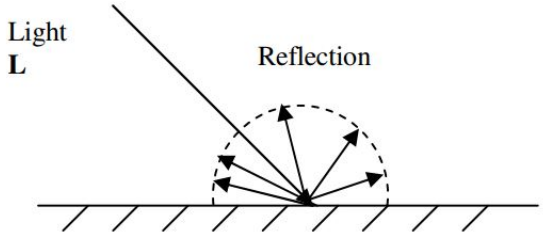

FIGURE 2.21: Uniform and diffuse reflection on a Lambertian surface [10].

5. **Applications**: Lambertian surfaces are used as reference models in radiometric compensation and interpretation of remote sensing data. They provide a standard for comparing the reflectance characteristics of different materials and help in correcting for variations caused by real-world surface properties.

6. **Radiometric Compensation**: In remote sensing, understanding Lambertian reflectance helps in radiometric compensating sensors and correcting data to ensure accurate measurement of surface properties. By comparing observed data with the Lambertian model, scientists can adjust for the effects of non-ideal surfaces and atmospheric conditions.

7. **Practical Examples**: Although perfect Lambertian surfaces do not exist, materials like matte white paint or certain types of soil can closely approximate Lambertian reflectance.

2.9.2 Applying Atmospheric Radiometric Compensation to the NDVI Measurement

To address the challenge posed by variability in the environmental and lighting conditions under which each image is captured, a standardized procedure is essential for systematic radiometric compensation to generate multispectral images with unit reflectance. This process is crucial for the accurate calculation of VIs. This study focuses on implementing a series of radiometric compensation models for multispectral images obtained under differing weather and illumination scenarios. The procedure begins by modifying the spectral reflectance by using a single Lambertian black foil and then progresses to modeling multiple points (six points) on Permaflect sheets with different reflectance percentages.

2.9.2.1 Radiometric Compensation by Using a Single Lambertian Black Foil for UAV Multispectral Imaging

In this analysis, a radiometric compensation model is developed using a Lambertian black foil spectral reflectance curve obtained from the datasheet, which is available at [11]. The spectral range of the sheet's reflectance is from 100 nm to 1400 nm, as depicted in Fig. 2.22. Then, using the MATLAB tool, the red channel of Fig. 2.22 is selected, and a mask is applied, as illustrated in Fig. 2.23. The best-fitted curve obtained from the linear interpolation of the spectral reflectance in Fig. 2.23 is evaluated, and its R and NIR bands are separated as shown in Fig. 2.24. Following the compensated curve derived from the red band, as shown in Fig. 2.24b, it is multiplied element-wise by a curve that incorporates solar irradiance, atmospheric humidity conditions, and fresh leaf reflection, as described in subsection 2.8.1.4. The result of the radiometric correction on the fresh vegetation in R band is evaluated and shown in Fig. 2.25. It is important to mention that, for an accurate compensating model, it is required to use multiple reference Lambertian sheets, which are used and described in detail in the following subsection.

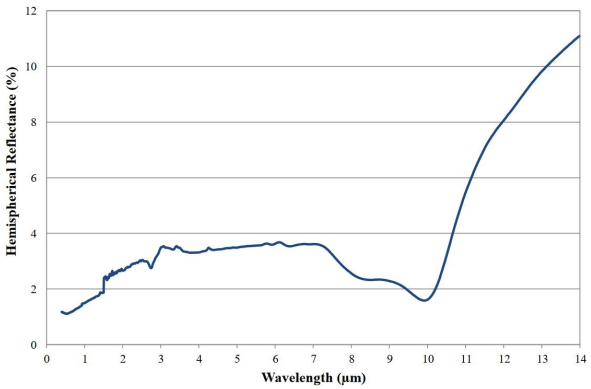

FIGURE 2.22: Lambertian black foil spectral reflectance curve selected from the datasheet [11].

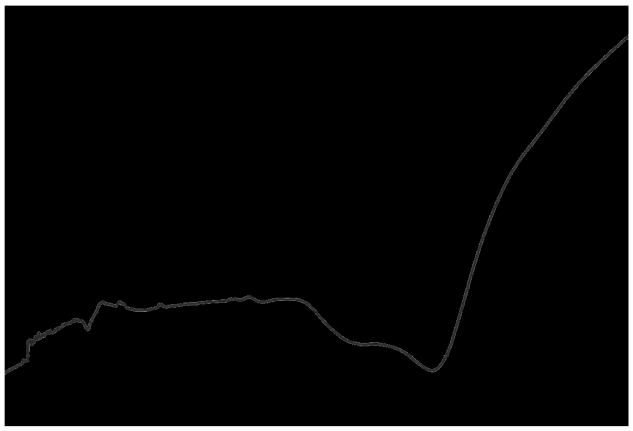

FIGURE 2.23: Red channel selection and mask application on the Lambertian black foil reflectance curve of Fig. 2.22.

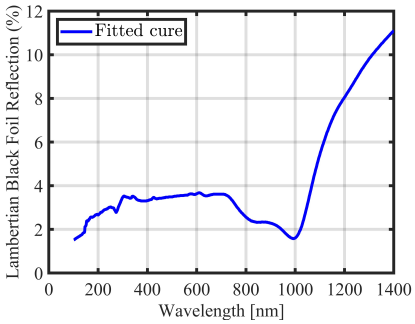

(A) Wavelength 100 - 1400 nm

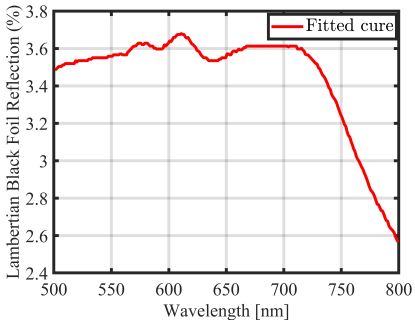

(B) Fitted curve in R band

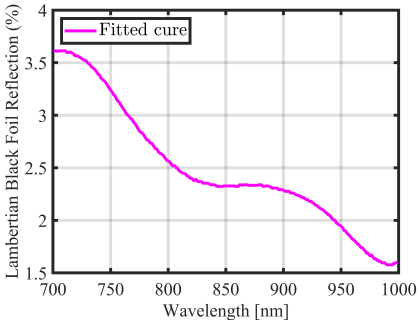

(C) Fitted curve in NIR band

FIGURE 2.24: The best-fitted curve obtained from Linear Interpolation of the spectral reflectance curve of Fig. 2.23 and is depicted within the wavelength range of (a) 100 nm to 1400 nm, (b) the R band, and (c) the NIR band.

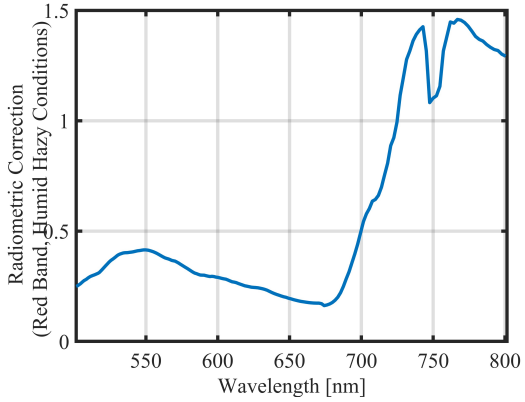

FIGURE 2.25: Radiometric correction was applied to the fresh vegetation reflection captured by the camera, taking into account the humid, hazy atmospheric conditions in the red band as well as the solar irradiance as incident light.

2.9.2.2 Radiometric Compensation by Using Multipel Points Diffuse Reflectance Coatings for UAV Multispectral Imaging

Diffuse reflectance coatings, like Spectraflect or Permaflect, are used on radiometric reference targets to provide a consistent and highly reflective surface. This ensures the sensor readings are accurate across the different wavelengths, including visible, NIR, and sometimes Ultraviolet (UV) bands. In UAV operations, radiometric reference targets and other reflective surfaces may be exposed to harsh environmental conditions. The ideal coatings should be non-specular, durable, highly reflective, and consistent across a broad range of wavelengths. Labsphere offers three specialized coatings—Spectraflect®, Permaflect®, and Infragold®—each designed for different environments and applications [5].

- **Spectraflect**: A barium sulfate coating ideal for UV-VIS-NIR range (300 to 2400 nm), offering over 98 % reflectance when applied thickly. It's thermally stable up to 160°C but not suitable for very humid conditions [5].
- **Permaflect**: A durable, water-resistant coating designed for harsh environments, effective in the visible to NIR range (350 to 1200 nm). It's stable up to 100°C and suitable for high humidity, but not recommended for UV applications [5].
- **Infragold**: A diffuse, electrochemically plated gold coating with high reflectance from 0.7 to 20 µm. It offers vacuum stability, no outgassing, and a laser damage threshold of 19.3 J cm^{-2} at 10.6 µm. Reflectance exceeds 94 % above 1 µm, with

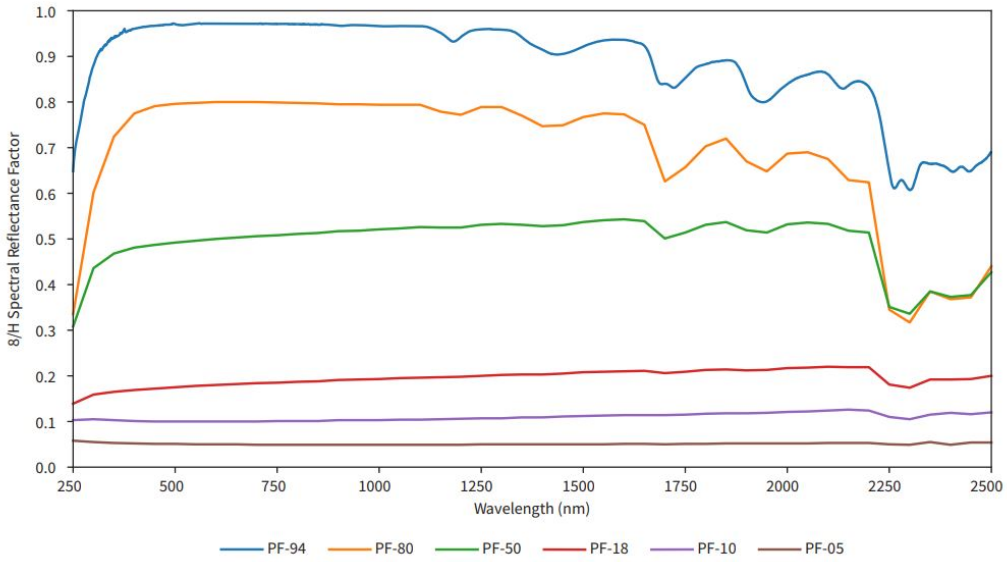

FIGURE 2.26: Typical 8 /H Reflectance Factors of Permaflect Sheets. The reflectance factors for various Permaflect sheets are as follows: PF-94 (94 % reflectance), PF-80 (80 % reflectance), PF-50 (50 % reflectance), PF-18 (18 % reflectance), PF-10 (10 % reflectance), and PF-5 (5 % reflectance). These sheets represent a range of reflectance values from very high to very low, used for calibrating and evaluating camera sensor performance across different lighting and surface conditions [5].

data traceable to National Institute of Standards and Technology (NIST). Commonly used in NIR-MIR applications like integrating spheres and space equipment, it can be applied to metals like aluminum, nickel, and steel.

Each coating is applied by spraying onto a prepared surface, with Spectraflect being ideal for optical components, and Permaflect for more demanding environments. This study focuses on the radiometric compensation of camera sensors using Permaflect sheets, which are durable, water-resistant, and maintain high reflectance in challenging environments. Permaflect (PF) sheets with varied reflectance levels—5 %, 10 %, 18 %, 50 %, 80 %, and 94 %—are employed to ensure comprehensive radiometric compensation across a range of lighting and surface conditions. These sheets, representing a wide spectrum of reflectance values as shown in Fig. 2.26, facilitate the evaluation and refinement of sensor accuracy in diverse reflective scenarios. As illustrated in Fig. 2.26, the 8°/H reflectance factor is a standardized measurement technique in which light is incident at an 8-degree angle relative to the surface normal, and the reflected light is measured hemispherically,

capturing reflections from all directions. This method offers a consistent basis for evaluating the influence of varying reflectance levels on sensor performance. The details of the reflectance percentages are described as follows:

- **Low Reflectance (5 % and 10 %)**:
  - 5 % **Reflectance**: This sheet simulates extremely low reflectance, useful for modeling sensor behavior under very dark or low-light conditions. It assesses the sensor's capability to accurately capture and measure minimal light reflections, which is critical for evaluating performance in shadowy or low-contrast environments.
  - 10 % **Reflectance**: Slightly higher than the 5 % level, this sheet provides insights into sensor handling of surfaces with marginally higher reflectance. It aids in fine-tuning sensor radiometric compensation for improved accuracy in conditions with limited light reflection but brighter than the lowest reflectance scenarios.

- **Moderate Reflectance (18 % and 50 %)**:
  - 18 % **Reflectance**: Commonly used as a standard radiometric compensation point, this sheet reflects typical gray card levels. It is instrumental in modeling sensor performance under balanced lighting conditions and offers a reference for average reflectance scenarios prevalent in everyday environments.
  - 50 % **Reflectance**: Representing a mid-range reflectance, this sheet is valuable for simulating standard conditions, ensuring accurate sensor radiometric compensation for surfaces with moderate reflectance. It helps assess sensor performance under typical lighting conditions and adjusts for common environmental brightness.

- **High Reflectance (80 % and 94 %)**:
  - 80 % **Reflectance**: This high reflectance level evaluates how the sensor performs with bright or reflective surfaces. It is crucial for understanding sensor behavior under high-intensity light conditions that may cause reflections and glare.
  - 94 % **Reflectance**: Near the maximum reflectance level, this sheet tests the sensor's capability to handle highly reflective surfaces. It models sensor performance in extremely bright environments, ensuring accuracy and minimizing distortions from intense light reflections.

Table 2.10, derived from the available datasheet [5], provides a comprehensive overview of the reflectance characteristics of various Permaflect sheets across different wavelengths from 250 to 2500 nm. Specifically, it details the reflectance values for PF-94 (with 94 % reflectance), PF-80 (with 80 % reflectance), PF-50 (with 50 % reflectance), PF-18 (with 18 % reflectance), PF-10 (with 10 % reflectance), and PF-5 (with 5 % reflectance). This table shows the reflective properties of the sheets at different spectral intervals.

TABLE 2.10: The detailed reflectance for various Permaflect sheets, PF-94 (94 % reflectance), PF-80 (80 % reflectance), PF-50 (50 % reflectance), PF-18 (18 % reflectance), PF-10 (10 % reflectance), and PF-5 (5 % reflectance) for separate wavelengths is derived from [5].

Wavelength	**Typical 8/H Reflectance Factor**					
(nm)	**5%**	**10%**	**18%**	**50%**	**80%**	**94%**
250	0.05	0.1	0.13	0.3	0.33	0.63
300	0.05	0.1	0.15	0.43	0.6	0.88
350	0.05	0.1	0.16	0.46	0.72	0.94
400	0.05	0.1	0.16	0.48	0.77	0.96
450	0.05	0.1	0.17	0.48	0.79	0.97
500	0.05	0.1	0.17	0.49	0.79	0.97
550	0.05	0.1	0.17	0.49	0.79	0.97
600	0.05	0.1	0.18	0.5	0.8	0.97
650	0.05	0.1	0.18	0.5	0.8	0.97
700	0.04	0.1	0.18	0.5	0.8	0.97
750	0.04	0.1	0.18	0.5	0.79	0.97
800	0.04	0.1	0.18	0.51	0.79	0.97
850	0.04	0.1	0.18	0.51	0.79	0.97
900	0.04	0.1	0.19	0.51	0.79	0.97
950	0.04	0.1	0.19	0.51	0.79	0.97
1000	0.04	0.1	0.19	0.52	0.79	0.96
1050	0.04	0.1	0.19	0.52	0.79	0.96
1100	0.04	0.1	0.19	0.52	0.79	0.96
1150	0.04	0.1	0.19	0.52	0.77	0.95
1200	0.04	0.1	0.19	0.52	0.77	0.94
1250	0.05	0.1	0.2	0.53	0.78	0.96
1300	0.05	0.1	0.2	0.53	0.78	0.96
1350	0.05	0.1	0.2	0.53	0.77	0.94
1400	0.05	0.1	0.2	0.52	0.74	0.91
1450	0.05	0.11	0.2	0.53	0.74	0.9
1500	0.05	0.11	0.2	0.53	0.76	0.92
... ..	..	..	..	..	..	..

2.9.2.3 Results

The workflow mentioned in Section 2.8 is completed by adding the radiometric compensation step before evaluating NDVI as shown in Fig. 2.27. To evaluate the impact

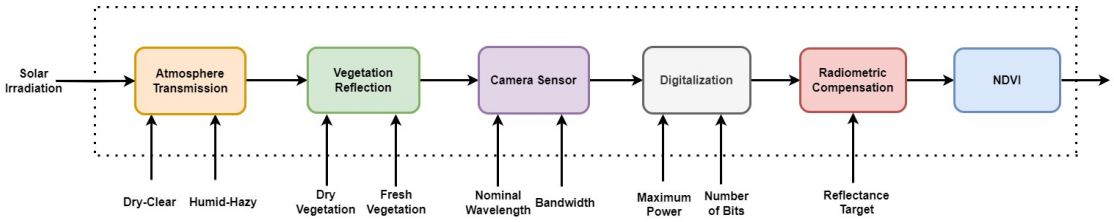

FIGURE 2.27: The proposed workflow for the NDVI evaluation incorporates the modeling of solar irradiation and atmospheric transmission under various conditions (including dry–clear and humid–hazy scenarios), vegetation reflection corresponding to both dry and fresh leaf states, as well as the performance of the camera sensor, digitization, and radiometric compensation steps.

of various sources of uncertainty on NDVI measurements, MCS is utilized. To develop the radiometric compensation model, Permaflect sheet reflectance data within the range of 500 nm to 800 nm is selected for the R band, and within the range of 700 nm to 1000 nm for the NIR band, as detailed in Table 2.10. The best-fitting curves for the selected spectral bands at distinct reflection percentages were obtained using a linear interpolation function, implemented through MATLAB software tools. Consequently, for each reflection percentage listed in Table 2.10, two curves—one for the R band and one for the NIR band—are generated. After that, the derived mathematical models and solar irradiance in Sections 2.8.1.1 are multiplied element-wise for both the R and NIR bands. The area under each curve is evaluated to model the sheet's reflectance, where solar irradiance acts as the incident light source. Then these models are multiplied element-wise with atmospheric conditions models as discussed in Section 2.8.1.2, the study achieves a comprehensive understanding of the effects of atmospheric conditions on solar irradiance transmission under varying scenarios, including dry-clear and humid-hazy conditions, on Permaflect sheet reflectance. Subsequently, by considering the use of the DJI P4-multispectral camera, as detailed in Subsection 2.6.2, the quantization and digitalization steps described in Section 2.8.1.5 are applied to the data. This process models the camera's behavior in capturing data from the Permaflect sheet in a real scenario and then converting the reflected light into a digital value. Then, the area under the curve, representing the energy reflected from the Permaflect sheet in a real scenario, is evaluated and illustrated in Figs 2.28, 4.34, 2.30, and 2.31. These results are presented separately for both the R and NIR bands and under the conditions of dry-clear and humid-hazy atmospheres.

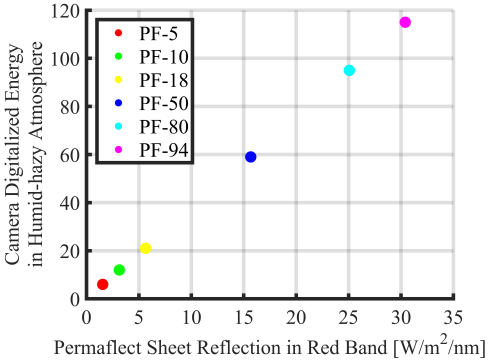

FIGURE 2.28: The energy reflected by the Permaflect Sheet in the R band relative to the energy captured by the camera in a humid-hazy atmosphere.

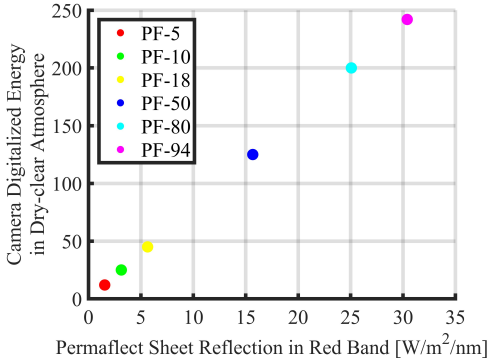

FIGURE 2.29: The energy reflected by the Permaflect Sheet in the R band relative to the energy captured by the camera in a dry-clear atmosphere.

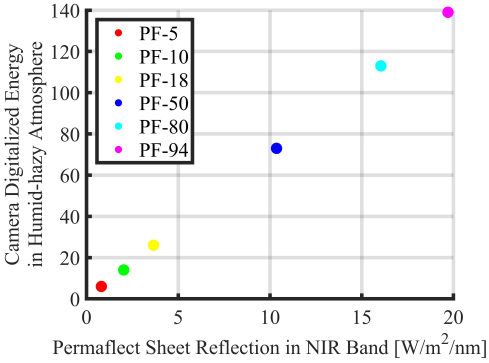

FIGURE 2.30: The energy reflected by the Permaflect Sheet in the NIR band relative to the energy captured by the camera in a humid-hazy atmosphere.

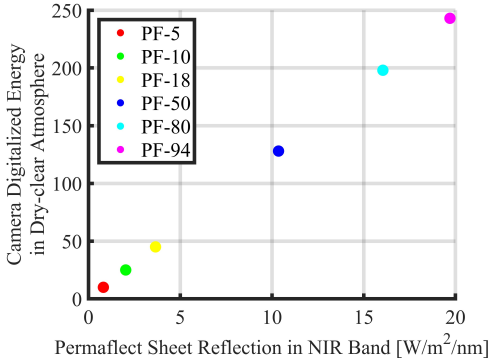

FIGURE 2.31: The energy reflected by the Permaflect Sheet in the NIR band relative to the energy captured by the camera in a dry-clear atmosphere.

FIGURE 2.32: Analysis of Permaflect sheet reflectance under incident solar irradiance, considering atmospheric transmittance in dry-clear and humid-hazy conditions, and subsequent energy capture and conversion to DNs by a camera sensor.

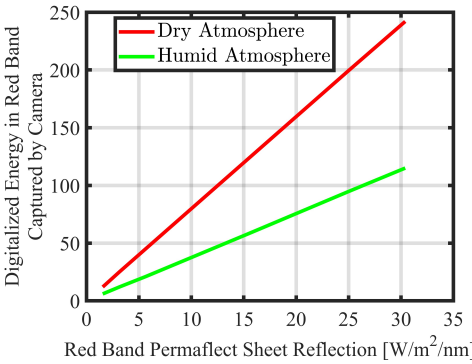

FIGURE 2.33: The energy reflectance of Permaflect Sheet in the R band relative to camera-recorded radiant energy

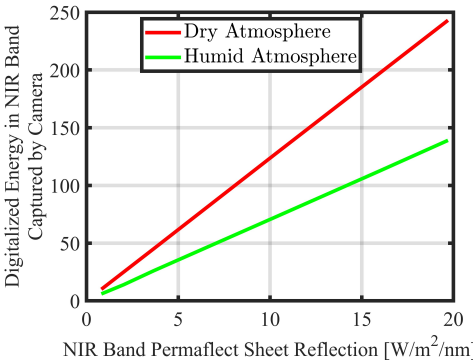

FIGURE 2.34: The energy reflectance of Permaflect Sheet in the NIR band relative to camera-recorded radiant energy

FIGURE 2.35: Linear interpolation of MATLAB functions to generate the optimal fitted curve for scattered data points in the R and NIR bands of points in Fig. 2.32, analyzed separately under both dry-clear and humid-hazy atmospheric conditions.

To develop a comprehensive radiometric compensation model, multiple Permaflect Sheets with reflectances of 5 %, 10 %, 18 %, 50 %, 80 %, 94 % were considered. Linear interpolation using MATLAB functions was employed to generate the optimal fitted curve for the scattered data points, as illustrated in Figs. 2.28, 4.34, 2.30, and 2.31. Subsequently, a radiometric compensation curve is derived based on the Permaflect Sheets' reflection when solar irradiance is incident light, in relation to the digitized Permaflect Sheets' reflected energy, while solar irradiance passes through the atmosphere for the R and NIR bands separately, under both dry–clear and humid–hazy atmospheric conditions. These radiometric compensation curves are evaluated and presented in Figs. 2.33 and 2.34, which are ready to use in the workflow shown in Fig. 2.27. To investigate the impact of atmospheric conditions and to perform radiometric compensation on the evaluation of NDVI measurements as proposed in Section 2.8, a MCS is conducted in five parts. The five parts are as follows:

A) NDVI uncertainty versus nominal wavelength

B) NDVI uncertainty versus standard deviation of solar irradiance

C) NDVI uncertainty versus camera SNR

D) NDVI uncertainty versus leaf state

E) NDVI uncertainty versus all uncertainty sources

In all five parts, to apply radiometric compensation based on the workflow shown in Fig. 2.27, the computed energy in the R and NIR bands is compared to the radiometric compensation curve in Fig. 2.35 before evaluating the NDVI values. The computed values are then replaced with the energy measured from the compensated curves at the corresponding points.

A) NDVI Uncertainty vs Nominal Wavelength

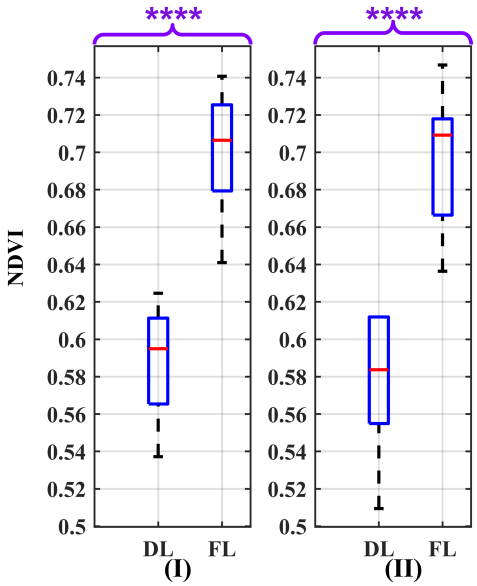

FIGURE 2.36: Box plots illustrating the effect of nominal wavelength as a source of uncertainty on NDVI values for atmosphere conditions: (I) Dry-clear, and (II) Humid-hazy, considering both DL and FL.

TABLE 2.11: Statistical parameters MED, first and third Quartiles (Q1, Q3), IQR and distance of first quartiles of fresh leaf and third quartiles of dry leaf when the effect of nominal wavelength as an uncertainty source on NDVI values for different LS, and ATMC is evaluated.

LS	ATMC	MED	Q1	Q3	IQR	$Q1_F - Q3_D$
Fresh	Humid-Hazy	0.710	0.664	0.715	0.051	0.049
	Dry-Clear	0.709	0.680	0.729	0.049	0.062
Dry	Humid-Hazy	0.582	0.551	0.615	0.064	0.049
	Dry-Clear	0.598	0.563	0.615	0.052	0.062

The method for evaluating NDVI values while considering variations in the nominal wavelength of the camera as a source of uncertainty follows the same approach described in Subsection 2.8.3.1. Additionally, the radiometric compensation is applied as previously outlined in this section. The results of this analysis are presented in Fig. 2.36, with detailed data provided in Table 2.11. When comparing DL conditions under dry-clear atmosphere (Fig. 2.36 (I)) with those under humid-hazy atmosphere (Fig. 2.36 (II)), the results indicate no significant difference; also, this is the same for FL. This shows that the radiometric compensation process effectively compensates for the variations in atmospheric conditions. The slight variation observed is attributed to the uncertainty in the nominal wavelength, which is negligible.

B) NDVI Uncertainty vs Solar Irradiance Standard Deviation

The procedure for evaluating NDVI uncertainty, considering the standard deviation of solar irradiance, follows the same approach outlined in Subsection 2.8.3.2, with radiometric compensation applied as described in this section. The analysis results are depicted in Fig. 2.37, with comprehensive data detailed in Table 2.12. A comparison between DL conditions under a dry-clear atmosphere (Fig. 2.37 (I)) and a humid-hazy atmosphere (Fig. 2.37 (II)) shows no statistically significant differences, a trend similarly observed for FL. This outcome suggests that the radiometric compensation process effectively mitigates the influence of varying atmospheric conditions. The minor variations observed are attributed to the uncertainty in the solar irradiance standard deviation, which is considered negligible.

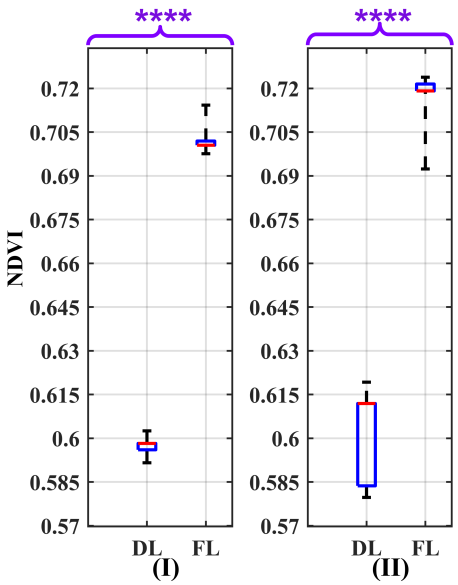

FIGURE 2.37: Box plots illustrating the effect of the variability in solar irradiance measurement as a source of uncertainty on NDVI values for atmosphere conditions: (I) Dry-clear, and (II) Humid-hazy, considering both DL and FL.

TABLE 2.12: Statistical parameters MED, first and third Quartiles (Q1, Q3), IQR and distance of first quartiles of fresh leaf and third quartiles of dry leaf when the effect of solar irradiance standard deviation as an uncertainty source on NDVI values for different LS, and ATMC is evaluated.

LS	ATMC	MED	Q1	Q3	IQR	$Q1_F - Q3_D$
Fresh	Humid-Hazy	0.719	0.719	0.722	0.003	0.107
	Dry-Clear	0.701	0.701	0.702	0.001	0.103
Dry	Humid-Hazy	0.612	0.584	0.612	0.028	0.107
	Dry-Clear	0.598	0.596	0.598	0.002	0.103

C) NDVI Uncertainty vs Leave State

The procedure for evaluating NDVI uncertainty, considering variations in NDVI values, follows the methodology outlined in Subsection 2.8.3.4, with radiometric compensation applied as detailed at the beginning of this section. The analysis results are presented in Fig. 2.38, with corresponding data provided in Table 2.13. A comparison of

DL conditions between a dry-clear atmosphere (Fig. 2.38 (I)) and a humid-hazy atmosphere (Fig. 2.38 (II)) shows no significant differences, a trend also observed for FL. This indicates that the radiometric compensation process successfully mitigates atmospheric effects. The minor observed variations are likely attributable to uncertainty in NDVI values, which is deemed negligible.

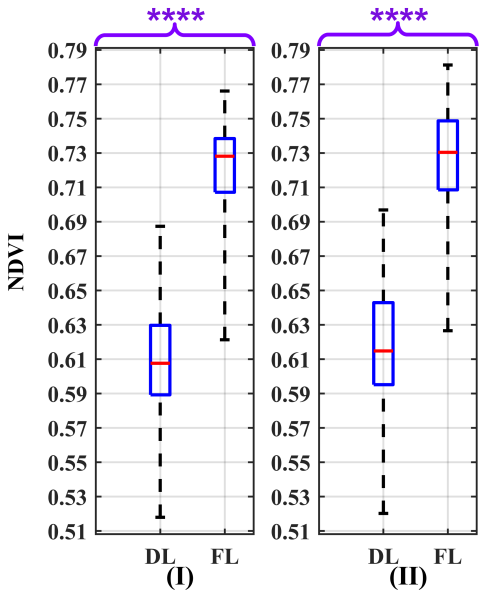

FIGURE 2.38: Box plots illustrating the effect of the variability of NDVI values as a source of uncertainty on NDVI values for atmosphere conditions: (I) Dry-clear, and (II) Humid-hazy, considering both DL and FL.

TABLE 2.13: Statistical parameters MED, first and third Quartiles (Q1, Q3), IQR and distance of first quartiles of fresh leaf and third quartiles of dry leaf when the effect of the variability of NDVI values as an uncertainty source on NDVI values for different LS, and ATMC is evaluated.

LS	ATMC	MED	Q1	Q3	IQR	$Q1_F - Q3_D$
Fresh	Humid-Hazy	0.730	0.709	0.749	0.040	0.066
	Dry-Clear	0.728	0.707	0.738	0.031	0.077
Dry	Humid-Hazy	0.615	0.595	0.643	0.048	0.066
	Dry-Clear	0.608	0.589	0.630	0.041	0.077

D) NDVI Uncertainty vs Camera SNR

The procedure for evaluating NDVI uncertainty, accounting for variations in camera SNR, follows the approach described in Subsection 2.8.3.3, with radiometric compensation applied as outlined earlier in this section. The analysis outcomes are illustrated in Fig. 2.39, with a comprehensive dataset provided in Table 2.14. When comparing a dry leaf under both dry-clear and humid-hazy atmospheric conditions (ADDL, AHDL) at SNR of (I) 40 dB, (II) 50 dB, and (III) 60 dB, no significant differences were detected. A similar pattern is observed for the fresh leaf under both dry-clear and humid-hazy atmospheric conditions (ADFL, AHFL). These results suggest that the radiometric compensation procedure successfully neutralizes the impact of different atmospheric conditions. The slight variations observed are likely due to uncertainties in camera SNR, which are considered to be insignificant.

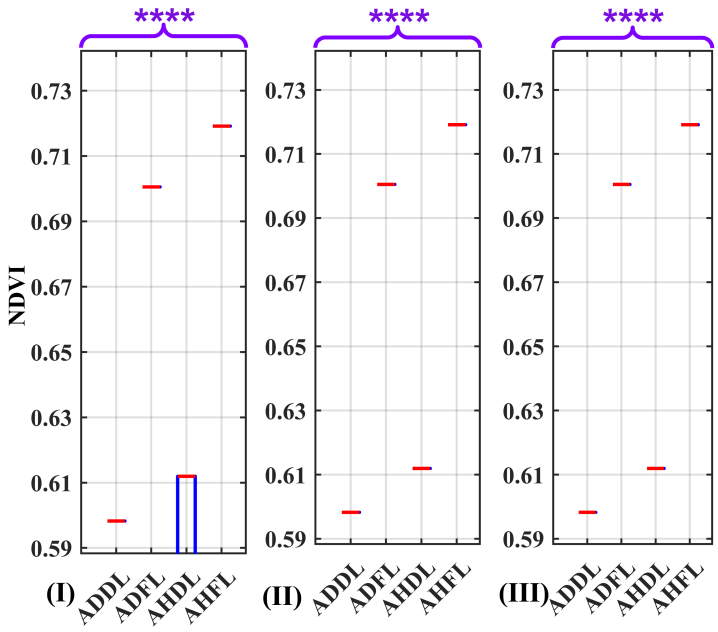

FIGURE 2.39: Box plots illustrating the influence of the camera sensor under three different SNR conditions: (I) SNR = 40 dB, (II) SNR = 50 dB, and (III) SNR = 60 dB, serving as uncertainty factors on NDVI values. The plot considers various atmospheric conditions and leaf states, including: ADDL, ADFL, AHDL, and AHFL.

TABLE 2.14: Statistical parameters MED, first and third Quartiles (Q1, Q3), IQR and distance of first quartiles of fresh leaf and third quartiles of dry leaf when the effect of camera SNR at 40 dB, 50 dB, and 60 dB as an uncertainty source on NDVI values for different LS, and ATMC is evaluated.

LS	ATMC	SNR[dB]	MED	Q1	Q3	IQR	$Q1_F - Q3_D$
Fresh	Humid-Hazy	40	0.719	0.719	0.719	0	0.107
		50	0.719	0.719	0.719	0	0.107
		60	0.719	0.719	0.719	0	0.107
	Dry-Clear	40	0.701	0.701	0.701	0	0.103
		50	0.701	0.701	0.701	0	0.103
		60	0.701	0.701	0.701	0	0.103
Dry	Humid-Hazy	40	0.612	0.584	0.612	0.028	0.107
		50	0.612	0.612	0.612	0	0.107
		60	0.612	0.612	0.612	0	0.107
	Dry-Clear	40	0.598	0.598	0.598	0	0.103
		50	0.598	0.598	0.598	0	0.103
		60	0.598	0.598	0.598	0	0.103

E) NDVI Uncertainty vs All Uncertainty Sources

The procedure for evaluating NDVI uncertainty, accounting for the combined effects of all uncertainty sources, follows the methodology outlined in Subsection 2.8.3.5, with radiometric compensation applied as described earlier in this section. The results of the analysis are shown in Fig. 2.40, with detailed data provided in Table 2.15. A comparison of a dry leaf under dry-clear and humid-hazy conditions (ADDL, AHDL) at SNR levels of (I) 40 dB, (II) 50 dB, and (III) 60 dB shows no significant differences. A similar trend is observed for a fresh leaf under the same conditions (ADFL, AHFL). These findings suggest that the radiometric compensation process successfully mitigates atmospheric variations, even when accounting for the combined effects of all uncertainty sources.

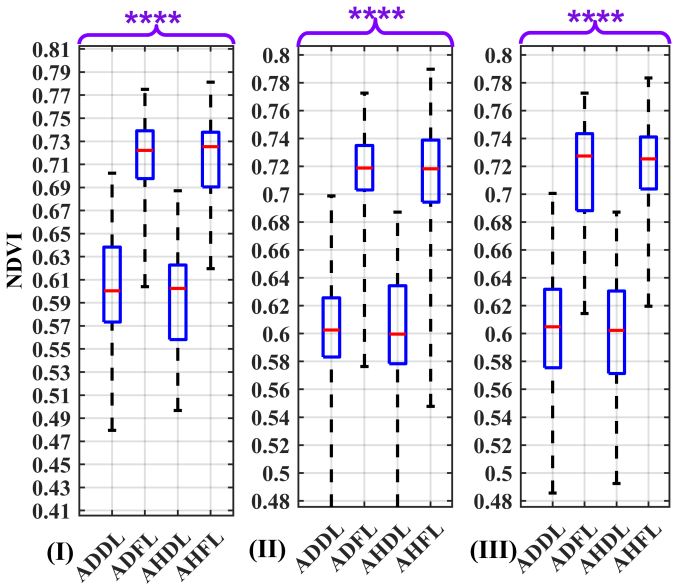

FIGURE 2.40: Box plots illustrating the effect of all uncertainty sources under three different SNR conditions: (I) SNR = 40 dB, (II) SNR = 50 dB, and (III) SNR = 60 dB, serving as uncertainty factors on NDVI values. The plot considers various atmospheric conditions and leaf states, including: ADDL, ADFL, AHDL, AHFL, AMDL, and AMFL [4].

TABLE 2.15: Statistical parameters MED, first and third Quartiles (Q1, Q3), IQR and distance of first quartiles of fresh leaf and third quartiles of the dry leaf when the effect of the combination of all uncertainty sources on NDVI values for different LS, and ATMC is evaluated.

LS	ATMC	SNR[dB]	MED	Q1	Q3	IQR	$Q1_F - Q3_D$
Fresh	Humid-Hazy	40	0.728	0.690	0.736	0.046	0.063
		50	0.720	0.689	0.740	0.051	0.052
		60	0.727	0.705	0.740	0.035	0.070
	Dry-Clear	40	0.725	0.695	0.740	0.055	0.060
		50	0.720	0.705	0.738	0.033	0.076
		60	0.723	0.680	0.742	0.062	0.045
Dry	Humid-Hazy	40	0.608	0.556	0.627	0.071	0.063
		50	0.601	0.580	0.637	0.057	0.052
		60	0.602	0.569	0.635	0.066	0.070
	Dry-Clear	40	0.605	0.570	0.640	0.060	0.055
		50	0.602	0.585	0.629	0.044	0.076
		60	0.609	0.577	0.635	0.058	0.045

2.9.3 Applying Uncertainty Sources Before Evaluating the Radiometric Compensation Curve

In subsection 2.9.2, during the evaluation of the radiometric compensation curve, the effect of uncertainty sources was not considered. However, in real-world scenarios, various uncertainty sources can influence the evaluation of the radiometric compensation curve. In this section, a combination of uncertainty sources, including variations in solar irradiance, the camera's nominal wavelength, and SNR under different atmospheric conditions (e.g., humid-hazy and clear dry environments), are taken into account. The results of these considerations are presented in Fig. 2.45.

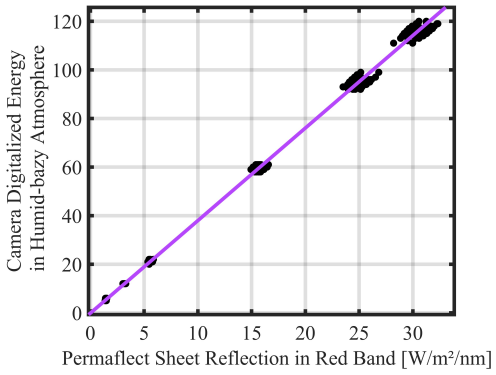

FIGURE 2.41: The energy reflected by the Permaflect Sheet in the R band relative to the energy captured by the camera in a humid-hazy atmosphere, while uncertainty sources affect the measurements.

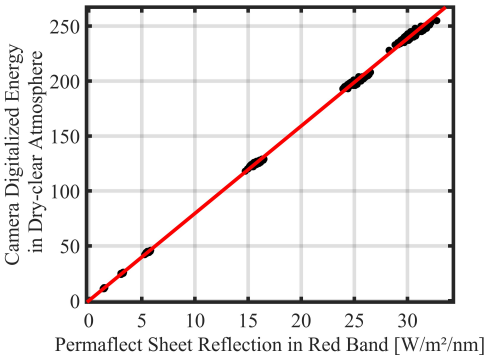

FIGURE 2.42: The energy reflected by the Permaflect Sheet in the R band relative to the energy captured by the camera in a dry-clear atmosphere while uncertainty sources affect the measurements.

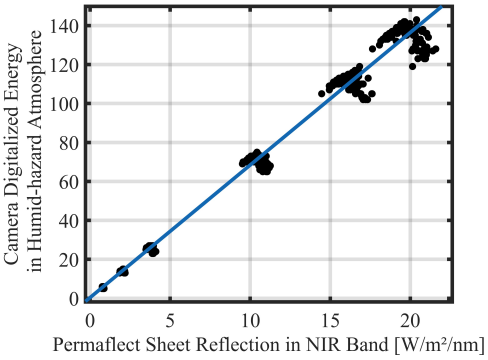

FIGURE 2.43: The energy reflected by the Permaflect Sheet in the NIR band relative to the energy captured by the camera in a humid-hazy atmosphere while uncertainty sources affect the measurements.

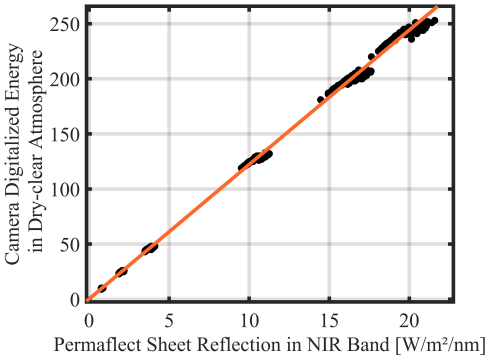

FIGURE 2.44: The energy reflected by the Permaflect Sheet in the NIR band relative to the energy captured by the camera in a dry-clear atmosphere while uncertainty sources affect the measurements.

FIGURE 2.45: An analysis of Permaflect sheet reflectance under incident solar irradiance, accounting for atmospheric transmittance in both dry-clear and humid-hazy conditions, as well as the subsequent energy capture and conversion to DNs by a camera sensor. The measurements are influenced by uncertainty sources, including variations in solar irradiance, the camera's nominal wavelength, and SNR across these atmospheric conditions.

In a humid-hazard atmospheric condition for R, while considering the effect of all uncertainty sources, the best-fitted curve with a 95% confidence level is a first-degree polynomial, as shown in Fig. 2.41. The equation for the curve is $f(x) = p_1 \cdot x + p_2$, where $p_1 = 3.810$ with a lower bound of 3.798 and an upper bound of 3.821, and $p_2 = -0.124$ with a lower bound of -0.328 and an upper bound of 0.080. The R-squared value is 0.999, and the RMSE is 1.655. Similarly, under the same atmospheric conditions for NIR, the best-fitted curve with a 95% confidence level is also a first-degree polynomial, as depicted in Fig. 2.43. In this case, $p_1 = 6.804$ with a lower bound of 6.750 and an upper bound of 6.857, and $p_2 = 0.386$ with a lower bound of -0.223 and an upper bound of 0.994. The R-squared value is 0.990, and the RMSE is 4.927. In a dry-clear atmospheric condition for R, accounting for all uncertainty sources, the best-fit curve at a 95% confidence level is a first-degree polynomial, as shown in Fig. 2.42. The equation is given by $f(x) = p_1 \cdot x + p_2$, where $p_1 = 7.955$ with a confidence interval of 7.944 to 7.947, and $p_2 = 0.028$ with a confidence range of -0.165 to 0.220. The model yields an R-squared value of 1.000 and an RMSE of 1.560. For NIR under the same atmospheric conditions, the best-fit curve at a 95% confidence level is also a first-degree polynomial, as shown in Fig. 2.44. Here, $p_1 = 12.203$ with a confidence interval between 12.173 and 12.234, and $p_2 = 0.180$ with a range of -0.167 to 0.528. The R-squared value is 0.999, and the RMSE is 2.813.

2.9.3.1 Experimental Part and Result

In this part, the process described in Section 2.9.2.3 is performed, with the key difference that uncertainty sources are considered during the evaluation of the radiometric compensation curve as shown in Fig. 2.45. The results are then analyzed for two aspects: A) NDVI uncertainty versus nominal wavelength, and B) NDVI uncertainty versus all uncertainty sources. After that, these results are compared with those presented in Section 2.8 and in the paper [4], where radiometric compensation was not applied.

A) NDVI Uncertainty vs Nominal Wavelength

To evaluate NDVI values, the approach described in Subsection 2.9.2.3 is performed, with the difference that for the step of radiometric compensation, the curve of Subsection 2.9.3 is used instead. The results of this analysis are presented in Fig. 2.46b, with detailed data provided in Table 2.16. As shown in Fig. 2.46b, by applying a threshold on NDVI value around 0.632, it is possible to distinctly differentiate between DL and FL across varying atmospheric conditions, even in the presence of this source of uncertainty. Furthermore, Fig. 2.46 shows the comparison of box plots of NDVI values that result from paper [4] or Subsection 2.8.3.1 before applying the radiometric compensation

step (a), and (b) after applying the radiometric compensation step. When comparing DL conditions under a dry-clear and humid-hazy atmosphere (ADDL and AHDL) in Fig. 2.46, it is clear that the box plots for ADDL and AHDL in panel (b) have totally overlapped with respect to those in panel (a). The results indicate that the radiometric compensation process effectively compensates for variations in atmospheric conditions. The slight variation observed is attributed to the uncertainty in the nominal wavelength, which is negligible. This result is the same for the comparison of FL states under both a dry-clear atmosphere and a humid-hazy atmosphere (ADFL and AHFL) before and after applying radiometric compensation.

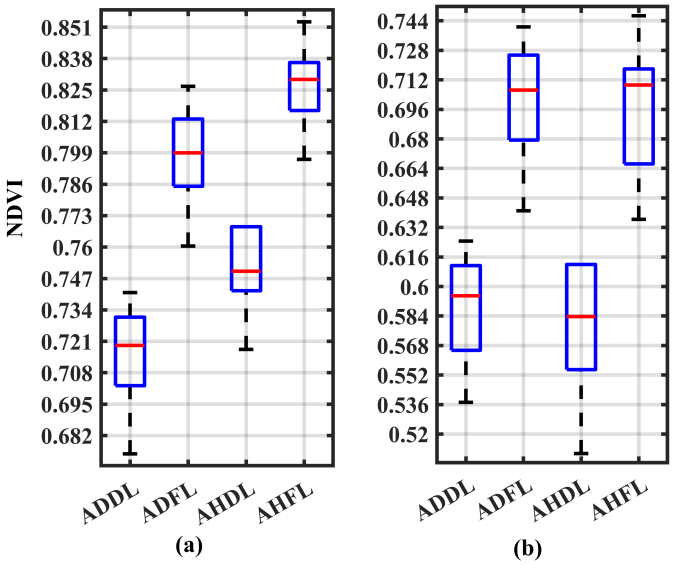

FIGURE 2.46: Box plots illustrate the effect of nominal wavelength as a source of uncertainty on NDVI values under different atmospheric conditions. The plot considers (a) results from paper [4] before applying the radiometric compensation step, and (b) after applying the radiometric compensation step in various atmospheric conditions and leaf states, including ADDL, ADFL, AHDL, AHFL, AMDL, and AMFL.

TABLE 2.16: Statistical parameters MED, first and third Quartiles (Q1, Q3), IQR and distance of first quartiles of fresh leaf and third quartiles of dry leaf when radiometric compensation curve is applied and the effect of nominal wavelength as an uncertainty source on NDVI values for different LS, and ATMC is evaluated.

LS	ATMC	MED	Q1	Q3	IQR	$Q1_F - Q3_D$
Fresh	Humid-Hazy	0.709	0.666	0.718	0.052	0.054
	Dry-Clear	0.706	0.679	0.725	0.046	0.068
Dry	Humid-Hazy	0.584	0.555	0.612	0.057	0.054
	Dry-Clear	0.595	0.565	0.611	0.046	0.068

B) NDVI Uncertainty vs All Uncertainty Sources

The procedure for evaluating NDVI uncertainty, accounting for the combined effects of all uncertainty sources including variations in solar irradiance, changing atmospheric conditions, nominal wavelength fluctuations in cameras, SNR, and variability of the NDVI within the two LS, follows the methodology outlined in Subsection 2.8.3.5 or in the paper [4], with radiometric compensation curve of Subsection 2.9.3 is applied. The results of the analysis for SNR=60 dB are shown in Fig. 2.47b, with detailed data provided in Table 2.17 for SNR levels of 40 dB, 50 dB, and 60 dB. Fig. 2.47b illustrates that setting a threshold of approximately 0.650 for NDVI values enables a clear distinction between DL and FL under diverse atmospheric conditions, even in the presence of a combination of all sources of uncertainty. Moreover, a comparison of DL conditions under dry-clear (ADDL) and humid-hazy (AHDL) atmospheres, as shown in Fig. 2.47 panels (a) and (b), reveals a complete overlapping of box plots for ADDL and AHDL in panel (b) compared to panel (a). This overlap suggests that the radiometric compensation process effectively adjusts for atmospheric variations. The minor observed variation, caused by uncertainty sources, is negligible. Similar results are observed when comparing FL conditions under both dry-clear (ADFL) and humid-hazy (AHFL) atmospheres before and after radiometric compensation. In addition, the results indicate that the inclusion of uncertainty sources in the radiometric compensation process has a measurable, though small, impact on NDVI retrieval. For dry and fresh leaves, accounting for these uncertainties results in a shift of approximately 0.050 in NDVI values compared to scenarios in which the uncertainty sources are not incorporated in the evaluation of the radiometric compensation step.

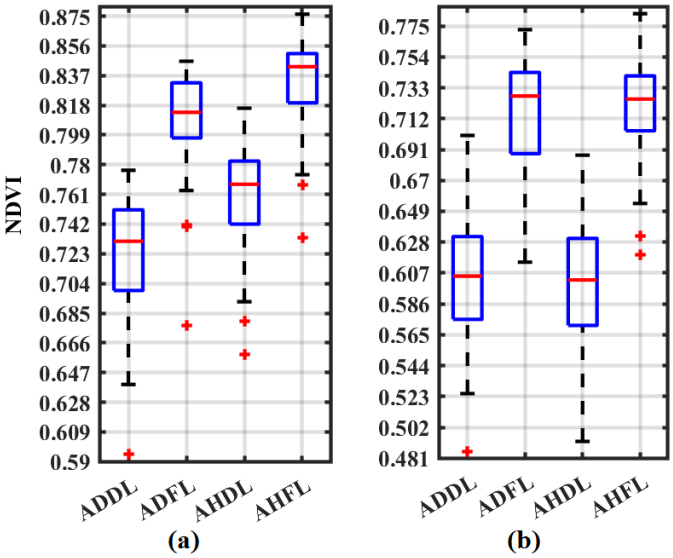

FIGURE 2.47: Box plots illustrating the effect of all uncertainty sources under SNR = 60 dB serving as uncertainty factors on NDVI values. (a) results from paper [4] before applying the radiometric compensation step, and (b) after applying the radiometric compensation step. The plot considers various atmospheric conditions and leaf states, including ADDL, ADFL, AHDL, AHFL, AMDL, and AMFL.

TABLE 2.17: Statistical parameters MED, first and third Quartiles (Q1, Q3), IQR and distance of first quartiles of fresh leaf and third quartiles of the dry leaf when the effect of the combination of all uncertainty sources on NDVI values for different LS, and ATMC is evaluated.

LS	ATMC	SNR[dB]	MED	Q1	Q3	IQR	$Q1_F - Q3_D$
Fresh	Humid-Hazy	40	0.725	0.690	0.738	0.048	0.067
		50	0.718	0.694	0.739	0.045	0.060
		60	0.725	0.704	0.741	0.037	0.073
	Dry-Clear	40	0.722	0.698	0.739	0.041	0.060
		50	0.719	0.703	0.735	0.032	0.077
		60	0.727	0.688	0.743	0.055	0.056
Dry	Humid-Hazy	40	0.602	0.558	0.623	0.065	0.067
		50	0.600	0.578	0.634	0.056	0.060
		60	0.602	0.571	0.631	0.060	0.073
	Dry-Clear	40	0.600	0.573	0.638	0.065	0.060
		50	0.603	0.583	0.626	0.043	0.077
		60	0.605	0.575	0.632	0.057	0.056

2.10 Proposed Radiometric Compensation Method

In remote sensing, the electromagnetic spectrum is crucial, especially for UAV-based multispectral and hyperspectral imaging. Atmospheric gases and aerosols alter solar irradiance before it reaches the Earth's surface, affecting reflected radiance—key for vegetation analysis. Understanding and mitigating these effects are essential for accurate data interpretation [103]. While satellites experience twice the atmospheric interference, UAVs operate at lower altitudes (100 m), where only the direct solar path to the ground is significant.

In this study, a novel radiometric compensation method is introduced, developed through two distinct phases, as illustrated in Fig. 2.48. Initially, the energy reflected from six Permaflect sheets with varying reflectance percentages is emulated, considering the sheets placed on the ground, with solar irradiance passing through the atmosphere and incident to the sheets, this workflow is shown in Fig. 2.48(a) and the result of this part is shown in (b). In the second phase, a Monte Carlo simulation is employed to statistically analyze the emulated reflected energy from the sheets and quantify the impact of uncertainty sources on their reflectance, thereby enabling the determination of their statistical distribution (Fig. 2.48(c)).

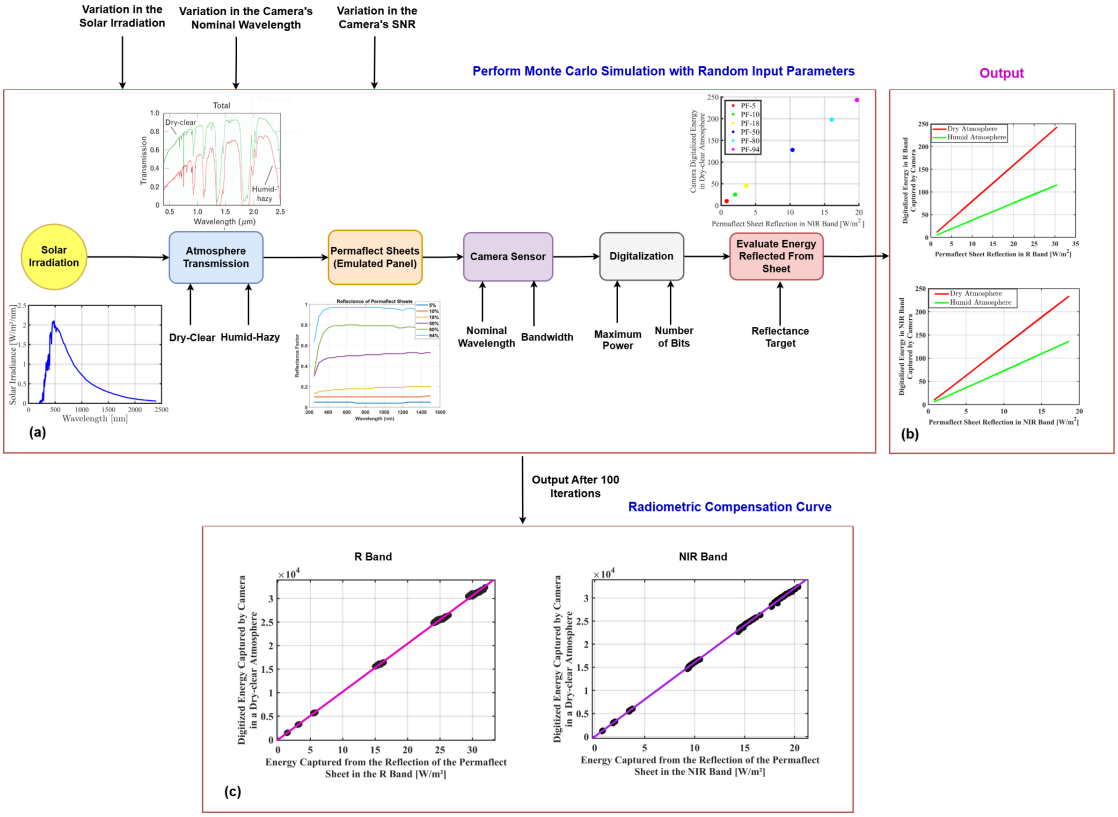

FIGURE 2.48: The proposed workflow for evaluating the radiometric compensation method includes: (a) modeling solar irradiation and atmospheric transmission under various conditions (including dry–clear and humid–hazy scenarios), emulating the reflection of reference panels based on Permaflect sheets' datasheets, and assessing the performance of the camera sensor and digitization process to model the energy reflected from the sheets, as would occur in a real-world scenario; (b) computing the initial radiometric compensation curve separately for the R and NIR bands; and (c) conducting a Monte Carlo simulation with 100 iterations to assess the impact of uncertainty sources on the evaluation in part (a), thereby generating the radiometric compensation curve while accounting for these uncertainties.

First, as shown in Fig. 2.48(a), it is necessary to model solar irradiance. The SSI dataset, measured by the SIM instrument, is publicly available [118]. The dataset includes 24-hour averaged measurements over a spectral range from 200 nm to 2400 nm, with spectral resolutions varying from 2 nm (for $wavelengths < 0.28\,\mu m$) to 45 nm (for

wavelengths $> 0.4\,\mu m$). Measurements were taken at a mean solar distance of 1 Astronomical Unit(AU) and zero relative line-of-sight velocity to the Sun (i.e., no movement), with an absolute uncertainty of approximately 0.2 %. The dataset includes information on Julian day, wavelength range, instrument mode, data version, irradiance values, associated uncertainties, and data quality metrics. For modeling solar irradiance, spectral bands within the R (500–800 nm) and NIR (700–1000 nm) wavelength ranges, each with a resolution of 45 nm, are selected from the SSI dataset, the data expressed in units of $W \cdot m^{-2} \cdot nm^{-1}$. Optimal fitting curves for these spectral bands are derived using linear interpolation, implemented with MATLAB software tools, specifically MATLAB R2024b [4].

For atmospheric transmission, the empirical method employed by [68] takes into account several factors, including gas absorption, water vapor, and scattering effects in dry-clear and humid-hazard conditions. In estimating surface reflectance, it is crucial to consider gas absorption by ozone (O_3), oxygen (O_2), methane (CH_4), and carbon dioxide (CO_2), which absorb solar radiation at specific wavelengths, thereby significantly impacting the received solar flux. Water vapor also exhibits strong absorption features, particularly at the wavelength bands 0.94 µm and 1.14 µm, complicating the retrieval of surface reflectance. Scattering by molecules is most prominent in the visible/near-infrared (VNIR) spectrum, while aerosols contribute significantly to scattering in the shortwave infrared (SWIR) due to their larger particle sizes [68]. Although aerosol absorption is generally minor compared to molecular absorption, it still plays a role in the overall scattering. Moreover, to distinguish between dry and humid atmospheric conditions, the histogram of water vapor reveals a bimodal distribution, representing two distinct conditions: the moist atmosphere, characterized by higher levels of water vapor, and the dry atmosphere, which shows lower levels of water vapor. The empirical method for atmospheric transmission, presented in [68], is used for modeling atmospheric transmission by utilizing the linear interpolation function in MATLAB, with fitting curves for the selected spectral bands in the R (500–800 nm) and NIR (700–1000 nm) ranges, with a resolution of 90 pm. The curves are expressed as the percentage of transmitted energy per nm. This model generalizes atmospheric behavior, making it applicable to any location on Earth.

By integrating solar irradiance and atmospheric transmission models, this study analyzes how varying atmospheric conditions—specifically dry-clear and humid-hazy environments—affect the transmission of solar irradiance. To capture these effects, spectral irradiance and atmospheric transmission curves are computed separately for each spectral band—R and NIR—and for each atmospheric condition [119]. These curves are sampled at 1 nm wavelength intervals, and their corresponding values are multiplied

element-wise to yield the transmitted spectral irradiance curve. This process is mathematically expressed as:

$$L_i(\lambda) = [S_{ir}(\lambda) + n_{ir}(\lambda)] \cdot [H_a(\lambda) + n_a(\lambda)] \tag{2.14}$$

where:

- $L_i(\lambda)$ is the transmitted spectral irradiance at wavelength λ, representing the effective irradiance reaching the Earth's surface. Units: $\mathrm{W} \cdot \mathrm{m}^{-2} \cdot \mathrm{nm}^{-1}$
- $S_{ir}(\lambda)$ is the spectral solar irradiance at the top of the atmosphere (TOA), typically modeled or measured based on standard solar spectra. Units: $\mathrm{W} \cdot \mathrm{m}^{-2} \cdot \mathrm{nm}^{-1}$
- $H_a(\lambda)$ is the atmospheric transmission function, describing the fraction of irradiance transmitted through the atmosphere at each wavelength under atmospheric condition a. Unitless, ranging from 0 (fully absorbed) to 1 (fully transmitted)
- $n_{ir}(\lambda)$ is used to model measurement accuracy and is represented as a Gaussian-distributed random variable with zero mean and a standard deviation defined by the measurement accuracy of $S_{ir}(\lambda)$. Its unit is $\mathrm{W} \cdot \mathrm{m}^{-2} \cdot \mathrm{nm}^{-1}$.
- $n_a(\lambda)$ models measurement accuracy, which is unitless, and is represented as an additive Gaussian noise random variable with zero mean and a standard deviation determined by the measurement accuracy of $H_a(\lambda)$.

For emulating the reflection from the panel, six Permaflect sheets are utilized. These durable, water-resistant sheets maintain high reflectance across diverse environments and cover a wide range of reflectance levels (5 %, 10 %, 18 %, 50 %, 80 %, and 94 %), spanning reflectance values from 250 nm to 2500 nm [5]. This variety in reflectance percentages and broad spectrum enables comprehensive radiometric compensation under varying lighting and surface conditions [134]. To model panel reflection, values in the 500 nm to 800 nm range for the R band and 700 nm to 1000 nm for the NIR band are selected, with a resolution of 5 nm, based on the Permaflect sheets' datasheet. The fitted curves are obtained using the MATLAB software tool. These curves represent the intrinsic reflectance characteristics of the sheets and are expressed as the percentage of reflected energy per nm, independent of solar irradiance and atmospheric effects.

For the next step, the modeling of the camera sensor consists of two steps: (I) measuring the OD according to the nominal wavelength and bandwidth of the camera sensors, and (II) digitizing the OD according to the full scale of the camera and the number of bits, as specified in the camera's datasheet [4]. For instance, the DJI Mavic 3M, along with its specifications [6], is considered in this study. This sensor incorporates

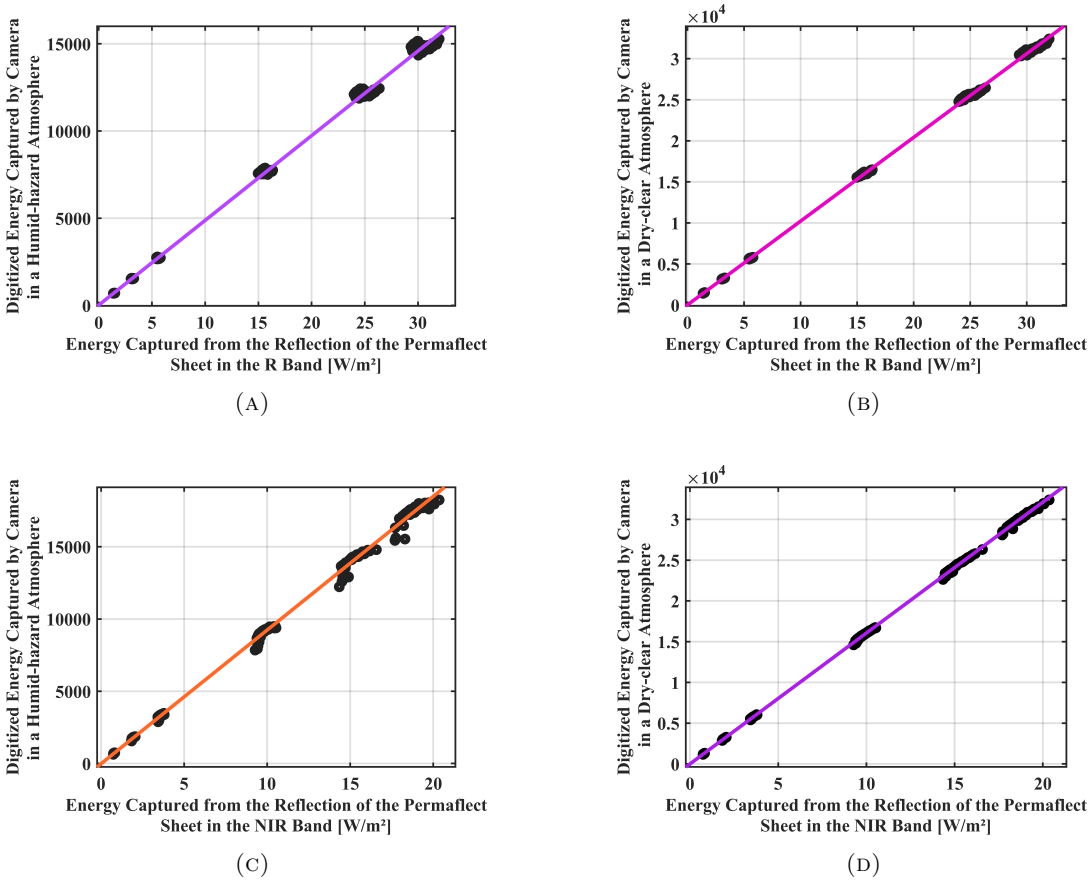

FIGURE 2.49: Radiometric compensation curves are evaluated based on the energy reflected by the Permaflect sheets relative to the energy captured by the camera after passing through atmospheric conditions, while uncertainty sources affect the measurements. (a) For the R band in the humid-hazy atmosphere, (b) for the R band in the dry-clear atmosphere, (c) for the NIR band in the humid-hazy atmosphere, and (d) for the NIR band in the dry-clear atmosphere.

non-overlap optical filters corresponding to the R channel centered at 650 nm ± 16 nm and the NIR channel at 860 nm ± 26 nm. In the modeling step, the system operates with a spectral bandwidth of 10 nm, employs an n-bit depth for digitization, and represents spectral information in terms of OD [116]. (I) OD characterizes the extent to which specific wavelengths of light or radiance are blocked by an optical filter. It is important to note that camera sensors do not measure radiance at a single, exact wavelength. Instead, they integrate radiance over a finite spectral bandwidth centered around the

nominal wavelength and report this aggregated value as the OD for the targeted spectral region. In this study, since irradiance is the measured quantity, the unit of measurement for OD is expressed in $\mathrm{W} \cdot \mathrm{m}^{-2}$. To formulate this step, it is important to mention that the radiation reflected by an object and measured by the camera sensor, $L_s(\lambda)$, is expressed as follows:

$$L_s(\lambda) = \rho(\lambda) \cdot L_i(\lambda) \tag{2.15}$$

Where $L_i(\lambda)$ is the incident irradiation upon the object, as mentioned in Equation (2.14), and $\rho(\lambda)$ generally denotes the material's spectral reflectance, a dimensionless metric [2]. However, in this context, $\rho(\lambda)$ refers to the panel reflectance. Then, the OD is measured using Equation (2.16).

$$OD(\lambda) = \int_{\lambda_n - \Delta\lambda + m_s}^{\lambda_n + \Delta\lambda + m_s} L_s(\lambda^*)\, d\lambda^* \tag{2.16}$$

Here, λ_n is the nominal wavelength combined with an uncertainty on the camera band (m_s). The term m_s represents a random variation drawn from a uniform distribution with zero mean and a standard deviation equal to the camera's uncertainty for each band. Its unit is nm, and $\Delta\lambda$ denotes half of the camera's bandwidth.

(II) To model the digitization function accurately, it is essential to first estimate the maximum energy expected in a real-world scenario. This value defines the full-scale range required for the digitization process. To estimate the maximum energy, a simplified scenario is considered, in which solar irradiance passes through the atmosphere and is fully reflected by a bare, object-free surface on the Earth's surface. To determine the peak spectral energy within the R and NIR wavelength bands, a sliding window technique is applied. This fixed-size window, matching the camera's bandwidth, scans across wavelength ranges centered around the sensor's nominal R and NIR bands. This approach accounts for possible variations in the sensor's central wavelength, ensuring that all potential spectral positions within the bands are considered. At each position of the sliding window, the method computes energy by integrating the product of the solar irradiance curve and the atmospheric transmission curve. This is done under both humid and dry atmospheric conditions to capture the range of possible environmental effects. For each configuration, the integrated energy (the area under the resulting curve) is calculated, and the highest value observed across all sampled intervals is recorded as the maximum energy for the respective spectral band. This process yields the maximum energy (E_{MAX}) values for R: $22.96\,\mathrm{W} \cdot \mathrm{m}^{-2}$ and for NIR: $16.79\,\mathrm{W} \cdot \mathrm{m}^{-2}$.

In the final step, the energy reflected from the sheet—resulting from solar irradiance that passed through the atmosphere, was reflected by the panel, and captured by the camera sensor (as described by Equation (2.16))—is evaluated and digitized to produce

a single n-bit digital value per panel. To convert the analog signal into a digital representation, the signal is first *normalized and scaled* to fit within the range of an n-bit unsigned integer (i.e., from 0 to $2^n - 1$). This is done using the following equation:

$$\text{digital} = \left\lfloor \frac{(2^{N_{\text{bit}}} - 1) \cdot \text{analog}}{E_{MAX}} \right\rceil \tag{2.17}$$

Here, N_{bit} corresponds to the number of bits of the camera. Following that, a best-fit curve is then fitted to the digitized data points to compute the radiometric compensation curve, as shown in Fig. 2.48(b).

Furthermore, in real-world applications, multiple uncertainty factors can influence the radiometric compensation curve. Therefore, variations in solar irradiance (expressed as $n_{ir}(\lambda)$), the camera's nominal wavelength (expressed as m_s), and the SNR, which is selected from 40 dB, 50 dB, and 60 dB, under different atmospheric conditions (e.g., humid-hazy and clear-dry environments) are taken into account when generating the radiometric compensation method. Here, $n_a(\lambda)$ is not considered since the uncertainty of each weather condition is not available in the dataset.

The three SNR values are selected based on a comprehensive review of the literature on multispectral cameras [125, 124]. This range is considered optimal for balancing signal strength and noise levels; therefore, these values are used to model variations in the camera's SNR.

Moreover, to assess the impact of these uncertainty factors on the generation of the radiometric compensation method, a Monte Carlo simulation with 100 iterations is conducted. The results of this analysis are presented in Fig. 2.48(c).

Afterward, the best-fitted curve is applied to the points under different atmospheric conditions for each band separately (i.e., $H_a(\lambda)$), as shown in Fig. 2.49. By testing polynomial degrees starting from one and comparing their RMSE values, the best-fitted curves were found to be of polynomial degree one with RMSE reported in Table 2.18. For higher-degree polynomials, the RMSE did not change significantly. Thus, first-degree polynomials ($p(x) = p_1 \cdot x + p_2$) are employed for the modeling process. Because negative energy values are not physically meaningful, p_2 is set to zero, and only the p_1 coefficients are provided for each curve. These coefficients are listed in Table 2.19 for both humid and dry conditions.

As the effects of uncertainty sources are considered, each radiometric compensation curve has lower and upper bounds for the p_1 parameter, resulting in two curves per spectral band. Accounting for both dry and humid atmospheric conditions doubles this to four curves per band. Since the study focuses on evaluating radiometric compensation for NDVI measurement using R and NIR bands, the total number of curves increases to eight per atmosphere.

Atmosphere & Band	**RMSE (in bit)**
Red Band - Humid Atm.	216.42
Red Band - Dry Atm.	204.70
NIR Band - Humid Atm.	235.95
NIR Band - Dry Atm.	109.43

TABLE 2.18: RMSE of the best-fitted polynomial curves (degree one) for radiometric compensation curves, with the R and NIR bands specified under different atmospheric conditions (humid and dry scenarios).

Atmosphere & Band	**Lower Bound** (LP1)	**Upper Bound** (UP1)
Red Band - Humid Atm. (HR_P1)	483.43	487.85
Red Band - Dry Atm. (DR_P1)	1017.60	1021.80
NIR Band - Humid Atm. (HNIR_P1)	921.21	929.04
NIR Band - Dry Atm. (DNIR_P1)	1604.40	1608.00

TABLE 2.19: Coefficients of the best-fitted polynomial curves (degree one) for radiometric compensation curves, where the R and NIR bands have lower and upper values for parameter P1, specified under different atmospheric conditions (humid and dry scenarios).

2.10.1 Study Area and Data Collection

I actively participated in research at the Agro-Environmental Research Centre 'El Chaparrillo' (IRIAF-CIAG, Ciudad Real, Spain) in September 2024. As a reminder of the pleasant and friendly working environment, I have included our group photo in Fig.A.1 in AppendixA.1, on page 188. The goal was to conduct a collaborative study involving advanced technologies, including a UAV equipped with a multispectral camera, and an NDVI handheld sensor, to validate the performance of the radiometric compensation method proposed in the above subsection using ground truth data from pistachio nuts to provide NDVI measurements compatible with the ones acquired by a reference NDVI measurement instrument. The dataset used in this study will be published soon.

The study was carried out at the experimental station of Finca Entresierra, part of the Centro de Investigación Agroambiental 'El Chaparrillo' (CIAG-IRIAF), located in Ciudad Real, Spain (38.9570° N, 3.9297° W) (Fig. 2.51a), under weather conditions observed from September 1st to 10th, 2024, with weather conditions detailed in Fig. 2.50. During this period, temperatures showed a cooling trend, with averages dropping from 26.03 °C to 19.33 °C, while humidity decreased from 47.99 % to 33.40 %. Maximum wind speeds ranged from 11.60 $\mathrm{m\,s^{-1}}$ to 5.22 $\mathrm{m\,s^{-1}}$, and solar radiation peaked at 25.27 $\mathrm{MJ\,m^{-2}}$. No

Ciudad Real

Date	Temp Average (°C)	Temp Max (°C)	Hour Tª Max	Temp Min (°C)	Hour Tª Min	Hum Average(%)	Hum Max (%)	Hour Hum Max	Hum Min (%)	Hour Hum Min	Vel Wind (m/s)	Dir Wind (°)	Vel V. Max (m/s)	Hour Vel Max V.	Dir V. Vel Max (°)	Rad (MJ/m2)	Precip (mm)	P. effect (mm)	Eto (mm)
01/09/2024	26,03	33,55	15:40	17,99	06:00	47,99	80,50	06:00	26,29	16:10	1,33	256,00	6,53	16:28	298,30	19,86	0,00	0,00	4,78
02/09/2024	25,71	34,23	15:10	16,71	05:40	44,53	81,20	05:50	24,27	16:00	1,32	263,60	7,38	17:14	292,70	18,81	0,00	0,00	4,71
03/09/2024	24,76	34,70	15:40	15,83	06:00	44,96	78,40	05:50	19,42	15:50	1,08	238,50	7,22	10:54	268,00	22,92	0,00	0,00	4,93
04/09/2024	23,23	32,34	15:00	14,03	04:40	41,17	66,71	02:40	21,17	15:00	1,43	292,10	7,14	12:54	321,90	25,27	0,00	0,00	5,33
05/09/2024	23,07	33,02	13:20	14,95	06:00	45,23	78,90	06:00	17,46	13:20	2,41	264,60	10,32	14:08	287,60	21,50	0,00	0,00	6,17
06/09/2024	21,54	29,78	13:10	12,47	23:50	37,53	62,47	06:00	19,62	15:10	2,48	251,90	11,60	13:31	289,80	23,80	0,00	0,00	5,93
07/09/2024	19,33	29,52	14:40	7,83	05:30	33,40	62,22	05:30	14,63	14:40	1,71	240,10	8,64	12:51	284,60	22,07	0,00	0,00	5,03
08/09/2024	20,00	29,24	15:00	9,85	06:10	37,86	56,13	05:10	25,22	12,20	2,12	261,30	9,32	15:19	288,40	23,53	0,00	0,00	5,37
09/09/2024	21,10	31,06	13:50	8,51	06:00	38,28	74,00	06:00	17,06	15:30	0,97	207,60	5,22	16:10	292,50	23,82	0,00	0,00	4,35
10/09/2024	22,59	32,48	15:50	10,46	06:00	35,62	71,10	05:10	15,30	15:50	0,95	248,10	5,64	13:09	287,00	23,40	0,00	0,00	4,40

FIGURE 2.50: The weather condition of Ciudad Real, Spain on September 2024.

precipitation was recorded. At the time of data collection, the pistachio trees were in the late growth stage, nearing harvest. The pistachio variety studied was 'Sirora,' widely cultivated in the Castilla La Mancha region (Spain).

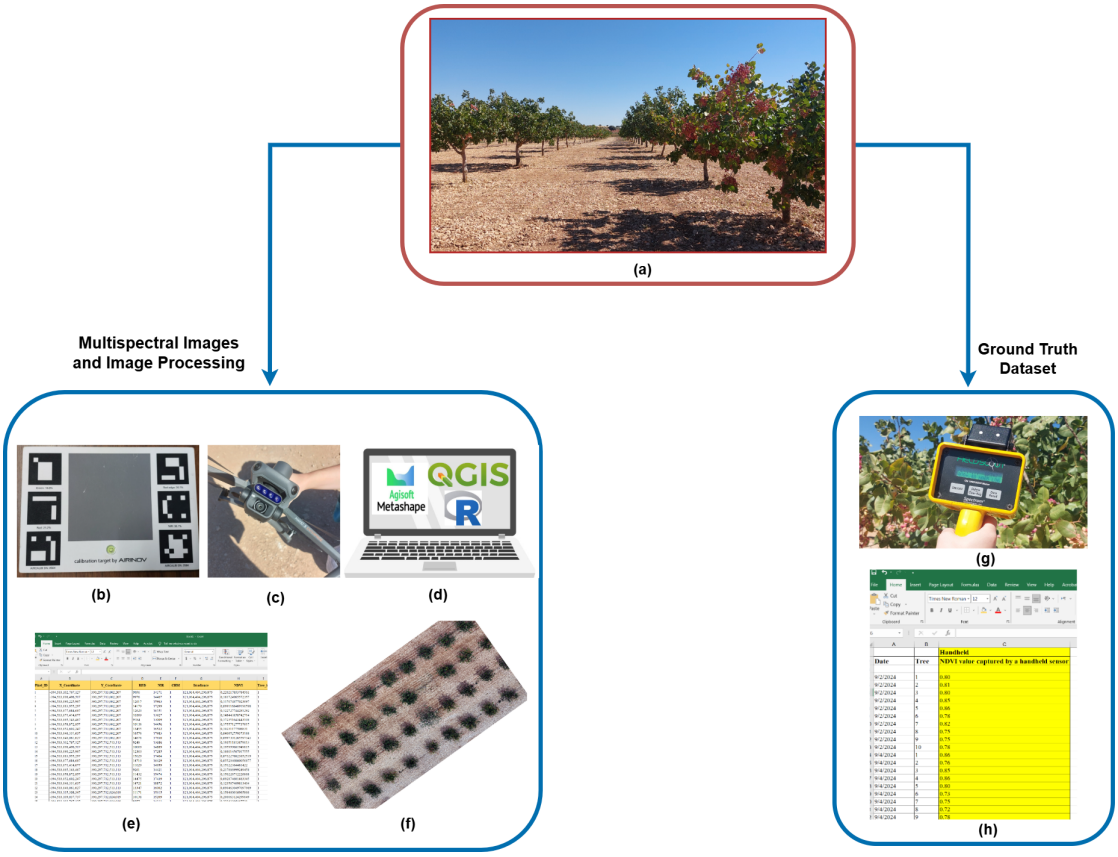

FIGURE 2.51: (a) Pistachio field on September 9, 2024, (b) The AIRcalin SN: 2564 calibration target by AIRINOV, positioned on the ground within the study area for the radiometric compensation process, (c) DJI Mavic 3 Multispectral UAV, (d) Software used for image processing, including Agisoft Metashape, R, and QGIS, (e) CSV files and (f) Orthomosaic TIFF file as the output of image processing, (g) FieldScout CM 1000 NDVI Meter: A handheld sensor used to measure the NDVI of the pistachio tree canopy as a ground truth reference [12], (h) Excel file as the output of ground truth data.

Multispectral imagery was captured using a DJI Mavic 3 Multispectral UAV, with details in Table 2.20 for the RGB camera and multispectral camera [6], under dry, stable atmospheric conditions to minimize variability in light intensity. The Mavic 3 camera

captures images with a 16 bit depth [6] (Fig. 2.51c). To ensure radiometric accuracy, an AIRcalin SN: 2564 reference panel (Fig. 2.51b) was placed on a uniform surface within the study area on the ground and imaged per flight for compensation. The panel is used to convert the raw DNs of all image pixels into reflectance values [135]. This panel includes a standardized gray reference surface with known reflectance values across four spectral bands, as detailed in Table 2.21.

Parameter	**Mavic 3M RGB Camera Specification**	**Mavic 3M Multispectral Camera Specification**
Image Sensor	4/3 CMOS, Effective Pixels: 20 MP	1/2.8-inch CMOS, Effective Pixels: 5 MP
Lens	FOV: 84° Equivalent Focal Length: 24 mm Aperture: f/2.8 to f/11 Focus: 1 m to ∞	FOV: 73.91° (61.2° x 48.10°) Equivalent Focal Length: 25 mm Aperture: f/2.0 Focus: Fixed Focus
ISO Range	100-6400	-
Shutter Speed	Electronic Shutter: 8-1/8000 s Mechanical Shutter: 8-1/2000 s	Electronic Shutter: 1/30 1/12800 s
Max Image Size	5280×3956 pixels	2592×1944 pixels
Photo Shooting Modes	Single Shot: 20 MP Timed: 20 MP JPEG: 0.7/1/2/3/5/7/10/15/20/30/60 s JPEG + RAW: 3/5/7/10/15/20/30/60 s Panorama: 20 MP (original material)	Single Shot: 5 MP Timelapse: 5 MP TIFF: 2/3/5/7/10/15/20/30/60 s
Video Resolution	H.264: 4K: 3840×2160@30fps FHD: 1920×1080@30fps	H.264 FHD: 1920×1080@30fps Video Content: NDVI/GNDVI/NDRE
Max Video Bitrate	4K: 130 Mbps FHD: 70 Mbps	Stream: 60 Mbps
Supported File System	exFAT	-
Image Format	JPEG/DNG (RAW)	TIFF
Video Format	MP4 (MPEG-4 AVC/H.264)	MP4 (MPEG-4 AVC/H.264)
Multispectral Bands	-	Green (G): 560 ± 16 nm Red (R): 650 ± 16 nm Red Edge (RE): 730 ± 16 nm Near Infrared (NIR): 860 ± 26 nm
Gain Range	-	1x-32x

Table 2.20: Mavic 3M RGB and Multispectral Camera Specifications [6].

Wavelength	**Percentage**
Green (550 nm)	16.9%
Red (650 nm)	21.2%
Red Edge (730 nm)	26.1%
Near-Infrared (NIR, 860 nm)	36.1%

TABLE 2.21: Wavelength and Corresponding Reflection Percentages for Different Bands of the AIRcalin SN: 2564 Reference Target.

2.10.1.1 Ground Truth Data Using NDVI Handheld Sensor

For ground truth measurements, the FieldScout CM 1000 NDVI Meter [7], a handheld sensor used to measure the NDVI value of crops, is utilized to measure the NDVI of the pistachio tree canopy (Fig.2.51g). From a metrological perspective, detailed specifications of the sensor are provided in Table 2.22. The measurement procedure involved an operator holding the handheld sensor, activating the trigger, and walking in a circular path around the tree. The sensor continuously recorded NDVI values during the circuit. Upon completing one full revolution, the trigger was released, thereby finalizing the NDVI measurement of the tree canopy.

TABLE 2.22: FieldScout CM 1000 NDVI Meter: Features and Specifications [7].

Feature	**Specification**
Measurement Sample	Plant leaves, turf grass canopy
Measurement System	Reflectance of 660 nm and 840 nm light
Measurement Area	Conical viewing area between 12 and 72 in
Minimum Distance	12 in (30.5 cm) from the lens
Maximum Distance	72 in (1.22 m), accuracy beyond unknown
Receptor	4 photodiodes (2 ambient, 2 reflected light)
Measurement Units	NDVI on a scale of -1 to 1
Measurement Interval	2 seconds per measurement
Uncertainty	±5% of reading
Data Logger	1,350 measurements with GPS, 3,250 without GPS
Battery	2 AAA batteries, approx. 3,000 measurements

The measured ground truth NDVI values for Tree IDs 1 through 10 (Fig. 2.51h) are reported in the column labeled `Sensor (NDVI ± Uncertainty)` in Table 2.24 for the four distinct dates: September 2, 4, 6, and 9, 2024. For each measured NDVI value, the NDVI sensor uncertainty of ±5%, as indicated in Table 2.22, is considered.

2.10.2 Image Acquisition and Processing

1. **Flight Planning:** The Mavic 3 Multispectral UAV was programmed using DJI Terra to follow a predefined flight path, ensuring consistent altitude, overlap, and exposure settings for all captured images.
2. **Calibration Target Placement:** The AIRINOV panel was placed on the ground to capture reference images before and after each flight, which were later used for radiometric compensation.
3. **Orthomosaic and Canopy Height Model (CHM) Generation:**

   The orthomosaics (Fig. 2.51f) and Canopy Height Model (CHM) were generated using **Agisoft Metashape Professional v1.7.6** (Agisoft LLC, St. Petersburg, Russia), processing multispectral UAV images. Two versions were generated to assess the impact of radiometric compensation:

   - **Uncorrected Version:** Used the original sensor data without any spectral adjustments.
   - **Corrected Version:** Applied radiometric calibration based on the AIRINOV reference panel to enhance spectral accuracy, Fig. 2.52a.

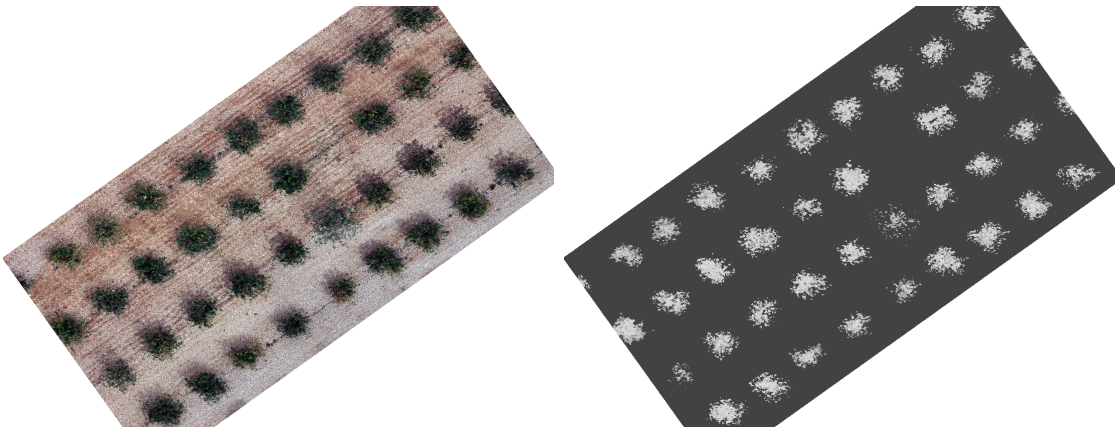

(A) (B)

FIGURE 2.52: Multispectral image and NDVI layer of the pistachio field captured on September 2, 2024. (a) Orthomosaic generated from calibrated images shown in QGIS software, (b) NDVI layer generated using the CHM method based on the orthomosaic shown in Fig. 2.52a.

   (a) **Image Import and Preprocessing:** The first step involved importing the TIFF-format multispectral images from the UAV sensor into Metashape.

Metashape uses sun sensor data. The sun sensor is a feature of the Mavic 3 Multispectral drone that measures sunlight intensity during flights. It helps improve the accuracy of multispectral images by compensating for changing light conditions, which is important for precise agricultural and environmental analysis. The software performs radiometric calibration automatically using the "Calibrate Reflectance" tool, which processes the reference panel images and the irradiance metadata from the sun sensor to compute spectral compensation factors for each band (Agisoft LLC, 2021). These factors are then applied to all images prior to generating the orthomosaic [136]. Additionally, it includes a vignetting compensation modeled by a third-order polynomial to ensure that the final reflectance values in each pixel of the orthomosaic (and consequently in the VI maps) remain consistent and comparable across the entire set of multispectral images.

- In the uncorrected version, the images were used directly without any modifications.
- In the corrected version, the images were used after scaling them based on coefficients.

(b) **Image Alignment and Point Cloud Generation:**
Once the images were imported, feature detection and matching were performed using Agisoft Metashape's proprietary algorithms. These detect keypoints that are stable under changes in viewpoint and lighting, and compute local descriptors for each keypoint to enable correspondence detection across overlapping images. This procedure is conceptually similar to the well-known Scale-Invariant Feature Transform (SIFT), although Agisoft has implemented custom algorithms optimized for higher alignment accuracy, according to the official technical information [137]. To improve geometric precision, camera parameters were optimized, correcting any lens distortions or perspective shifts. After alignment, a dense point cloud was generated, providing a detailed 3D representation of the study area, including both terrain and vegetation.

(c) **Digital Surface Model (DSM) and Orthomosaic Generation:** The next step involved generating a Digital Surface Model (DSM) from the dense point cloud. The DSM represented the elevation of all features in the scene, including the ground, vegetation, and any structures. Height values were interpolated, and compensations were applied to enhance model accuracy.
From this data, two distinct multispectral orthomosaics were produced:

- The uncorrected orthomosaic was generated directly from the original UAV images, preserving the sensor's raw digital number values.

- The corrected orthomosaic was generated from the radiometrically compensated images, where DN values were converted to reflectance in Metashape using the reference panel, irradiance data from the sun sensor, and a vignetting compensation modeled by a third-order polynomial. This adjustment enhanced the spectral accuracy and reliability of the dataset.

(d) **Canopy Height Model (CHM) Creation:** To extract the canopy height, a Digital Terrain Model (DTM) was created by filtering out vegetation and structures, leaving only the bare ground elevation. The Canopy Height Model (CHM) was then obtained by subtracting the DTM from the DSM, effectively isolating the canopy height above ground level, Fig. 2.52b.

This method enables measurement of canopy height variations across the pistachio orchard, providing valuable insights into the spatial distribution of vegetation. The CHM enables the segmentation of images based on canopy presence, distinguishing areas with vegetation from those without. This differentiation facilitates analysis of vegetation structure and distribution, enhancing NDVI analysis.

(e) **Irradiance Mapping and Voronoi Diagram Creation:** Before extracting spectral and structural metrics, spatial interpolation of irradiance values was performed to generate a continuous surface from the discrete UAV image metadata, following a similar procedure as in [138].

To achieve this:

- The EXIF metadata from the multispectral UAV images was analyzed, extracting key information, including geographic coordinates (latitude, longitude) and irradiance values recorded at the moment of image capture.
- These discrete measurements were then used as seed points for a Voronoi tessellation, which divided the study area into non-overlapping polygons, each representing the region closest to a given UAV image.

By assigning the irradiance value of each UAV image to its corresponding Voronoi polygon, a spatially continuous irradiance raster was generated. This raster was then resampled to match the resolution of the orthomosaic and CHM, ensuring consistency across all datasets. The final irradiance map was exported as a GeoTIFF file and integrated with other remote sensing and GIS outputs.

(f) **Data Extraction and CSV Generation:** The next step was to extract relevant spectral and structural metrics for further analysis. This was done

using spatial masking and statistical aggregation, ensuring that only meaningful values from tree canopy regions were included in the final dataset. In the following the step-by-step procedure is listed:

- **Tree-Level Statistical Aggregation:** A vector shapefile (a shapefile is a GIS format that stores the location, shape, and attributes of geographic features) containing tree locations was used to define the sampling areas. This ensured that the analysis was focused precisely on individual trees rather than surrounding vegetation or background elements. For each tree, key statistical metrics (including mean, median, standard deviation, and variance) were calculated across all available variables: Red, NIR, CHM, Irradiance, and NDVI. These aggregated values provided a high-level summary of tree health and structural characteristics. The results were stored in a CSV file, facilitating further comparative analyses and interpretations.
- **Pixel-Level Data Collection:** A more granular approach was taken by extracting raw pixel values from within each tree canopy. Each pixel was assigned a Tree ID, along with its precise X and Y geographic coordinates, allowing for spatially explicit analyses. This pixel-level dataset enabled a deeper examination of spectral variability within individual trees and allowed for fine-scale comparisons between different trees or treatment conditions.

The complete dataset was exported to a separate CSV file (Fig. 2.51e).

All data processing and statistical analyses were performed using **R** (version 4.2.X, R Core Team 2019), utilizing the `raster`, `spatstat`, and `exifr` packages for spatial data manipulation and UAV metadata extraction.

2.10.3 Segmentation and Data Analysis of the NDVI Measurements

2.10.3.1 Calculating NDVI Using Multispectral Images and Sunlight Sensor Data from the Mavic 3M

The NDVI is calculated from multispectral images using the reflectance values of the NIR and R spectral bands mentioned in the Mavic 3M white paper [1], as follows:

$$NDVI = \frac{NIR_{ref} - Red_{ref}}{NIR_{ref} + Red_{ref}} \tag{2.18}$$

In this equation, NIR_{ref} and Red_{ref} are the reflectance values of the NIR and R bands, which are unitless ratios and computed as follows [1]:

$$\begin{aligned} NIR_{ref} &= \frac{NIR_{reflected}}{NIR_{incident}} = \frac{NIR_{camera}}{NIR_{LS}} \times \rho_{NIR} \times \frac{p_{Cam_{NIR}}}{p_{LS_{NIR}}} \\ &= \frac{NIR_{camera} \times p_{Cam_{NIR}}}{NIR_{LS} \times p_{LS_{NIR}}} \times \rho_{NIR} \end{aligned} \tag{2.19}$$

$$\begin{aligned} Red_{ref} &= \frac{Red_{reflected}}{Red_{incident}} = \frac{Red_{camera}}{Red_{LS}} \times \rho_{NIR} \times \frac{p_{Cam_{Red}}}{p_{LS_{Red}}} \\ &= \frac{Red_{camera} \times p_{Cam_{Red}}}{Red_{LS} \times p_{LS_{Red}}} \times \rho_{NIR} \end{aligned} \tag{2.20}$$

where X_{camera} denotes the signal value from the multispectral camera in a given band, expressed in DN (representing the raw pixel value from the sensor), while X_{LS} represents the corresponding signal from the sunlight sensor, expressed in units of $\mathrm{W} \cdot \mathrm{m}^{-2} \cdot \mathrm{nm}^{-1}$. The conversion between these values is governed by a conversion parameter, which defines the relationship between the camera and sunlight sensor signal values, as reported in the white paper [1]. To ensure consistency, both reflected and incident light measurements must be expressed in the same units, and the multispectral camera and sunlight sensor should possess matching photosensitivity characteristics [1]. Given that their signals share a linear relationship, conversion can be performed using the formula $\rho_{NIR} \times \frac{p_{Cam_x}}{p_{LS_x}}$ [1]. All spectral bands are calibrated relative to the standard, unitless NIR band, ρ_{NIR}, employing compensation parameters p_{Cam_x} for camera signals recorded in DN format, and p_{LS_x} for sunlight sensor signals measured in units of $\mathrm{W}^{-1} \cdot \mathrm{m}^2 \cdot \mathrm{nm}$.

Then, the NIR band, as an example, is selected to continue the process. First, the following camera-related values are required: NIR_{camera} and $p_{Cam_{NIR}}$ [1].

$$NIR_{camera} = \frac{(I_{NIR} - I_{BlackLevel})}{\left(NIR_{gain} \times \frac{NIR_{etime}}{10^6}\right)} \tag{2.21}$$

The input values for NIR_{camera} in Equation (2.21), as well as those for the R band, are extracted from the image metadata, as described in the white paper [1]. The normalized raw pixel value I_{NIR} and the black-level value $I_{BlackLevel}$ are obtained by dividing their original values by 2^{bitnum}, where the bit depth is specified in [EXIF: Bits Per Sample]. Additional parameters such as black level, sensor gain NIR_{gain}, and exposure time NIR_{etime} are provided in the [XMP: drone-dji] section of the metadata. These values are used to compute the image signal NIR_{camera}, while the corresponding compensation

parameter $pCam_{NIR}$ is taken from [Sensor Gain Adjustment]. For the sunlight sensor, the values NIR_{LS} and pLS_{NIR} are used to calculate the product $NIR_{LS} \times pLS_{NIR}$, which is stored as [Irradiance] in the same metadata [1]. The metadata of an image captured by the Mavic 3 in the R and NIR bands on September 2, 2024, is shown in Fig. 2.53.

To evaluate the input parameters of Equation (2.21), metadata from 30 randomly selected multispectral images are analyzed for each day. The analysis shows that most metadata parameters remain consistent across the images. For parameters that exhibit variation, their average values are used in the evaluation.

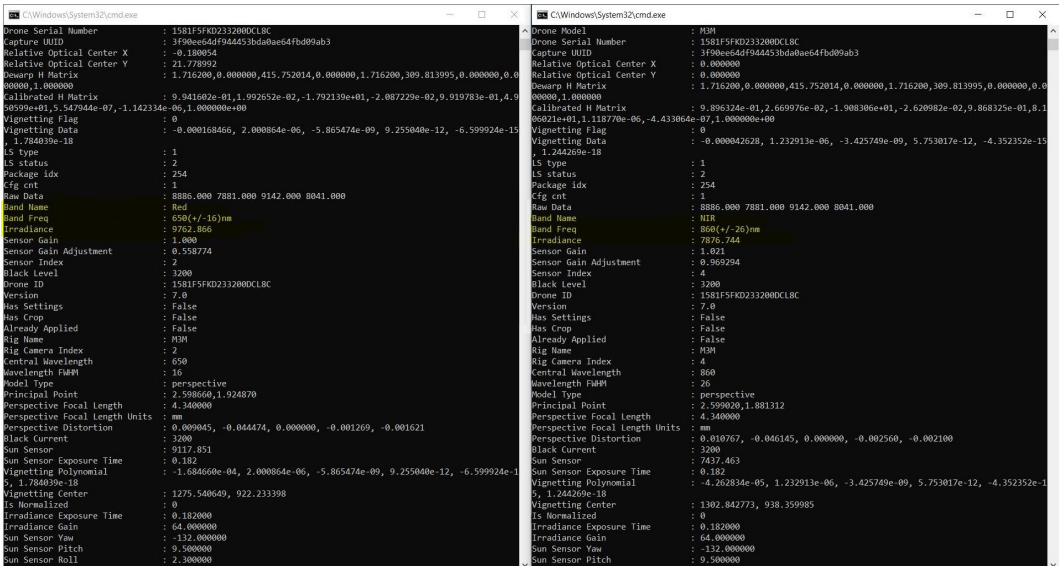

FIGURE 2.53: Metadata of an image captured by Mavic 3 in the R and NIR bands on September 2, 2024.

Among the parameters, the most significant change is observed in solar irradiance. The analysis of solar irradiance values (Fig. 2.56) shows that on September 2, the IQR is significantly higher than on other days, indicating greater variability in irradiance. For the R band, the IQR on September 2 spans approximately 8000 to 10 000 (the camera operates at a 16-bit depth), while for the NIR band, it ranges from around 6900 to 8200. Despite this high variability, irradiance values on September 2 remain lower than on the other days, whereas September 4 exhibits the highest irradiance among all four dates. This highlights fluctuations in irradiance over time, with distinct variations across the four days, emphasizing the dynamic nature of solar irradiance and justifying the need for a radiometric compensation procedure. Fig. 2.54 shows box plots of the Mavic 3 sensor

gain adjustment for (A) the R band and (B) the NIR band. Additionally, Fig. 2.55 presents the Mavic 3 sensor gain for (A) the R band and (B) the NIR band on these dates.

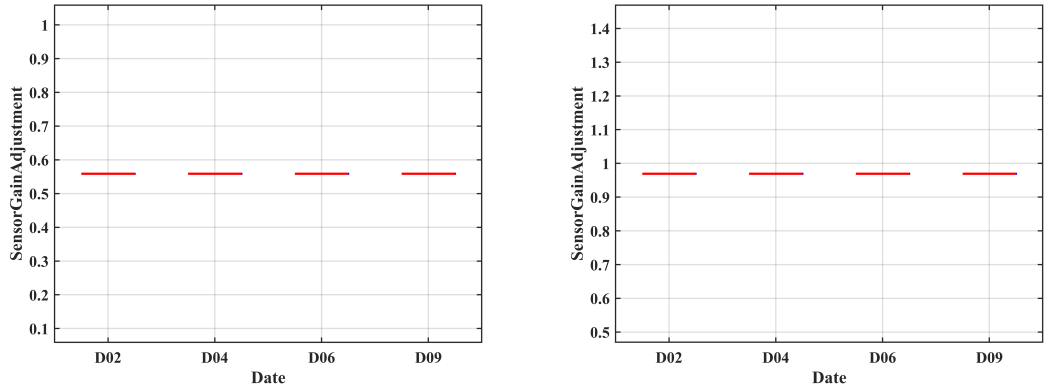

(A) R band (B) NIR band

FIGURE 2.54: Box plot of the Mavic 3 sensor gain adjustment on four different dates: September 2, 4, 6, and 9, 2024 for (A) the R band and (B) the NIR band.

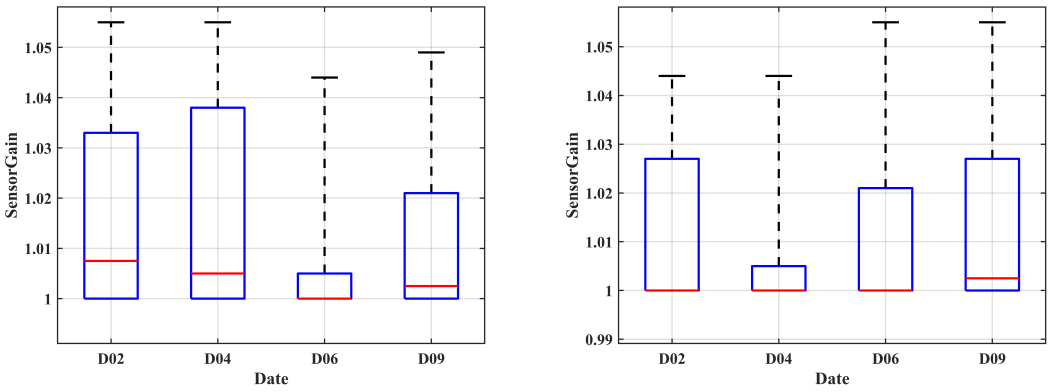

(A) R band (B) NIR band

FIGURE 2.55: Box plot of the Mavic 3 sensor gain on four different dates: September 2, 4, 6, and 9, 2024 for (A) the R band and (B) the NIR band.

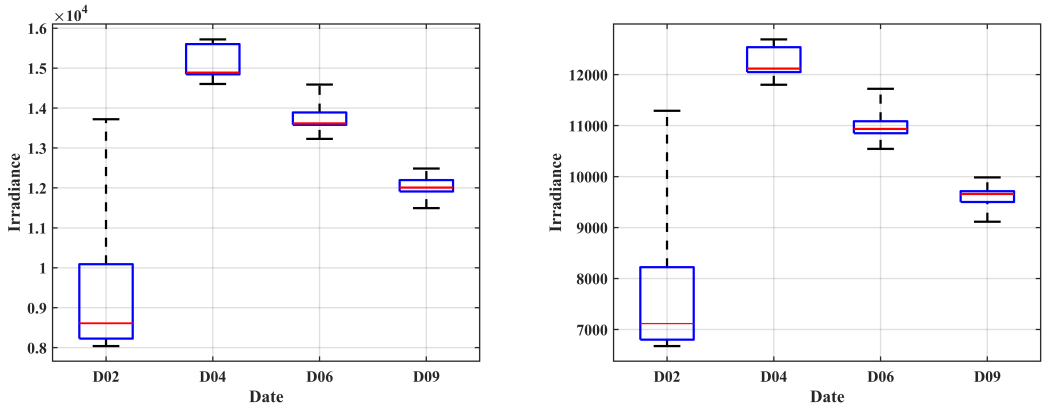

(A) R band (B) NIR band

FIGURE 2.56: Box plot of solar irradiance recorded on four different dates: September 2, 4, 6, and 9, 2024. (A) Irradiance values extracted from the R channel of multispectral images and (B) from the NIR channel.

The MATLAB code that converts the raw pixel values from the images into reflectance values, based on the aforementioned information, is provided in Appendix A.1 on page 189.

2.10.3.2 Analysis of Data Extracted from a Multispectral Image in QGIS Software

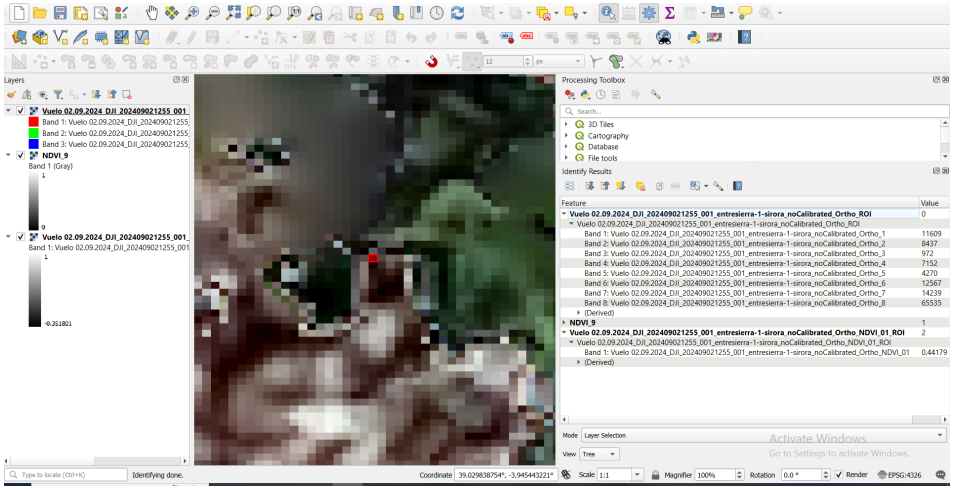

FIGURE 2.57: Selected pixel on a multispectral orthomosaic image and the extracted NDVI layer. The pixel is not a leaf, and its NDVI value is 0.44.

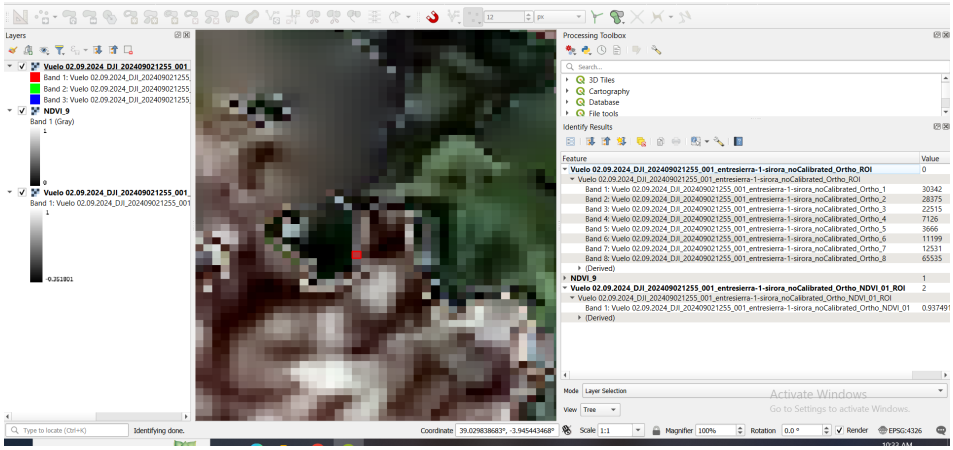

FIGURE 2.58: Selected pixel on a multispectral orthomosaic image and the extracted NDVI layer. The pixel is not a leaf, and its NDVI value is 0.94.

The output orthomosaic and NDVI TIFF files from Section 2.10.2 are opened in QGIS Software (Version 3.38) to check whether the points on multispectral layers and NDVI

layer are related to trees or not. By selecting random pixels and checking their NDVI values and spatial images at corresponding points, it is revealed that although the CHM method effectively extracts canopy height data for pistachio trees, not all extracted NDVI values correspond to the tree's leaves. For example, the NDVI values of randomly selected pixels were 0.44 and 0.94, which do not actually correspond to the leaves, as shown in Figs. 2.57 and 2.58. To ensure that only leaf pixels are considered, an NDVI threshold range of 0.50 to 0.85 is applied to the NDVI map, generating a new map. This range is determined through a manual trial-and-error process. However, this threshold alone is not sufficient to determine the leaf area; therefore, an additional process is applied to the green band of the multispectral images.

For this, random leaf-covered areas are manually selected, and the corresponding green band reflectance values are extracted. The analysis reveals that, applying a reflectance threshold between 2000 and 40 000 in DN (based on the 16-bit depth of the camera) to the green band, effectively delineates leaf regions. Based on this threshold, a new green band layer is generated. The extracted green band layer is then multiplied pixel-by-pixel with the NDVI-CHM layer, producing an output that emphasizes vegetated areas while incorporating tree canopy height data.

This integration enhances vegetation differentiation. The R and NIR reflectance values of the resulting pixels are then extracted for further analysis, and their maps are shown in Fig. 2.59a for R and Fig. 2.59b for NIR. To better analyze the data, the histogram and box plot of these two figures are presented in Fig. 2.60 and 2.61.

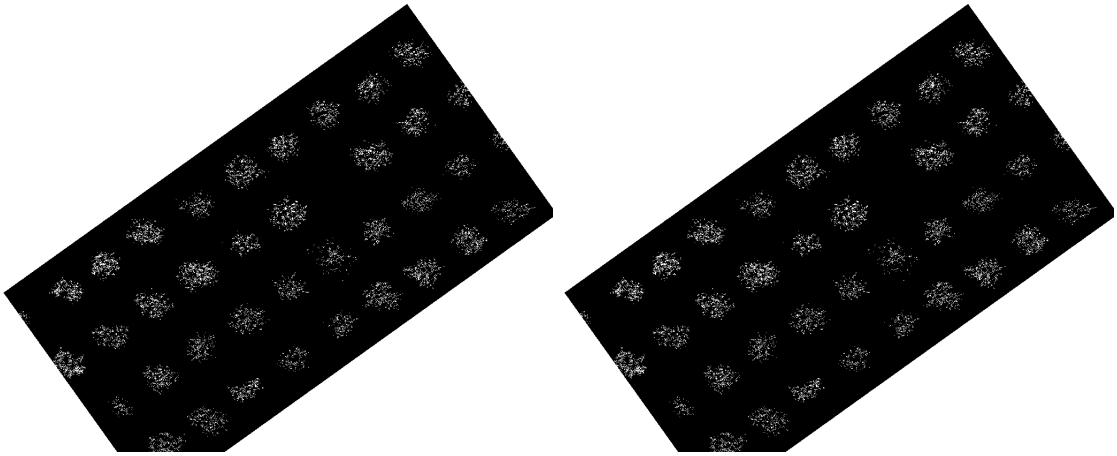

(A) (B)

FIGURE 2.59: Maps generated by multiplying the selected green layer with the NDVI-CHM map with (a) the R band and (b) the NIR band on the 2nd of September.

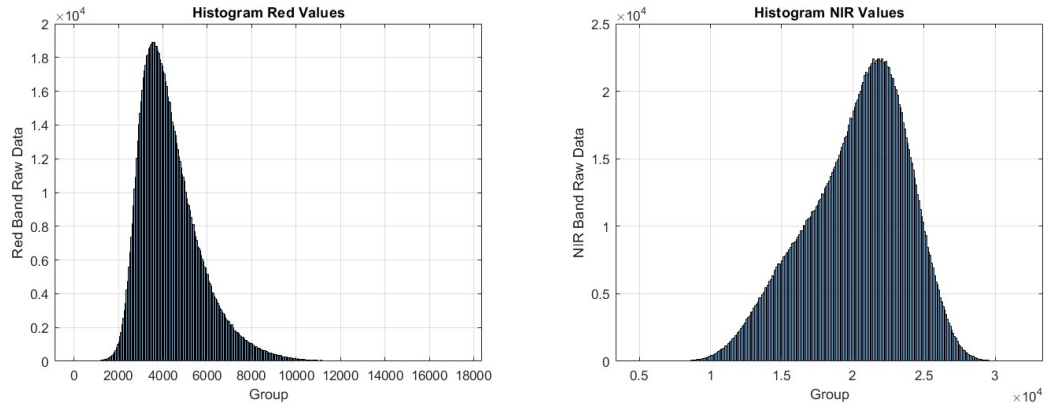

(A) (B)

FIGURE 2.60: Histogram of (a) the R channel and (b) the NIR channel after multiplying the green map of the leaf area with the NDVI layer, derived from CHM on September 2, 2024. The analysis was performed using QGIS software with multispectral images acquired by the Mavic 3.

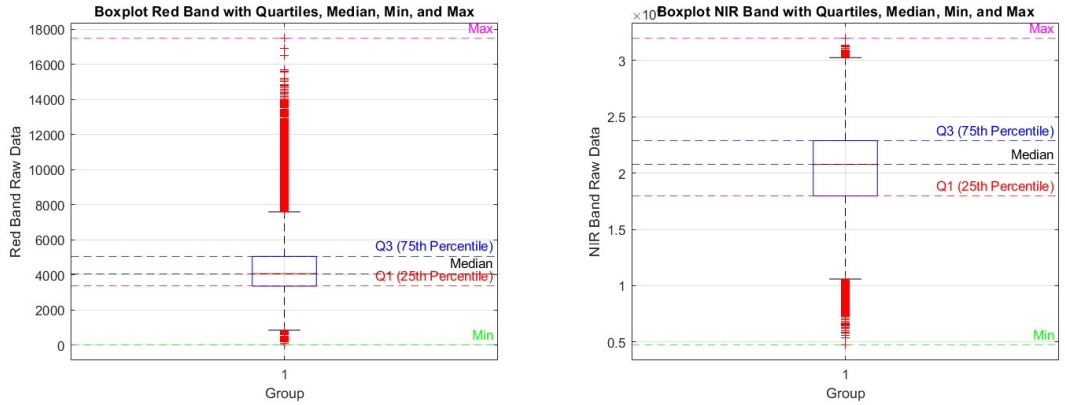

(A) (B)

FIGURE 2.61: Box plot of (A) the R channel and (B) the NIR channel after multiplying the green map of the leaf area with the NDVI layer, derived from CHM on September 2, 2024. The analysis was performed using QGIS software with multispectral images acquired by the Mavic 3.

These visualizations demonstrate that both R and NIR reflectance values conform to a Gaussian distribution pattern and the approximate reflectance ranges for leaf regions

Date (Sep)	R Band		NIR Band	
	Average	Std. Deviation	Average	Std. Deviation
02	4022.77	2147.14	18432.20	3542.96
04	3928.47	3036.01	16732.31	4850.91
06	4272.60	3406.08	16974.90	5129.85
09	4838.18	3703.32	19347.98	5686.32

TABLE 2.23: Mean and standard deviation of R and NIR bands in September.

are identified as 2700–5700 for the R band and 15 500–21 500 for the NIR band. This statistical pattern — characterized by a symmetric, unimodal shape — was consistent across different acquisition dates, allowing us to define reflectance ranges based on the mean and standard deviation for each day. Consequently, the reflectance ranges were subsequently normalized. Since the R and NIR values exhibit a Gaussian distribution, this pattern could be applied to data from other days as well. Given the Gaussian distribution of the data, z-score normalization was applied to standardize the DN values for September 2. For subsequent dates, specific R and NIR value ranges were determined using the mean and standard deviation computed for each respective day, as detailed in Table 2.23, in order to adjust the normalized Gaussian pattern for each specific day.

Then, the Pixels whose raw data fall within these defined ranges are extracted from the spatial dataset for each individual day, ensuring the selection of regions corresponding to leaf-covered areas.

2.11 Experimental Part and Results

2.11.1 Validation of the Proposed Radiometric Compensation Method Using In-Field Reflectance Measurements of a Reference Panel

To validate the proposed radiometric compensation method, reflectance measurements of an AIRINOV reference panel acquired in the field using the UAV Mavic 3M camera—processed according to the specifications outlined in its white paper [1] to convert raw data into reflectance—are compared with simulation results from the Monte Carlo model described in Section 2.10. This comparison evaluates the agreement between the experimentally measured reflectance values of the reference target and the estimated radiometric compensation curves. Since the measurements were taken under dry atmospheric conditions, the simulated radiometric compensation curves for the R and NIR bands under dry atmosphere conditions are used for validation. The correspondence

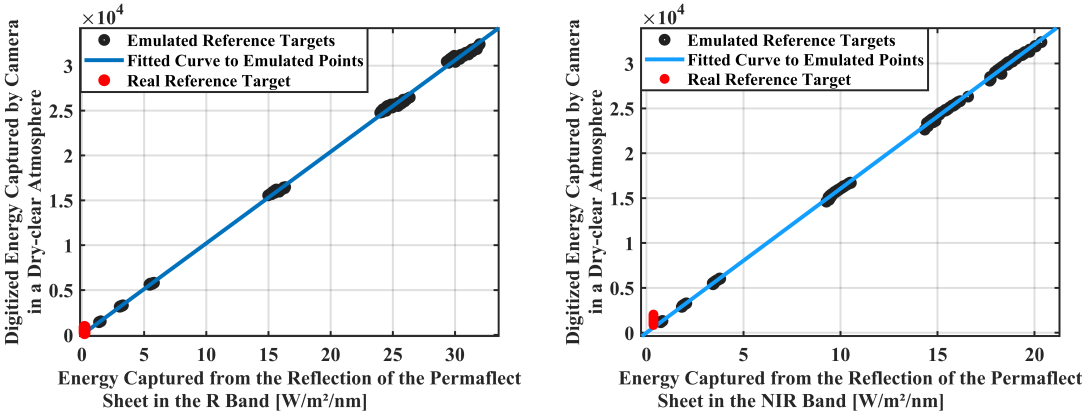

FIGURE 2.62: Comparison of reflectance measurements from an in-field AIRINOV reference panel (red points) acquired using the UAV Mavic 3M, alongside simulated radiometric compensation curves under dry atmospheric conditions: (a) R band and (b) NIR band.

between the measured data points from real reference target(shown in red color) and the simulated curves is illustrated in Fig. 2.62.

2.11.2 Conventional Radiometric Compensation Method

This section evaluates the performance of radiometric compensation performed in Agisoft Metashape software using the reflection ratio of the real AIRINOV reference panel and assesses how closely the corrected NDVI values align with actual ground truth data. To this end, NDVI values, both before and after compensation, are extracted from the CSV file as described in Section 2.10.2, and their corresponding box plots are generated and compared with the ground truth data. As a case study, the NDVI values for Tree ID 1 (Fig. 2.63(a,b)) and Tree ID 2 (Fig. 2.63(c,d)) on September 2, 4, 6, and 9, 2024, are compared with the ground truth data. The results indicate that none of the evaluated NDVI values represented by the blue boxes (spanning from the first quartile, Q1, to the third quartile, Q3) overlap with the ground truth data, both prior to and following radiometric compensation. Similarly, this process has been done for all the other trees, and their box plots show the same results and do not overlap with their respective ground truth values, regardless of whether the data is compensated or not. These findings suggest that the radiometric compensated, relying solely on the reference board and Agisoft Metashape software, did not yield the expected improvements. On the contrary,

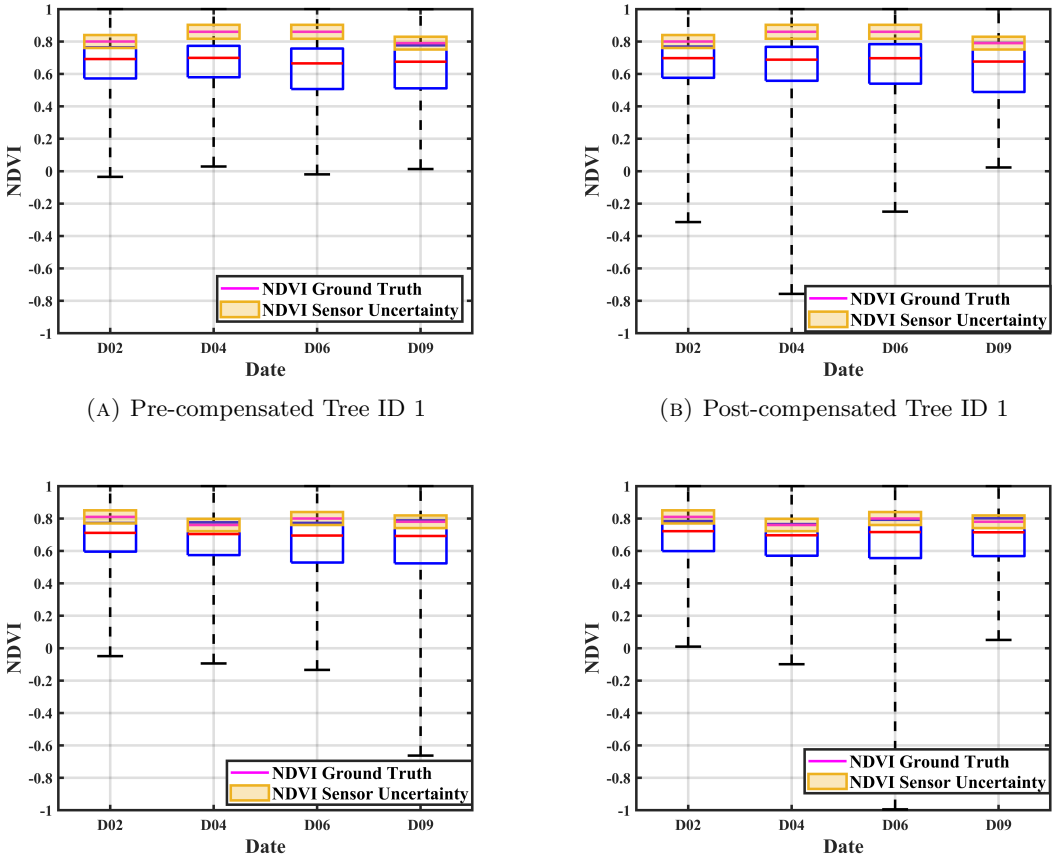

(A) Pre-compensated Tree ID 1

(B) Post-compensated Tree ID 1

(C) Pre-compensated Tree ID 2

(D) Post-compensated Tree ID 2

FIGURE 2.63: The blue box plots represent NDVI values derived from Mavic 3 multispectral images, while the orange box plots show ground truth measurements from a handheld NDVI sensor. Data were collected from a pistachio orchard at IRIAF-CIAG, Ciudad Real, Spain, on September 2, 4, 6, and 9, 2024. The plots correspond to two different Tree IDs: (a, b) represent Tree_ID One, with (a) depicting pre-compensation values and (b) post-compensated values; (c, d) represent Tree_ID Two, with (c) depicting pre-compensated values and (d) post-compensated values. compensation was performed in Agisoft Metashape software using reflectance values from the AIRINOV reference board.

the compensation process resulted in a degradation of NDVI measurement accuracy, as evidenced by an increased spread of outliers across a broader range of values.

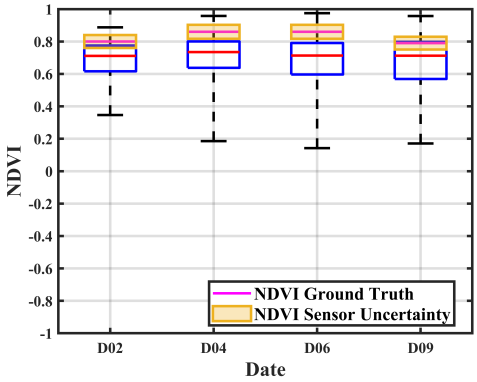

(A) Pre-compensation Tree ID 1

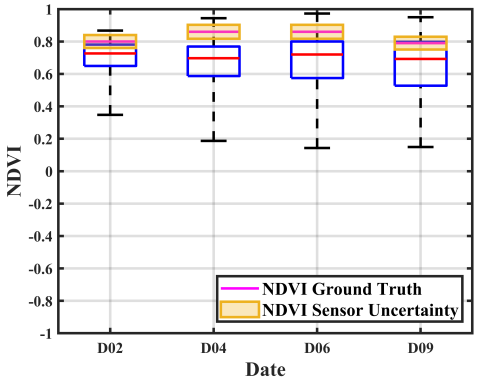

(B) Compensated by conventional method

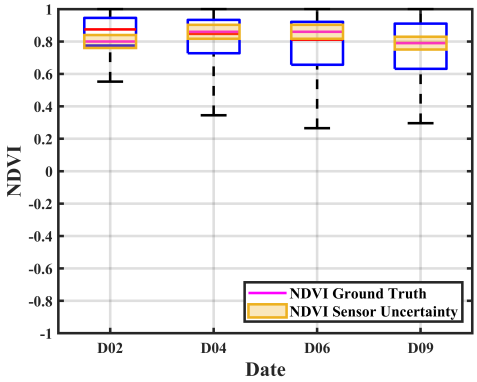

(C) Compensated by proposed method - Dry atmosphere

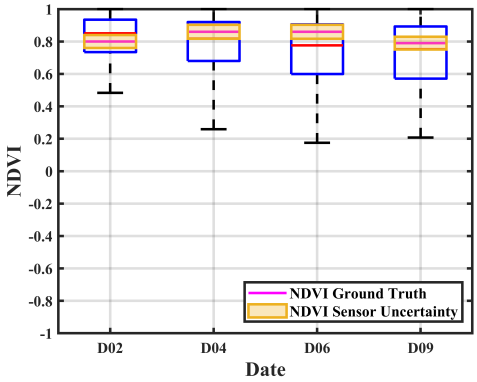

(D) Compensated by proposed method - Humid atmosphere

FIGURE 2.64: The distribution of NDVI values computed from the R and NIR leaf reflectance within the ROI for Tree ID 1 on September 2, 4, 6, and 9 is presented. These values are evaluated using (a) the conventional method in Agisoft Metashape software before compensation, (b) the conventional method in Agisoft Metashape software after compensation, (c) applying the proposed radiometric compensation method under dry-clear atmospheric conditions, and (d) under humid-hazy atmospheric conditions.

2.11.3 Results of the Radiometric Compensation Method in Dry Atmosphere

To test the proposed radiometric compensation method, the R and NIR values from the uncorrected CSV file in Section 2.10.2 are selected within the leaf area range, which

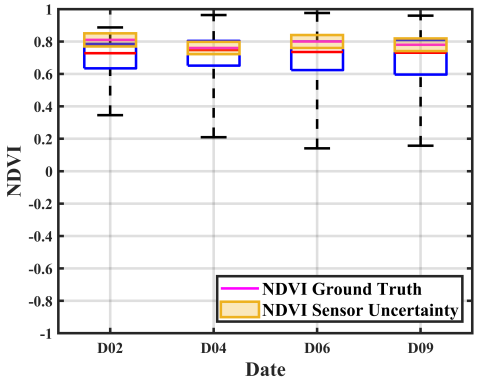

(A) Pre-compensation Tree ID 2

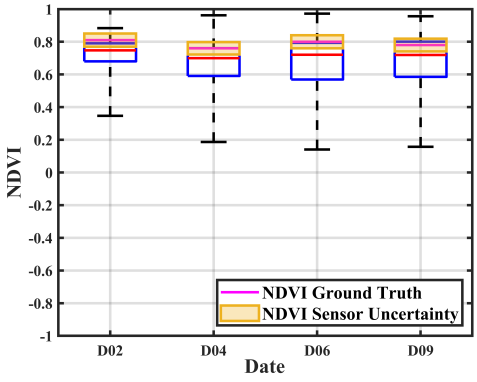

(B) Compensated by conventional method

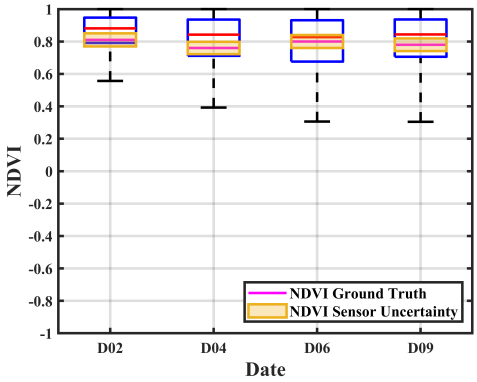

(C) Compensated by proposed method - Dry Atmosphere

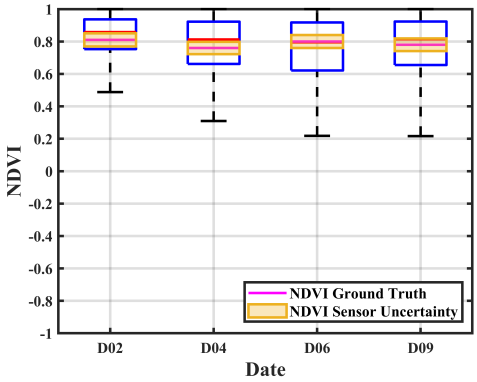

(D) Compensated by proposed method - Humid Atmosphere

FIGURE 2.65: The distribution of NDVI values computed from the R and NIR leaf reflectance within the ROI for Tree ID 2 on September 2, 4, 6, and 9 is presented. These values are evaluated using (a) the conventional method in Agisoft Metashape software before compensation, (b) the conventional method in Agisoft Metashape software after compensation, (c) applying the proposed radiometric compensation method under dry-clear atmospheric conditions, and (d) under humid-hazy atmospheric conditions.

defines our ROI, as described in Subsection 2.10.3.2. Additionally, their values are greater than the camera's black level, which is 3200. The raw data are then converted into reflectance values for R and NIR separately based on Equation (2.21). Then these uncorrected leaf reflectance are ready to compensate by proposed radiometric compensation curves as outlined in Section 2.10 for dry atmosphere. Since uncertainty sources

influence the evaluation of the radiometric compensation method, 8 radiometric compensation curves are generated for dry atmospheric conditions. After applying these compensation curves to compensate the uncorrected R and NIR values, the NDVI value is computed based on Equation (2.18). The resulting NDVI remains largely consistent across different compensation curves, suggesting that uncertainty sources have minimal impact on the radiometric compensation process.

Therefore, two radiometric compensation curves, utilizing the lower P1 coefficients for the first-degree polynomial of R and NIR compensation curves under dry, are selected. These curves are applied to the uncorrected R and NIR leaf reflectance values of all ten pistachio trees in the field, after which their NDVI values are computed. The median, first, and third quartiles of the computed NDVI values are presented in Table 2.24 for dry atmospheric conditions, corresponding to the dates of September 2, 4, 6, and 9. These values are compared to the NDVI ground truth measurements recorded by the NDVI Handel sensor, accounting for sensor-related uncertainties. The comparison demonstrates a high compatibility between the compensated NDVI values and the ground truth measurements.

As an illustrative example, the distribution of NDVI values, computed from the R and NIR leaf reflectance (within the ROI) for Tree ID 1(Fig. 2.64) and Tree ID 2 (Fig. 2.65), are presented. The NDVI values before and after compensation of the R and NIR reflectance in the Agisoft Metashape software are shown in panels (a) and (b), while the compensated R and NIR values, derived from the proposed radiometric combination (With P1 representing the lower bounds of polynomial degree one), are presented for the dry atmosphere (panel (c)).

A direct comparison between panels (b) and (c) reveals that, under dry atmospheric conditions, the NDVI values within the blue boxes increase by approximately 0.08 to 0.14 after applying the proposed radiometric compensation method. This indicates that the proposed approach not only ensures the compensated NDVI values closely align with ground truth data but also outperforms the conventional compensation method used in Agisoft Metashape software. The illustrative process was performed for all the other trees, which yielded the same results. These findings highlight the effectiveness of the proposed radiometric compensation in enhancing the accuracy of NDVI measurements.

ID	Date	Median	Q1	Q3	Sensor (NDVI ± U)	Comp?
1	2	0.87	0.77	0.94	0.80 ± 0.04	✓
	4	0.85	0.73	0.93	0.86 ± 0.04	✓
	6	0.81	0.66	0.92	0.86 ± 0.04	✓
	9	0.78	0.64	0.90	0.79 ± 0.04	✓
2	2	0.87	0.78	0.94	0.81 ± 0.04	✓
	4	0.84	0.71	0.94	0.76 ± 0.04	✓
	6	0.82	0.67	0.92	0.80 ± 0.04	✓
	9	0.81	0.66	0.92	0.78 ± 0.04	✓
3	2	0.87	0.77	0.94	0.80 ± 0.04	✓
	4	0.83	0.71	0.93	0.85 ± 0.04	✓
	6	0.80	0.67	0.91	0.79 ± 0.04	✓
	9	0.80	0.66	0.92	0.85 ± 0.04	✓
4	2	0.88	0.79	0.95	0.85 ± 0.04	✓
	4	0.85	0.72	0.94	0.86 ± 0.04	✓
	6	0.79	0.65	0.91	0.84 ± 0.04	✓
	9	0.83	0.69	0.93	0.86 ± 0.04	✓
5	2	0.85	0.75	0.93	0.86 ± 0.04	✓
	4	0.81	0.70	0.92	0.80 ± 0.04	✓
	6	0.77	0.64	0.89	0.81 ± 0.04	✓
	9	0.72	0.60	0.86	0.78 ± 0.04	✓
6	2	0.86	0.77	0.94	0.78 ± 0.04	✓
	4	0.84	0.72	0.93	0.73 ± 0.04	✓
	6	0.82	0.69	0.93	0.75 ± 0.04	✓
	9	0.80	0.66	0.91	0.88 ± 0.04	✓
7	2	0.86	0.76	0.94	0.82 ± 0.04	✓
	4	0.83	0.71	0.92	0.75 ± 0.04	✓
	6	0.80	0.66	0.91	0.73 ± 0.04	✓
	9	0.78	0.62	0.91	0.78 ± 0.04	✓
8	2	0.85	0.75	0.93	0.75 ± 0.04	✓
	4	0.83	0.71	0.93	0.72 ± 0.04	✓
	6	0.80	0.66	0.91	0.70 ± 0.04	✓
	9	0.80	0.64	0.92	0.74 ± 0.04	✓
9	2	0.83	0.74	0.91	0.75 ± 0.04	✓
	4	0.82	0.70	0.92	0.78 ± 0.04	✓
	6	0.80	0.66	0.91	0.86 ± 0.04	✓
	9	0.78	0.64	0.90	0.73 ± 0.04	✓

ID	Date	Median	Q1	Q3	Sensor (NDVI ± U)	Comp?
10	2	0.86	0.77	0.94	0.78 ± 0.04	✓
	4	0.85	0.73	0.94	0.78 ± 0.04	✓
	6	0.82	0.69	0.92	0.85 ± 0.04	✓
	9	0.83	0.68	0.92	0.88 ± 0.04	✓

TABLE 2.24: Comparison of the compensated NDVI values (using the proposed method) derived from multispectral images of ten pistachio trees, collected on September 2, 4, 6, and 9, 2024, under dry conditions, with ground truth NDVI measurements. The check mark indicates compatibility (Comp?) between NDVI values measured by the handheld sensor and those computed using the proposed method.

2.11.4 Results of the Radiometric Compensation Method in Humid Atmosphere

As the dataset was collected under dry atmospheric conditions, and it is not feasible to alter the weather to a humid state for the same field and plant, so a dataset for humid atmospheric conditions is not available. To evaluate the extent of variation introduced by the proposed radiometric compensation method under humid conditions on data obtained under dry atmospheric conditions, a comparative analysis was conducted. The procedure is the same as subsection 2.11.3. By examining Panels (c) and (d) of Figs. 2.64 and 2.65 for Tree ID 1 and 2, alongside Table 2.25 (humid atmosphere) and Table 2.24 (dry atmosphere), it is evident that for all trees, the compensated NDVI values have a nearly identical Q3, while their Q1 is lower under humid conditions than under dry conditions. This indicates that the IQR is wider in a humid atmosphere compared to a dry one. This finding is consistent with expectations, as the P1 coefficient of the radiometric compensation curve, as shown in Table 2.19, is around twice as large for dry conditions as for humid conditions. Consequently, the broader IQR observed under humid conditions can be attributed to this difference in radiometric compensation.

ID	Date	Median	Q1	Q3	Sensor (NDVI ± U)	Comp?
1	2	0.84	0.73	0.93	0.80 ± 0.04	✓
	4	0.82	0.68	0.92	0.86 ± 0.04	✓
	6	0.77	0.60	0.90	0.86 ± 0.04	✓
	9	0.74	0.58	0.88	0.79 ± 0.04	✓
2	2	0.85	0.73	0.93	0.81 ± 0.04	✓
	4	0.81	0.66	0.92	0.76 ± 0.04	✓
	6	0.78	0.61	0.91	0.80 ± 0.04	✓
	9	0.78	0.60	0.91	0.78 ± 0.04	✓
3	2	0.85	0.73	0.93	0.80 ± 0.04	✓
	4	0.80	0.66	0.91	0.85 ± 0.04	✓
	6	0.77	0.62	0.90	0.79 ± 0.04	✓
	9	0.76	0.60	0.90	0.85 ± 0.04	✓
4	2	0.86	0.75	0.94	0.85 ± 0.04	✓
	4	0.82	0.68	0.93	0.86 ± 0.04	✓
	6	0.75	0.59	0.90	0.84 ± 0.04	✓
	9	0.80	0.64	0.91	0.86 ± 0.04	✓
5	2	0.82	0.71	0.92	0.86 ± 0.04	✓
	4	0.78	0.65	0.90	0.80 ± 0.04	✓
	6	0.73	0.59	0.87	0.81 ± 0.04	✓
	9	0.67	0.54	0.83	0.78 ± 0.04	✓
6	2	0.83	0.72	0.93	0.78 ± 0.04	✓
	4	0.81	0.67	0.92	0.73 ± 0.04	✓
	6	0.79	0.63	0.91	0.75 ± 0.04	✓
	9	0.77	0.61	0.89	0.88 ± 0.04	✓
7	2	0.83	0.72	0.92	0.82 ± 0.04	✓
	4	0.79	0.65	0.91	0.75 ± 0.04	✓
	6	0.76	0.60	0.89	0.73 ± 0.04	✓
	9	0.74	0.56	0.90	0.78 ± 0.04	✓
8	2	0.82	0.71	0.92	0.75 ± 0.04	✓
	4	0.80	0.66	0.91	0.72 ± 0.04	✓
	6	0.77	0.61	0.90	0.70 ± 0.04	✓
	9	0.76	0.58	0.90	0.74 ± 0.04	✓
9	2	0.79	0.69	0.90	0.75 ± 0.04	✓
	4	0.79	0.65	0.90	0.78 ± 0.04	✓
	6	0.76	0.61	0.89	0.86 ± 0.04	✓
	9	0.73	0.58	0.88	0.73 ± 0.04	✓

ID	Date	Median	Q1	Q3	Sensor (NDVI ± U)	Comp?
10	2	0.84	0.73	0.92	0.78 ± 0.04	✓
	4	0.82	0.68	0.92	0.78 ± 0.04	✓
	6	0.79	0.63	0.91	0.85 ± 0.04	✓
	9	0.79	0.63	0.91	0.88 ± 0.04	✓

TABLE 2.25: Comparison of compensated NDVI values (using the proposed method) from multispectral images of ten pistachio trees, collected on September 2, 4, 6, and 9, 2024, under humid conditions, with ground truth NDVI measurements. The check mark indicates compatibility (Comp?) between NDVI values measured by the handheld sensor and those computed using the proposed method.

2.12 Conclusions and Future Work

In PA, VIs such as NDVI play a vital role in assessing plant health and detecting variations in vegetation across fields through remote sensing data. However, the accuracy of these indices can be influenced by factors such as atmospheric conditions and sensor errors, making radiometric compensation essential. This study aims to evaluate the uncertainty model for NDVI measurement. The first preliminary model models the variability of the NDVI while examining the variation of wavelength in the camera sensor's nominal wavelength as an uncertainty source. The resulting uncertainty values range from 0.03 to 0.09 for both dry and fresh. Then the model goes close to reality and was extended by considering OD captured by the multispectral camera within its nominal wavelength and limited bandwidth. The findings indicate that the nominal wavelength of the camera sensor is a significant source of uncertainty, with values ranging from approximately 0.03 to 0.1 for both dry and fresh vegetation. For instance, when the NDVI of a fresh leaf is determined to be 0.814, accounting for its uncertainty of 0.055, the true estimate of the NDVI value for the fresh leaf can fall within the range of $(0.759, 0.869)$, which overlaps with the corresponding range for the dry leaf. Consequently, distinguishing between dry and fresh leaves based solely on the given NDVI values is not precise. After that, a workflow has been designed to evaluate the uncertainty associated with the NDVI by investigating various factors influencing its measurement. This workflow specifically examines how atmospheric conditions affect solar irradiation and vegetation reflectance, as captured by a multispectral UAV camera operating in the R and NIR bands. The research also takes into account OD captured by a multispectral camera within its variation of nominal working wavelength and limited bandwidth, as well as camera SNR. Moreover, the variability of solar irradiance and the variability of the NDVI within the two leaf states are considered. By utilizing MCS, the effect of

each uncertainty source and its combined impact on the NDVI measurement is evaluated. The Wilcoxon Rank Sum Test is used to examine the overlap of NDVI values between dry and fresh leaves under diverse air conditions after uncertainty sources are applied. The results indicate an absence of overlap, so by establishing a threshold, it is possible to distinguish between fresh and dry leaves under different air conditions. However, this threshold is changed when the environmental conditions change, and it is dependent on atmospheric conditions. Furthermore, the results show that, although uncertainty sources affect the NDVI measurement, the variation of NDVI values (based on IQR values) is not significant; therefore, NDVI values remain stable. In addition, the results highlight that the variability of the NDVI within the two considered leaf states, atmospheric conditions, and the camera sensor's nominal wavelength as sources of uncertainty significantly affect NDVI measurements. On the other hand, the other uncertainty sources, solar standard deviation, and camera SNR have minimal effects on NDVI measurements. Then, the proposed workflow is finalized with the inclusion of a radiometric compensation step. A comprehensive radiometric compensation model was developed and implemented using Permaflect Sheets with varying reflectance values. The robustness of this approach was evaluated across multiple experimental parameters, including NDVI uncertainty due to variations in the camera's nominal wavelength, solar irradiance, leaf state, camera SNR, and the combined effects of all uncertainty sources. Results indicate no statistically significant differences in NDVI measurements between dry-clear and humid-hazy atmospheres. This observed consistency suggests that the radiometric compensation model effectively mitigates the influence of fluctuating atmospheric conditions, thereby ensuring the precision and reliability of NDVI assessments. To validate the radiometric compensation method, the study compared the values obtained using the proposed method with those from a real in-field reference panel. Then the model was applied to multispectral images captured by a UAV over pistachio trees under dry atmospheric conditions. The compensated NDVI values were compared with both the conventional approach used in Agisoft Metashape software and ground truth data. The findings demonstrate that the proposed radiometric compensation method significantly enhances the accuracy of NDVI measurements, providing more reliable insights for plant monitoring. However, a limitation of the current study is the lack of a systematic comparison against alternative radiometric compensation methodologies using standardized datasets. While Agisoft Metashape was included as a reference tool, the comparison was limited to the specific dataset collected in this study. Future research should aim to benchmark the proposed method against other state-of-the-art approaches using publicly available and standardized datasets. This would enable more comprehensive performance evaluations and enhance the generalizability of the findings.

Additionally, the field validation was carried out in a single agricultural setting—a

pistachio orchard in Spain—which may constrain the applicability of the results to other contexts. To strengthen the robustness of the model, future studies should consider a wider range of agricultural environments and incorporate additional sources of uncertainty, such as flight parameters (e.g., altitude and image overlap), environmental conditions (e.g., temperature and humidity), sensor tilt, and other relevant variables.

It is also recommended to evaluate the radiometric compensation method not only on healthy vegetation but also on stressed or diseased plants, and across various crop types. Testing the method under a broader range of atmospheric conditions and geographic regions will further improve its reliability and adaptability.

Moreover, applying the proposed approach to other VIs beyond NDVI would broaden its applicability and increase its overall value for PA.

Chapter 3

Use of ML for PA: Plant Disease Identification

Many PA measurements rely on vegetation reflection from RGB or multispectral imaging captured by UAV [2], but the quality of these images is affected by variables such as atmospheric conditions, light exposure, flight parameters, and camera characteristics like wavelength tolerance and SNR [3]. These factors must be considered when analyzing UAV-captured images [4].

Classification of RGB or multispectral images is the process of assigning predefined categories or classes to individual pixels within an image based on the spectral signatures extracted from different wavelength bands. Before the classification phase, feature extraction is a crucial step. Relevant features, such as the mean, SD, and other statistical pixel evaluations, provide essential information for constructing a classifier to identify objects or scenes of interest in the images [139].

In the literature, several studies, such as [140, 141, 142], used ML and DL algorithms for vegetation disease identification and classification, but the assessment of the variability of ML/DL identification and classification against several uncertainty sources are missing. This research objective encompasses capturing RGB images of yellow rust winter wheat diseases using UAVs, analyzing the labeled images for disease identification and classification, and performing a sensitivity analysis of a trained classification algorithm against several uncertainty sources, such as blurring. The study utilizes MATLAB image processing tools to extract meaningful features, employing a one-way ANOVA to identify and prioritize critical features for disease diagnosis, and using ML classification approaches for predicting the plant disease level. Additionally, by manipulating the images and adding non-idealities, including blurring, variations in light conditions, and noise affecting the images, the sensitivity of the provided classification approach is assessed. This chapter is structured as follows. Section 3.1 describes the related works. The proposed workflow and ML algorithms for vegetation disease identification and

classification are discussed in Section 3.2. Section 3.3 reports preliminary experimental results. The sensitivity analysis of the provided ML model is assessed in Section 3.4. The last section highlights the outcome and gives some suggestions.

The content of this chapter has been published at the IEEE International Workshop on Metrology for Agriculture and Forestry (MetroAgriFor) in 2024 [143].

3.1 Related Work

The study [141] explores the effectiveness of a low-cost five-band multispectral camera and a low-altitude UAV platform for automatically detecting wheat yellow rust. The researchers carefully designed experiments involving the infection of winter wheat with varying levels of yellow rust fungi. Aerial multispectral images were captured at different developmental stages of the disease using UAVs operating at altitudes of 16–24 meters, providing high-resolution imagery with ground resolutions of 1–1.5 cm/pixel. Objectives include discriminating healthy and infected plants, selecting optimal spectral bands and indices, and developing a cost-effective monitoring system for farmland scales. The researchers developed an automated yellow rust detection system by employing ML techniques, specifically a random forest classifier, trained on labeled UAV aerial multispectral imagery. The experimental results demonstrated promising performance, with an average Precision, Recall, and Accuracy of 89.2 %, 89.4 %, and 89.3 %, respectively, achieved at a diseased stage (45 days after inoculation). Furthermore, the study identified the top three Spectral VIs for discriminating between healthy and infected wheat plants as Radiometric Vegetation Index (RVI), NDVI, and Optimized Soil-Adjusted Vegetation Index (OSAVI), with NIR and R identified as the top two spectral bands for effective disease detection.

The study [144] addresses the challenge of detecting yellow rust disease in winter wheat fields using UAVs and advanced image analysis techniques. By using high-resolution images captured by UAVs equipped with hyperspectral sensors, the researchers developed a new computer model based on DL. The model, based on Deep Convolutional Neural Network (DCNN), utilizes multiple Inception-ResNet layers for feature extraction and optimization. By integrating spatial and spectral information, the model exhibited strong performance throughout the entire growth cycle, particularly during the advanced stages of disease progression. The overall accuracy of the proposed model (85.0 %) surpassed that of the random forest classifier (77.0 %), highlighting the efficacy of integrating both spectral and spatial information for enhancing the precision of crop disease detection with high-resolution UAV hyperspectral imagery.

The study [145] addresses the challenging task of detecting wheat yellow rust severity using a real-time yellow rust detection algorithm named Efficient Dual Flow UNet (DF-UNet) to detect different levels of yellow rust based on UAV multispectral images. The authors introduce a pruning strategy and an SCA (Spatial and Channel Attention) module to enhance the network's receptive field and improve category differentiation efficiency. Building upon these enhancements, a novel DF-UNet architecture is proposed to tackle the severity classification problem. Through comparative analysis, the proposed method is evaluated against other state-of-the-art algorithms. Results indicate that the proposed model achieves an outstanding overall accuracy of 96.9 %, with a total of 8.67 million coefficients utilized in the algorithm and computational operations.

The research [146] showcases the efficacy of a UAV equipped with an aerial multispectral sensor for diagnosing yellow rust infection in spring wheat crops. The captured multispectral images underwent thorough feature engineering, with disease-centric VIs and Grey-Level Co-occurrence Matrix (GLCM) texture features crafted to analyze spectral and spatial dimensions, respectively. A ML pipeline, incorporating Support Vector Machine (SVM), Random Forest (RF), and MLP algorithms, was devised to classify healthy, mildly infected, and severely infected plots in the field. Additionally, a custom 3-Dimensional Convolutional Neural Network (3DCNN) utilizing feature learning was employed as an alternative prediction method. The study identified red-edge and NIR spectral bands as crucial for distinguishing between healthy and severely infected wheat. Furthermore, specific VIs and texture features were found to be highly correlated with disease severity. The 3D-CNN-based wheat disease monitoring achieved the accuracy level 79.0 % for the spectral-spatio-temporal fused data model.

In multispectral imaging, the acquired data is typically represented as a data cube, where each pixel contains information across multiple spectral bands (spatial dimensions x spectral bands). RGB imaging captures data in a three-dimensional format where each pixel contains color information represented by three channels: Red, Green, and Blue. Usually, low-cost UAVs are equipped with RGB cameras, while UAVs with multispectral cameras are much more expensive. The novelty of this study lies, firstly, in the utilization of an RGB camera to evaluate the efficacy of a classifier in distinguishing various levels of unhealthy and healthy wheat states, a task typically carried out using multispectral or hyperspectral cameras in PA applications [60, 147]. The adoption of an RGB camera significantly reduces platform costs. Secondly, a sensitivity analysis of ML algorithms, which is missing in the literature, is considered for the provided ML classification in this research.

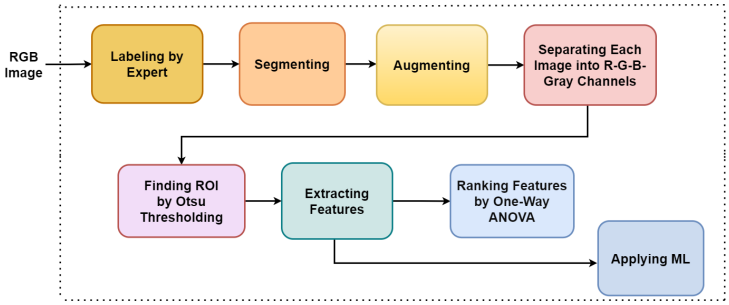

FIGURE 3.1: Proposed workflow from labeling images by experts, to extracting features, applying One-Way ANOVA, and classifying yellow rust wheat disease by using ML.

3.2 Proposed Workflow

The proposed workflow is depicted in Fig. 3.1. Experts label segments of the RGB image into six classes: healthy and five levels of yellow rust infection (15 %, 30 %, 50 %, 60 %, and 100 %). These labeled segments are then selected for manual segmentation in MATLAB, utilizing 97 images. From each class, 20 % of the images are randomly selected to form the test set, while the remaining images are allocated to the training set. Due to the limited number of images, various augmentation techniques are applied independently to the training and test sets to increase their size. These augmentation methods include contrast adjustment, blurring, motion blur application, Gaussian and speckle noise introduction, and image translation. The initial number of images and the augmentation ratios for each class, corresponding to wheat sickness levels of 100 %, 60 %, 50 %, 30 %, 15 %, and 0 %, are paired sequentially as follows: (36,5), (9,22), (13,15), (14,14), (16,12), and (9,22). After applying augmentation, each class results in 200 images, yielding a total of 1200 images. Of these, 80 % of images (960) are allocated for training and validation, while the remaining 20 % (240) are reserved for the test set. Following augmentation, each image is transformed into a four-channel representation comprising Grayscale, Green, Blue, and Red channels. Otsu's thresholding method is then employed on each channel to delineate ROI corresponding to plant leaves. The performance of the Otsu method for ROI detection under different ambient light conditions was explored by manually testing the global threshold scaling factor in the range from 0.5 to 2 for four channels of the ROI. This evaluation helped determine how varying the global threshold affects the detection performance of the ROI, ensuring more robust detection across varying conditions. After testing, the best ratio was found to be 0.8, providing the optimal balance for accurate ROI detection. This ensures that the detection process is less sensitive to changes in brightness or contrast across different scenes.

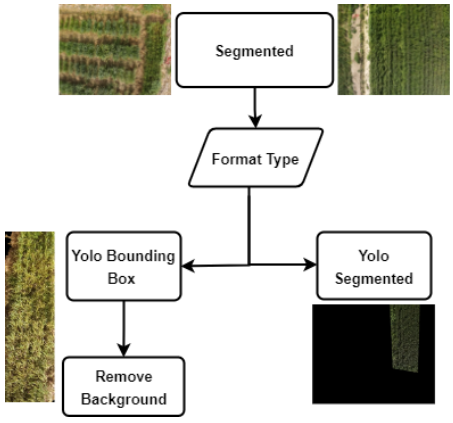

FIGURE 3.2: The process of identifying the ROI of the images within the dataset.

Thereafter, the preprocessed images are subjected to feature extraction procedures, encompassing statistical metrics such as mean, SD, entropy, and so on in both the time and frequency domains. To identify the prominent features for distinguishing between healthy and unhealthy plant states, a one-way ANOVA is conducted on each extracted feature across all images and classes. Consequently, various ML algorithms are applied to the extracted features and their corresponding labels in the training set and test set separately to verify the efficacy of each algorithm in classification tasks. The subsequent section will provide a detailed presentation of each step in the workflow.

3.3 Preliminary Experimental Results

3.3.1 Dataset

The RGB imagery was acquired from winter wheat fields located in the Ahvaz province of Iran, utilizing the RGB camera integrated into the DJI-P4 multispectral camera. The camera offers a resolution of about 2 megapixels. Image acquisition occurred over the period from September 11th to September 15th, 2023. The image acquisition process was performed at altitudes ranging from 28 to 31 meters. Expert annotators labeled the images using two distinct methodologies: one subset was annotated using bounding box coordinates, while the remaining images were labeled based on segmented areas. Each bounding box is defined by five parameters: the class label (wheat sickness level), the normalized x- and y-coordinates of the box's center, and its width and height, both relative to the image dimensions. Segmented areas are represented by the class label and a series of normalized (x, y) coordinates outlining the polygon boundary (refer to

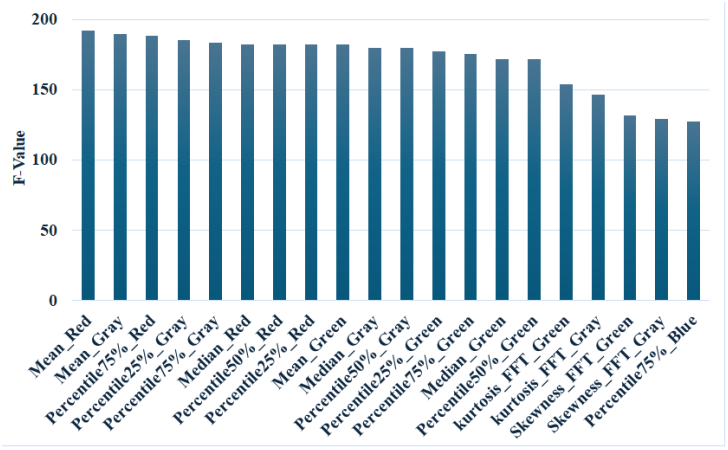

FIGURE 3.3: Top 20 features ranked by F-value of the One-way ANOVA for each channel of the RGB image and its grayscale one.

Fig. 3.2). In some cases, the background is manually removed in the bounding box format.

3.3.2 Features ranking

In this study, a comprehensive suite of statistical analyses was employed, encompassing measures such as the mean, SD, variance, entropy, skewness, kurtosis, median, and various percentiles (25th, 50th, and 75th) applied to a single channel of ROI images in both the time and frequency domains. Subsequently, a one-way ANOVA was conducted for each of these features across all images within all classes. The resulting F-values were then sorted to identify the top 20 features, which were depicted in Fig. 3.3. During the analysis, as shown in Fig. 3.3, particular emphasis was placed on the significance of the Red, Gray, and Green channels, which were deemed as the most crucial for discerning patterns within the data. Conversely, the Blue channel exhibited comparatively lower sensitivity in capturing variations among the image classes.

3.3.3 Classification performance

Utilizing the Classification Learner application within MATLAB, a comprehensive exploration of ML classification algorithms was conducted on both training and testing dataset features. Regarding datasets, initially, the images are separated into test and training/validation sets; the test set is completely independent from the training set. 20 % of the images are used for testing (240 images), while the remaining are used

for training/validation (960 images). Then training/validation images are subjected to a 5-fold cross-validation procedure to avoid overfitting. In this setup, 80 % of the training/validation images are used for training (768 images), and 20 % (192 images) is reserved for validation. This strategy was employed to reduce the risk of overfitting and to improve the robustness of the model. In addition, the classification model did not see the images used for testing during training. Among ML classification algorithms, the Standard Neural Network algorithm exhibited notably high accuracy, achieving 88.5 % on the training set. Conversely, the algorithm yielded lower accuracy, reaching 76.2 % after the evaluation of the test set. The Standard Neural Network utilized in this study is a Wide Neural Network based on the Feedforward Neural Network architecture. This architecture consists of one input layer, one fully connected hidden layer, and one output layer. The single hidden layer contains 100 neurons. Normalization layers were implemented to standardize the input data, enhancing the model's performance by ensuring that the data is centered and scaled appropriately. The lower accuracy of the Wide Neural Network on the test set prompted its exclusion from further consideration. Following a comprehensive evaluation, the Linear Discriminant Analysis (LDA) algorithm was identified as the preferred model, demonstrating superior performance with an accuracy of 85.0 % on the test set. Consequently, it was selected as the preferred classification approach for detecting yellow rust disease. LDA is a supervised learning algorithm for classification tasks in ML. It identifies a linear combination of features to separate classes, projecting data onto a lower-dimensional space to maximize class separation based on assumptions of Gaussian distribution, equal covariance matrices, and linear separability [148, 149, 150]. The LDA algorithm works as follows: (1) data preparation: LDA requires labeled data, where each data point is associated with a class label, (2) compute the mean of each class, (3) compute the total mean of all data, (4) calculate the between-class scatter matrix S_b, which represents the spread between different classes. S_b is computed as the sum of the outer products of the differences between class mean vectors and the overall mean vector, (5) computes the within-class scatter matrix S_w, which represents the spread of data within each class. S_w is computed as the sum of scatter matrices of individual classes, (6) compute eigenvectors and eigenvalues: solve the generalized eigenvalue problem $S_w^{-1} S_b \mathbf{w} = \lambda \mathbf{w}$, where $\mathbf{w}$ is the eigenvector and λ is the eigenvalue. The eigenvectors represent the directions (linear discriminants) that maximize the separation between classes, and the eigenvalues represent the amount of variance explained by each discriminant. (7) Select discriminants: sorting eigenvectors in descending order according to their corresponding eigenvalues. These eigenvectors define the subspace onto which the data will be projected. The first k eigenvectors are then used as a lower-dimensional space, (8) projecting the original data onto the subspace spanned by the selected eigenvectors. This results in a lower-dimensional representation

TABLE 3.1: The performance analysis of the LDA algorithm while applying it to the test dataset.

ML Algorithm	**Accuracy (Validation)**	**Accuracy (Test)**
Linear Discriminant Analysis	85.5%	85.0%
Standard Neural Network	88.5%	76.2%

of the data while maximizing class separability, and (9) classification: after dimensionality reduction, standard classification algorithms (e.g., nearest neighbors, support vector machines) can be applied to the transformed data for classification tasks [151, 152].

Table 3.1 presents the accuracy scores based on Equation (3.1) attained during validation and testing for both the Standard Neural Network and LDA algorithms. Additionally, Fig. 3.4 illustrates the confusion matrix resulting from applying the Standard Neural Network algorithm to the training dataset, while Fig. 3.5 depicts the confusion matrix derived from executing the LDA algorithm on the test dataset. Further analysis of the LDA algorithm's performance based on the test dataset's confusion matrix reveals precision Equation (3.2), recall Equation (3.3), F1 values Equation (3.4), for each class and Macro F1-score Equation (3.5) as the average of F1 values along with the other respective averages, as detailed in Table 3.2. The experimental results demonstrated promising performance, with an average Precision, Recall, and F1 of 84.9 %, 85.0 %, and 84.8 %, respectively, achieved at the diseased state levels.

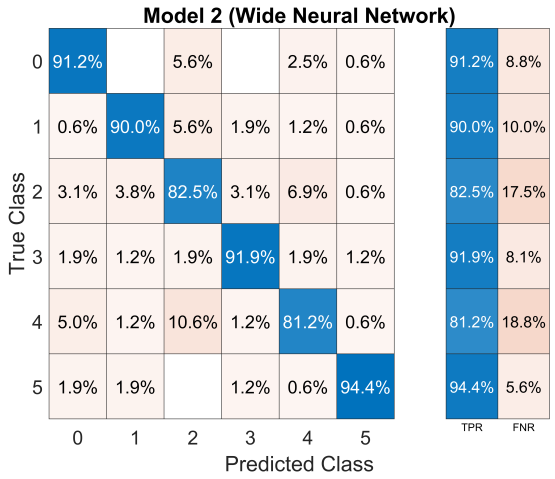

FIGURE 3.4: The confusion matrix resulting from applying the Standard Neural Network algorithm to the training dataset.

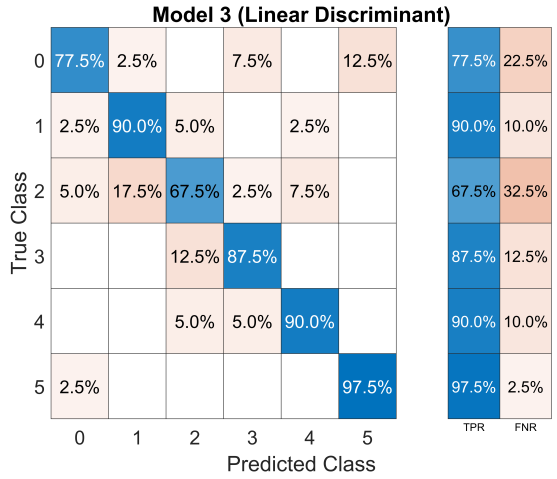

FIGURE 3.5: The confusion matrix resulting from applying the LDA algorithm to the test dataset.

$$Classificationaccuracy = \frac{Number\ of\ Correct\ Predictions}{Total\ Number\ of\ Predictions} \tag{3.1}$$

$$Precision(class\ c) = \frac{TP(class\ c)}{TP(class\ c) + FP(class\ c)} \tag{3.2}$$

$$Recall(class\ c) = \frac{TP(class\ c)}{TP(class\ c) + FN(class\ c)} \tag{3.3}$$

$$F1(class\ c) = 2 \cdot \frac{Precision(class\ c) \cdot Recall(class\ c)}{Precision(class\ c) + Recall(class\ c)} \tag{3.4}$$

$$MacroF1 - score = \frac{1}{N} \cdot \sum_{i=1}^{N} (F1 - Score(classc)) \tag{3.5}$$

TABLE 3.2: The detailed performance analysis of the LDA algorithm while applying it to the test dataset with different sickness levels.

Sickness %	**Class**	**Precision**	**Recall**	**F1**
100	0	88.6%	77.5%	82.7%
60	1	81.8%	90.0%	85.7%
50	2	75.0%	67.5%	71.1%
30	3	85.4%	87.5%	86.4%
15	4	90.0%	90.0%	90.0%
0	5	88.6%	97.5%	92.9%
Average	**-**	**84.9%**	**85.0%**	**84.8%**

3.4 Sensitivity Analysis of the LDA Model

To assess the model's sensitivity, various sources of uncertainty, including blurring, varying light conditions, contrast adjustments, Gaussian noise, speckle noise, and their combinations, were introduced to the test dataset 100 times repeatedly. Random numbers were drawn from a uniform distribution to induce variation in the parameters of these uncertainty sources. Each image in the test set is processed individually, with various uncertainty sources applied systematically. For instance, in the case of blurring, the SD is randomly varied between 0.0001 and 1.1 during each iteration. For speckle noise, the variance is randomly adjusted from 0 to 0.038. In terms of light conditions, brightness is altered within a range of -0.25 to 0.35. The variance for Gaussian noise is modified from 0 to 0.025, while random values are varied between 0.6 to 2.3 for contrast. Additionally, when considering the combination of all uncertainty sources, all parameters are simultaneously altered to evaluate their collective impact on the images.

The accuracy results of the LDA model after 100 iterations are presented in Table 3.3. Statistical parameters such as the Min, Max, mean, MED, Q1, Q3, and IQR are used to assess the accuracy of the model. These metrics are utilized because the accuracy result of the model does not follow a Gaussian distribution. According to the box plot of the model sensitivity versus various uncertainty sources, which is depicted in Fig. 3.6, a higher Med value indicates greater accuracy of the model, while a higher IQR value illustrates higher variability of the model to specific noise. Among the various uncertainty sources, the Med accuracy value in the presence of blurring, measured at 85.8 %, surpasses that of speckle noise, which stands at 84.6 %, as well as all other noise types. This indicates that the model's sensitivity to uncertainty sources when subjected to blurring noise and speckle noise is more robust than the others. While the model's accuracy is highest with blurring followed by speckle noise, the IQR of the model under

TABLE 3.3: Statistical parameters: Min, Max, Mean, MED, First and Third Quartiles (Q1, Q3), and IQR of LDA model accuracy resulting from the model sensitivity analysis with various uncertainty sources.

Uncertainty Source	Min	Max	Mean	Med	Q1	Q3	IQR
Blurring	52.5%	89.2%	78.3%	85.8%	67.3%	87.9%	20.6%
Contrast	31.7%	88.8%	62.0%	58.8%	47.7%	76.9%	29.2%
Gussie Noise	71.3%	89.2%	79.1%	77.9%	74.8%	83.5%	8.8%
Light Condition	40.0%	87.9%	69.8%	72.9%	57.5%	80.8%	23.3%
Speckel Noise	79.2%	87.9%	84.6%	84.6%	83.5%	85.8%	2.3%
Combination All	12.9%	85.8%	47.1%	47.7%	36.3%	58.5%	22.3%

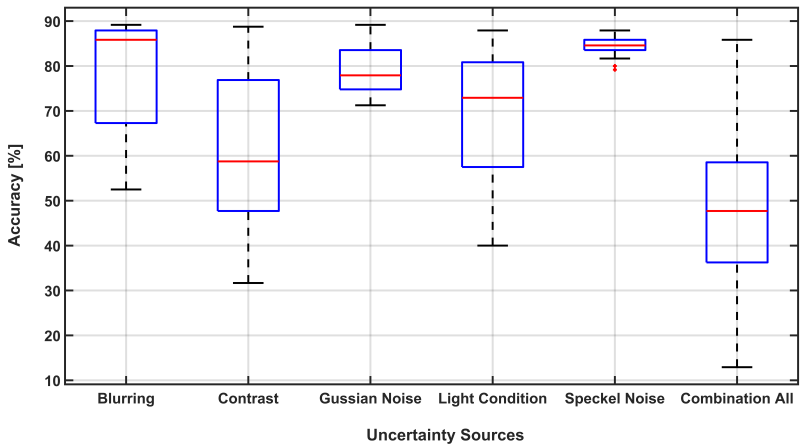

FIGURE 3.6: Sensitivity analysis of the LDA model while applying various uncertainty sources.

blurring conditions (20.6 %) far exceeds that under speckle noise (2.3 %), indicating higher sensitivity of the model to blurring uncertainty source compared to speckle noise. Moreover, the model exhibits the lowest sensitivity to speckle noise in comparison to other noise types.

Analysis of box plots and IQRs reveals that contrast significantly impacts model variability, followed by lighting conditions and blurring noise. Gaussian and speckle noise showed lower variability individually and collectively. The model was more robust to speckle noise, with a higher median accuracy and lower IQR, while it was highly sensitive to contrast noise, exhibiting a lower median accuracy and higher IQR.

3.5 Conclusions and Future Work

This study develops a workflow for detecting yellow rust wheat disease using RGB images captured by UAVs from a winter wheat farm. The proposed approach involved extracting meaningful features from the images using image processing tools, conducting a one-way ANOVA to identify critical features, and applying ML algorithms for disease classification. Based on the one-way ANOVA analysis of features extracted from the Red, Green, and Blue channels of RGB images and their grayscale ones in discerning patterns, the Blue channel has less effect in discerning the yellow rust pattern disease.

Moreover, the findings revealed that the LDA algorithm exhibited superior performance, with an accuracy of 85.0 % on the test set with six classes, outperforming other ML algorithms. Consequently, the LDA algorithm was selected as the preferred model for yellow rust disease classification. However, its accuracy is lower compared to UAV hyperspectral images used for binary classification of the same disease, as reported in the paper [60], with accuracies ranging from 92 % to 96 %, the use of an RGB camera significantly reduces platform costs.

The ML algorithms work on a dataset which was carefully partitioned to ensure that the test set remained fully independent from the training/validation set, with 5-fold cross-validation applied to the training data to reduce overfitting and improve robustness. Nevertheless, the dataset remains limited in size and diversity, which may affect the model's generalizability to different environments or wheat varieties.

To address this, future work will focus on expanding the dataset with images from multiple growing conditions, crop types, and locations to enhance the model's generalizability.

Also, this study conducted a sensitivity analysis of the ML algorithm, which was missed in the literature, to assess its robustness against uncertainties, such as blurring and other noises affecting the acquired images. The model showed strong resilience to speckle noise but high sensitivity to contrast noise. To address this, future studies will incorporate radiometric compensation for the RGB channels using target reference points to manage lighting variations. Additionally, the segmentation process could potentially be automated through the utilization of ML or DL algorithms, thereby enhancing efficiency and reducing manual intervention. Furthermore, future work will focus on analyzing the performance of the ML algorithm with a reduced number of features. Finally, this research offers valuable insights for crop management, supporting sustainable and efficient farming practices. Future research can explore other sources of uncertainty and assess the scalability of the workflow for different crop diseases and environments.

Chapter 4

Use of IoT for PA: Monitoring the Health State of Trees

Taking care of trees and plants is now more critical than ever due to factors like overpopulation, rapid urbanization, and changes in the environment [153]. Trees are not only essential for maintaining the environment, but they also greatly influence human activities. Having healthy trees brings various advantages to humans, such as stopping soil erosion, absorbing carbon dioxide, purifying the air, reducing noise pollution, filtering dust, and improving the design of landscapes. Essentially, trees help to alleviate global warming by absorbing greenhouse gases [154, 155, 8]. Furthermore, in several cities, municipal governments take measures to manage and protect heritage trees from chronically stressful regimes in terms of harsh microclimate and soil conditions [156, 8]. Thus, it is essential to monitor them for a long time to assess the natural and human causes of tree losses to make recommendations for future heritage tree conservation [156, 8]. A highly effective system for assessing the health of trees is crucial for monitoring and providing early warnings of potential issues. The conventional approaches to evaluating tree health entail expert-driven manual evaluations that are constrained in terms of the temporal intervals and frequency of assessments, and they demand substantial labor input from tree specialists, which is not very efficient. With the advancement of technology, diverse ways of monitoring tree health based on remote sensing have been suggested. These new ways could overcome the limits of manual methods [154, 8].
Remote sensing refers to using several technologies to monitor and measure physical quantities from a target. This technique is used in various fields like land surveying, geography, and other earth sciences, as well as in the IoT realm. In IoT, a "Thing" refers to any device embedding sensors capable of collecting and transmitting data across the Internet network without the need for manual intervention [157, 8]. This research aims to present the architecture of an IoT system for the health state monitoring of trees. In particular, the physical layer and the adopted sensors will be described. In the following,

a brief review of systems for environmental monitoring, the architecture and the metrological characteristics of the adopted sensor nodes and the gateway architecture, and the implementation of this system are presented. Finally, the last part summarizes some relevant topics discussed in the research and describes future activities in the field [8]. The content of this chapter has been published at the IEEE 7th International Conference on Internet of Things and Applications (IoT) in 2023 [8].

4.1 Related Work

The authors in [153] introduce an IoT-based framework for intelligent urban tree management. This system monitors various tree attributes such as air quality, solar radiation, and acoustic pollution to optimize urban planning and afforestation strategies. The architecture comprises three segments: (i) Sensor Node, (ii) Cloud Integration, and (iii) User Experience. It employs a range of sensors connected to a Raspberry Pi 3. The Raspberry Pi 3 is linked to the Internet through an Arduino Shield with NarrowBand IoT (NB-IoT) and LTE (Long Term Evolution) Cat-M1 modules. Sensors include DHT22 for temperature and relative humidity, MQ135 for gas, YL-69 for moisture, Light Dependent Resistor (LDR), SEN-9198 for vibration, air quality, sound, and MCP3008 for 8-channel analog input as the Raspberry Pi does not directly support analog inputs. Each tree has specialized NB-IoT and LTE module sensors for direct communication with an IoT cloud server. Data is analyzed, categorized, and sent to a mobile app via IBM Cloud API for easy access and action. While this approach focuses on urban monitoring, another direction has been explored by Trinovita et al. [158] introduces an IoT-based framework for autonomous plant fertilization and irrigation. This system is controllable and observable via an Android-based smartphone interface. Powered by solar photovoltaic energy, the framework is constructed using specific components, including a 100 Wp solar module, a 30 A solar charge controller, a deep-cycle battery, an Arduino Microcontroller Unit (MCU), an ESP8266WiFi module, a DHT11 sensor for air temperature and relative humidity, a soil moisture sensor, and a 12 V DC electric solenoid valve. In practice, for instance, when the soil moisture sensor detects dry soil and the air temperature sensor indicates cool atmospheric conditions, the MCU activates the electric solenoid valve. This results in the discharge of water containing fertilizer onto the soil until an adequate moisture level is achieved. The research outlined in [159] introduced an integrated framework that merges the IoT with crop cultivation, employing cloud computing to oversee crop growth. This architectural model consists of three layers: (i) the physical layer, (ii) the IoT layer, and (iii) the com-op layer, offering comprehensive management for monitoring and automation. The physical layer acts as the automation hub, controlling the smart agricultural system using various sensors like soil moisture, temperature, motion detection, water level, and photosynthesis sensors.

The IoT layer collects data from the physical layer and forwards it to the com-op layer for processing. Within the com-op layer, security protocols are applied for secure data transmission across cloud services. This layer serves as a data repository for both raw and processed data. The analyzer processes data, determines subsequent actions, and executes processes based on the analysis outcomes. This framework provides a robust system for addressing various agricultural challenges, including quality management and supply-chain control. Despite their contributions, these previous systems fall short in terms of integrating multiple physiological and environmental parameters. To address this gap, the present work introduces a novel system with the following key innovations: (i) a specialized monitoring system for assessing tree health, encompassing measurements such as trunk variation, sap flow, LAI, and NDVI for evaluating greenness, (ii) precise monitoring of environmental factors that include not only air relative humidity and temperature but also various gas concentrations, and (iii) a Low-Power Wide Area Network (LPWAN) modular design utilizing Long Range (LoRa), technology, which offers advantages in terms of energy conservation in battery-powered nodes, capacity enhancement, and cost-effectiveness [160, 8]. LoRa is a spread spectrum modulation technique derived from chirp spread spectrum (CSS) technology and is the first low-cost implementation of chirp spread spectrum for commercial use. Long-range wireless radio frequency technology is a long-range, low-power wireless chipset, often referred to as LPWAN, suitable for implementing networks of devices requiring wireless connectivity [161]. LoRa uses bands of radio frequency sub gigahertz free as 433 MHz, 868 MHz (Europe) and 915 MHz (North America) allowing long-range transmissions (over 10 km in rural areas, 3 km to 5 km in highly urbanized areas) with low energy consumption [161]. A comparison of the sensor quantity aspect of the design presented in this research with the other research referenced in this section can be found in Table 4.1 [8].

TABLE 4.1: Comparison of the design parameters in terms of sensor quantities concerning state-of-the-art [8] © 2023 IEEE.

Quantities\Research	**This Research**	**In Research [153]**	**In Research [158]**	**In Research [159]**
Motion Detection	Trunk variation	Piezo Vibration Sensor	-	✓
Photosynthesis	PAR	LDR	-	✓
SAP flow	✓	-	-	✓
NDVI	✓	-	-	-
LAI	✓	-	-	-
Soil Moisture	-	✓	✓	✓
Sound Sensor	-	✓	-	-
Tree's stability	✓	-	-	-
Fire Detection	✓	-	-	-
Temperature, Humidity	✓	✓	✓	✓
Other Environmental Node	Wind Speed and Direction, Dew Point, Pressure, Precipitation	-	-	Air Flow
Measuring Gas Concentration	OPC, SO2, NO2, CO, CO2, VOC	NOx, Alchohol, NH3, benzene, CO, CO2, etc	-	-

4.2 The Architecture of Treelogy Systems

According to [162], a comprehensive architecture for an IoT system includes four layers: (i) the physical layer, (ii) the data exchange layer, (iii) the information integration layer, and (iv) the application service layer as shown in Fig. 4.1.

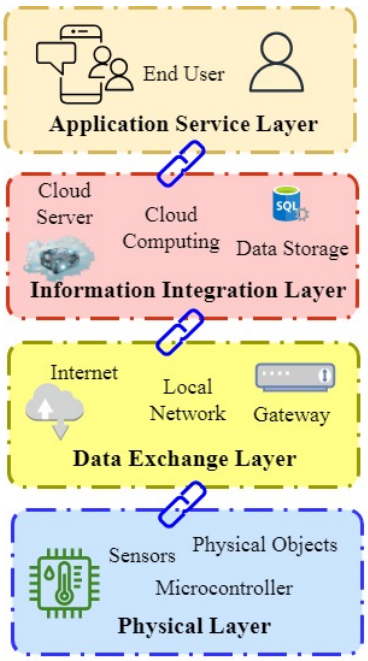

FIGURE 4.1: General architecture of an IoT-based system.

The physical layer consists of sensor nodes designed to enable the monitoring and control of physical quantities of objects. These nodes include components such as microcontrollers, smart sensors that communicate the measurement data to the microcontroller, power supplies, and wireless and/or wired transceivers enabling communication between nodes. The data exchange layer facilitates Internet connectivity for sensor nodes. It involves collecting data from sensors and transmitting it over the Internet. This layer can be implemented in two ways: concentrator nodes or gateways connecting sensor nodes to the Internet, or direct Internet connectivity for sensor nodes. The former conserves power, suitable for battery-powered nodes. The information integration layer, also known as the middleware layer, handles the storage, analysis, and processing of large amounts of data from the data exchange layer. It utilizes technologies like databases, cloud computing, and big data processing to provide concise and user-friendly information to end users. The application service layer offers services that let users manage the

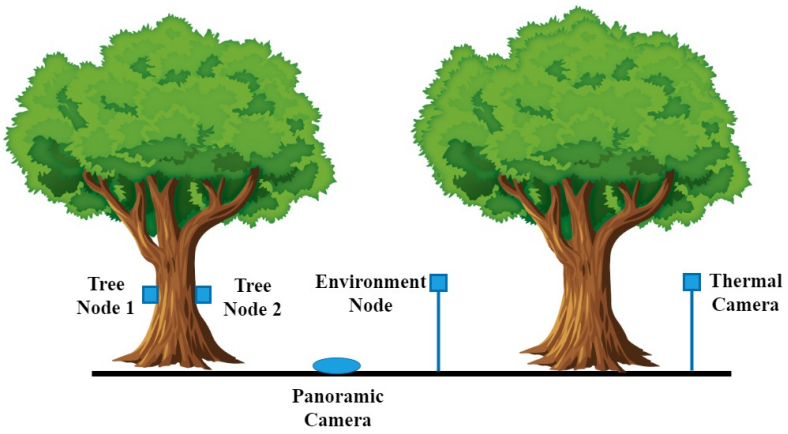

FIGURE 4.2: The proposed *Treelogy* system [8] © 2023 IEEE.

IoT system using the integrated information provided by the integration layer. Users can view information and give commands to the IoT nodes through this layer. To adapt this model to the specific requirements of tree health monitoring, the proposed IoT system for tree health monitoring is based on the above-mentioned four-layer structure. In the following, the physical and data exchange layers of the tree monitoring system are presented [8]. The monitored physical quantities refer to internal tree characteristics, tree stability, visual inspection, and environmental parameters. These factors change over time and significantly impact tree growth, necessitating continuous monitoring. The proposed system captures measurements, gathers data, and transmits them to the cloud server and the Internet. To understand how these layers are implemented in practice, the physical layer of the proposed Treelogy system is depicted in Fig. 4.2. This layer encompasses a gateway and diverse nodes, including tree nodes 1 and 2, a node with a thermal and panoramic camera, and an environmental node. Each of these nodes is equipped with an MCU and a LoRa Transceiver. Certain sensors establish communication with the MCU using serial digital interfaces, while the outputs of other sensors are presented in analog format. The functioning of the MCU embedded in each sensor node is as follows: it remains in sleep mode at all times and wakes up when a Real-Time Clock (RTC) event occurs. This event is generated based on a pre-defined sampling period. Upon waking up, the MCU acquires measurements using either the built-in nalog-to-Digital Converter (ADC) for analog sensors or the digital interfaces for digital sensors. Subsequently, each digital value is scaled based on the sensor's sensitivity coefficient to yield a meaningful digital output. Then, the MCU transmits the acquired data to the

gateway via LoRa, and then returns to sleep mode [8]. The integrated board (B-L72Z-LRWAN1, STM32L72CZY6TR MCU) compactly accommodates the LoRa, transceiver chip with its antenna and the MCU and these two are communicated via the Serial Peripheral Interface (SPI) [8]. The data exchange layer encompasses the wireless sensor network, specifically the implemented LoRa communication protocol that facilitates data exchange between the sensors and the gateway. This layer also involves the protocol utilized to transmit on-demand data to the Cloud via the Internet. It means that the database is on the gateway and the data are available on demand through the Internet connection [8]. In the following subsections, a hardware implementation of the gateway, nodes, and a comprehensive overview of each node, along with its associated sensors, is provided.

4.2.1 Gateway

This serves as the central coordinating unit (or master node) within the distributed measurement system. Its primary functions include managing communication with sensor nodes and synchronizing system timing. Additionally, it incorporates a database for efficient data storage and retrieval.

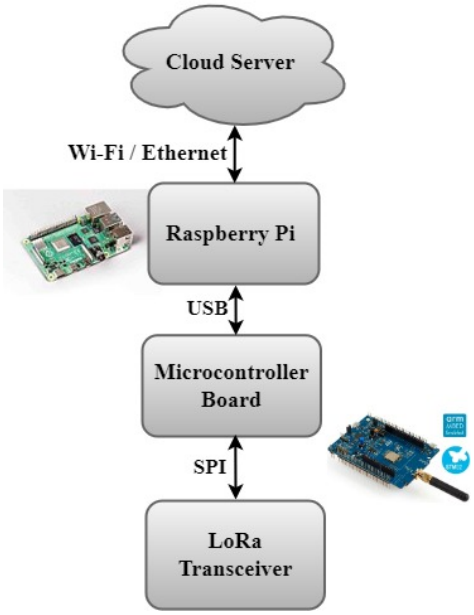

FIGURE 4.3: The architecture of gateway node [8] © 2023 IEEE.

The implementation of the gateway is depicted in Fig. 4.3 and encompasses an MCU, a LoRa, a transceiver, and a Raspberry Pi. Within this layer, an LoRa Transceiver and an MCU are utilized to handle the data acquisition, which is transmitted by each node and sent via USB to the Raspberry Pi module. Raspberry Pi stands as an excellent choice for an IoT gateway due to its compact size, low power consumption, and versatility. Its small size, coupled with its ability to be powered via a simple micro-USB cable, renders it highly versatile for deployment across various scenarios. The Raspberry Pi contains an InfluxDB time-series database and serves Grafana as a web-based application for data visualization and user interaction. Additionally, the system maintains a local table acting as a whitelist, which enumerates the authorized devices permitted to connect to the network. Each device entry in this table is uniquely identified by an ID address and is associated with its corresponding measurement type. Moreover, its diverse connectivity options, encompassing Ethernet, Wi-Fi, and Bluetooth, facilitate simplifying the connection with a wide array of IoT devices [8].

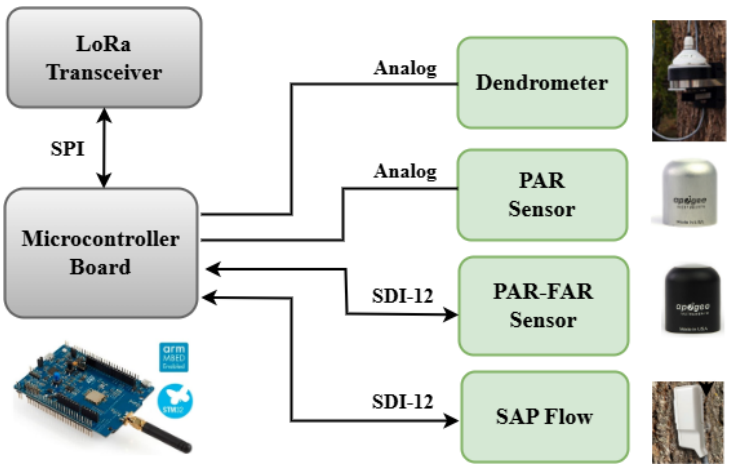

FIGURE 4.4: The architecture of tree node 1

TABLE 4.2: Tree node 1, sensors' information [8] © 2023 IEEE.

Sensor Name	Measured Quantities	Measurement Range	Metrological Characteristics
Dendrometer DBV60	Trunk Increments	60 mm Circumference	Resolution: 1 μm
Sensor ExPAR SQ-612-SS	Radiation in a range of 400 to 750 nm ±5 nm	0 to 4000 $\mu mol \cdot m^{-2} \cdot s^{-1}$	± 5 %
Sensor **PAR-FAR!** S2-411-SS	Radiation reflected from surfaces in Red = 389 to 692 nm ± 5 nm NIR = 700 to 750 nm ± 5 nm	Red = 0 $to 87.6 W/m^2$ NIR= 0 to 58 W/m^2	± 5 %
Sensor SFM-5 Sap Flow	Sap Flow Rate	-200 to >+1000 cm/hr heat velocity	<3 % or ±0.1 cm/hr heat velocity

4.2.2 Tree Node 1

Following the definition of the gateway architecture, this node tracks key physiological parameters of the tree, including trunk circumference, sap flow, and photosynthetically Photosynthetically Active Radiation (PAR) across different wavelengths. The sensors for this node are illustrated in Fig. 4.4, encompassing a dendrometer, SAP Flow, PAR, and NDVI Sensors. Detailed information regarding the measured quantities, measurement ranges, and metrological characteristics of these sensors can be found in Table 4.2, [8]. Fig. 4.5 depicts the overall schematic of the node, whereas Fig. 4.6 provides a detailed representation of its circuit diagram.

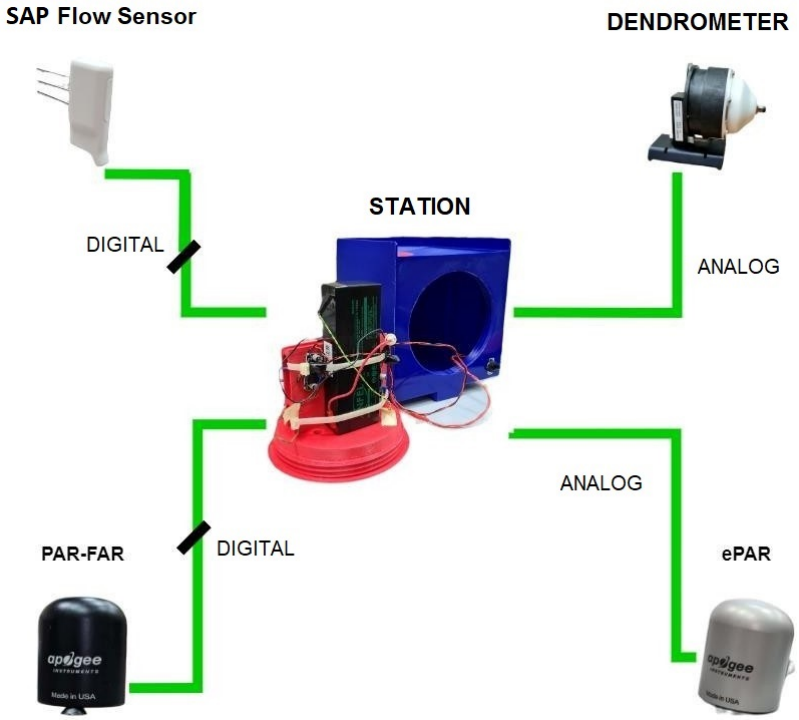

FIGURE 4.5: General schematic of Tree Node 1.

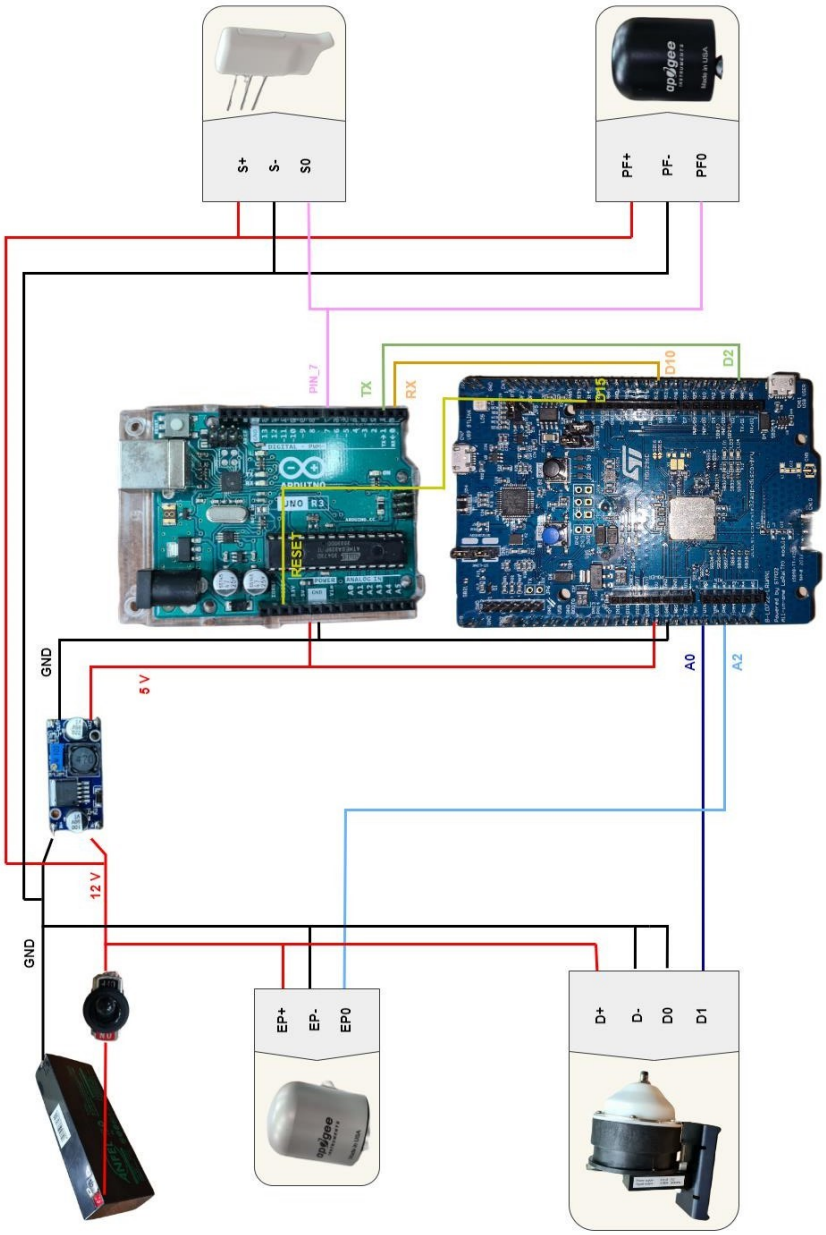

FIGURE 4.6: Circuit diagram of Tree Node 1.

4.2.2.1 Dendrometer DBV60

A dendrometer sensor is used to measure plant growth, specifically the circumference or diameter of trees. High-resolution dendrometers track daily stem size changes, contracting during the day due to transpiration and expanding at night as moisture is absorbed. The DBV60 Band Dendrometer utilizes a stainless-steel band around a tree to precisely measure trunk circumference (1 μm resolution) [163]. It provides an analog output in voltage proportional to the measured trunk circumference [8].

4.2.2.2 ExPAR sensor SQ-612-SS

The energy required for photosynthesis is referred to as PAR. Typically, it is quantified as photosynthetic photon flux density, expressed in micromoles per square meter per second ($\mu mol \cdot m^{-2} \cdot s^{-1}$). The Extended Photosynthetically Active Radiation (ePAR) sensor has been developed to gauge overall photon intensity across an extended spectrum spanning from 400 to 750 nm [8]. The sensor generates an analog output that falls within the interval of 0 to 4000 $\mu mol \cdot m^{-2} \cdot s^{-1}$ of ± 5 % [164]. This analog output is transmitted to the MCU [8].

4.2.2.3 PAR-FAR sensor S2-441-SS

Radiation reflected from surfaces, like plant canopies and soil, carries valuable object information. Reflectance quantifies reflected radiation over incoming radiation on a surface. A common index calculated from reflectance measurements is the NDVI, which provides a measure of surface greenness. The PAR-FAR sensor S2-441-SS is a distinctive two-channel digital sensor designed for the measurement of reflection within the Red (389 nm to 692 nm) and Near-InfraRed (NIR) (700 nm to 750 nm) wavelengths [165]. The measurement range is approximately 0 to 87.6 $\mathrm{W\,m^{-2}}$ for Red and 0 to 58 $\mathrm{W\,m^{-2}}$ for NIR, accompanied by a precision of $\pm 5\%$[165]. The PAR-FAR sensor is connected to the MCU via the SDI-12 (Serial Digital Interface) protocol, a low-power, ASCII-based communication standard operating at 1200 baud. Specifically designed for environmental monitoring applications, SDI-12 enables multiple sensors to share a single data line, reducing wiring complexity. Communication is initiated by the data logger or microcontroller, which sends command strings to addressed sensors.

4.2.2.4 SFM-5 Sap Flow sensor

The SFM-5 sap flow sensor functions based on the heat ratio method (HRM), a technique that estimates sap flow velocity by introducing a heat pulse into the sapwood and measuring the resulting temperature differentials upstream and downstream of the

heat source. This method enables the detection of both upward (acropetal) and downward (basipetal) sap movement, making it suitable for monitoring bidirectional flow dynamics within plant vascular systems. The sensor is designed for application in trees with stem diameters greater than 1 cm, offering minimally invasive installation and reliable performance across a range of species. The sensor provides a measurement range from -200 to >+1000 cm/h of heat velocity, with an accuracy of better than 3% or ±0.1 cm/h [166]. This sensor employs the SDI-12 communication protocol to transmit data to the MCU [8].

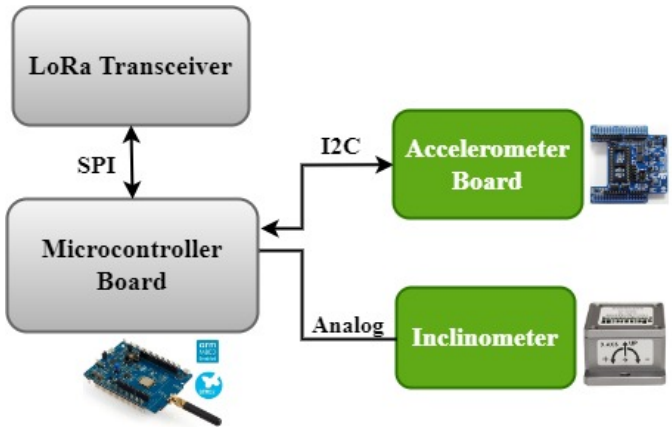

FIGURE 4.7: The architecture of tree node 2 [8] © 2023 IEEE.

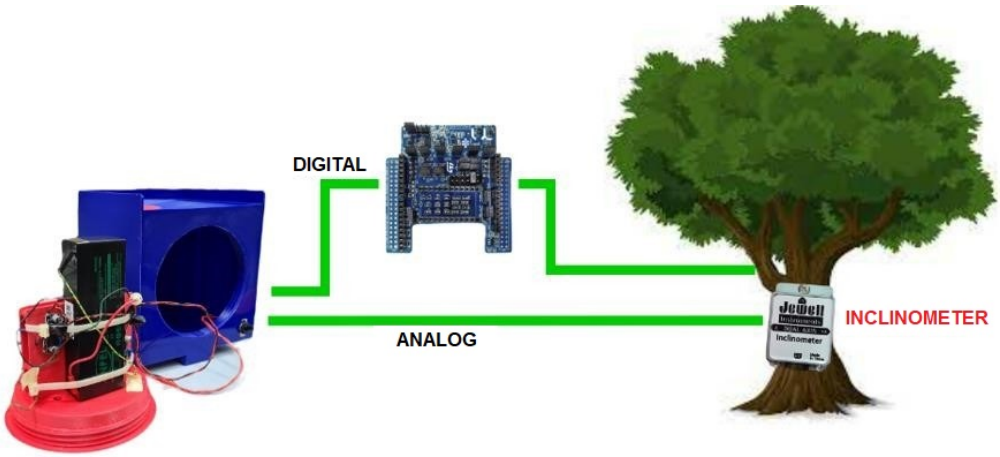

FIGURE 4.8: General schematic of Tree Node 2.

4.2.3 Tree Node 2

While Tree Node 1 focuses on internal physiological signals, Tree Node 2 extends the system's capabilities by monitoring the trunk's inclination and vibration, providing insights into structural stability. In the setup of Tree node 2, an accelerometer board and an inclinometer sensor are combined to measure the tree's stability aspects, including inclination and acceleration, as well as wind-induced acceleration effects (illustrated in Fig. 4.7). For detailed information on the measured quantities, measurement ranges, and metrological characteristics of these sensors, refer to Table 4.3, [8]. Fig. 4.8 illustrates the general schematic of this node, while Fig. 4.9 presents its circuit diagram.

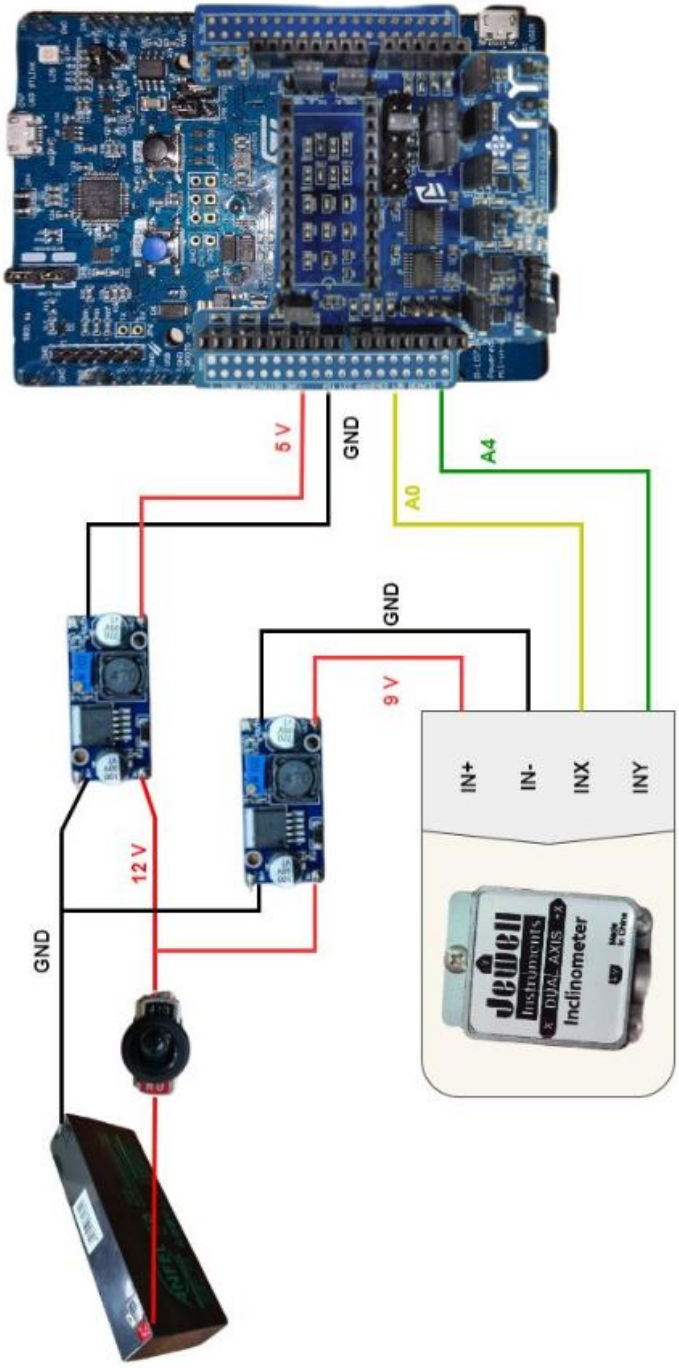

FIGURE 4.9: Circuit diagram of Tree Node 2.

TABLE 4.3: Tree node 2, sensors' information [8] © 2023 IEEE.

Sensor Name	Measured Quantities	Measurement Range	Metrological Characteristics
Sensor AML Analog MEMS Inclinometer	Angle, slope, or tilt of the object	±10 °	0.05 °
X-NUCLEO-IKS01A3, LSM6DSL, Accelerometer Boar	Acceleration	±2, ±4, ±8, ±16 g	1.8 mg

4.2.3.1 Sensor Inclinometer

Jewell's high-precision inclinometer sensor is employed for precise measurement of object angles, slopes, or tilts within the ranges of ±10 °. The sensor produces an analog output that is sent to the MCU. This inclinometer offers an accuracy of 0.05 ° and operates by measuring the angle relative to the object's gravitational orientation [167, 8]. The Dual-Axis Inclinometer [AML-2-10-V1] (Fig. 4.10a) is designed to detect angular movements along two orthogonal reference axes, referred to as the X and Y axes. For each axis, the sensor converts movement into a proportional voltage. By combining the output signals, the inclination with respect to the XY plane can be calculated (Fig. 4.10b). In addition, the main characteristic of the inclinometer is mentioned in Table 4.4.

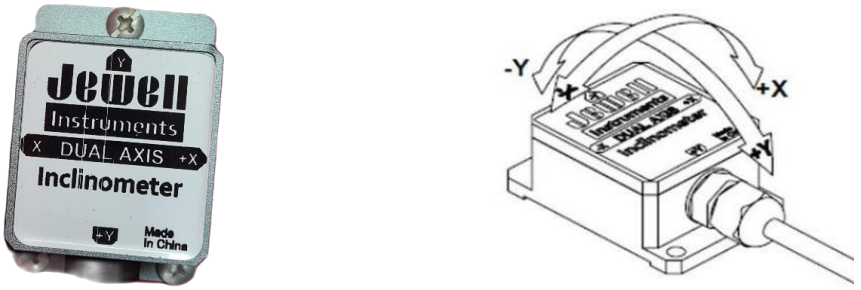

(A) Inclinometer (B) Axes of the inclinometer

FIGURE 4.10: Inclinometer sensor.

Main Characteristics	
Dual-axis functionality	Yes
Resolution	0.05°
Measurement range	±10°
Temperature coefficient	±0.02 °/°C
High tolerance to shocks and vibrations	Yes
Operating temperature range	−40 °C to 85 °C
Analog output	0-5 V DC
Cable length	1 meter

TABLE 4.4: Specifications of the inclinometer

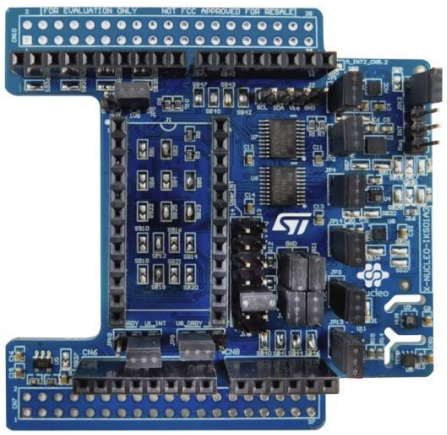

FIGURE 4.11: X-NUCLEO-IKS1A3 board [13].

4.2.3.2 X-NUCLEO-IKS1A3, LSM6DSL, Accelerometer Board

Complementing the inclinometer's angle measurements, an accelerometer positioned on a tree's trunk measures the vibration that affects the tree and its swaying motion, influenced by factors like weight, flexibility, wood density, and wind force. Variances in tree size and shape lead to distinct responses to wind [168]. This sensor quantifies movement within ±2, ±4, ±8, and ±16 g-forces (g) with 1.8 mg accuracy [13]. The sensor interfaces with the MCU using the Inter-Integrated Circuit (I2C) protocol [8]. The X-NUCLEO-IKS01A3 (Fig. 4.11) consists of environmental sensors and Microelectromechanical Systems (MEMS) motion sensors, including a triaxial accelerometer used for

vibration monitoring. The algorithm implemented on the board for measuring vibrations operates by sampling the accelerometer data at a frequency of 10 Hz. For each sample, the acceleration magnitude is computed using the three spatial components (x, y, z) as $a = \sqrt{x^2 + y^2 + z^2}$. These magnitudes are stored in a buffer over a defined time window. Once the buffer is filled, the algorithm extracts the maximum acceleration value, which represents the peak vibration intensity during that period. This peak value is then transmitted to the gateway, providing a concise yet informative representation of the vibration data while optimizing communication efficiency. The X-NUCLEO-IKS01A3 is compatible with the Arduino Uno R3 connector layout and includes the following components:

- A three-axis accelerometer and gyroscope [LSM6DSO].
- A three-axis magnetometer [LIS2MDL].
- A three-axis accelerometer [LIS2DW12].
- A temperature and humidity sensor [HTS221].
- A pressure sensor [LPS22HH].
- A temperature sensor [STTS751].
- The X-NUCLEO-IKS1A3 interfaces with an STM32 microcontroller via I2C pins [13].

4.2.4 Thermal and camera Node

Beyond physical and structural health, visual and thermal imagery play a crucial role in detecting early signs of stress. Therefore, a thermal camera for fire detection and a panoramic camera for the evaluation of the LAI produce substantial data volumes demanding robust processing. To address this, they interface with a powerful Raspberry Pi as a data acquisition board. This Raspberry Pi subsequently communicates with a remote gateway through an LoRatransceiver. The LoRa transceiver establishes USB connectivity with the Raspberry Pi. Fig. 4.12 illustrates these interconnections. Table 4.5 provides a comprehensive overview of quantified attributes, measurement ranges, and metrological specifications for these sensors [8].

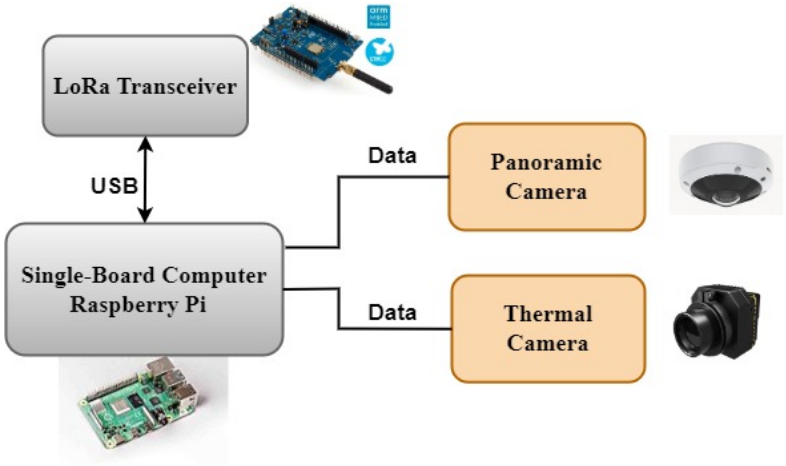

FIGURE 4.12: The architecture of Cameras' node [8] © 2023 IEEE.

TABLE 4.5: Cameras node, sensors' information [8] © 2023 IEEE.

Sensor Name	Measured Quantities	Measurement Range	Metrological Characteristics
Thermal Camera FLIR-AX8	Temperature	−10 °C to +150 °C (14 °F to 302 °F)	±2 °C (±3.6 °F) or ±2 % of reading (+10 to +100 °C at +10 to +35 °C ambient)
Panoramic AXIS M3077-PLVE Network Camera	RGB imaging, video streaming, and audio streaming	360 ° overview	Resolution: Overview: 2016x2016 to 160x160 Panorama: 2560x1440 to 192x72

4.2.4.1 Panoramic AXIS M3077-PLVE Network Camera

This digital camera, featuring a 1/1.8" progressive scan RGB CMOS and a 6 MP sensor [169], serves as a powerful tool for capturing high-resolution images of various scenes. The Camera utilizes a digital Ethernet interface operating over the TCP/IP protocol suite to facilitate network communication and data transmission. The camera is employed for the assessment of the LAI of the tree. Its positioning is designed to be situated on the ground, capturing upward-looking views of the tree canopy. The imagery is acquired using a Raspberry Pi, and subsequently, the LAI is determined by quantifying the area covered by leaves in relation to the total area [8]. The LAI is estimated from RGB imagery using a custom algorithm implemented in Python, utilizing the OpenCV library. Specifically, the algorithm isolates the green channel from the input image, applies a predefined intensity threshold, and counts the number of pixels exceeding this threshold. The LAI is then computed as the ratio, expressed as a percentage, between the number of green pixels above the threshold and the total number of pixels in the image. This method provides a simple yet effective approach for assessing vegetation coverage based on color segmentation techniques.

4.2.4.2 Thermal Camera FLIR-AX8

This sensor integrates imaging capabilities with continuous temperature monitoring within a range of $-10\,^{\circ}\mathrm{C}$ to $+150\,^{\circ}\mathrm{C}$, featuring an uncertainty of $\pm 2\,^{\circ}\mathrm{C}$ and alert functionality [170]. Thermal camera images are captured by the Raspberry Pi, and a temperature threshold is employed to identify occurrences of fires. Upon fire detection, an event is triggered, and a notification is transmitted using the LoRa, transceiver [8]. The camera uses a digital Ethernet interface based on the TCP/IP protocol for communication.

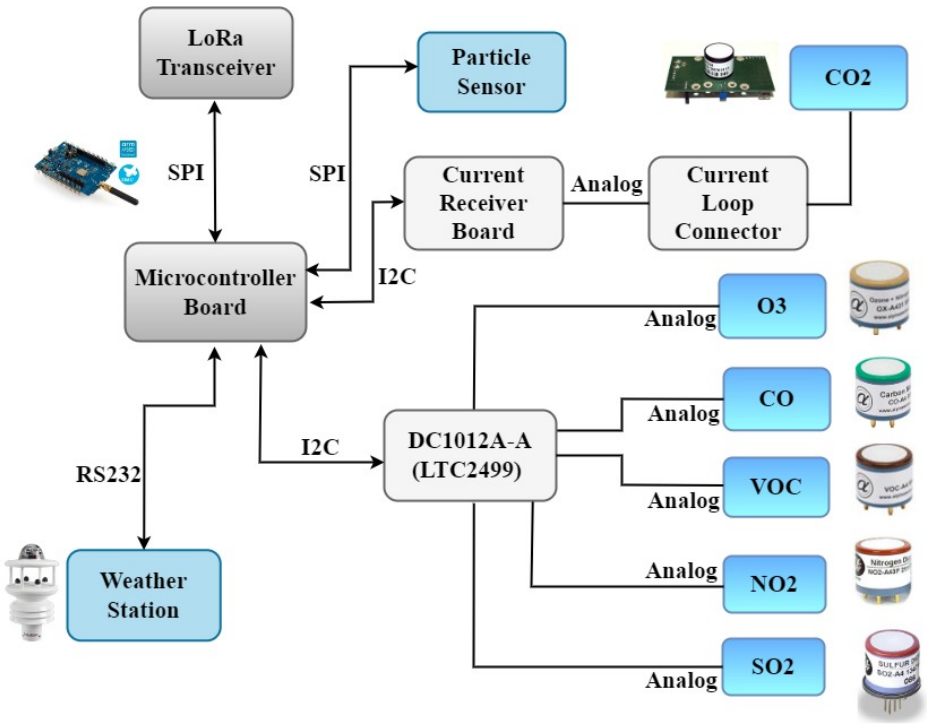

FIGURE 4.13: The architecture of the environmental node [8] © 2023 IEEE.

TABLE 4.6: Environmental node, sensors' information [8] © 2023 IEEE.

Sensor Name	Measured Quantities	Measurement Range	Metrological Characteristics
Alphasense OPC-N3	Particle	Measuring the particles having a size from 0.35 to 40 μm	Not Specified
Alphasense SO2-A4	Sulfur Dioxide concentration	0 to 50 mg/L	$\pm$15 μg/L
Alphasense NO2-A4	Nitrogen Dioxide concentration	0 to 20 mg/L	$\pm$15 μg/L
Alphasense O3-A4	Ozone concentration	0 to 5 mg/L	$\pm$5 μg/L
Alphasense CO-A4	Carbon Monoxide concentration	0 to 500 mg/L	$\pm$20 μg/L
Alphasense VOC-A4	Volatile Organic Compounds	0 to 190 mg/L	$\pm$20 μg/L
Alphasense IRC-A1	Carbon Dioxide concentration	0 to 5000 mg/L (IAQ)	Zero repeatability: $\pm$10 mg/L Full-scale repeatability: $\pm$50 mg/L
Weather Station Maximet GMX600	Wind Speed	0.01 m/s to 60 m/s	$\pm$ 3 % to 40 m/s, $\pm$ 5 % to 60 m/s
	Wind Direction	0-359 °	$\pm$ 3 ° to 40 m/s, $\pm$ 5 ° to 60 m/s
	Temperature	-40 °C to +70 °C	$\pm$ 0.3 °C @ 20 °C
	Humidity	0-100 %	$\pm$ 2 % @ 20 °C (10 %-90 % RH)
	Dew Point	-40 °C to +70 °C	$\pm$ 0.3 °C @ 20 °C
	Pressure	300-1100 hPa	$\pm$ 0.5 hPa @ 25 °C
	Precipitation	0 to >300 mm/hr	Resolution: 0.08 mm Repeatability: 3 %

4.2.5 Environmental Node

To complete the system's holistic monitoring approach, this is the most complex node, designed to monitor environmental conditions and the chemical composition of the air surrounding the tree. It is equipped with chemical sensors for detecting compounds in the atmosphere and a weather station to measure temperature, atmospheric pressure, humidity, dew point, wind speed and direction, and precipitation levels. This node is depicted in Fig. 4.13 and it includes particulate sensors, Sulfur Dioxide (SO2), Nitrogen Dioxide (NO2), Ozone (O3), CO2, Carbon Monoxide (CO), Volatile Organic Compound (VOC)s sensors, and a weather station. Detailed information about the quantified measured values, corresponding measurement ranges, and associated metrological specifications for these sensors is presented in Table 4.6, [8]. The output of five gas sensors (O3, CO, NO2, VOC, SO2) is analog voltage and each requires a differential ADC channel. As the MCU has only three single-ended channels, the DC1012A-A board with the LTC2499 24-Bit ADC is employed, offering up to eight differential input channels. Communication between the board and the MCU is facilitated through the I2C interface [8]. Fig. 4.14 illustrates the comprehensive schematic of the environmental node, while Fig. 4.15 presents a detailed circuit diagram of the node.

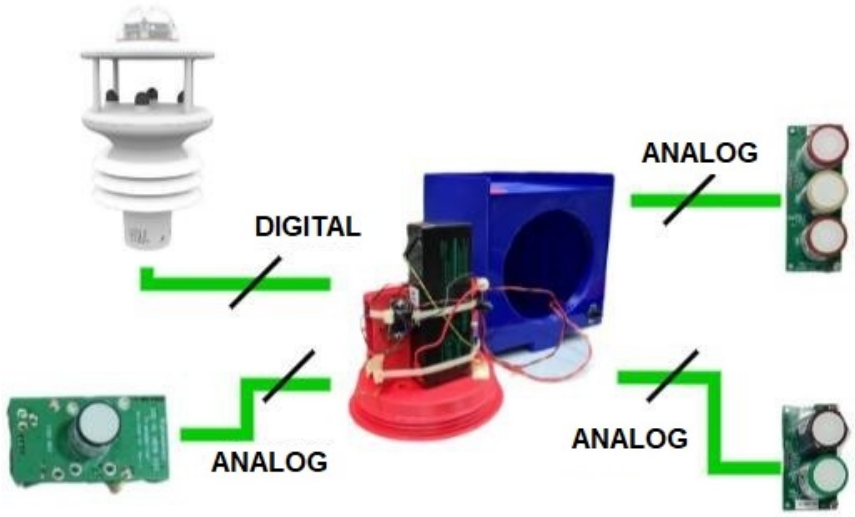

FIGURE 4.14: General schematic of the environmental node.

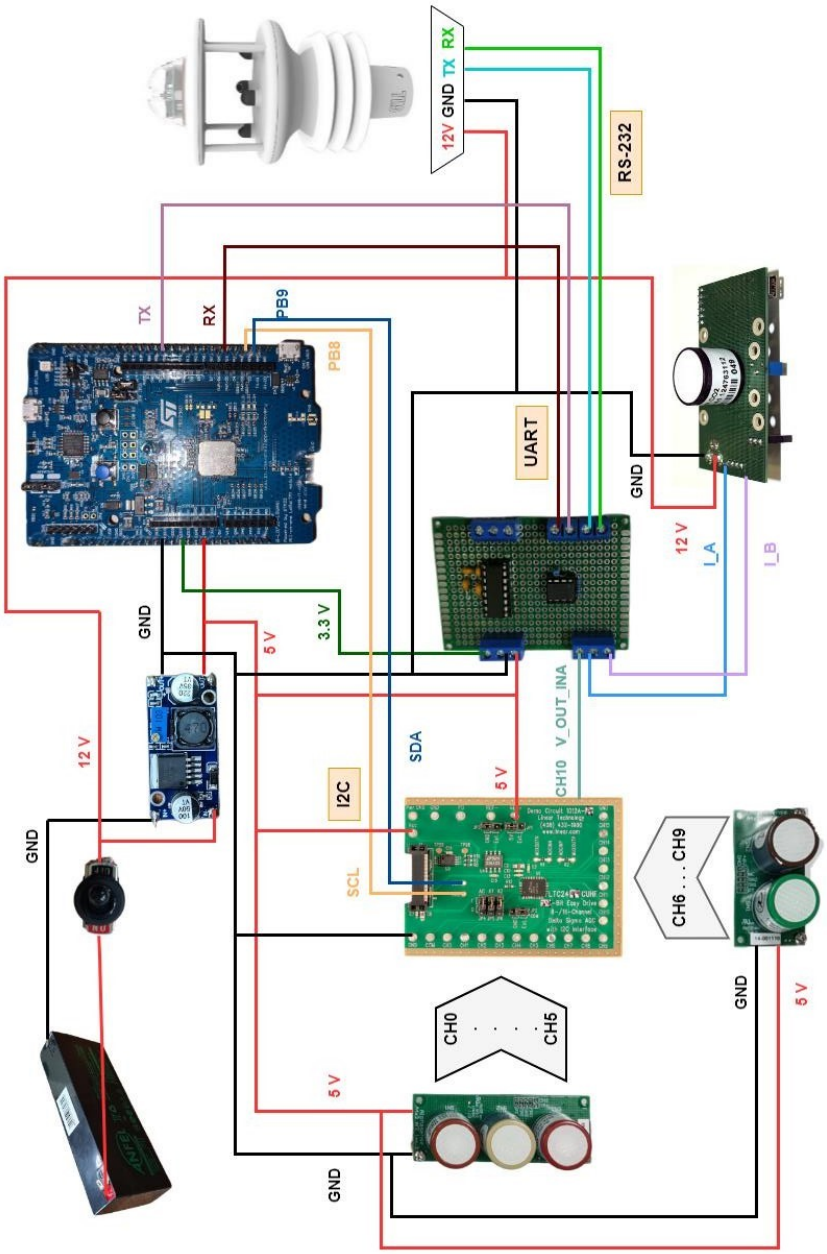

FIGURE 4.15: Circuit diagram of the environmental node.

4.2.5.1 Alphasense OPC-N3, Particulate Sensors

Plants have built-in stress tolerance, but they suffer significant harm from Particulate Matter (PM) or dust deposition. PM is a mixture of solid particles and liquid droplets with varying sizes and compositions. This hampers photosynthesis and protein synthesis, and makes them susceptible to damage from microorganisms and insects. Plants adapt by responding metabolically, physiologically, biochemically, and genotypically to PM pollution [171]. The Alphasense OPC-N3 sensor operates on the principle of laser light scattering. As air is drawn through the sensing chamber, particles suspended in the air pass through a focused laser beam. These particles scatter the incident light, and the scattered light is detected by a photodiode placed at a specific angle. The intensity and pattern of the scattered light are analyzed to estimate the size and concentration of the particles. By counting the number of scattered light events and classifying them according to intensity, the sensor determines particle size distribution within a range of approximately 0.35 µm to 40 µm with a measurement range up to 2000 $\mu g\, m^{-3}$ [172]. This technique enables real-time monitoring of PM concentrations in the air. The sensor communicates with the MCU via the SPI protocol [8].

4.2.5.2 Alphasense SO2-A4

Plant exposure to SO2 generally hampers physiological, morphological, and biochemical processes. Prolonged exposure disrupts photosynthesis and energy metabolism. However, low-level SO2 exposure benefits plants as sulfur is essential for growth, aiding in the synthesis of sulfur-containing amino acids [173]. The Alphasense SO2-A4 sensor is based on electrochemical (fuel cell) sensing technology. It operates by allowing SO2 gas to diffuse through a membrane into the sensor's electrochemical cell, which contains a working electrode, counter electrode, and reference electrode immersed in an electrolyte. At the working electrode, SO2 undergoes an oxidation reaction, generating electrons. A simultaneous reduction reaction occurs at the counter electrode. These electrochemical reactions produce a current directly proportional to the concentration of SO2 in the surrounding air. The resulting signal is processed and converted into concentration units using pre-calibrated response factors. This method provides high specificity and sensitivity for low-concentration SO2 detection. The sensor measures concentrations in the range of 0 to 50 mg/L, with an accuracy of ±15 µg/L [172, 8].

4.2.5.3 Alphasense NO2-A4

This sensor measures NO2 ($0-20\ mg/L$) with $\pm 15\ \mu g/L$ accuracy [174]. While nitrogen is important for plants, excessive oxides of nitrogen, especially NO2 levels beyond the

natural background, can harm plant growth and yield. NO2 can harm crop cells directly and impact growth indirectly by contributing to the formation of ozone (O3) and aerosols [175, 8]. The Alphasense NO2-A4 sensor operates using electrochemical sensing principles. It consists of a working electrode, a counter electrode, and a reference electrode immersed in an electrolyte. As nitrogen dioxide gas diffuses into the sensor through a porous membrane, it undergoes a redox reaction at the working electrode. Specifically, NO2 is reduced or oxidized depending on the electrode potential, generating a current proportional to the gas concentration. This current is measured and processed using calibration data to yield an accurate concentration value. The electrochemical method enables selective, low-power, and high-sensitivity detection of NO2 in ambient air.

4.2.5.4 Alphasense O3-A4

O3, a pale blue gas with a distinct smell, can combine with other pollutants to create 'Smog'. It damages plants by entering leaves and oxidizing tissue during respiration. This sensor measures O3 ($0-5\ mg/L$) with $\pm 5\ \mu g/L$ accuracy [176, 8]. The Alphasense O3-A4 sensor is based on electrochemical sensing technology. When ozone gas enters the sensor through a small membrane, it reaches a liquid electrolyte where it reacts with the working electrode. This reaction creates a small electrical current. The size of this current depends on how much ozone is present in the air. The sensor measures this current and uses it to calculate the ozone concentration. This method provides high sensitivity and is well-suited for detecting low levels of ozone in the environment.

4.2.5.5 Alphasense CO-A4

CO endangers health by diminishing oxygen to vital organs and contributes to greenhouse gases like CO2 and ozone, warming the atmosphere. Trees absorb CO and alleviate this by purifying the air. This sensor measures CO ($0-500\ mg/L$) with $\pm 20\ \mu g/L$ precision [172, 8]. The sensor operates on the principle of electrochemical detection. CO diffuses through a gas-permeable membrane into an electrochemical cell containing a working electrode, counter electrode, and reference electrode immersed in an electrolyte. At the working electrode, CO undergoes an oxidation reaction, producing electrons that generate a current proportional to the gas concentration. The resulting electrical signal is then processed and calibrated to provide a quantitative measure of ambient CO levels. This method ensures high sensitivity, selectivity, and low power consumption, making it suitable for real-time environmental monitoring.

4.2.5.6 Alphasense VOC-A4, Volatile Organic Compounds

VOCs are low-molecular-weight organic chemicals that readily vaporize under ambient atmospheric conditions. Vegetation, especially trees, naturally emits various VOCs such as monoterpenes, which serve ecological functions including pollinator attraction, defense against herbivory, and intra-plant signaling. In the atmosphere, VOCs react with nitrogen oxides and sunlight to form secondary pollutants such as tropospheric ozone and secondary organic aerosols, thereby influencing air quality and climate. The Alphasense VOC-A4 sensor enables the quantification of ambient VOC concentrations within a measurement range of 0 to 190 mg/L, with a resolution of ±20 µg/L [172, 8]. The sensor employs an electrochemical detection mechanism. VOC molecules diffuse through a gas-permeable membrane into the electrochemical cell, where they interact with the working electrode. Upon contact, the VOCs undergo redox reactions, typically oxidation, which generate an electrical current proportional to the concentration of target gases. The magnitude of this current is measured and translated into gas concentration values through calibration algorithms. This technique offers high sensitivity and selectivity for a range of organic vapors while maintaining low power consumption, making it suitable for continuous environmental monitoring applications.

4.2.5.7 Alphasense IRC-A1, CO2

CO2 plays a fundamental role in plant physiology as a primary substrate for photosynthesis. However, insufficient ambient CO2 concentrations can impair growth and metabolic functions in vegetation. The Alphasense IRC-A1 sensor is designed to quantify CO2 concentrations in the range of 0 to 5000 mg/L, with a repeatability of ±10 mg/L at zero and ±50 mg/L at full-scale output [172, 8]. This sensor is well-suited for applications involving Indoor Air Quality (IAQ), safety, combustion monitoring, and high-CO2 process control. The sensor operates on the principle of non-dispersive infrared (NDIR) spectroscopy, employing a pyroelectric infrared detector. In this method, infrared radiation emitted from a source passes through a sample chamber containing ambient air. CO2 molecules selectively absorb radiation at specific wavelengths, primarily around 4.26 µm. The amount of absorbed infrared light is proportional to the CO2 concentration in the chamber. A pyroelectric detector measures the reduction in transmitted radiation, and this signal is processed to yield a quantitative concentration value. Unlike typical sensors that output voltage directly, the IRC-A1 produces a current output signal. This is transmitted via a current loop to a current receiver board, where it is converted into a voltage using a precision shunt resistor. The analog voltage is then digitized by an ADC and communicated to the MCU via the I^2C protocol. The full signal acquisition and transmission path is illustrated in Fig. 4.13 [8].

4.2.5.8 Weather Station Maximet GMX600

Weather station sensors are integral in monitoring and quantifying meteorological parameters. The MaxiMet GMX600, placed within three dual-louvered radiation shields to shield it from direct solar radiation, is equipped with sensors that measure various atmospheric variables, including wind speed, wind direction, ambient temperature, relative humidity, atmospheric pressure, and precipitation [177]. A summary of the measurement ranges and detailed sensor characteristics is provided in Table 4.6. The working principles of the sensors are as follows:

- Wind Speed and Direction: The system uses an ultrasonic anemometer. It works by emitting ultrasonic pulses between pairs of transducers. The time it takes for the pulses to travel between these transducers is used to calculate the wind speed and direction based on the changes in travel time caused by the wind.
- Ambient Temperature: Temperature is measured using a thermistor, a temperature-sensitive resistor. As temperature increases or decreases, the resistance of the thermistor changes, and this change is used to determine the temperature of the surrounding environment.
- Relative Humidity: A capacitive humidity sensor is employed, which consists of a hygroscopic material. The dielectric constant of this material changes with moisture content, allowing the sensor to determine the relative humidity based on this variation.
- Atmospheric Pressure: A piezoresistive barometric pressure sensor is used to measure the atmospheric pressure. As the air pressure changes, it causes a strain in the sensor's material, which is detected as a change in resistance. This resistance change is proportional to the pressure, allowing accurate pressure measurements.
- Precipitation: The sensor detects precipitation using either a piezoelectric or optical rain sensor. A piezoelectric sensor measures the impact of raindrops on a surface, converting the mechanical stress from the impact into an electrical signal. An optical rain sensor uses light to detect the presence of raindrops by measuring the interruption of a light beam.
- Dew Point: The dew point is the temperature at which air becomes saturated with moisture and begins to condense. It is calculated from the ambient temperature and relative humidity data provided by the sensors. The dew point is useful for predicting weather conditions like fog, frost, or rain.

Data from these sensors is transmitted to the MCU using the RS232 serial communication protocol [8]. This completes the multi-node design of the Treelogy system, which now encompasses internal, structural, visual, and environmental monitoring for a comprehensive tree health assessment.

4.3 Experimental Evidence

With the full architecture in place, the next step involves validating system functionality and reliability. All sensor configurations and their connectivity with LoRa and the Raspberry Pi have been tested in the LESIM Lab (Laboratory of Signal and Measurement Information Processing). Sensors are also calibrated based on their datasheets. LoRa node has been configured to function with a sampling rate of 5 minutes.

This configuration of the distributed measurement system comprises two fundamental operational phases: Data Acquisition and Data Transmission & Storage. The system employs three sensor nodes—Physiology (Tree Node 1), Stability (Tree Node 2), and Environment (Tree Node 3)—to systematically capture physical field data and critical parameters essential for assessing tree health and structural stability. The procedural framework outlining the sequential steps involved in these operations is as follows:

- **Gateway Node Initialization:** The system is initialized by powering on the Gateway node, which activates its two fundamental components: the Raspberry Pi and the B-L072Z-LRWAN1 board.
- **Time Synchronization:** The Raspberry Pi prompts the user to input the current date and time to synchronize the system's internal clock.
- **Reset Command:** The system remains waiting for the RESET command, which must be manually executed on the B-L072Z-LRWAN1 board via the designated reset button.
- **Configuration Setup:** The Raspberry Pi transmits a configuration table (which serves as a whitelist of devices that can connect to the network) to the B-L072Z-LRWAN1 board. This table contains specific instructions for each sensor node, including:
  - A time offset indicating the point at which measurements should commence.
  - The sampling period for data collection.
- **Node Activation:** Following the transmission of the configuration table, the sensor nodes (Tree Node 1, Tree Node 2, and Environmental Node) are powered

on. Each node transmits its unique ID and type to the Gateway node's B-L072Z-LRWAN1 board.

- **Parameter Assignment:** The Gateway node assigns the time offset and sampling period to each respective sensor node, based on the configuration table. For security purposes, this step is executed only if the node's ID is pre-listed in the configuration table.
- **Measurement Process:** Each sensor node waits until the assigned time offset is reached before initiating the measurement process. Upon completion of each sampling period, the sensor nodes transmit their recorded data, including their ID and type, to the Gateway node. The Gateway node logs this data in its database.
- **Continuous Monitoring:** From this stage onward, the sensor nodes transmit measurement data periodically to the Gateway node by the established sampling schedule, ensuring continuous monitoring. The data is then stored in the InfluxDB database embedded on the Raspberry Pi for efficient time-series data management and easy retrieval for analysis.

To evaluate the performance of the system and ensure effective alignment between the experimental data and the expected values, as outlined by the sensor specifications, a series of experimental tests were conducted. These tests were performed after assembling the nodes within their respective enclosures, which were fabricated using 3D printing technology. These enclosures serve dual purposes: providing circuit protection and facilitating the on-site assembly of the nodes. Each node was individually tested, and the experimental setup involved the following components:

- **Analysis of Communication Between Nodes**: Each node incorporates multiple communication protocols and data exchange interfaces to facilitate interaction between different sensors. To verify that all sensors within each node function correctly, a series of experimental tests was conducted. Specifically, the normal operation of the distributed measurement system was simulated. Each node is expected to transmit measurement data from all sensors every 5 minutes. For the test, a 30-minute measurement interval was selected, resulting in 6 samples per sensor. The data collected after each measurement cycle was transmitted via the LoRa network to the Gateway node.
- **Data Validation:** The collected data are stored in an InfluxDB database, a high-performance, time-series database optimized for storing and querying timestamped data. This database is hosted locally on the Raspberry Pi, allowing efficient storage and retrieval of environmental and sensor measurements.

To visualize and analyze the data, Grafana—a powerful open-source analytics and interactive visualization web application—is used. Grafana connects directly to the InfluxDB database and provides customizable dashboards to display real-time data through unified charts and graphs. This setup allows users to monitor trends, detect anomalies, and validate experimental results by comparing them against reference values or known inputs applied to the system. Figures 4.16 and 4.17 present screenshots of the Grafana dashboards used during the experiments to monitor various parameters, including tilt, vibration, growth increment, SAP flow, wind speed, precipitation, CO2, CO, NO2, and OX concentration (where OX denotes the combined concentration of O3 and NO2).

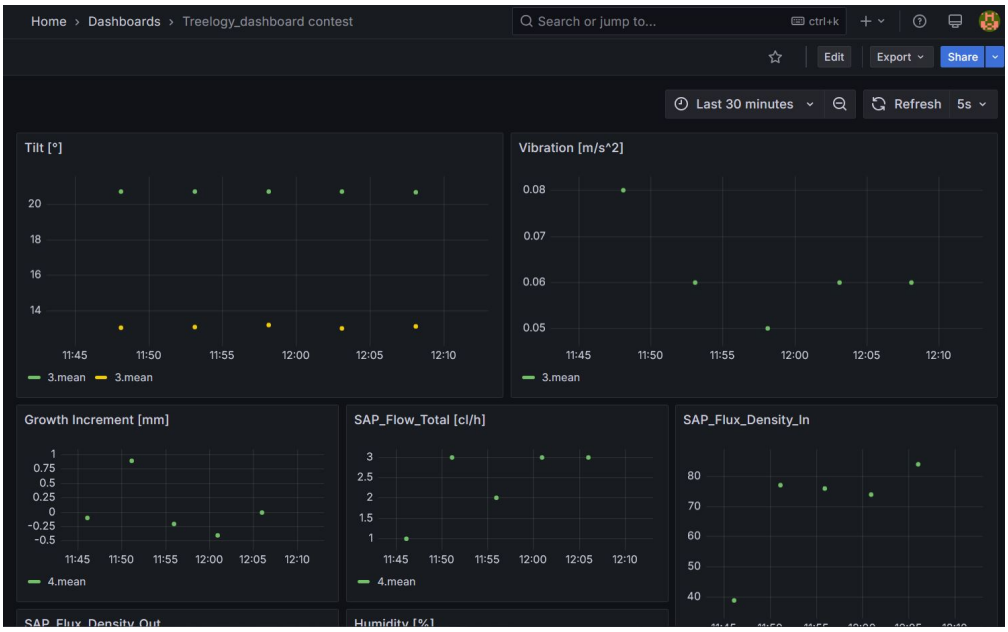

FIGURE 4.16: The Grafana dashboard displays real-time sensor data from the monitoring system, including tilt, vibration, growth increment, and SAP flow.

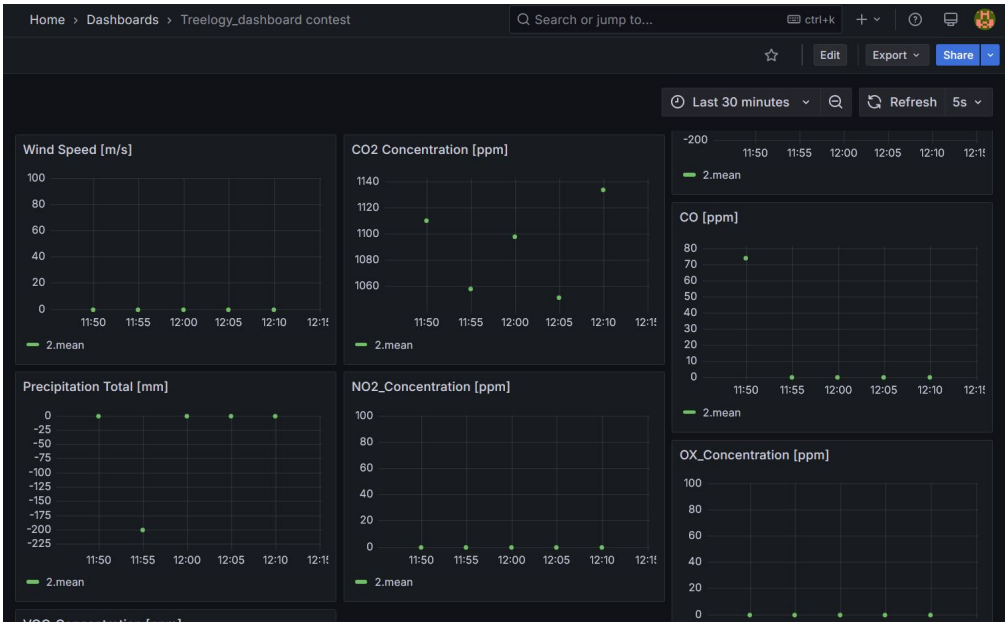

FIGURE 4.17: The Grafana dashboard displays real-time sensor data from the monitoring system, including wind speed, precipitation, CO2, CO, NO2, and OX concentration.

- **Power Consumption Analysis**: To evaluate the power consumption of each node, a stabilized power supply and a multimeter in ammeter configuration were used to measure the average current absorbed by each node. This information is crucial for estimating the operating duration of the node before the battery is depleted. Furthermore, based on the consumption data, an analysis was performed to assist in selecting an appropriate battery that would support the desired uptime of each node.

4.3.1 Stability Node Analysis

The stability node is summarized by the following signals:

- **Input**: 12V A.D. power supply
- **Output**: X-axis inclination
- **Output**: Y-axis inclination
- **Output**: Vibration

The experiment involves two distinct *rest* states, in which the sensor remains inactive and unperturbed externally, and one *forcing* state. During the forcing phase, the node was subjected to tilting along different axes at various angles within a 10–20 minute interval.

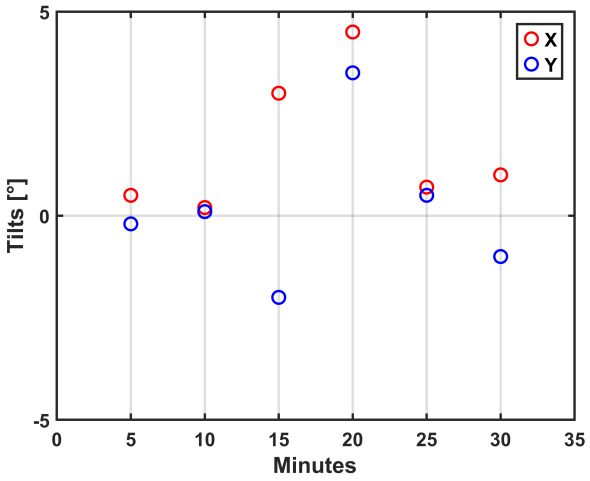

FIGURE 4.18: Test inclination, Tilts along X and Y axes.

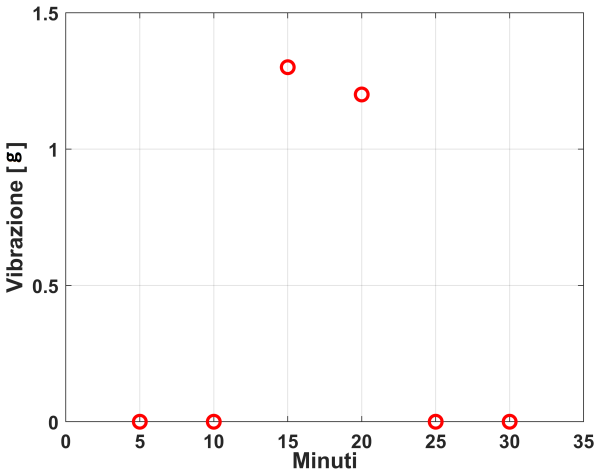

FIGURE 4.19: Test vibration.

As illustrated in Fig. 4.18, the stress response of the node within the specified range is evident. A similar procedure was conducted for the vibration measurements in units of g, as presented in Fig. 4.19. The g-value is calculated from a buffer containing the magnitudes of several tri-axial acceleration measurements. In this case, two distinct states are observed: a *forcing* state, lasting from 10 to 20 minutes, and a *rest* state during the remaining period. As shown, during the forcing phase (induced by shaking the node), the sensor records an acceleration value approximately equal to the gravitational acceleration, 9.81 m/s^2. Conversely, during the rest intervals, the sensor output is essentially zero, indicating no significant motion or acceleration.

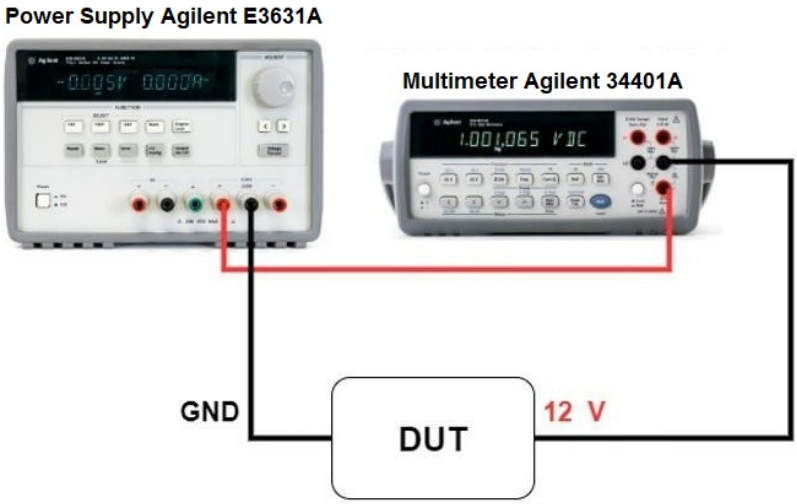

FIGURE 4.20: Setup for Power Consumption Measurement.

Fig 4.20 illustrates the setup for measuring the current consumption of the node. This configuration, along with the following procedure, is applied consistently across all nodes. The approach to obtaining a reliable estimate of current consumption and, consequently, the battery life is as follows:

1. The 300-second sampling period is divided into two intervals: during one interval, the node operates in the *MEASUREMENT* configuration, while in the other, it is in the *REST* state.

2. The extreme values (minimum and maximum) of the current absorbed by the node are recorded, both during the *MEASUREMENT* and *REST* states, using the appropriate functionality of the multimeter.

3. The arithmetic mean of the two extreme values is calculated to obtain a reference current for each of the two states.

4. The final step involves calculating the weighted average current, with the time intervals of each state serving as weights.

Table 4.7 provides current consumption data for the Stability Node in MEASURE and REST states. The difference in power consumption between the *MEASUREMENT* and *REST* states is not significantly large, as this node is equipped with only two sensors. However, for other nodes with additional sensors, the difference in power consumption is greater.

TABLE 4.7: Power consumption during different states (Stability Node).

	MEASURE	**REST**
MIN [mA]	65.3231	60.2391
MAX [mA]	76.5883	63.8147
TIME [s]	90	210
AVERAGE [mA]	70.955	62.027
AVERAGE WEIGHTED [mA]	*64.71 ± 0.04*	

Fig. 4.21 illustrates the operational duration of the node as a function of the sampling period, given a battery capacity of 2.3 Ah. To introduce an additional degree of freedom, a graph was generated where the battery lifespan is expressed as a function of both the sampling period and the battery capacity, as shown in Fig. 4.22.

As expected, increasing the battery capacity directly extends the operational duration of the node. However, an interesting observation is that increasing the sampling period does not result in a significantly large gain in operational duration, assuming the same battery capacity.

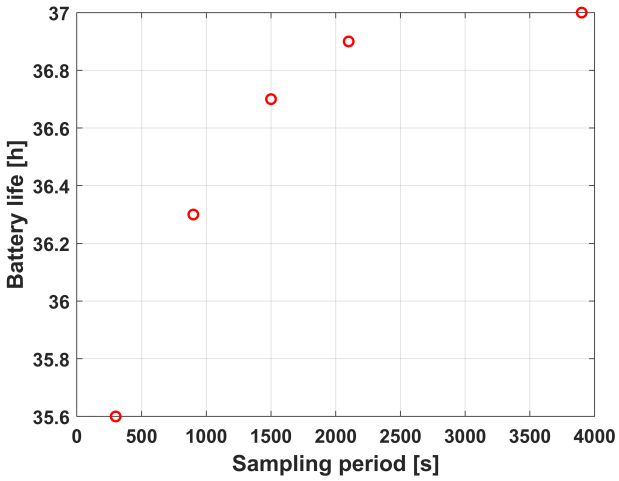

FIGURE 4.21: Operational Duration of a 2.3 Ah Battery.

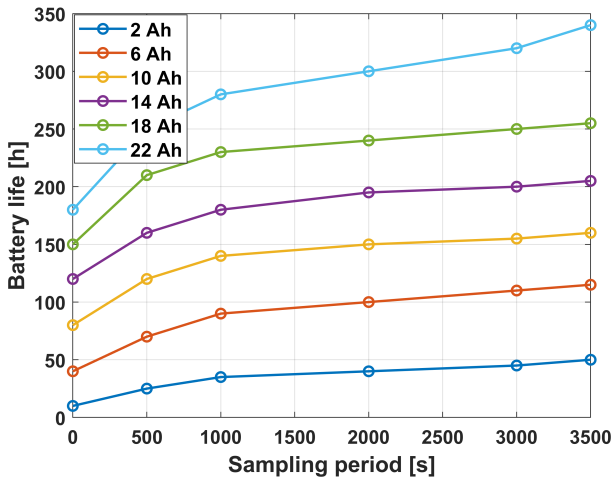

FIGURE 4.22: Battery Life as a Function of Capacity (Ah) and Sampling Period.

4.3.2 Analysis Data Acquisition of Physiology Node

The physiological monitoring of the physiology node is characterized by the following signals:

- **Input**: 12V A.D. power supply.

- **Output - Dendrometer**: Measurement of trunk circumference growth.
- **Output - ePAR**: Photosynthetically Active Radiation (PAR) measurement.
- **Output - PAR-FAR**: Ratio of PAR to FAR radiation and the percentage of FAR in the total absorbed light radiation.
- **Output - Sap Flow**: Total sap flow, along with the internal and external sap flow density.

The simulation consistently includes two distinct states: *rest* and *stress*. As evident from Fig. 4.23, dendrometer sensor forcing is applied during the 10– 20 minute interval, increasing approximately 22 mm.

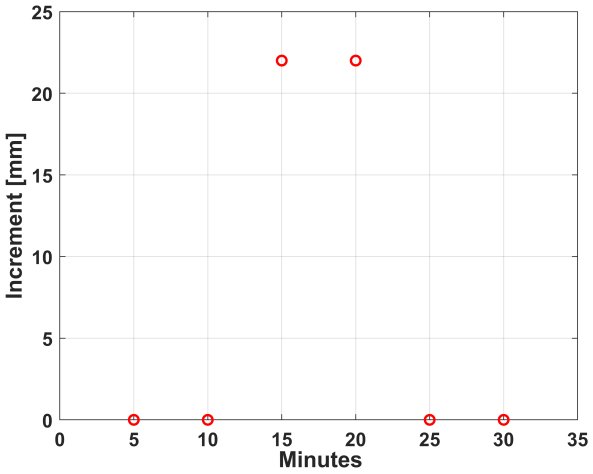

FIGURE 4.23: Test dendrometer.

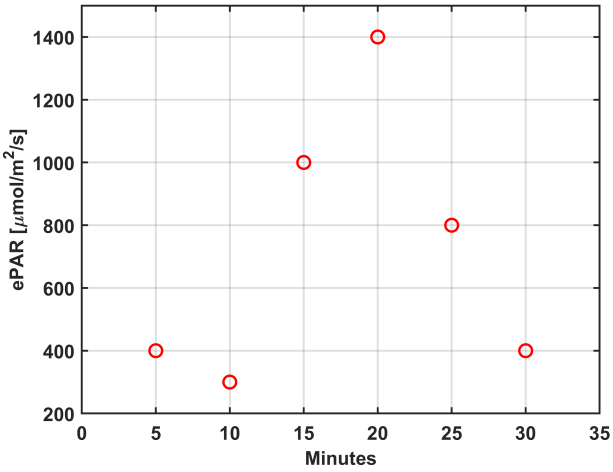

FIGURE 4.24: Test ePAR.

Regarding the ePAR sensor test, to simulate light radiation from the external environment, the sensor was exposed to artificial light, specifically the flash of a mobile phone. The *rest* states were achieved by isolating the sensor from light exposure, resulting in a significantly lower detected radiation level, as shown in Fig. 4.24.

Fig. 4.25a–4.25b illustrate the output of the PAR-FAR sensor under forced conditions using two different light sources: white light (mobile phone flash) and yellow light (a standard office lamp).

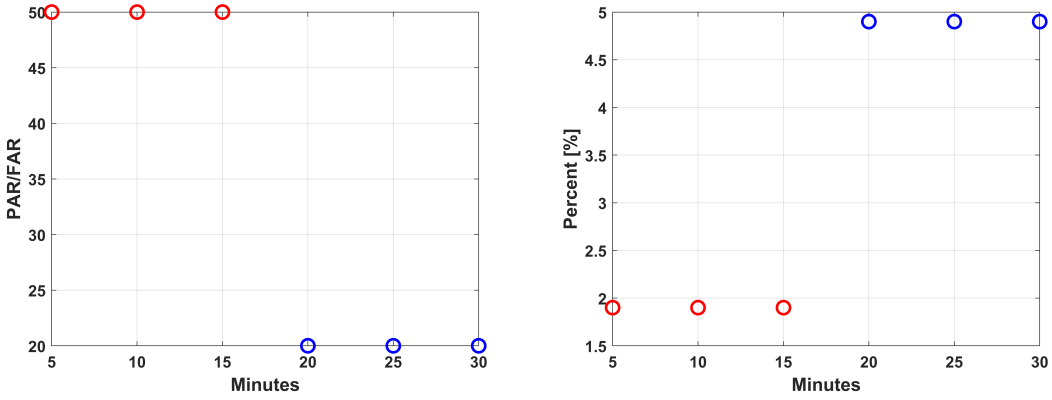

(A) Test PAR-FAR (report)

(B) Test PAR-FAR (percentage)

FIGURE 4.25: Test PAR-FAR Flow.

The variation in light sources resulted in distinct sensor responses. By highlighting the outputs in red for white light and in blue for yellow light, it is evident that white light exhibits a significantly higher PAR content compared to FAR, whereas the opposite is observed for yellow light.

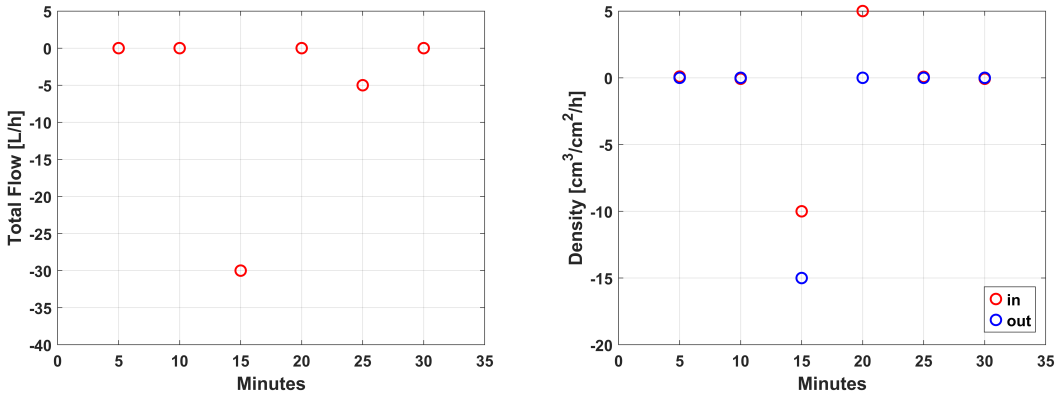

(A) Test SAP Flow (total). (B) Test SAP Flow (density).

FIGURE 4.26: Test SAP Flow.

Figs. 4.26a–4.26b present the results of the SAP-Flow sensor tests. Since a real tree was not available, the applied force was simulated by wrapping the sensor probes with fingers, thereby mimicking the sap flow. Notably, negative values are also observed in the results. The sign of the measurement is a critical parameter, as it indicates the direction of sap flow within the Xylem (Xylem is the part of a plant that carries water from the roots to the leaves). Positive values correspond to the flow towards the roots, while negative values indicate movement in the opposite direction. Two distinct sap flow densities can be measured: *in* and *out*, depending on the pair of thermistors being analyzed. Specifically, the *in* density represents the flow directed towards the heartwood of the trunk, whereas the *out* density corresponds to the flow towards the outer layers.

Additionally, for this node, an estimation of power consumption and an analysis of battery lifespan were conducted (Table. 4.8).

By analyzing the table and comparing it with the data from the Stability Node, it is immediately evident that this node exhibits a greater discrepancy in current consumption between the *MEASURE* and *REST* states. Additionally, the duration of the *MEASURE* state is significantly longer. As a result, this node consumes more than twice the current of the Stability Node, leading to a considerably shorter battery life. The following graph

TABLE 4.8: Current Consumption Measurements for Different States

	MEASURE	**REST**
MIN [mA]	59.975,3	59.964,2
MAX [mA]	286.544,1	60.458,7
TIME [s]	215	85
AVERAGE [mA]	173.260	60.211
AVERAGE WEIGHTED [mA]	*141.231 ± 0.06*	

(Fig. 4.27) illustrates the operational duration of the Physiology Node as a function of the sampling period, assuming a battery capacity of 2.3 Ah.

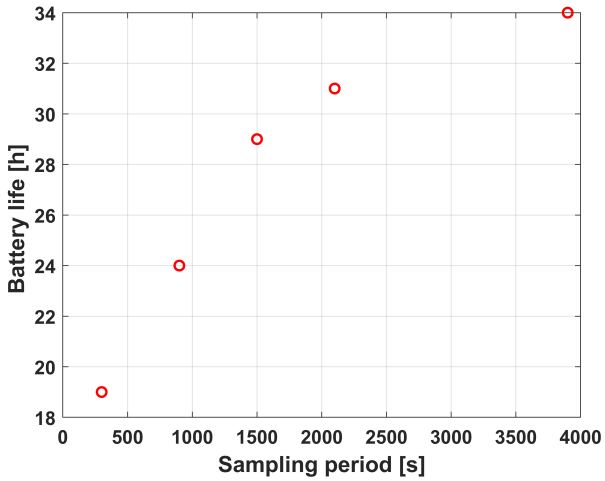

FIGURE 4.27: Operational Duration of a 2.3 Ah Battery.

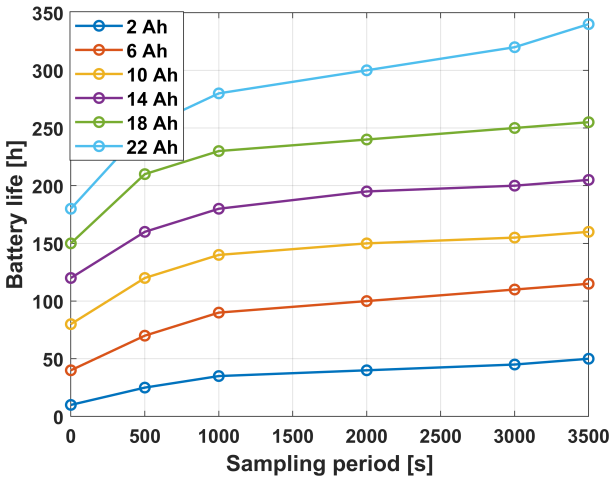

FIGURE 4.28: Operational Duration of a 2.3 Ah Battery.

In this case, the increase in battery life as a function of the sampling period is significantly more evident. Specifically, with a sampling period of 300 seconds, the estimated operational duration is approximately 19 hours, whereas for a sampling period of one hour, it extends to nearly 38 hours. This behavior is primarily attributed to the higher power consumption and prolonged duration of the *MEASUREMENT* state. The most influential factor in this increased consumption is the SAP-Flow sensor.

The graph (Fig. 4.28) illustrates the operational lifespan of the node as a function of both battery capacity (Ah) and the sampling period.

4.3.3 Environmental Node Analysis

To evaluate the most complex part of the system, the environmental monitoring node is characterized by the following signals:

- **Input**: 12V A.D. power supply.
- **Output - Weather Station**: Measurement of temperature, atmospheric pressure, relative humidity, wind speed, wind direction, corrected wind direction, and dew point.
- **Output - Electrochemical Sensors**: Measurement of gas concentrations, including CO, CO_2, NO_2, VOCs, NO_2, and OX.

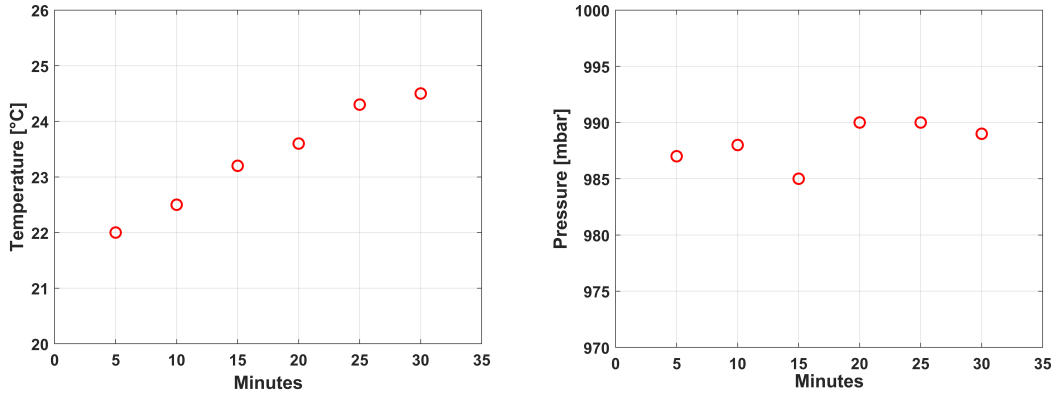

(A) Test weather station forecast (temperature). (B) Test weather station forecast (pressure).

FIGURE 4.29: Test weather station, temperature-pressure.

The Figs. 4.29a-4.29b above present the graphs corresponding to temperature and pressure measurements acquired by the MaxiMet GMX 600 weather station. Six values were sampled over a 30-minute interval, during which an attempt was made to induce variations in the recorded outputs. Regarding temperature, a heat source was applied to provoke an increase in its value. However, for pressure, it was not possible to induce a significant variation. Consequently, the recorded pressure values remain close to the atmospheric pressure of the indoor environment where the experimental test was conducted.

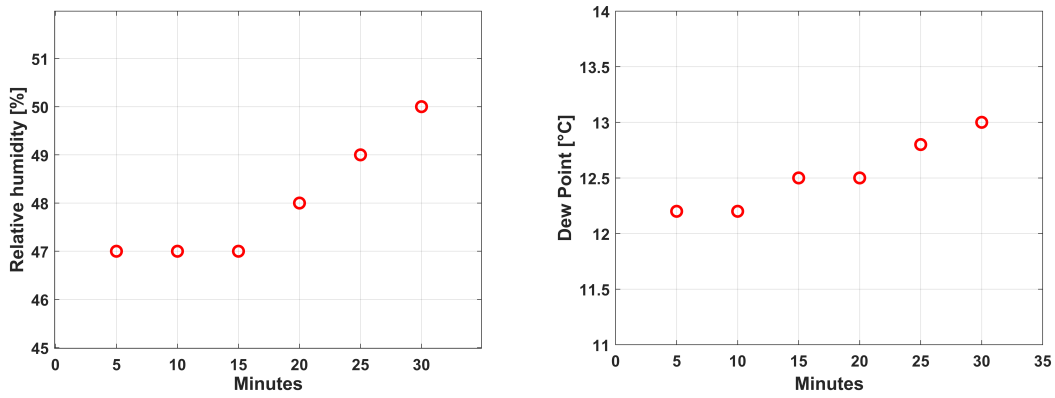

(A) Test weather station forecast (Rh %). (B) Test weather station forecast (dew point).

FIGURE 4.30: Test weather station, Rh % - dew point.

An attempt was also made to induce variations in relative humidity and dew point temperature. Specifically, it can be observed that the dew point increases as relative humidity and temperature rise, as it is directly proportional to these two physical quantities (Fig. 4.30a–4.30b).

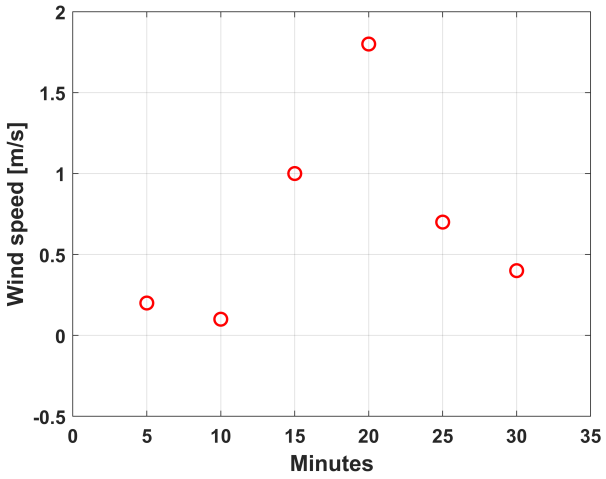

FIGURE 4.31: Test weather station forecast (speed wind).

Wind was simulated using a breath. As shown in the 10– 20 minute interval, a noticeable increase in wind speed is observed compared to the resting conditions in the preceding moments (Fig. 4.31).

The weather station also allows for the measurement of wind direction, providing two values: the wind direction and the corrected wind direction. The difference between these values lies in the reference points used for measurement. In the first case, the reference is the north of the weather station, while in the case of the corrected direction, the reference is the true cardinal point of north (Figs. 4.32a–4.32b).

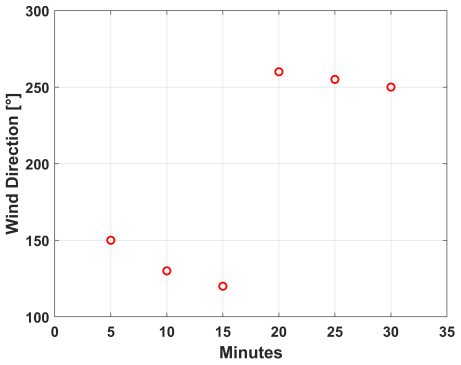

(A) Test weather station forecast (direction wind).

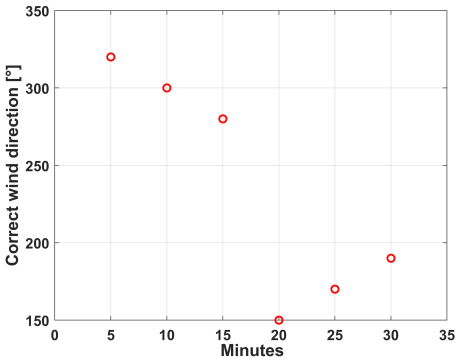

(B) Test weather station forecast (direction wind correct).

FIGURE 4.32: Test weather station, direction wind.

As shown in Figs 4.33-4.38, the simulated trend of the concentrations is consistent across all gases. Specifically, the simulation of their presence in the air occurs simultaneously, with the gases being introduced by blowing on the sensitive parts of the sensors. Except for carbon dioxide, which exhibits an offset due to its normal concentration in the air, all other gases show zero concentration in the absence of blowing.

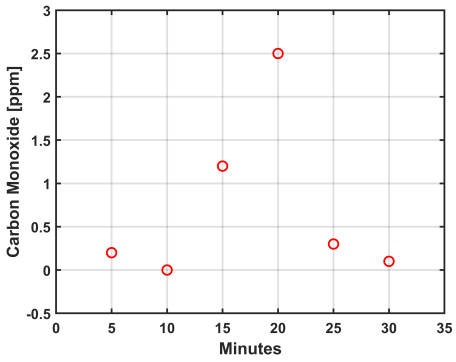

FIGURE 4.33: Concentration CO.

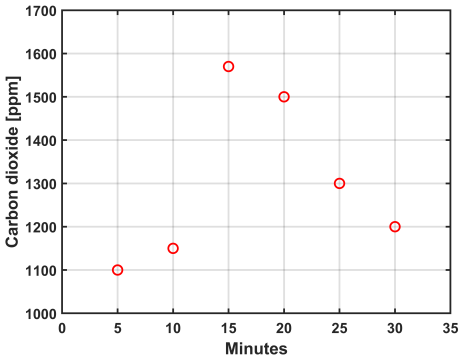

FIGURE 4.34: Concentration CO2.

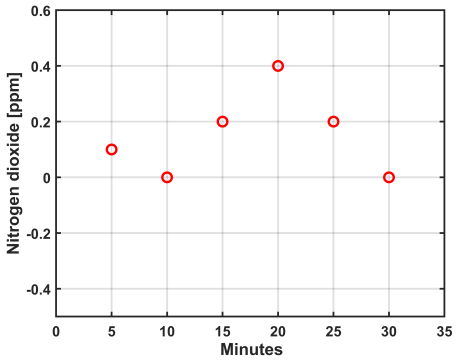

FIGURE 4.35: Concentration NO2.

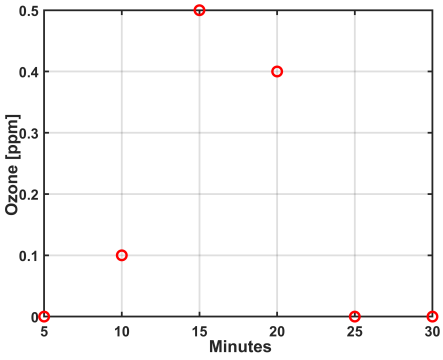

FIGURE 4.36: Concentration O3.

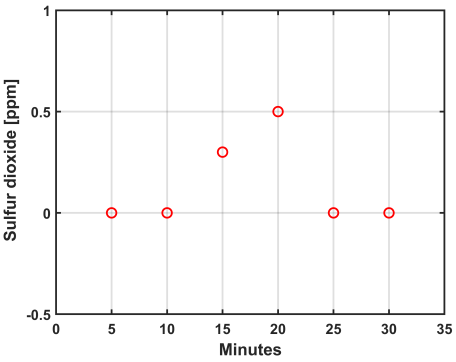

FIGURE 4.37: Concentration SO2.

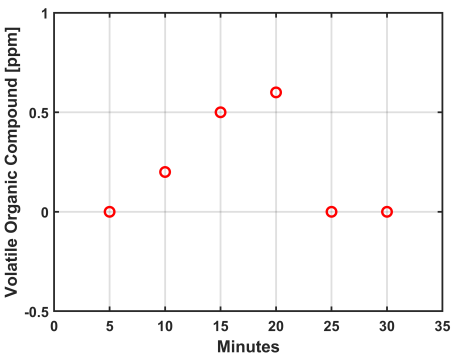

FIGURE 4.38: Concentration VOC.

FIGURE 4.39: Concentration of gases over time.

Additionally, an analysis of the power consumption and battery life was conducted for the Environment Node (Table 4.9).

TABLE 4.9: Current Consumption Measurements for the Environment Node

	MEASURE	**REST**
MIN [mA]	130.591,7	130.299,1
MAX [mA]	220.025,1	219.611,1
TIME [s]	12	288
AVERAGE [mA]	175.308	174.955
AVERAGE WEIGHTED [mA]	*174.969 ± 0.07*	

By examining the table and comparing it with the data from the Stability and Physiology nodes, it is evident that this node exhibits the highest average current consumption. Furthermore, there is almost no difference in consumption between the *REST* and *MEASUREMENT* states. The logical conclusion is that the Environment Node is the one most affected in terms of battery life.

The graph (Fig. 4.40) illustrates the operational lifetime of the Environment Node as a function of the sampling period, assuming a 2.3 Ah battery.

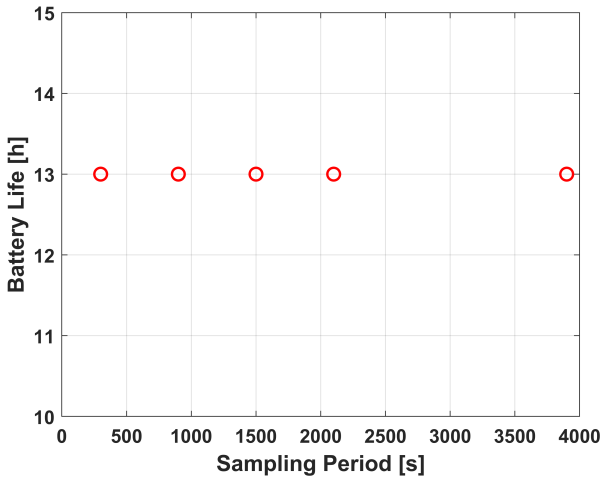

FIGURE 4.40: Duration of operation for a 2.3 Ah battery.

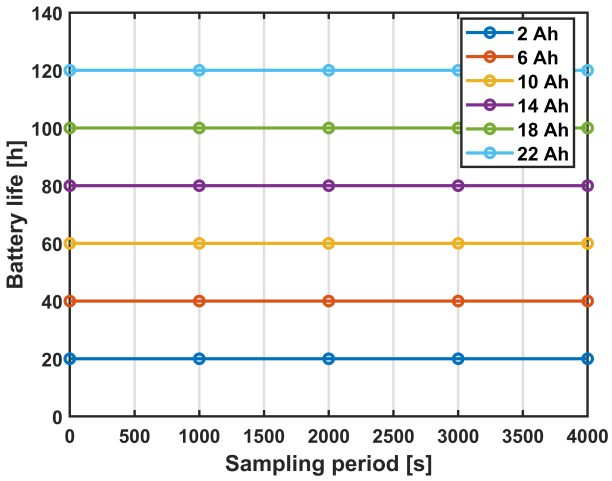

FIGURE 4.41: Duration of operation as a function of battery capacity (Ah) and sampling period.

A noticeable trend in the battery duration is observed: it does not increase with an increase in the sampling period. This result is expected, as the consumption in both states is essentially identical. Therefore, altering the sampling frequency does not have a significantly beneficial effect on power consumption. On the other hand, increasing the battery capacity successfully leads to an increase in operational duration, reaching just over 120 hours with a relatively large 22 Ah battery (Fig. 4.41). In conclusion, we can confirm the initial hypothesis that this node is the most power-intensive in terms of consumption.

4.4 Conclusions and Future Work

Based on the successful implementation and testing of the proposed multi-node architecture, this research introduced an innovative IoT-based architecture for the automated monitoring of tree health, integrating various sensors and electronic devices to enable real-time data collection and analysis. The experimental validation demonstrated the feasibility of a distributed measurement system, confirming its potential for environmental monitoring and tree health supervision. However, some challenges remain, particularly in terms of power consumption and the long-term operational sustainability of sensor nodes, which could limit large-scale deployment in extensive forests or urban green spaces.

Future work will focus on optimizing the system for real-world implementation by improving energy efficiency through smart power management strategies, such as adaptive node activation and the integration of renewable energy sources like photovoltaic panels. Additionally, incorporating drones and high-resolution satellite imagery can enhance large-scale tree health mapping, while ML algorithms can enable predictive analysis, identifying early signs of stress or disease. These advancements will help refine the system, making it a more effective tool for long-term environmental monitoring and conservation efforts.

Chapter 5

Conclusions and Future Work

PA has shown significant potential to improve both productivity and sustainability in farming by utilizing remote sensing technologies, and data analytics. The success of PA largely depends on the accuracy and reliability of these measurement systems, as they form the foundation for informed, data-driven decisions. However, challenges such as sensor inaccuracies, environmental variability, and limitations in calibration processes can affect data quality, ultimately reducing the effectiveness and value of the insights generated.

This study specifically addresses the challenges related to the reliability of measurements in remote sensing applications, with a focus on the NDVI, one of the most widely used VIs for crop health assessment. A comprehensive workflow was developed and validated to quantify the uncertainty associated with NDVI measurements derived from multispectral imagery. Initial investigations identified the nominal wavelength of the multispectral camera sensor as a significant source of uncertainty. To more accurately reflect real-world conditions, the model was subsequently refined by incorporating the sensor's OD. The model was applied to multispectral datasets collected from both dry and fresh Douglas fir leaves. Results demonstrated that uncertainty-induced deviations in NDVI values ranged approximately from 0.03 to 0.1, potentially limiting the ability to reliably distinguish between different vegetation states, fresh and dry leaves.

Subsequently, the workflow was extended to incorporate additional sources of uncertainty by integrating parameters such as the sensor's SNR and the variability of solar irradiance under diverse atmospheric conditions. Utilizing MCS techniques, the model quantitatively evaluated both the individual and combined impacts of these uncertainty sources on NDVI values derived from multispectral imagery of Douglas fir leaves. The results revealed that variability in the sensor's nominal wavelength and atmospheric conditions exerted the most significant influence on NDVI measurements, whereas other factors, such as the standard deviation of solar irradiance and the camera's SNR, exhibited comparatively minimal effects. Notably, IQR analysis of NDVI values indicated that despite the presence of uncertainty, NDVI values remained relatively stable. To

statistically assess the separability of vegetation states, the Wilcoxon Rank Sum Test was employed to examine the degree of overlap in NDVI distributions between fresh and dry leaves following the application of uncertainty sources. The findings demonstrated a clear separation between the NDVI distributions of fresh and dry leaves, suggesting that a classification threshold can be established. However, this threshold is sensitive to environmental fluctuations and must be dynamically adjusted to maintain accuracy under varying atmospheric conditions.

To address inconsistencies in NDVI measurements caused by atmospheric variability, a radiometric compensation model was developed and implemented. This model integrates emulated Permaflect reference panels with reflectance values ranging from 5% to 94%, representing diverse lighting and surface conditions, and applied a MCS to account for uncertainty sources during evaluation. The model was then validated using a physical reference panel. Then the model was applied to multispectral images captured by a UAV over pistachio orchards under dry atmospheric conditions. The method's performance was assessed by comparing the resulting NDVI values with both ground truth data and those derived from the conventional radiometric correction in Agisoft Metashape. Results showed that the proposed model significantly improves NDVI accuracy by effectively correcting atmospheric-induced deviations, enhancing the reliability of vegetation monitoring.

In addition to radiometric analysis, the study explored complementary techniques to support PA applications through the use of ML. A methodology for detecting yellow rust disease in winter wheat was proposed using RGB imagery captured by UAVs. The approach involved feature extraction, statistical analysis using one-way ANOVA, and classification through ML algorithms—most notably, LDA—which enabled accurate disease identification. Although the LDA accuracy achieved using RGB imagery was lower than that of the model used hyperspectral images, the significantly reduced cost and operational simplicity make RGB-based approaches appealing for practical implementation. To assess the robustness of the model, a sensitivity analysis was conducted to evaluate its performance under various uncertainty sources, including blurring, lighting variability, and noise affecting the images. The results indicated that while the model was resilient to speckle noise, it showed vulnerability to contrast variations, highlighting the necessity for radiometric normalization of the RGB channels.

Furthermore, another part of the study focused on designing an IoT-based system to enable real-time monitoring of environmental conditions and tree health through the deployment of distributed sensor nodes. The proposed system incorporates LoRa, to facilitate reliable and energy-efficient data transmission between sensor-integrated nodes and a central gateway. A detailed analysis of the selected sensors is presented, encompassing their measurement principles, functional specifications, and integration within the

IoT framework. Additionally, the system's performance was evaluated through experimental testing conducted under controlled conditions in the LESIM laboratory, focusing on both sensor accuracy and energy consumption to assess the feasibility of long-term deployment.

In summary, a critical gap in the field of PA lies at the intersection of measurement science (metrology) and the challenges posed by real-world, uncontrolled environmental conditions. In PA, quantification relies on data captured under natural, dynamic settings—conditions that inherently involve sources of uncertainty beyond human control. Therefore, a key role of metrology in PA is to understand, quantify, and, where possible, compensate for these uncertainty sources to enhance the reliability of measurements. This study focuses on one widely used VI, the NDVI, as a representative metric to investigate how both systematic and environmental uncertainties affect measurement accuracy. A comprehensive methodology was developed to assess and model the impact of these uncertainty sources—such as sensor characteristics and atmospheric variability—on NDVI values. A compensation model was proposed to correct for atmospheric effects, demonstrating improved measurement reliability. However, further work is needed to generalize this approach for broader application across different crops, sensors, and conditions. Additionally, the study examined how uncertainties influence ML applications in PA, particularly those based on image data. By analyzing the sensitivity of ML models to various sources of noise and variability, the research identified which factors most significantly degrade model performance, informing future efforts to build more robust systems.

Future Work

Building upon the current findings, several directions for future research are recommended:

- **Extended Uncertainty Modeling:** Incorporate additional sources of uncertainty such as UAV flight parameters (e.g., altitude, image overlap), environmental variables (e.g., temperature, humidity), and sensor orientation to improve the robustness of the uncertainty quantification framework.
- **Generalization of Radiometric Compensation:** Evaluate the performance of the proposed radiometric compensation model across a variety of vegetation types and states, including stressed or diseased plants, and expand the methodology to other VIs beyond NDVI to increase its general applicability. Furthermore, it is crucial to continue testing and refining the method, assessing its performance

under a broader range of atmospheric conditions to improve its robustness and adaptability.

- **Benchmarking Against State-of-the-Art:** Conduct a comprehensive comparison of the proposed compensation method with existing state-of-the-art techniques using publicly available and standardized datasets. This benchmarking will enable thorough performance evaluation and enhance the generalizability of the findings.
- **Enhanced Monitoring through Integration of Diverse Data Sources:** Combining high-resolution satellite imagery with UAV data allows for more detailed and frequent monitoring of agricultural fields. This integration improves spatial, spectral resolution (seeing finer details on the ground) and temporal resolution (capturing data more often), which helps in detecting changes in crop health, soil conditions, and environmental stress more accurately and in a timely manner.
- **Automation of Segmentation and Classification Tasks:** By applying ML and DL techniques, tasks such as identifying crop types, mapping field boundaries, and detecting anomalies can be automated with high accuracy. This reduces the need for manual analysis, saves time, and ensures consistent results, making it easier for farmers and agronomists to make informed decisions based on reliable, real-time data.
- **Performance Evaluation of ML Algorithms with Feature Reduction and Compensation Method Integration:** Evaluate the effectiveness of ML algorithms under feature and dimensionality reduction strategies to enhance computational efficiency and model generalization. Furthermore, incorporate radiometric and other compensation techniques into RGB image processing workflows to improve robustness against noise, illumination variability, and environmental inconsistencies.
- **Scalability and Cross-Domain Application:** Test the developed methodologies across different crop types, climatic zones, and agricultural systems to evaluate scalability and operational viability in diverse agroecological contexts.
- **Energy Optimization in IoT Systems:** Investigate energy-efficient designs for IoT-based monitoring systems through adaptive power management, low-power communication protocols, and the integration of renewable energy sources such as photovoltaic panels to facilitate long-term field deployment.

Appendix A

Teamwork Image and MATLAB Code for Raw Data Conversion

A.1 Teamwork Image

The Fig. A.1 serves as a reminder of working with the kind and friendly team members of the project in Spain.

FIGURE A.1: A memorable moment of collaboration with the kind and welcoming project team in Spain, captured during our work together in September 2024.

A.2 MATLAB code for converting raw DN values to reflected ones based on the Mavic 3M white paper [1].

Listing A.1: MATLAB Code for Raw Data Conversion

```
% This is a comment in gray
bit_depth = 15; % Bit depth
black_level_offset = 3200; % Black level offset

% Sensor gain coefficients for R and NIR bands
sensor_gain_R = [1.016, 1.017, 1.006, 1.012];
sensor_gain_NIR = [1.013, 1.006, 1.010, 1.015];

% Estimated sensor calibration factor and exponential term
sensor_calibration_factor = 0.182000;
exp_factor = exp(6);

% Sensor gain adjustment factors for radiometric correction
gain_adjustment_R = 0.558774;
gain_adjustment_NIR = 0.969294;

% Normalize image data by bit depth
normalization_factor = 2^bit_depth;
I_black_level = black_level_offset / normalization_factor;

%%% Converting raw DN values to reflected values for Red Band
I_R = RawData.RED ./ normalization_factor;
camera_R = (I_R - I_black_level) ./ (sensor_gain_R(j) ...
    * (sensor_calibration_factor / exp_factor));
E_camera_R = camera_R .* gain_adjustment_R;

%%% Converting raw DN values to reflected values for NIR Band
I_NIR = RawData.NIR_T ./ normalization_factor;
camera_NIR = (I_NIR - I_black_level) ./ (sensor_gain_NIR(j) ...
    * (sensor_calibration_factor / exp_factor));
E_camera_NIR = camera_NIR .* gain_adjustment_NIR;
```

Achievements and Certifications During My PhD

1 Awards

I'm honored to share that my paper [8], titled *"IoT-based System for Monitoring Health State of Trees"*, received the Best Paper Award at "the 7th International Conference on Internet of Things and Its Applications (2023)", as shown in Fig. 2.

FIGURE 2: Best paper award (IoT 2023).

2 Participation in Conferences

Over the past few years, I've had the opportunity to actively participate in several international conferences, where I shared my research with the broader scientific community:

- **MetroAgriFor 2022 – IEEE International Workshop on Metrology for Agriculture and Forestry**: Presented my work [2] titled *"UAV in Precision*

Agriculture: a Preliminary Assessment of Uncertainty for Vegetation Health Index", as shown in Fig. 3.

FIGURE 3: Presentation at IEEE MetroAgriFor 2022.

- **MetroAgriFor 2023 – IEEE International Workshop on Metrology for Agriculture and Forestry**: Presented the paper [3], *"Uncertainty Model for NDVI Estimation from Multispectral Camera Measurements"*, Fig. 4.

FIGURE 4: Presentation at IEEE MetroAgriFor 2023.

- **IoT 2023 – The 7th IEEE International Conference on Internet of Things and Its Applications**: Presented the award-winning paper [8], *"IoT-based System for Monitoring Health State of Trees"*, as illustrated in Fig. 5.

FIGURE 5: Presentation at International Conference on Internet of Things and Its Application (IoT 2023).

- **MetroAgriFor 2024 – IEEE International Workshop on Metrology for Agriculture and Forestry**: Presented my most recent work [143] titled *"Performance Assessment of Machine Learning Algorithms for Yellow Rust Wheat Disease Classification with UAV RGB Images"*, Fig. 6.

FIGURE 6: Presentation at IEEE MetroAgriFor 2024.

3 Summar Schools

I actively participated in **International PH.D. School "ITALO GORINI"** in the years of 2022 (Fig. 7), 2023 (Fig. 8), 2024 (Fig. 9)

FIGURE 7: International PH.D. School "ITALO GORINI" 2022.

FIGURE 8: International PH.D. School "ITALO GORINI" 2023.

FIGURE 9: International PH.D. School "ITALO GORINI" 2024.

4 Others

- In 2023, I actively contributed to the **establishment of a collaborative agreement between Sharif University of Technology (Iran) and the University of Sannio (Italy)**, as illustrated in Fig. 10.

ACCORDO PER LA COOPERAZIONE CULTURALE E SCIENTIFICA TRA L'UNIVERSITA' DEGLI STUDI DEL SANNIO E SHARIF UNIVERSITY OF TECHNOLOGY

AGREEMENT OF CULTURAL AND SCIENTIFIC COOPERATION BETWEEN UNIVERSITA' DEGLI STUDI DEL SANNIO AND SHARIF UNIVERSITY OF TECHNOLOGY

Disposizioni generali

General Provisions

Considerando che l'interscambio culturale e scientifico é imprescindibile affinché le istituzioni accademiche sviluppino le proprie attività formative e di ricerca;

Given that cultural and scientific exchange is indispensable to academic institutions to develop their educational and research activities;

Considerando che per raggiungere l'obiettivo sopra menzionato è necessario promuovere accordi culturali e scientifici tra istituzioni di alta formazione in Paesi diversi;

Given that, for the above-stated purpose, it is necessary to promote and encourage direct cultural agreements between institutions of higher learning in different countries;

Dopo aver verificato l'interesse reciproco

Having verified the mutual interest that

Università degli Studi del Sannio

Il Rettore Prof. Gerardo Canfora

Data 20/9/23

Prof. Biagio Simonetti
Erasmus+ Rector's delegate

Timbro

Sharif University of Technology

The Rector Prof. Rasool Jalili

Data

Seal

Aug. 27th 2023

FIGURE 10: Contributing to the establishment of a collaborative agreement between Sharif University of Technology (Iran) and the University of Sannio (Italy) – 2023.

- In September 2024, I **participated in a research activity at the Agro-Environmental Research Centre 'El Chaparrillo' (IRIAF-CIAG, Ciudad Real, Spain)**, as shown in Fig. 11. This collaborative effort focused on conducting an advanced field study employing state-of-the-art technologies—including a UAV equipped with a multispectral camera and a handheld NDVI sensor—to collect precise ground truth data from a pistachio orchard.

IRIAF
Instituto Regional de Investigación y Desarrollo Agroalimentario y Forestal
Consejería de Agricultura, Ganadería y Desarrollo Rural
Castilla-La Mancha

CERTIFICATE OF ATTENDANCE

26th of September 2024

To whom it may concern,

This is to certify that the PhD student Fatemeh Khalesi from the Università degli Studi del Sannio has actively participated in a research stay in our department at Agro-Environmental Research Centre 'El Chaparrillo' (IRIAF-CIAG, Ciudad Real, Spain), from 9th to 12th of September 2024, with the goal of doing a collaborative study involving advanced technologies, including a drone equipped with a multispectral camera, an NDVI handheld sensor combined with fieldwork, to understand the maturity of pistachio nuts.

Yours sincerely,

Dr. Raquel Martínez Peña
Principal Investigator of Woody Crops Department

Ctra. Toledo - Albacete, s/n
13700 Tomelloso, Ciudad Real
Tel: 926 50 80 60
e-mail: secretaria_iriaf@jccm.es
iriaf.castillalamancha.es
www.castillalamancha.es

FIGURE 11: Collaborative study and fieldwork on pistachio orchards at IRIAF-CIAG, Ciudad Real, Spain – 2024.

- In 2024, I **completed an online course titled *"Neural Networks and Deep Learning"* offered by Coursera**. I successfully passed the course with the highest grade, as shown in Fig. 12.

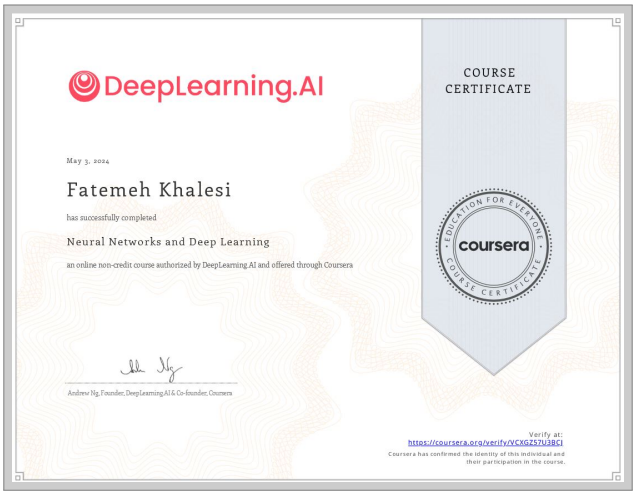

FIGURE 12: Certificate of successful completion of the online course *"Neural Networks and Deep Learning"* on the Coursera platform – 2024.

Bibliography

[1] D. Inc., "Mavic 3M image processing guide," 2025. Last accessed 06 February 2025.

[2] F. Khalesi, P. Daponte, L. D. Vito, F. Picariello, and I. Tudosa, "UAV in precision agriculture: a preliminary assessment of uncertainty for vegetation health index," in *2022 IEEE Workshop on Metrology for Agriculture and Forestry (MetroAgriFor)*, pp. 94–99, IEEE, 2022. © 2022 IEEE. Reprinted with permission.

[3] F. Khalesi, P. Daponte, L. De Vito, F. Picariello, and I. Tudosa, "Uncertainty Model for NDVI Estimation from Multispectral Camera Measurements," in *2023 IEEE International Workshop on Metrology for Agriculture and Forestry (MetroAgriFor)*, pp. 444–448, 2023. © 2023 IEEE. Reprinted with permission.

[4] F. Khalesi, I. Ahmed, P. Daponte, F. Picariello, L. D. Vito, and I. Tudosa, "The uncertainty assessment by the monte carlo analysis of NDVI measurements based on multispectral UAV imagery," *Sensors*, vol. 24, no. 9, p. 2696, 2024.

[5] Labsphere, "Reflectance Coatings and Materials." https://www.labsphere.com/wp-content/uploads/2024/05/ReflectanceCoatingsMaterialsTechGuideRev04.pdf, 2023. Last accessed 15 August 2024.

[6] "Dji mavic 3M," 2025. Last accessed 23 February 2025.

[7] E. Scientific, "Fieldscout NDVI specification," 2025. Last accessed 06 February 2025.

[8] F. Khalesi, P. Daponte, L. D. Vito, F. Picariello, and I. Tudosa, "IoT-based system for monitoring health state of trees," in *2023 7th International Conference on Internet of Things and Applications (IoT)*, pp. 1–7, IEEE, 2023. © 2023 IEEE. Reprinted with permission.

[9] X. Tagle, *Study of radiometric variations in Unmanned Aerial Vehicle remote sensing imagery for vegetation mapping.* PhD thesis, 06 2017.

[10] P. Liu, W. L. Woo, and S. S. Dlay, "One colored image based 2.5 D human face reconstruction," in *2009 17th European Signal Processing Conference*, pp. 2584–2588, IEEE, 2009.

[11] E. O. Company, "200 x 260mm Sheet of Lambertian Black Foil, Adhesive." https://gisgeography.com/multispectral-vs-hyperspectral-imagery-explained/https://www.edmundoptics.com/p/20-x-26cm-sheet-of-lambertian-black-foil-adhesive/47295/. Last accessed 11 August 2024.

[12] I. Spectrum Technologies, "FieldScout CM 1000 NDVI Meter." https://www.specmeters.com/FieldScout-CM1000-NDVI-Meter, 2025. Last accessed 04 Februry 2025.

[13] "X-NUCLEO-IKS01A3." https://www.st.com/en/ecosystems/x-nucleo-iks01a3.html#st_all-features_sec-nav-tab. Last accessed 27 January 2025.

[14] J. A. Taylor, "Precision agriculture," in *Encyclopedia of Soils in the Environment (Second Edition)* (M. J. Goss and M. Oliver, eds.), pp. 710–725, Oxford: Academic Press, second edition ed., 2023.

[15] P. Singh, P. C. Pandey, G. P. Petropoulos, A. Pavlides, P. K. Srivastava, N. Koutsias, K. A. K. Deng, and Y. Bao, "Hyperspectral remote sensing in precision agriculture: Present status, challenges, and future trends," in *Hyperspectral remote sensing*, pp. 121–146, Elsevier, 2020.

[16] S. Getahun, H. Kefale, and Y. Gelaye, "Application of precision agriculture technologies for sustainable crop production and environmental sustainability: A systematic review," *The Scientific World Journal*, vol. 2024, no. 1, p. 2126734, 2024.

[17] P. Singh, P. Pandey, G. Petropoulos, A. Pavlides, P. Srivastava, N. Koutsias, K. Deng, and Y. Bao, "Hyperspectral remote sensing in precision agriculture: Present status, challenges, and future trends," in *Hyperspectral remote sensing*, pp. 121–146, Elsevier, 2020.

[18] R. P. Sishodia, R. L. Ray, and S. K. Singh, "Applications of remote sensing in precision agriculture: A review," *Remote sensing*, vol. 12, no. 19, p. 3136, 2020.

[19] N. Delavarpour, C. Koparan, J. Nowatzki, S. Bajwa, and X. Sun, "A technical study on UAV characteristics for precision agriculture applications and associated practical challenges," *Remote Sensing*, vol. 13, no. 6, p. 1204, 2021.

[20] P.Radoglou-Grammatikis, P.Sarigiannidis, T.Lagkas, and I.Moscholios, "A compilation of uav applications for precision agriculture," *Computer Networks*, vol. 172, p. 107148, 2020.

[21] N. Xing, W. Huang, Q. Xie, Y. Shi, H. Ye, Y. Dong, M. Wu, G. Sun, and Q. Jiao, "A transformed triangular vegetation index for estimating winter wheat leaf area index," *Remote Sensing*, vol. 12, no. 1, p. 16, 2019.

[22] M. V. Priya, R. Kalpana, S. Pazhanivelan, R. Kumaraperumal, K. P. Ragunath, G. Vanitha, A. Nihar, P. J. Prajesh, and V. Vasumathi, "Monitoring vegetation dynamics using multi-temporal normalized difference vegetation index (NDVI) and enhanced vegetation index (EVI) images of tamil nadu," *Journal of Applied and Natural Science*, vol. 15, no. 3, pp. 1170–1177, 2023.

[23] T. Konno and K. Homma, "Prediction of areal soybean lodging using a main stem elongation model and a soil-adjusted vegetation index that accounts for the ratio of vegetation cover," *Remote Sensing*, vol. 15, no. 13, p. 3446, 2023.

[24] G. Mulero, D. Jiang, D. J. Bonfil, and D. Helman, "Use of thermal imaging and the photochemical reflectance index (PRI) to detect wheat response to elevated CO2 and drought," *Plant, Cell & Environment*, vol. 46, no. 1, pp. 76–92, 2023.

[25] S. Mohanty, P. C. Pandey, P. Singh, V. Dugesar, and P. K. Srivastava, "Vegetation discrimination based on chlorophyll prediction in marshy wetland using unmanned aerial vehicles," *Aquatic Conservation: Marine and Freshwater Ecosystems*, vol. 34, no. 5, p. e4170, 2024.

[26] P. Cofta, K. Karatzas, and C. Orłowski, "A conceptual model of measurement uncertainty in IoT sensor networks," *Sensors*, vol. 21, no. 5, p. 1827, 2021.

[27] P. R. Tozer, "Uncertainty and investment in precision agriculture–is it worth the money?," *Agricultural systems*, vol. 100, no. 1-3, pp. 80–87, 2009.

[28] D. J. Hand, *Measurement: A very short introduction*. Oxford University Press, 2016.

[29] "Measurement Uncertainty." https://jcgm.bipm.org/vim/en/2.26.html, 2025. Last accessed 31 May 2025.

[30] M. M. Tahat, K. M. Alananbeh, Y. A. Othman, and D. I. Leskovar, "Soil health and sustainable agriculture," *Sustainability*, vol. 12, no. 12, p. 4859, 2020.

[31] H. S. El-Beltagi, A. Basit, H. I. Mohamed, I. Ali, S. Ullah, E. A. Kamel, T. A. Shalaby, K. M. Ramadan, A. A. Alkhateeb, and H. S. Ghazzawy, "Mulching as a sustainable water and soil saving practice in agriculture: A review," *Agronomy*, vol. 12, no. 8, p. 1881, 2022.

[32] M. Rastogi, S. M. Kolur, A. Burud, T. Sadineni, M. Sekhar, R. Kumar, and A. Rajput, "Advancing water conservation techniques in agriculture for sustainable resource management: A review," *Journal of Geography, Environment and Earth Science International*, vol. 28, no. 3, pp. 41–53, 2024.

[33] A. Wasay, Z. Ahmed, A. Abid, A. Sarwar, and A. Ali, "Optimizing crop yield through precision agronomy techniques," *Trends in Biotechnology and Plant Sciences*, vol. 2, no. 1, pp. 25–35, 2024.

[34] M. A. John, I. Bankole, O. Ajayi-Moses, T. Ijila, T. Jeje, and P. Lalit, "Relevance of advanced plant disease detection techniques in disease and Pest Management for Ensuring Food Security and Their Implication: A review," *American Journal of Plant Sciences*, vol. 14, no. 11, pp. 1260–1295, 2023.

[35] F. Silva, C. Queirós, M. Pereira, T. Pinho, T. Barroso, S. Magalhães, J. Boaventura, F. Santos, M. Cunha, and R. Martins, "Precision Fertilization: A critical review analysis on sensing technologies for nitrogen, phosphorous and potassium quantification," *Computers and Electronics in Agriculture*, vol. 224, p. 109220, 2024.

[36] H. Mirzakhaninafchi, M. Singh, A. K. Dixit, A. Prakash, S. Sharda, J. Kaur, and A. M. Nafchi, "Performance assessment of a sensor-based variable-rate real-time fertilizer applicator for rice crop," *Sustainability*, vol. 14, no. 18, p. 11209, 2022.

[37] W. de Vries, J. Kros, J. C. Voogd, and G. H. Ros, "Integrated assessment of agricultural practices on large scale losses of ammonia, greenhouse gases, nutrients and heavy metals to air and water," *Science of the total Environment*, vol. 857, p. 159220, 2023.

[38] S. Faisal, M. P.-L. Ooi, S. K. Abeysekera, Y.-C. Kuang, and D. Fletcher, "Roadmap for Measurement and Applications: Uncertainty Quantification and Visualization for Optimal Decision-Making in Hyperspectral Imaging-Based Precision Agriculture," *IEEE Instrumentation & Measurement Magazine*, vol. 28, no. 1, pp. 23–32, 2025.

[39] A. Čolaković and M. Hadžialić, "Internet of Things (IoT): A review of enabling technologies, challenges, and open research issues," *Computer networks*, vol. 144, pp. 17–39, 2018.

[40] I. U. Din, M. Guizani, S. Hassan, B.-S. Kim, M. K. Khan, M. Atiquzzaman, and S. H. Ahmed, "The Internet of Things: A review of enabled technologies and future challenges," *Ieee Access*, vol. 7, pp. 7606–7640, 2018.

[41] K. Balakrishnan, R. Dhanalakshmi, R. Gopalakrishnan, *et al.*, "Clock synchronization in industrial Internet of Things and potential works in precision time protocol: Review, challenges and future directions," *International Journal of Cognitive Computing in Engineering*, vol. 4, pp. 205–219, 2023.

[42] P. Dowd, "Accuracy and Precision," in *Encyclopedia of Mathematical Geosciences*, pp. 1–4, Springer, 2023.

[43] "International vocabulary of metrology – basic and general concepts and associated terms (VIM)." https://www.bipm.org/documents/20126/2071204/JCGM_200_2012.pdf. Last accessed 18 April 2025.

[44] "A calibration." https://jcgm.bipm.org/vim/en/2.39.html, 2025. Last accessed 31 May 2025.

[45] "A calibration." https://ncc.nesdis.noaa.gov/documents/documentation/JCGM_100_2008_E.pdf, 2025. Last accessed 31 May 2025.

[46] J. Sun, Y. Zhang, Y. Zhang, P. Li, and G. Teng, "Precision seeding compensation and positioning based on multisensors," *Sensors*, vol. 22, no. 19, p. 7228, 2022.

[47] R. Nikkilä, I. Seilonen, and K. Koskinen, "Software architecture for farm management information systems in precision agriculture," *Computers and electronics in agriculture*, vol. 70, no. 2, pp. 328–336, 2010.

[48] M. S. Basir, D. Buckmaster, A. Raturi, and Y. Zhang, "From pen and paper to digital precision: a comprehensive review of on-farm recordkeeping," *Precision Agriculture*, vol. 25, no. 5, pp. 2643–2682, 2024.

[49] A. Michailidis, C. Charatsari, T. Bournaris, E. Loizou, A. Paltaki, D. Lazaridou, and E. D. Lioutas, "A First View on the Competencies and Training Needs of Farmers Working with and Researchers Working on Precision Agriculture Technologies," *Agriculture*, vol. 14, no. 1, p. 99, 2024.

[50] T. P. Kharel, A. J. Ashworth, P. R. Owens, and M. Buser, "Spatially and temporally disparate data in systems agriculture: Issues and prospective solutions," *Agronomy Journal*, vol. 112, no. 5, pp. 4498–4510, 2020.

[51] E. Duncan, A. Glaros, D. Z. Ross, and E. Nost, "New but for whom? discourses of innovation in precision agriculture," *Agriculture and Human Values*, vol. 38, pp. 1181–1199, 2021.

[52] A. Ahmed, I. Parveen, S. Abdullah, I. Ahmad, N. Alturki, and L. Jamel, "Optimized data fusion with scheduled rest periods for enhanced smart agriculture via blockchain integration," *Ieee Access*, vol. 12, pp. 15171–15193, 2024.

[53] D. Popescu, F. Stoican, G. Stamatescu, L. Ichim, and C. Dragana, "Advanced UAV–WSN system for intelligent monitoring in precision agriculture," *Sensors*, vol. 20, no. 3, p. 817, 2020.

[54] A. Morales, R. Guerra, P. Horstrand, M. Diaz, A. Jimenez, J. Melian, S. Lopez, and J. F. Lopez, "A multispectral camera development: From the prototype assembly until its use in a UAV system," *Sensors*, vol. 20, no. 21, p. 6129, 2020.

[55] Y. Guo, J. Senthilnath, W. Wu, X. Zhang, Z. Zeng, and H. Huang, "Radiometric calibration for multispectral camera of different imaging conditions mounted on a UAV platform," *Sustainability*, vol. 11, no. 4, p. 978, 2019.

[56] N. Tantalaki, S. Souravlas, and M. Roumeliotis, "Data-driven decision making in precision agriculture: The rise of big data in agricultural systems," *Journal of agricultural & food information*, vol. 20, no. 4, pp. 344–380, 2019.

[57] H. M. Jawad, R. Nordin, S. K. Gharghan, A. M. Jawad, and M. Ismail, "Energy-efficient wireless sensor networks for precision agriculture: A review," *Sensors*, vol. 17, no. 8, p. 1781, 2017.

[58] M. N. Mowla, N. Mowla, A. S. Shah, K. M. Rabie, and T. Shongwe, "Internet of Things and wireless sensor networks for smart agriculture applications: A survey," *IEEe Access*, vol. 11, pp. 145813–145852, 2023.

[59] M. H. Anisi, G. Abdul-Salaam, and A. H. Abdullah, "A survey of wireless sensor network approaches and their energy consumption for monitoring farm fields in precision agriculture," *Precision Agriculture*, vol. 16, pp. 216–238, 2015.

[60] A. Terentev, V. Dolzhenko, A. Fedotov, and D. Eremenko, "Current state of hyperspectral remote sensing for early plant disease detection: A review," *Sensors*, vol. 22, no. 3, p. 757, 2022.

[61] G.Messina and G.Modica, "Applications of UAV thermal imagery in precision agriculture: State of the art and future research outlook," *Remote Sensing*, vol. 12, no. 9, 2020.

[62] L.Caturegli, M.Gaetani, M.Volterrani, S.Magni, A.Minelli, A.Baldi, G.Brandani, M.Mancini, A.Lenzi, S.Orlandini, *et al.*, "Normalized difference vegetation index versus dark green colour index to estimate nitrogen status on bermudagrass hybrid and tall fescue," *Int. Journal of Remote Sensing*, vol. 41, no. 2, pp. 455–470, 2020.

[63] A. Sassu, F. Gambella, L. Ghiani, L. Mercenaro, M. Caria, and A. L. Pazzona, "Advances in unmanned aerial system remote sensing for precision viticulture," *Sensors*, vol. 21, no. 3, p. 956, 2021.

[64] T. Adão, J. Hruška, L. Pádua, J. Bessa, E. Peres, R. Morais, and J. Sousa, "Hyperspectral imaging: A review on uav-based sensors, data processing and applications for agriculture and forestry," *Remote sensing*, vol. 9, no. 11, p. 1110, 2017.

[65] A. Kyratzis, D. Skarlatos, G. Menexes, V. Vamvakousis, and A. Katsiotis, "Assessment of vegetation indices derived by uav imagery for durum wheat phenotyping under a water limited and heat stressed mediterranean environment," *Frontiers in Plant Science*, vol. 8, p. 267511, 2017.

[66] H. Ge, H. Xiang, F. Ma, Z. Li, Z. Qiu, Z. Tan, and C. Du, "Estimating plant nitrogen concentration of rice through fusing vegetation indices and color moments derived from uav-rgb images," *Remote Sensing*, vol. 13, no. 9, p. 1620, 2021.

[67] L. Qiao, W. Tang, D. Gao, R. Zhao, L. An, M. Li, H. Sun, and D. Song, "Uav-based chlorophyll content estimation by evaluating vegetation index responses under different crop coverages," *Computers and electronics in agriculture*, vol. 196, p. 106775, 2022.

[68] M. Griffin and H. Burke, "Compensation of hyperspectral data for atmospheric effects," *Lincoln Laboratory Journal*, vol. 14, no. 1, pp. 29–54, 2003.

[69] N. Solano-Alvarez, J. Valencia-Hernández, S. Vergara-Pineda, J. Millán-Almaraz, I. Torres-Pacheco, and R. Guevara-González, "Comparative Analysis of the NDVI and NGBVI as Indicators of the Protective Effect of Beneficial Bacteria in Conditions of Biotic Stress," *Plants*, vol. 11, no. 7, p. 932, 2022.

[70] G. Lee, J. Hwang, and S. Cho, "A novel index to detect vegetation in urban areas using uav-based multispectral images," *Applied sciences*, vol. 11, no. 8, p. 3472, 2021.

[71] V. Kopačková-Strnadová, L. Koucká, J. Jelének, Z. Lhotáková, and F. Oulehle, "Canopy top, height and photosynthetic pigment estimation using parrot sequoia multispectral imagery and the unmanned aerial vehicle (uav)," *Remote Sensing*, vol. 13, no. 4, p. 705, 2021.

[72] S. Verovka and Z. Veres, "The software solution for precise agriculture using the NDVI index," in *2022 IEEE 17th International Conference on Computer Sciences and Information Technologies (CSIT)*, pp. 490–494, IEEE, 2022.

[73] J. Peng, H. Nieto, M. Andersen, K. Kørup, R. Larsen, J. Morel, D. Parsons, Z. Zhou, and K. Manevski, "Accurate estimates of land surface energy fluxes and irrigation requirements from uav-based thermal and multispectral sensors," *ISPRS Journal of Photogrammetry and Remote Sensing*, vol. 198, pp. 238–254, 2023.

[74] M. Kedzierski, D. Wierzbicki, A. Sekrecka, A. Fryskowska, P. Walczykowski, and J. Siewert, "Influence of lower atmosphere on the radiometric quality of unmanned aerial vehicle imagery," *Remote Sensing*, vol. 11, no. 10, p. 1214, 2019.

[75] A. Jenerowicz, D. Wierzbicki, and M. Kedzierski, "Radiometric correction with topography influence of multispectral imagery obtained from unmanned aerial vehicles," *Remote Sensing*, vol. 15, no. 8, p. 2059, 2023.

[76] L. Deng, Z. Mao, X. Li, Z. Hu, F. Duan, and Y. Yan, "UAV-based multispectral remote sensing for precision agriculture: A comparison between different cameras," *ISPRS Journal of Photogrammetry and Remote Sensing*, vol. 146, pp. 124–136, 2018.

[77] L. Qiao, D. Gao, R. Zhao, W. Tang, L. An, M. Li, and H. Sun, "Improving estimation of lai dynamic by fusion of morphological and vegetation indices based on uav imagery," *Computers and Electronics in Agriculture*, vol. 192, p. 106603, 2022.

[78] L. Deng, X. Hao, Z. Mao, Y. Yan, J. Sun, and A. Zhang, "A subband radiometric calibration method for uav-based multispectral remote sensing," *IEEE Journal of Selected Topics in Applied Earth Observations and Remote Sensing*, vol. 11, no. 8, pp. 2869–2880, 2018.

[79] L. Daniels, E. Eeckhout, J. Wieme, Y. Dejaegher, K. Audenaert, and W. Maes, "Identifying the Optimal Radiometric Calibration Method for UAV-Based Multispectral Imaging," *Remote Sensing*, vol. 15, no. 11, 2023.

[80] S. Luo, X. Jiang, K. Yang, Y. Li, and S. Fang, "Multispectral remote sensing for accurate acquisition of rice phenotypes: Impacts of radiometric calibration and unmanned aerial vehicle flying altitudes," *Frontiers in Plant Science*, vol. 13, p. 958106, 2022.

[81] S. Huang, L. Tang, J. Hupy, Y. Wang, and G. Shao, "A commentary review on the use of normalized difference vegetation index (NDVI) in the era of popular remote sensing," *Journal of Forestry Research*, vol. 32, no. 1, pp. 1–6, 2021.

[82] C. Köppl, R. Malureanu, C. Dam-Hansen, S. Wang, H. Jin, S. Barchiesi, J. Sandí, R. Muñoz-Carpena, M. Johnson, A. Durán-Quesada, and P. Bauer-Gottwein, "Hyperspectral reflectance measurements from UAS under intermittent clouds: Correcting irradiance measurements for sensor tilt," *Remote Sensing of Environment*, vol. 267, p. 112719, 2021.

[83] B. Banerjee, S. Raval, and P. Cullen, "Uav-hyperspectral imaging of spectrally complex environments," *International Journal of Remote Sensing*, vol. 41, no. 11, pp. 4136–4159, 2020.

[84] X. Zhou, C. Liu, Y. Xue, A. Akbar, S. Jia, Y. Zhou, and D. Zeng, "Radiometric calibration of a large-array commodity cmos multispectral camera for uav-borne remote sensing," *International Journal of Applied Earth Observation and Geoinformation*, vol. 112, p. 102968, 2022.

[85] B. Gao, M. Montes, C. Davis, and A. Goetz, "Atmospheric correction algorithms for hyperspectral remote sensing data of land and ocean," *Remote sensing of environment*, vol. 113, pp. S17–S24, 2009.

[86] B. Ayhan, C. Kwan, B. Budavari, L. Kwan, Y. Lu, D. Perez, J. Li, D. Skarlatos, and M. Vlachos, "Vegetation detection using deep learning and conventional methods," *Remote Sensing*, vol. 12, no. 15, p. 2502, 2020.

[87] R. Jiang, P. Wang, Y. Xu, Z. Zhou, X. Luo, Y. Lan, G. Zhao, A. Sanchez-Azofeifa, and K. Laakso, "Assessing the operation parameters of a low-altitude UAV for the collection of NDVI values over a paddy rice field," *Remote Sensing*, vol. 12, no. 11, p. 1850, 2020.

[88] R. de Souza, C. Buchhart, K. Heil, J. Plass, F. Padilla, and U. Schmidhalter, "Effect of time of day and sky conditions on different vegetation indices calculated from active and passive sensors and images taken from uav," *Remote Sensing*, vol. 13, no. 9, p. 1691, 2021.

[89] H. Zhu, Y. Huang, Z. An, H. Zhang, Y. Han, Z. Zhao, F. Li, C. Zhang, and C. Hou, "Assessing radiometric calibration methods for multispectral UAV imagery and the influence of illumination, flight altitude and flight time on reflectance, vegetation index and inversion of winter wheat AGB and LAI," *Computers and Electronics in Agriculture*, vol. 219, p. 108821, 2024.

[90] A. M. Poncet, T. Knappenberger, C. Brodbeck, M. Fogle Jr, J. N. Shaw, and B. V. Ortiz, "Multispectral UAS data accuracy for different radiometric calibration methods," *Remote Sensing*, vol. 11, no. 16, p. 1917, 2019.

[91] N. Ndou, K. Thamaga, Y. Mndela, and A. Nyamugama, "Radiometric compensation for occluded crops imaged using high-spatial-resolution unmanned aerial vehicle system," *Agriculture*, vol. 13, no. 8, p. 1598, 2023.

[92] L. Daniels, E. Eeckhout, J. Wieme, Y. Dejaegher, K. Audenaert, and W. H. Maes, "Identifying the optimal radiometric calibration method for UAV-based multispectral imaging," *Remote Sensing*, vol. 15, no. 11, p. 2909, 2023.

[93] H. Ahn, C. Kim, S. Lim, C. Jin, J. Kim, and C. Choi, "Minimizing seam lines in UAV multispectral image mosaics utilizing irradiance, vignette, and BRDF," *Remote Sensing*, vol. 17, no. 1, 2025.

[94] A.Basiri, V.Mariani, G.e.Silano, M.Aatif, L.Iannelli, and L.Glielmo, "A survey on the application of path-planning algorithms for multi-rotor uavs in precision agriculture," *Journal of Navigation*, vol. 75, no. 2, p. 364–383, 2022.

[95] N.Amarasingam, S.Salgadoe, K.Powell, L.F.Gonzalez, and S.Natarajan, "A review of uav platforms, sensors, and applications for monitoring of sugarcane crops," *Remote Sensing Applications: Society and Environment*, p. 100712, 2022.

[96] R.Sun, Q.Cheng, G.Wang, and W.Y.Ochieng, "A novel online data-driven algorithm for detecting UAV navigation sensor faults," *Sensors*, vol. 17, no. 10, p. 2243, 2017.

[97] Y.Lan, Y.Huang, D.Martin, and W.Hoffmann, "Development of an airborne remote sensing system for crop pest management: system integration and verification," *Applied Engineering in Agriculture*, vol. 25, no. 4, pp. 607–615, 2009.

[98] C. Zeng, D. King, M. Richardson, and B. Shan, "Fusion of multispectral imagery and spectrometer data in uav remote sensing," *Remote Sensing*, vol. 9, no. 7, p. 696, 2017.

[99] H.Cetin, J.T.Pafford, and T.G.Mueller, "Precision agriculture using hyperspectral remote sensing and gis," in *Proc. of 2nd Int. Conf. on Recent Advances in Space Technologies, 2005. RAST 2005.*, pp. 70–77, IEEE, 2005.

[100] H.Niu, D.Hollenbeck, T.Zhao, D.Wang, and Y.Chen, "Evapotranspiration estimation with small UAVs in precision agriculture," *Sensors*, vol. 20, no. 22, p. 6427, 2020.

[101] A.Prakash, "Thermal remote sensing: concepts, issues and applications," *Int. Archives of Photogrammetry and Remote Sensing*, vol. 33, no. B1; PART 1, pp. 239–243, 2000.

[102] M.J.Rycroft, "Electromagnetic radiation principles and concepts as applied to space remote sensing," *Handbook of Satellite Applications*, pp. 833–846, 2017.

[103] M. Mashala, T. Dube, B. Mudereri, K. Ayisi, and M. Ramudzuli, "A systematic review on advancements in remote sensing for assessing and monitoring land use and land cover changes impacts on surface water resources in semi-arid tropical environments," *Remote Sensing*, vol. 15, no. 16, p. 3926, 2023.

[104] G. Shaw and H. Burke, "Spectral imaging for remote sensing," *Lincoln laboratory journal*, vol. 14, no. 1, pp. 3–28, 2003.

[105] P.Olsson, A.Vivekar, K.Adler, V. Millan, A.Koc, M.Alamrani, and L.Eklundh, "Radiometric correction of multispectral uas images: Evaluating the accuracy of the parrot sequoia camera and sunshine sensor," *Remote Sensing*, vol. 13, no. 4, p. 577, 2021.

[106] T.H.Kurz and S.J.Buckley, "A review of hyperspectral imaging in close range applications," 2016.

[107] A.K.Taloor, D.S.Manhas, and G.C.Kothyari, "Retrieval of land surface temperature, normalized difference moisture index, normalized difference water index of the ravi basin using landsat data," *Applied Computing and Geosciences*, vol. 9, p. 100051, 2021.

[108] N.Agam, Y.Cohen, J.A.J.Berni, V.Alchanatis, D.Kool, A.Dag, U.Yermiyahu, and A.Ben-Gal, "An insight to the performance of crop water stress index for olive trees," *Agricultural Water Management*, vol. 118, pp. 79–86, 2013.

[109] K.E.Alordzinu, J.Li, Y.Lan, S.A.Appiah, A. Aasmi, and H.Wang, "Rapid estimation of crop water stress index on tomato growth," *Sensors*, vol. 21, no. 15, p. 5142, 2021.

[110] *Evaluation of measurement data-Guide to the expression of uncertainty in measurement, JCGM 100:2008*. 2008.

[111] P.J.Zarco-Tejada, J.R.Miller, G.H.Mohammed, and T.L.Noland, "Chlorophyll fluorescence effects on vegetation apparent reflectance: I. leaf-level measurements and model simulation," *Remote Sensing of Environment*, vol. 74, no. 3, pp. 582–595, 2000.

[112] M.Govender, K.Chetty, and H.Bulcock, "A review of hyperspectral remote sensing and its application in vegetation and water resource studies," *Water Sa*, vol. 33, no. 2, pp. 145–151, 2007.

[113] "VISIBLE AND NEAR-INFRARED LEAF REFLECTANCE SPECTRA, 1992-1993." https://daac.ornl.gov/ACCP/guides/leafspec.html. Last accessed 8 May 2023.

[114] "P4-multispectral camera." https://www.dji.com/it/p4-multispectral/. Last accessed 8 May 2023.

[115] E.Christophe, C.Mailhes, and P.Duhamel, "Hyperspectral image compression: adapting SPIHT and EZW to anisotropic 3-D wavelet coding," *IEEE Transactions on Image processing*, vol. 17, no. 12, pp. 2334–2346, 2008.

[116] M.Aboras, H.Amasha, and I.Ibraheem, "Early detection of melanoma using multispectral imaging and artificial intelligence techniques," *American Journal of Biomedical and Life Sciences*, vol. 3, no. 2-3, pp. 29–33, 2015.

[117] "USGS Spectral Library Version 7 Sample Description." https://crustal.usgs.gov/speclab/data/HTMLmetadata/Aspen_Aspen-1_green-top_ASDFRa_AREF.html. Last accessed 20 September 2023.

[118] "Erik richard (2022), TSIS SIM level 3 solar spectral irradiance 24-hour means v09, greenbelt, md, USA, goddard earth sciences data and information services center (GES DISC)." https://disc.gsfc.nasa.gov/datasets/TSIS_SSI_L3_24HR_13/summary?keywords=TSIS_SSI_L3_24HR_12. Last accessed 26 March 2025.

[119] A. Cracknell, *Introduction to remote sensing*. CRC press, 2007.

[120] *Evaluation of measurement data — Supplement 1 to the "Guide to the expression of uncertainty in measurement" — Propagation of distributions using a Monte Carlo method*. 2008.

[121] G. M. Mahmoud and R. S. Hegazy, "Comparison of GUM and monte carlo methods for the uncertainty estimation in hardness measurements," *International Journal of Metrology and Quality Engineering*, vol. 8, p. 14, 2017.

[122] Z. Chen, "Power electronic converter systems for direct drive renewable energy applications," in *Electrical drives for direct drive renewable energy systems*, pp. 106–135, Elsevier, 2013.

[123] "Signal to Noise Ratio (SNR) Educational Notes." https://www.princetoninstruments.com/learn/camera-fundamentals/signal-to-noise-ratio. Last accessed 12 December 2023.

[124] J. Yang, D. Liu, J. Xue, B.and Lyu, J. Liu, F. Li, X. Ren, W. Ge, B. Liu, X. Ma, and B. Lyu, "Design and ground verification for multispectral camera on the mars tianwen-1 rover," *Space Sci. Rev.*, vol. 218, Apr. 2022.

[125] Y. Zhang, H. Wang, H. Li, J. Sun, H. Liu, and Y. Yin, "Optimization Model of Signal-to-Noise Ratio for a Typical Polarization Multispectral Imaging Remote Sensor," *Sensors*, vol. 22, no. 17, 2022.

[126] "AQ600 Multispectral Camera Wide Aperture and High-Resolution Multispectral Camera." https://www.jouav.com/products/aq600.html. Last accessed 1 April 2024.

[127] R. Minařík, J. Langhammer, and J. Hanuš, "Radiometric and atmospheric corrections of multispectral μmca camera for uav spectroscopy," *Remote Sensing*, vol. 11, no. 20, p. 2428, 2019.

[128] Y. Tu, S. Phinn, K. Johansen, and A. Robson, "Assessing radiometric correction approaches for multi-spectral uas imagery for horticultural applications," *Remote Sensing*, vol. 10, no. 11, p. 1684, 2018.

[129] J. Kelcey and A. Lucieer, "Sensor correction and radiometric calibration of a 6-band multispectral imaging sensor for uav remote sensing," *The International Archives of the Photogrammetry, Remote Sensing and Spatial Information Sciences*, vol. 39, pp. 393–398, 2012.

[130] F. Chen, P. Zhang, G. Zheng, and S. Wang, "Measurement and analysis of infrared radiation characteristics of uav," in *Third International Computing Imaging Conference (CITA 2023)*, vol. 12921, pp. 1511–1517, SPIE, 2023.

[131] L. Deng, X. Hao, Z. Mao, Y. Yan, J. Sun, and A. Zhang, "A subband radiometric calibration method for uav-based multispectral remote sensing," *IEEE Journal of Selected Topics in Applied Earth Observations and Remote Sensing*, vol. 11, no. 8, pp. 2869–2880, 2018.

[132] C. Wang and S. Myint, "A simplified empirical line method of radiometric calibration for small unmanned aircraft systems-based remote sensing," *IEEE Journal of selected topics in applied earth observations and remote sensing*, vol. 8, no. 5, pp. 1876–1885, 2015.

[133] K. Xu, Y. Gong, S. Fang, K. Wang, Z. Lin, and F. Wang, "Radiometric calibration of uav remote sensing image with spectral angle constraint," *Remote Sensing*, vol. 11, no. 11, p. 1291, 2019.

[134] F. Khalesi, I. Ahmed, P. Daponte, F. Picariello, L. De Vito, and I. Tudosa, "Uncertainty assessment of NDVI measurement with radiometric compensation by means of monte carlo analysis," in *IEEE I2MTC*, IEEE, 2025.

[135] S. Gennaro, P.Toscano, M.Gatti, S.Poni, A.Berton, and A.Matese, "Spectral comparison of uav-based hyper and multispectral cameras for precision viticulture," *Remote Sensing*, vol. 14, no. 3, p. 449, 2022.

[136] A. LLC, "Agisoft Metashape User Manual, Professional Edition, Version 1.8," 2022. Last accessed 02 June 2025.

[137] D. Semyonov, "Topic: Algorithms used in Photoscan," 2011. Last accessed 02 June 2025.

[138] S. Vélez *et al.*, "Speeding up uav-based crop variability assessment through a data fusion approach using spatial interpolation for site-specific management," *Agricultural Technologies*, vol. XX, pp. XX–XX, 2024.

[139] Y. Tian, P. Guo, and M. R. Lyu, "Comparative studies on feature extraction methods for multispectral remote sensing image classification," in *2005 IEEE International Conference on Systems, Man and Cybernetics*, vol. 2, pp. 1275–1279, IEEE, 2005.

[140] J. Su, D. Yi, B. Su, Z. Mi, C. Liu, X. Hu, X. Xu, L. Guo, and W. H. Chen, "Aerial visual perception in smart farming: Field study of wheat yellow rust monitoring," *IEEE transactions on industrial informatics*, vol. 17, no. 3, pp. 2242–2249, 2020.

[141] J. Su, L. Cunjia, M. Coombes, X. Hu, C. Wang, X. Xu, Q. Li, L. Guo, and W. Chen, "Wheat yellow rust monitoring by learning from multispectral UAV aerial imagery," *Computers and electronics in agriculture*, vol. 155, pp. 157–166, 2018.

[142] Q. Pan, M. Gao, P. Wu, J. Yan, , and S. Li, "A deep-learning-based approach for wheat yellow rust disease recognition from unmanned aerial vehicle images," *Sensors*, vol. 21, no. 19, p. 6540, 2021.

[143] F. Khalesi, A. Talaeizadeh, A. Alasty, P. Daponte, L. De Vito, and F. Picariello, "Performance assessment of machine learning algorithms for yellow rust wheat disease classification with uav rgb images," in *2024 IEEE International Workshop on Metrology for Agriculture and Forestry (MetroAgriFor)*, pp. 450–455, IEEE, 2024. © 2024 IEEE. Reprinted with permission.

[144] X. Zhang, L. Han, Y. Dong, Y. Shi, W. Huang, L. Han, P. González-Moreno, H. Ma, H. Ye, and T. Sobeih, "A deep learning-based approach for automated yellow rust disease detection from high-resolution hyperspectral UAV images," *Remote Sensing*, vol. 11, no. 13, p. 1554, 2019.

[145] T. Zhang, Z. Yang, Z. Xu, and J. Li, "Wheat yellow rust severity detection by efficient DF-UNet and UAV multispectral imagery," *IEEE Sensors Journal*, vol. 22, no. 9, pp. 9057–9068, 2022.

[146] C. Nguyen, V. Sagan, J. Skobalski, and J. I. Severo, "Early detection of wheat yellow rust disease and its impact on terminal yield with multi-spectral UAV-imagery," *Remote Sensing*, vol. 15, no. 13, p. 3301, 2023.

[147] T. Fahey, H. Pham, A. Gardi, R. Sabatini, D. Stefanelli, I. Goodwin, and D. W. Lamb, "Active and passive electro-optical sensors for health assessment in food crops," *Sensors*, vol. 21, no. 1, p. 171, 2020.

[148] F. Zhu, J. Gao, J. Yang, and N. Ye, "Neighborhood linear discriminant analysis," *Pattern Recognition*, vol. 123, p. 108422, 2022.

[149] J. Ghosh and S. B. Shuvo, "Improving classification model's performance using linear discriminant analysis on linear data," in *2019 10th International Conference on Computing, Communication and Networking Technologies (ICCCNT)*, pp. 1–5, IEEE, 2019.

[150] S. Shalev-Shwartz and S. Ben-David, *Understanding machine learning: From theory to algorithms*. Cambridge university press, 2014.

[151] A. Moslemi, "A tutorial-based survey on feature selection: Recent advancements on feature selection," *Engineering Applications of Artificial Intelligence*, vol. 126, p. 107136, 2023.

[152] A. Tharwat, T. Gaber, A. Ibrahim, and A. E. Hassanien, "Linear discriminant analysis: A detailed tutorial," *AI communications*, vol. 30, no. 2, pp. 169–190, 2017.

[153] S.Bilal, R.M.Sahith, and M.Piyush, *IoT-Based Smart Tree Management Solution for Green Cities*, vol. 67. Springer Science and Business Media Deutschland GmbH, 2020.

[154] Y.Wei, K. H.Wang, Y.Liu, CK.Wu, H.Zhu, Y.T.Chow, and F.H.Hung, "Proximity environmental feature based tree health assessment scheme using Internet of Things and Machine Learning algorithm," *Sensors*, vol. 19, no. 14, p. 3115, 2019.

[155] H.Wang, Y.Wei, H.Zhu, Y.Liu, C.K.Wu, and K.F.Tsang, "NB-IoT based tree health monitoring system," in *2019 IEEE International Conference on Industrial Technology (ICIT)*, pp. 1796–1799, IEEE, 2019.

[156] C.Y.Jim, "Monitoring the performance and decline of heritage trees in urban Hong Kong," *Journal of Environmental Management*, vol. 74, no. 2, pp. 161–172, 2005.

[157] R.A.Mouha, "Internet of Things (IoT)," *Journal of Data Analysis and Information Processing*, vol. 9, no. 2, pp. 77–101, 2021.

[158] Z.J.Trinovita, M.R.Nurtam, I.Laksmana, P.Putera, I.A.Putri, *et al.*, "The implementation of the Internet of Things (IoT) on an automatic plant watering and fertilizing system based on solar electricity," in *IOP Conference Series: Earth and Environmental Science*, vol. 1097, p. 012057, IOP Publishing, 2022.

[159] S.Kaushik, N.M.Maytham, K.Pardeep, R.Soundar, and K.Seifedine, "Smart agriculture management system using Internet of Things," *Telkomnika*, vol. 18, pp. 1275–1284, 2020.

[160] R.S.Sinha, Y.Wei, and S.Hwang, "A survey on LPWA technology: LoRa and NB-IoT," *Ict Express*, vol. 3, no. 1, pp. 14–21, 2017.

[161] "LoRaWAN: Long range wireless protocols." Last accessed 22 January 2025.

[162] P.Daponte, F.Lamonaca, F.Picariello, L. Vito, G.Mazzilli, and I.Tudosa, "A survey of measurement applications based on IoT," in *2018 Workshop on Metrology for Industry 4.0 and IoT*, pp. 1–6, IEEE, 2018.

[163] "Volt Band Dendrometer Manual, DBV60." https://ictinternational.com/wp-content/uploads/2023/08/DBV60-Manual-2020-07.pdf. Last accessed 24 August 2023.

[164] "SQ-612-SS." https://www.apogeeinstruments.com/sq-612-ss-400-750-nm-0-2-5-v-output-epar-sensor/#product-tab-information. Last accessed 16 August 2023.

[165] "PAR-FAR Sensor." https://www.apogeeinstruments.com/s2-441-ss-sdi-12-par-far-sensor/#product-tab-information. Last accessed 20 August 2024.

[166] "SFM-5 Sap flow sensor." https://ugt-online.de/en/solutions/sfm-5-sap-flow-sensor/. Last accessed 16 August 2023.

[167] "AML Analog MEMS Inclinometer Series." https://jewellinstruments.com/products/inertial-tilt-sensors/inclinometer/mems-i/aml-analog-mems-inclinometer-series/. Last accessed 16 August 2023.

[168] T. Emmerik, S.Steele-Dunne, R.Hut, P.Gentine, M.Guerin, R.S.Oliveira, J.Wagner, J.Selker, and N. D. Giesen, "Measuring tree properties and responses using low-cost accelerometers," *Sensors*, vol. 17, no. 5, p. 1098, 2017.

[169] "AXIS M3077-PLVE Network Camera." Last accessed 16 August 2023.

[170] "FLIR AX8." https://www.flir.com/products/ax8-automation/?vertical=rd+science&segment=solutions. Last accessed 16 August 2023.

[171] P.K.Rai, "Impacts of particulate matter pollution on plants: Implications for environmental biomonitoring," *Ecotoxicology and environmental safety*, vol. 129, pp. 120–136, 2016.

[172] "Alphasense Datasheets." https://www.alphasense.com/downloads/. Last accessed 16 August 2023.

[173] H.K.Lee, I.Khaine, M.J.Kwak, J.H.Jang, T.Y.Lee, J.K.Lee, I.R.Kim, K.W.Il, K.S.Oh, and S.Y.Woo, "The relationship between SO 2 exposure and plant physiology: A mini review," *Horticulture, Environment, and Biotechnology*, vol. 58, pp. 523–529, 2017.

[174] "Alphasense NO2-A4." https://pdf.directindustry.com/pdf/alphasense/no2-a4/16860-592350.html. Last accessed 16 August 2023.

[175] D.B.Lobell, S. Tommaso, and J.A.Burney, "Globally ubiquitous negative effects of nitrogen dioxide on crop growth," *Science Advances*, vol. 8, no. 22, p. eabm9909, 2022.

[176] "Alphasense O3-A4." https://pdf.directindustry.com/pdf/alphasense/o3-a4/16860-592348.html. Last accessed 16 August 2023.

[177] "GMX600 Compact Weather Station." https://gillinstruments.com/wp-content/uploads/2022/08/1957-010-Maximet-gmx600-Iss-10.pdf. Last accessed 16 August 2023.